PHYSICS REPORTS (Review Section of Physics Letters) 208, Nos. 4 & 5 (1991) 267–394. North-Holland

THE R-PROCESS AND NUCLEOCHRONOLOGY

John J. COWAN

Department of Physics and Astronomy, University of Oklahoma, Norman, OK 73019, USA

Friedrich-Karl THIELEMANN

Department of Astronomy, Harvard University, Cambridge, MA 02138, USA

and

James W. TRURAN

Department of Astronomy and Astrophysics, University of Chicago, Chicago, IL 60637, USA

Editor: D.N. Schramm Received April 1991

Contents:

THE R-PROCESS AND NUCLEOCHRONOLOGY

John J. COWAN

Department of Physics and Astronomy, University of Oklahoma, Norman, OK 73019, USA

Friedrich-Karl THIELEMANN

Department of Astronomy, Harvard University, Cambridge, MA 02138, USA

and

James W. TRURAN

Department of Astronomy and Astrophysics, University of Chicago, Chicago, IL 60637, USA

NORTH-HOLLAND

Abstract:

The r-process of nucleosynthesis is the process which is responsible for the synthesis of approximately half of the nuclear species in nature that are more massive than iron. This process of heavy-element synthesis involves the progressive buildup of heavier isotopes via neutron captures proceeding on neutron-rich isotopes, interspersed by beta decays. Its abundance features clearly reflect nuclear properties – the maxima are related to the magic neutron numbers $N = 50$, 82 and 126. It probes our knowledge of the properties of nuclei far from the region of beta stability, even through the position of the neutron drip line. The r-process also forms the important long-lived nuclear chronometers ^{232}Th, ^{238}U and ^{235}U that are utilized for dating the Galaxy.

While the astrophysical site for r-process nucleosynthesis is not yet identified, its association with massive stars undergoing type II supernova events is strongly suggested. This can be deduced from the observation that r-process nuclei are already present in the oldest and most metal-deficient stars, which are the tracers of the chemical evolution of the Galaxy. The massive stars that become type II supernovae evolve fastest and contribute their ejecta to the interstellar medium at the earliest beginnings of the chemical evolution of the Galaxy.

When utilizing the knowledge of the r-process production ratios of the long-lived chronometer nuclei, their observed ratios in primitive meteorites and our (limited) knowledge of star formation throughout galactic evolution, one can put limits on the duration of galactic nucleosynthesis, the age of the Galaxy and the universe. The latter has a large uncertainty but is comparable with ages estimated from globular clusters and cosmology.

This paper will provide a review of the basic physics underlying the r-process, the operation of the mechanisms for r-process nucleosynthesis, the possible astrophysical sites, their time evolution in galactic evolution models, and the inferred ages of the Galaxy.

1. Introduction

Nucleosynthesis studies are generally concerned with the diverse processes by which the heavy elements observed in nature were synthesized in astrophysical environments. It is now understood that most of the elements in nature heavier than helium are the products of thermonuclear reactions in stars and supernova explosions. Cosmological Big Bang nucleosynthesis is found to account for the observed primordial concentrations of ^{1}H, ^{2}H, ^{3}He, ^{4}He and ^{7}Li [Boesgaard and Steigman 1985]. The interactions of cosmic rays with the constituents of the interstellar medium yield the light elements ^{6}Li, ^{9}Be, ^{10}B and ^{11}B. While there exist ideas that some heavier nuclei can be produced in inhomogeneous big bang scenarios, the dominant fraction of the remaining nuclei are synthesized in stellar environments. The various nuclear processes occurring in stars and supernovae, which are responsible for nuclear energy generation and for the formation of the heavy elements, were identified and defined in the now classic papers by Burbidge et al. [1957] and by Cameron [1957]. General reviews of nucleosynthesis include those by Trimble [1975], Truran [1984] and Woosley [1986].

Nucleosynthesis products can be distinguished on the basis both of the nuclear physics and of the astrophysical setting. Charged-particle thermonuclear reactions dominate the production of the heavy elements through approximately iron and nickel. Stellar evolution is defined by a sequence of alternate stages of gravitational contraction to higher temperatures and densities and the thermonuclear burning of the available fuel at these temperatures. In more massive stars ($M > 10\ M_\odot$), such phases of stellar energy generation and nucleosynthesis continue through the formation of an iron core, core collapse and a type II supernova event. Explosive charged-particle nucleosynthesis conditions are also achieved in the shock heating and ejection of matter in both type I and type II supernovae (see, e.g., the review by Woosley and Weaver [1986] and references therein).

Since the nuclei in the vicinity of iron are the most stable, in the sense that they are characterized by the highest binding energies per nucleon, it is clear that no further stable phases of stellar evolution are possible. Moreover, the effectiveness of charged-particle-induced fusion reactions is further constrained by the fact that the high temperatures demanded to overcome the increasing Coulomb barriers also drive rapid photonuclear reactions. It follows that the synthesis of nuclei past the iron group involves neutron-capture reaction mechanisms. As we shall discuss in the next section, there are two quite distinct neutron-capture processes that dominate the production of the heavy nuclei: the s-process and the r-process. Reviews of the s-process have been provided by Ulrich [1973, 1982], Truran [1980], Mathews and Ward [1985], and Käppeler et al. [1989].

This review is concerned with the mechanism of nucleosynthesis by rapid neutron captures (the r-process). Earlier reviews of the r-process include those by Hillebrandt [1978], Schramm [1982], Mathews and Ward [1985], and Mathews and Cowan [1990]. The r-process is an important nucleosynthesis mechanism for a number of reasons: (1) it is responsible for the production of approximately one half of all the stable nuclei observed in nature in the heavy-element region $A > 60$; (2) it is the nucleosynthesis mechanism that forms the important long-lived galactic nuclear chronometers ^{232}Th, ^{235}U, ^{238}U and ^{244}Pu; (3) it serves to provide useful clues to and constraints upon the nuclear properties of neutron-rich heavy nuclei; and (4) it provides an important probe of the temperature–density conditions in explosive events which contain highly neutronized matter.

The plan of this report proceeds as follows. The nature of the r-process is described in section 2 and the observed r-process abundances in galactic matter are reviewed. A discussion of the nuclear physics of the r-process is presented in section 3. The set of equations which govern r-process nucleosynthesis and its solution are outlined in section 4. There follow detailed discussions of the possible sites and astrophysical models for the operation of the r-process in section 5, and the implications of these models for the chemical evolution of r-process abundances over the history of the Galaxy in section 6. Section 7 presents the discussion of specific long-lived isotopes and their use for nucleocosmochronology, i.e. the determination of the duration of r-process nucleosynthesis over galactic history. A summary and conclusions follow in section 8.

2. The nature of the r-process and r-process abundances

Nucleosynthesis theory predicts that the formation of most of the nuclear species of mass $A > 60$ occurs in nature as a consequence of neutron-capture processes. Strong support for this view is provided by the patterns of heavy-element abundances characteristic of solar system matter [Cameron 1982a; Anders and Ebihara 1982; Anders and Grevesse 1989], as illustrated in fig. 2.1. The abundance features in the heavy-element region are seen to be correlated with the positions of the neutron shell closures at neutron numbers $N = 50$, 82 and 126. The splitting of the abundance peaks in the mass regions $A = 80$–90, 130–140 and 190–210, in fact, reveals signatures of two distinct neutron fluxes. This has led historically to the definition of two nucleosynthesis processes that are identified with quite different astrophysical environments.

The distinction is made here largely on the basis of the relative lifetimes for neutron captures (τ_n) and beta decays (τ_β). The condition that $\tau_n > \tau_\beta$, where τ_β is a characteristic lifetime for beta-unstable nuclei *near* the valley of beta stability, ensures that, as captures proceed, the neutron-capture path will itself remain close to the valley of beta stability. This defines the astrophysical s-process of neutron capture. The s-process flow path through a representative region is illustrated in fig. 2.2. The short beta-decay timescales, in comparison with the neutron-capture timescales, constrain the flow to the vicinity of the valley of stability. In the mass region $A > 209$, we encounter only unstable nuclei. Also, beta-stable nuclei may undergo alpha decay, back to $A < 209$, on timescales that are short compared to the s-process neutron-capture timescale. The small cross sections for neutron capture away from the closed-shell configurations at $N = 50$, 82 and 126 along the s-process neutron-capture path (the valley of

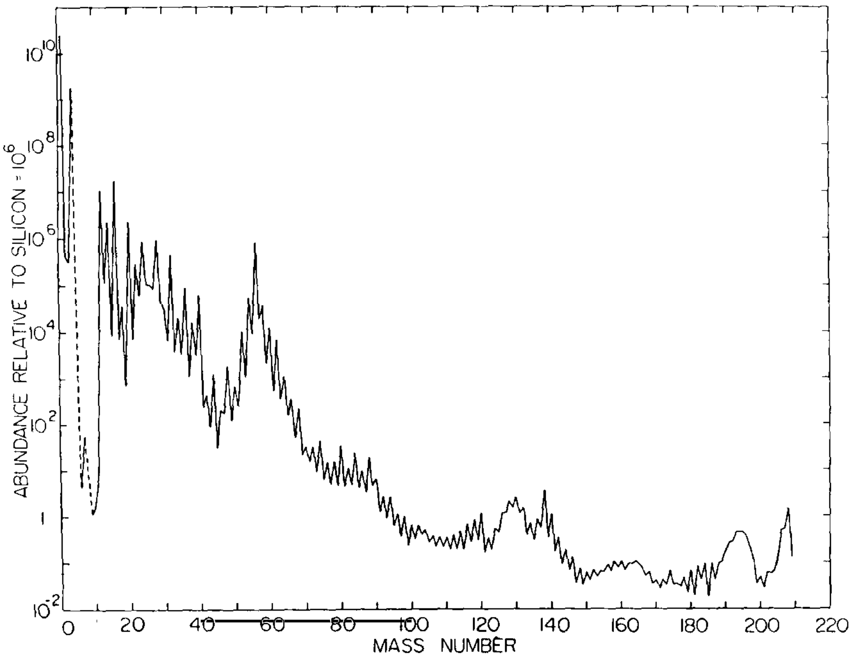

Fig. 2.1. Heavy-element abundances characteristic of solar-system matter [Cameron 1982a] (see Anders and Grevesse [1989] for updated values).

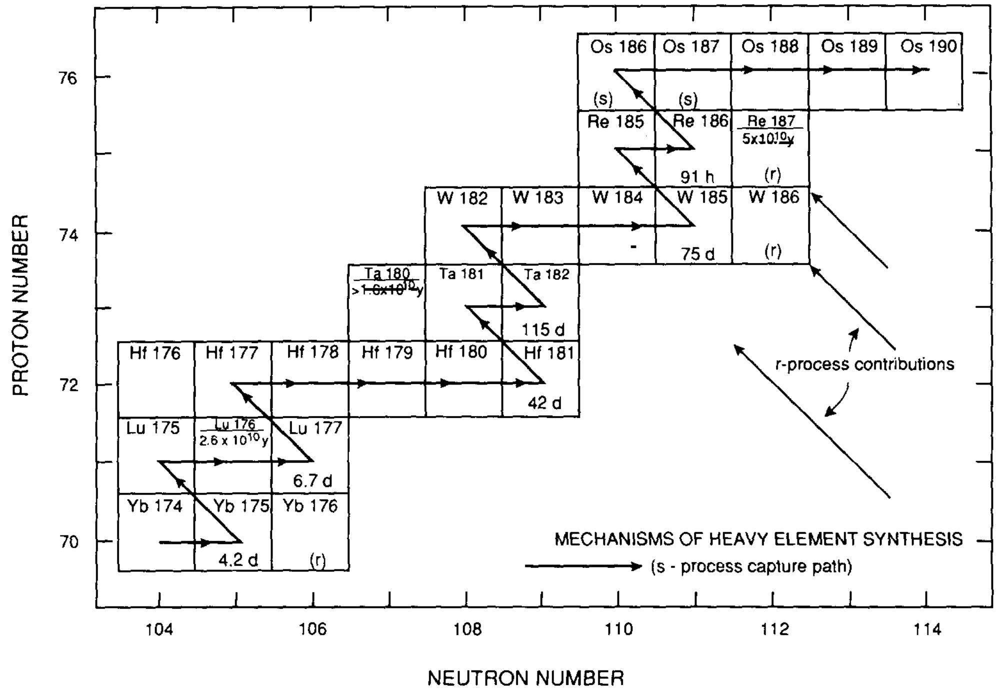

Fig. 2.2. A typical portion of the heavy-element region illustrating the characteristics of heavy-element synthesis (after Truran [1973]). The s-process path, which is constrained to the valley of beta stability, is indicated. Neutron-rich isotopes (r) formed by the r-process are identified.

beta stability) give rise to the pronounced abundance peaks at strontium ($A = 88$), barium ($A = 138$) and lead ($A = 208$), which involve isotopes with magic neutron numbers.

In the limit of large neutron densities ($\tau_n \ll \tau_\beta$), it follows that successive neutron captures will proceed into the neutron-rich regions well off the beta-stable valley. For the large neutron fluxes characteristic of this process, the closed neutron shells at neutron numbers $N = 82$ and 126 are encountered in the neutron-rich regions at lower proton numbers (rather than along the beta-stable valley), and thus at a smaller mass number A. Following the exhaustion of the neutron flux, the capture products approach the position of the valley of beta stability by beta decay. The broad abundance features in the vicinity of mass numbers $A = 80$, $A = 130$ and $A = 190$, which are located at smaller mass numbers than the s-process peaks, are believed to be formed in this manner. Neutron-rich isotopes, such as ^{176}Yb, ^{186}W and ^{187}Re, shown in fig. 2.2, which lie off the s-process capture path are also the result of the beta decays. This r-process neutron-capture mechanism is expected to operate in an environment characterized by a very high neutron flux.

The early work by Cameron [1955, 1957] and Burbidge et al. [1957] established the basic characteristics of these two processes and the timescales for their operation. The modes of operation of the two neutron-capture mechanisms are fundamentally the same. Both demand an appropriate source of free neutrons and (ultimately) an abundance of seed nuclei on which they are to be captured. For the s-process, iron-peak nuclei constitute the seeds, while neutrons are provided by reactions such as ^{13}C(α, n)^{16}O and ^{22}Ne(α, n)^{25}Mg, which arise during the normal course of the evolution of red giants. The conditions required for the r-process include a high ratio of free neutrons to heavy seed nuclei, perhaps suggestive of a supernova environment. The neutron flux generally associated with the r-process is sufficiently high that the most neutron-rich isotopes along the r-process capture path have beta-decay lifetimes less than one second and more typically 10^{-2} to 10^{-1} s.

In contrast, lower limits on the lifetimes of critical nuclei participating in the s-process range from about 10 to 100 years. It is thus quite understandable why the s-process has been found to be associated with earlier, largely hydrostatic phases of stellar evolution, while the r-process is instead believed to be associated with supernovae. In particular, the identification of red-giant stars as an active site of s-process nucleosynthesis seems firm, as the presence both of technetium and of enchanced abundances of strontium, yttrium, zirconium, barium and lanthanum in some categories of red giants supports the view that heavy elements are synthesized in the interiors of these stars and subsequently carried to the surface by convection.

As studies proceeded, the complexity of the s-process mechanism began to emerge. Clayton et al. [1961] determined that no single neutron exposure could account for the distribution of the s-process elements in solar system matter. Seeger et al. [1965] demonstrated that an exponential distribution of exposures does provide a reasonable fit. Questions concerning the solution of the s-process network equations, the role of beta decays, and the timescale of the s-process were addressed by a number of authors. The problem that remained was to identify the stellar environment. Peters [1968] performed detailed calculations of s-process synthesis in massive stellar cores near the end of the helium-burning phase and concluded that the maximum neutron exposures that could be achieved in this environment were less than that characterizing solar-system matter; subsequent studies have confirmed this result [Lamb et al. 1977; Prantzos et al. 1990]. Recent studies of the more promising s-process environment provided by the convective helium-burning shells of thermally pulsing red-giant stars are surveyed in several recent reviews and papers [Mathews and Ward 1985; Käppeler et al. 1989; Gallino et al. 1988; Hallowell and Iben 1989].

It is possible to isolate and thus to identify the individual s-process and r-process contributions to solar-system abundances. The procedure is based on the ability to reproduce successfully the empirically determined products of neutron-capture cross section times s-process abundance, σN_s, for shielded isotopes formed only by the s-process. Recent reviews of progress in our understanding of the σN_s curve have been provided by Mathews and Ward [1985] and Käppeler et al. [1989]. Significant improvements in fitting this curve have recently been achieved with the use of an improved set of experimental neutron-capture cross sections [Bao and Käppeler 1987] and the updated abundance compilation of Anders and Grevesse [1989]. The effects of these improvements are evident in fig. 2.3, where the σN_s curve of Käppeler et al. [1982] is compared with that of Käppeler et al. [1989]. The main s-process component is shown in this figure as a heavy, full curve, with the contribution from the weak component in the low-mass region being indicated by a lighter curve. After this curve is defined for

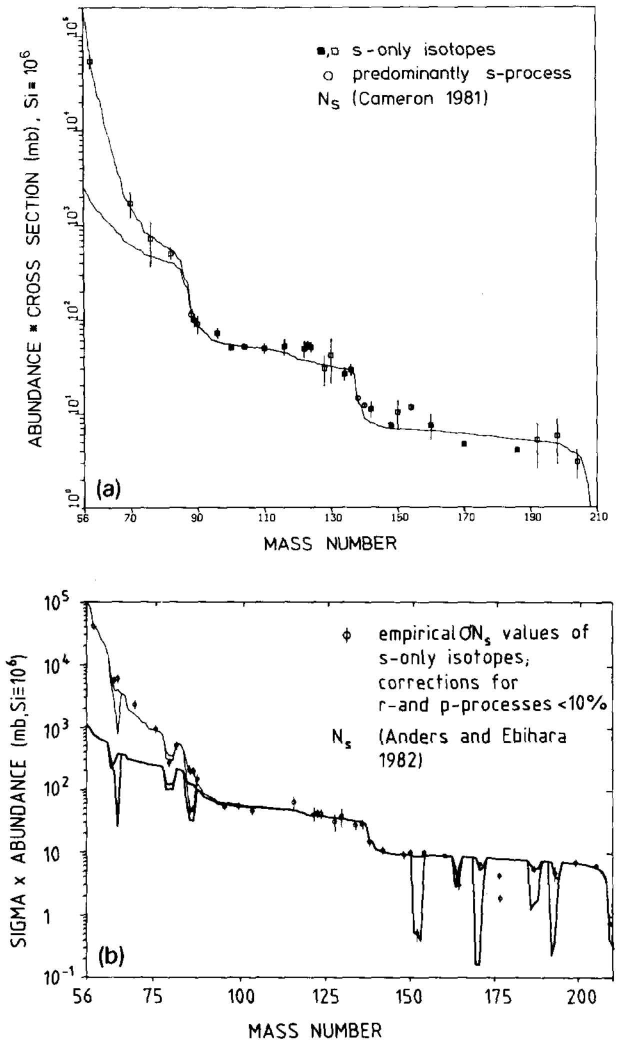

Fig. 2.3. The product of cross section times s-process abundance versus mass number. Comparison of the calculated curves from (a) Käppeler et al. [1982] (with N_s from Cameron [1982a]) with (b) Käppeler et al. [1989] (with N_s from Anders and Ebihara [1982]). Symbols with error bars denote the empirical products of pure or almost pure s-isotopes (from Käppeler et al. [1989]).

pure s-process nuclei, it can then be utilized to determine the s-process contributions, N_s, for all other nuclei. Käppeler et al. [1989] argue that the present σN_s curve is accurate to ±10%.

With such accuracy, it becomes possible to provide a far more reliable estimate of the r-process abundance contributions. The r-process residuals $N_r = N_\odot - N_s$, obtained by Käppeler et al. [1989], are plotted in fig. 2.4, together with the abundances of the r-only isotopes. Numerical values for the points on these curves are also compiled in table 2.1, taken from table 4 of Käppeler et al. [1989]. We consider these to represent the best estimate of the solar-system r-process abundance pattern currently available. We note, in particular, the substantial agreement between the calculated distribution of r-process abundances (residuals) and that of the r-only isotopes. Throughout our subsequent discussions, we shall utilize the empirically determined r-process abundances of Käppeler et al. [1989] as the standard to which all theoretical calculations are to be compared.

The r-process and s-process abundance patterns as determined by Cameron [1982b] are shown in fig. 2.5. An important distinguishing feature of s-process and r-process nucleosynthesis processes is clearly evident in this figure: s-process abundances show pronounced odd–even variations, while such effects are substantially reduced or largely absent in the r-process abundance pattern. It is generally believed that the reduced odd–even variations in the r-process abundances are partly a consequence of the effects of beta-delayed neutron emission, as the nuclei formed along the r-process path approach the valley of beta stability via beta decay [Cameron et al. 1970; Kodama and Takahashi 1975].

Interest in the astrophysical r-process event has been maintained by the continued desire to understand this important source of heavy nuclei and its astrophysical site. In addition, accurate predictions are required of the important cosmochronological production ratios $^{232}\mathrm{Th}/^{238}\mathrm{U}$, $^{235}\mathrm{U}/^{238}\mathrm{U}$, $^{244}\mathrm{Pu}/^{238}\mathrm{U}$ and $^{129}\mathrm{I}/^{127}\mathrm{I}$. This has ensured that r-process nucleosynthesis remains an active area for research. The fact that nuclei from the valley of beta stability through to the neutron drip line can in principle participate in the r-process buildup of heavy and possibly superheavy nuclei, reflects the complexity of the problem.

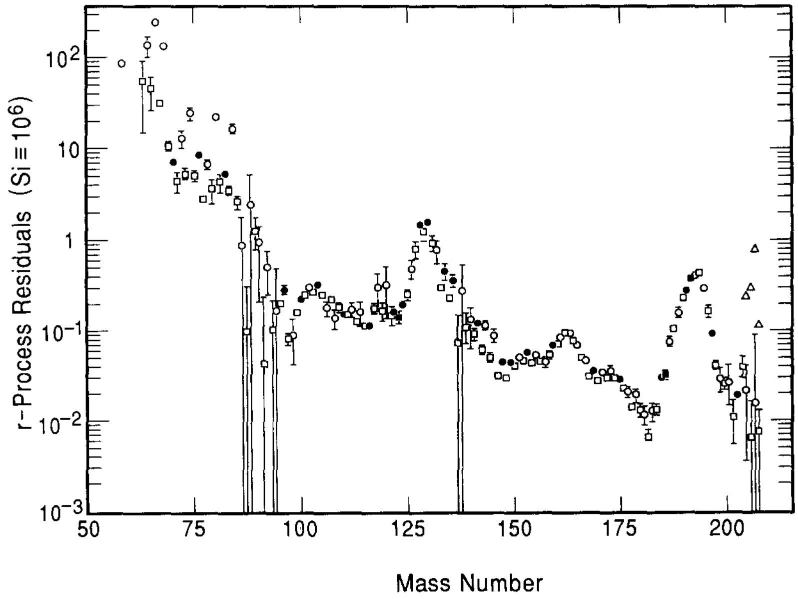

Fig. 2.4. R-process residuals, $N_r = N_\odot - N_s$ (open symbols) and r-only isotopes (filled symbols) from Käppeler et al. [1989].

Table 2.1
R-process residuals and r-only abundances from Käppler et al. [1989]

Mass number	Element	$N_r = N_\odot - N_s$ [a] (Si = 10^6)	Mass number	Element	$N_r = N_\odot - N_s$ [a] (Si = 10^6)	Mass number	Element	$N_r = N_\odot - N_s$ [a] (Si = 10^6)
63	Cu	60.0 ± 44.0	113	Cd	0.0134 ± 0.014	166	Er	0.0722 ± 0.0041
64	Ni	150.0 ± 39.0	114	Cd	0.170 ± 0.056	167	Er	0.0530 ± 0.0027
64	Zn		115	In	0.119 ± 0.013	168	Er	0.0483 ± 0.0040
65	Cu	49.0 ± 21.0	116	Cd	**0.119 ± 0.008**	169	Er	
65	Zn		117	Sn	0.194 ± 0.034	169	Tm	0.0320 ± 0.0025
66	Zn	265 ± 16.0	118	Sn	0.315 ± 0.145	170	Er	**0.0376 ± 0.0017**
67	Zn	34 ± 2.7	119	Sn	0.175 ± 0.043	170	Tm	
68	Zn	145 ± 14.0	120	Sn	0.341 ± 0.199	170	Yb	
69	Ga	11.6 ± 1.6	121	Sb	0.155 ± 0.037	171	Tm	
70	Zn	**7.81 ± 0.79**	122	Sn	**0.174 ± 0.016**	171	Yb	0.0292 ± 0.0013
71	Ga	4.7 ± 1.2	123	Sb	**0.150 ± 0.027**	172	Yb	0.0356 ± 0.0025
72	Ge	14.0 ± 3.0	124	Sn	**0.215 ± 0.020**	173	Yb	0.0311 ± 0.0016
73	Ge	5.67 ± 0.86	125	Te	0.269 ± 0.042	174	Yb	0.0367 ± 0.0048
74	Ge	27.3 ± 4.4	126	Te	0.518 ± 0.126	175	Lu	0.0309 ± 0.0037
75	As	5.33 ± 0.75	127	I	0.850 ± 0.189	176	Yb	**0.0300 ± 0.0011**
76	Ge	**9.20 ± 0.95**	128	Te	**1.560 ± 0.187**	176	Hf	
77	Se	3.04 ± 0.30	129	Xe	1.314 ± 0.277	177	Hf	0.0241 ± 0.0020
78	Se	7.21 ± 0.94	130	Te	**1.690 ± 0.203**	178	Hf	0.0215 ± 0.0030
79	Se	3.87 ± 1.13	131	Xe	0.995 ± 0.218	179	Hf	0.0146 ± 0.0015
79	Br		132	Xe	0.829 ± 0.268	180	Hf	0.0197 ± 0.0040
80	Se	24.3 ± 1.99	133	Cs	0.316 ± 0.023	181	Ta	0.0133 ± 0.0023
80	Kr		134	Xe	**0.482 ± 0.097**	182	W	0.0116 ± 0.0029
81	Br	4.64 ± 1.11	135	Ba	0.242 ± 0.017	183	W	0.0067 ± 0.0016
81	Kr		136	Xe	**0.391 ± 0.078**	184	W	0.0128 ± 0.0034
82	Se	**5.71 ± 0.74**	137	Ba	0.074 ± 0.082	185	W	
83	Kr	3.75 ± 0.47	138	Ba	<0.29	186	Re	0.0141 ± 0.0024
84	Kr	18.00 ± 2.45	139	La	0.111 ± 0.035	186	W	0.0314 ± 0.0029
85	Kr	2.79 ± 0.47	140	Ce	0.131 ± 0.075	186	Os	
85	Rb		141	Pr	0.095 ± 0.016	187	Re	**0.0333 ± 0.0041**
86	Kr	0.93	142	Ce	**0.129 ± 0.007**	187	Os	
86	Sr		143	Nd	0.0647 ± 0.0073	188	Os	0.0793 ± 0.0094
87	Rb	0.10 ± 0.22	144	Nd	0.121 ± 0.015	189	Os	0.1108 ± 0.0113
87	Sr		145	Nd	0.0521 ± 0.0060	189	Os	0.1676 ± 0.0188
88	Sr	2.55 ± 2.84	146	Nd	0.092 ± 0.017	190	Os	0.1676 ± 0.0188
89	Y	1.31 ± 0.50	147	Pm	0.0331 ± 0.0030	191	Os	
90	Zr	0.99 ± 0.77	148	Nd	**0.0477 ± 0.0033**	191	Ir	0.2413 ± 0.0155
91	Zr	0.04 ± 0.21	149	Sm	0.0316 ± 0.0028	192	Os	**0.2929 ± 0.0288**
92	Zr	0.54 ± 0.28	150	Nd	**0.0468 ± 0.0033**	192	Ir	
93	Zr	0.11 ± 0.12	151	Sm	0.0426 ± 0.0038	192	Pt	
94	Zr	0.17 ± 0.34	151	Eu		193	Ir	**0.4084 ± 0.0261**
95	Mo	0.213 ± 0.024	152	Eu	0.0523 ± 0.0054	193	Pt	
96	Zr	**0.300 ± 0.039**	152	Gd		194	Pt	0.4312 ± 0.0451
97	Mo	0.087 ± 0.015	153	Eu	0.0481 ± 0.0042	195	Pt	0.4572 ± 0.0463
98	Mo	0.093 ± 0.051	153	Gd		196	Pt	0.3123 ± 0.0349
99	Tc	0.172 ± 0.014	154	Sm	**0.0605 ± 0.0045**	197	Au	0.1756 ± 0.0279
99	Ru		155	Gd	0.0462 ± 0.0023	198	Pt	**0.0986 ± 0.0099**
100	Mo	**0.242 ± 0.013**	156	Gd	0.0559 ± 0.0035	199	Hg	0.0434 ± 0.0056
101	Ru	0.266 ± 0.017	157	Gd	0.0469 ± 0.0025	200	Hg	0.0298 ± 0.0094
102	Ru	0.327 ± 0.036	158	Gd	0.0460 ± 0.0052	201	Hg	0.0265 ± 0.0045
103	Rh	0.289 ± 0.028	159	Tb	0.0546 ± 0.0071	202	Hg	0.0256 ± 0.0120
104	Ru	**0.348 ± 0.019**	160	Gd	**0.0722 ± 0.0034**	203	Tl	0.0115 ± 0.0059
105	Pd	0.269 ± 0.024	161	Dy	0.0746 ± 0.0035	204	Hg	**0.0204 ± 0.0023**
106	Pd	0.193 ± 0.035	162	Dy	0.0888 ± 0.0050	205	Tl	0.0412 ± 0.0146
107	Ag	0.239 ± 0.026	163	Dy	0.0982 ± 0.0005	205	Pb	
108	Pd	0.145 ± 0.037	163	Ho		206	Pb	0.2233 ± 0.0434
109	Ag	0.196 ± 0.024	164	Dy	0.0977 ± 0.0056	207	Pb	0.2800 ± 0.0471
110	Pd	**0.164 ± 0.013**	164	Er		208	Pb	0.1184 ± 0.1672
111	Cd	0.162 ± 0.014	165	Ho	0.0818 ± 0.0047	209	Bi	0.0930 ± 0.0127
112	Cd	0.184 ± 0.037						

[a] All values which appear in boldface are $N_{\odot r}$ r-only nuclei (Si = 10^6).

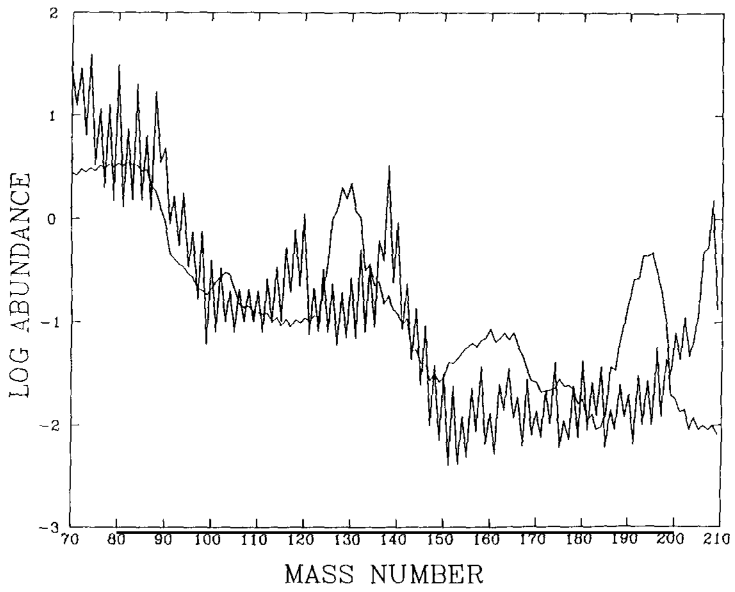

Fig. 2.5. S-process and r-process abundances after Cameron [1982b]; the curve exhibiting small odd–even oscillations is due to the r-process, while that exhibiting pronounced odd–even oscillations is due to the s-process.

In an early study of the r-process mechanism by Seeger et al. [1965], a constant temperature and neutron density were assumed. These, together with a knowledge of the neutron capture, neutron photodisintegration, and beta-decay rates, allow one to define a flow path on the neutron-rich side of the valley of beta stability. Competition between neutron capture and photodisintegration reactions, for the specified conditions, determines the distribution of nuclei along each isotope chain, while the beta-decay lifetimes of the more neutron-rich isotopes dictate the rate of buildup to higher Z. Cameron et al. [1970] argued rather that a proper dynamical study of r-process synthesis must be based on the time-dependent conditions that are expected in the appropriate astrophysical environment. For such conditions, a more accurate and realistic treatment of the complex sequences of nuclear transformations may be demanded.

The site of r-process nucleosynthesis remains a mystery (although, as we shall see, there are strong clues from recent abundance observations). The required high neutron densities and corresponding short timescales are strongly suggestive of a violent event, associated perhaps with a supernova environment. A number of possible models have been explored, with varying degrees of success. These range from examinations of the expansion of neutron-rich matter from the innermost layers ejected in supernova explosions, to studies of conditions resulting from the traversal of supernova shocks through the helium and carbon shells, to neutron-star collisions, and other exotic suggestions.

Proposed models for r-process nucleosynthesis may be conveniently grouped into two broad classes: those involving the expansion and cooling of neutron-rich matter and those concerned with the passage of supernova shock waves through the carbon and helium shells. The former class involves such diverse models as the expansion of neutronized matter from the vicinity of the mass cut in supernova explosions that result in neutron-star remnants [Burbidge et al. 1957; Cameron et al. 1970; Schramm 1973; Hillebrandt et al. 1976], neutronized jets resulting from the collapses of rotating (or magnetized) stars [LeBlanc and Wilson 1970; Meier et al. 1976; Symbalisty et al. 1985], and neutronized jets produced in neutron-star collisions with black holes or a second neutron star [Lattimer and Schramm 1974, 1976; Symbalisty and Schramm 1982]. This work has been nicely reviewed in far greater detail by Hillebrandt [1978], while a very useful general discussion of the conditions required for the r-process is given by Norman and Schramm [1979].

Studies of r-process synthesis occurring after the passage of a supernova shock wave through the outer layers of the stellar core have dealt specifically with the helium shell [Truran et al. 1978a,b; Thielemann et al. 1979; Cowan et al. 1980] and the carbon shell [Lee et al. 1979; Wefel et al. 1981]. These studies have been motivated in part by the many new identifications of stable isotope anomalies in meteorites and the suggestion of their possible relation to neutron-capture properties. The general characteristics of these two classes of studied r-process environments are discussed in section 5, after we have first reviewed the nuclear properties of neutron-rich nuclei and the formalisms for r-process calculations.

The gross features of solar-system r-process abundance patterns can be reasonably well reproduced in such calculations as are noted above: the positions of the r-process peaks, their relative sizes and the absence of substantial odd–even abundance variations. There are, of course, matters of detail on which the calculations differ. A major question here concerns the rates of beta decay. For any model to be successful, it is essential that the beta-decay lifetimes be compatible both with timescales dictated by the prevailing neutron fluxes and with the imposed stellar or dynamic timescales. Very different estimates of beta-decay rates were utilized in these different studies.

The revised beta-decay rates of Klapdor et al. [1984] tend to be higher than the Senbetu [1973] rates utilized by Schramm [1973] and the gross theory predictions of Takahashi et al. [1973] used by Hillebrandt et al. [1976], but they were a factor of a few slower than those calculated by Cameron et al. [1970], based on the methods described by Hansen [1966]. New examinations have led to sets of further improved quasiparticle RPA calculations [Staudt et al. 1989, 1990; Möller and Randrup 1990]. Critical questions concerning the operation of the r-process in the context of realistic hydrodynamic models of supernova events must be addressed. It is worth noting that a mass of only $\sim 10^{-6}\ M_{\odot}$ per supernova

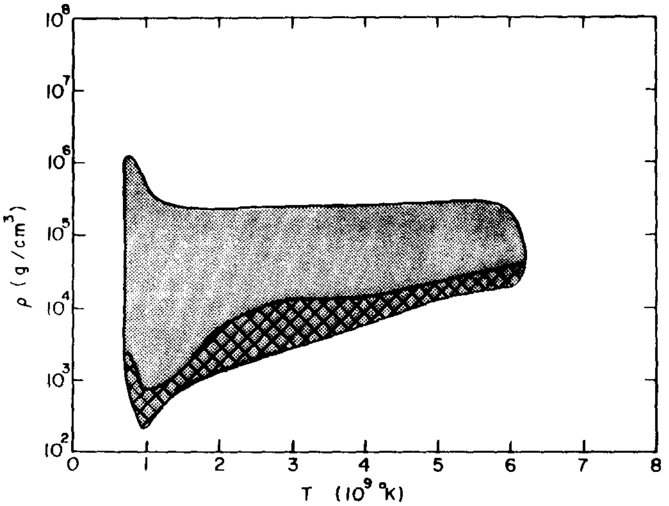

Fig. 2.6. Region of the ρ–T plane in which the seed-nucleus production rate is compatible with the r-process (from Norman and Schramm [1979]). In the shaded region at least 1% (by mass) of the initial α-particles and neutrons are converted into nuclei with $A \geq 24$ in 0.1–30 s. In the cross-hatched region there remain sufficient neutrons, after seed-nucleus production, to allow an r-process to occur.

event needs to be processed in this manner to provide galactic requirements of r-process nuclei [Truran and Cameron 1971].

Norman and Schramm [1979] attempted to characterize the astrophysical conditions required for the operation of the r-process. Rather than study a particular site, they made a study of initial temperatures, densities, neutron/proton ratios and chemical compositions that might lead to the production of r-process nuclei. They identified suitable conditions for which the heavy-element seeds are simultaneously produced during the r-process (i.e. the classical r-process). The region of the T–ρ plane in which the seed-nucleus production rate is compatible with r-process nucleosynthesis is illustrated in fig. 2.6. Norman and Schramm [1979] also found a different set of conditions under which a low neutron-flux r-process (e.g. the helium-driven r-process) can operate.

3. Nuclear physics of the r-process

Figure 3.1 shows the r-process capture path (for a detailed discussion of the effects that determine its location see section 4.1). In fact only within the last few years has it been possible to determine the half-lives of a few nuclei in the bends at magic numbers where the path comes closest to stability (^{80}Zn: Lund et al. [1986], Gill et al. [1986]; ^{130}Cd: Kratz et al. [1986]). Nuclear properties of fundamental importance in r-process calculations are neutron-capture cross sections, beta-decay half-lives and rates of beta-delayed neutron emission; for nuclei with $Z > 80$, beta-delayed fission and neutron-induced fission are also important. The neutron cross sections can be calculated with the statistical model (Hauser–Feshbach) as outlined in section 3.4 as long as the nuclear level densities in the compound nucleus are sufficiently high to justify such an approach. For excitation energies in the compound nucleus of only 2–3 MeV (as indicated for the path in fig. 3.1) this is not the case, but no better treatments are currently available. This statistical method requires the knowledge of the relevant physical quantities (e.g. optical potentials, giant-dipole resonance parameters for gamma widths,

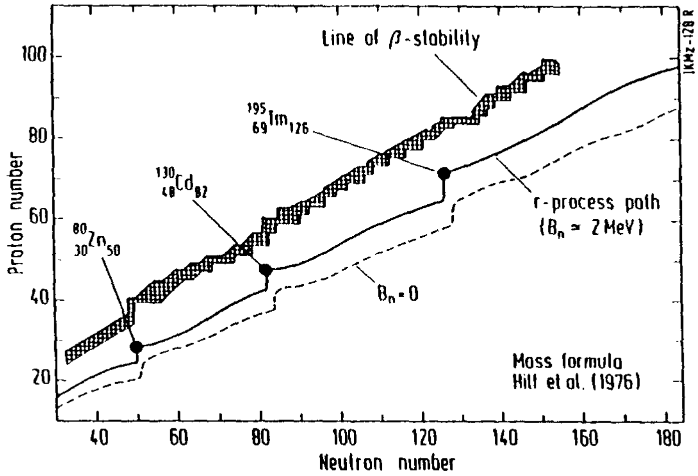

Fig. 3.1. The position of the r-process path between the valley of stability and the neutron-drip line. Magic neutron numbers ($N = 50, 82, 126$) cause bends and the path comes closest to stability where the longest beta-decay half-lives are encountered. Experimental information is presently only available at these locations (^{80}Zn and ^{130}Cd), where the abundance maxima originate.

level-density parameters, reaction Q-values), either from experiment or theory. For the vast majority of nuclei in the r-process path, no experimental information is available.

It is possible, however, to deduce many of these quantities from a nuclear mass formula. Similar considerations hold true for the prediction of fission barrier heights. Therefore, it is essential to find the most reliable predictions for nuclei far off stability. We begin this section with a discussion of nuclear masses in section 3.1 and fission barriers in section 3.2. An overview of beta-decay half-lives is presented in section 3.3. The cross-section calculations are then discussed in section 3.4 and extended to neutron-induced and beta-delayed fission in section 3.5.

Before proceeding with a detailed discussion of these individual topics, we would first like to point out a fact which might sound trivial but is critical. Since a number of different quantities are needed in r-process calculations, it will not be possible generally to obtain them all from one source. Taking them from different sources, however, raises the question of consistency. As an example, let us consider the calculations for beta-delayed fission and neutron emission. In order to perform such calculations, one needs a mass formula to predict the Q-values for beta decay, beta-delayed neutron emission and beta-delayed fission. The fission channel is determined by the height of the fission barrier. Fission barriers are calculated with the aid of a macroscopic–microscopic treatment, which involves a macroscopic droplet-model part and Strutinsky shell corrections. The macroscopic part corresponds to a specific choice of mass-formula parameters. Since the fission barriers depend on the adopted mass-formula parameters, it follows that the same mass formula should be utilized for predicting the beta-decay Q-values.

While this might sound confusing, the neglect of this point can lead to drastic consequences. The calculations of Thielemann et al. [1983a] made use of the "best available mass formula", i.e., Hilf et al. [1976], which is characterized by a relatively steep mass parabola and therefore large Q_β-values. The "best available fission barrier heights" came from Howard and Möller [1980], who used mass-formula parameters close to those of Myers [1976], and whose mass formula is characterized by a flatter mass parabola. The result was that the fission barriers were too small in comparison with the Q_β-values, and the effect of beta-delayed fission in the actinide region was overestimated, with important effects on isotopic ratios which are used in nuclear chronology.

In principle, the calculations for the beta strength function show the same dependence. The preferred approach is to determine the intrinsic Q_β-value by calculating the energies of states in the daughter nucleus which are fed by beta transitions. Using an inconsistent mass formula might then lead to beta strength below the ground state of the daughter nucleus or strength which is shifted to too high excitation energies. Earlier calculations like that of Klapdor et al. [1984] did not list the corresponding Q_β-values. The new quasiparticle RPA calculations [Staudt et al. 1989, 1990] are performed for a set of different mass formulae. We want to stress that the best choice is always a consistent set of calculations employing the best mass formula. When such a consistent set is, however, not available, it may be more advisable to use a consistent set based on a less accurate mass formula than a mixed set.

3.1. *Nuclear masses*

Nuclear masses probably have the most decisive influence on the operation of the r-process. They determine the position of the neutron drip line $[M(Z, N) + m_n = M(Z, N + 1)]$, the neutron separation energies (i.e. Q-values of neutron captures), and the Q-values for beta decays. The solar r-process abundance pattern and its associated peaks define the position of the r-process path in the (N, Z) nuclear chart. Because the r-process path is characterized by roughly constant neutron separation energies, nuclear masses determine the neutron separation energy in the r-process path, and ultimately also the neutron density and the astrophysical conditions required to reproduce the solar abundance pattern. Since the great majority of the required masses are also for nuclei far from stability (see fig. 3.1), theoretical extrapolations based upon nuclear mass formulae are required.

Nuclear mass formulae originally involved the simple liquid-drop model [von Weizsäcker 1935; Bethe and Bacher 1936]. More recent approaches include the effects of density distributions (including neutron skin effects), binding as a function of nuclear density, deformation, nucleon pairing (odd–even effects), and shell corrections [Strutinsky 1968], in order to adjust an average macroscopic approach by microscopic corrections. The mass is then given by

$$M(Z, N, \text{shape}) = M_{\text{macr}}(Z, N, \text{shape}) + M_{\text{micr}}(Z, N, \text{shape})\,. \tag{3.1}$$

A major step towards these improvements was the introduction of the droplet model by Myers and Swiatecki [1969]. The droplet model still involves an expansion of the nuclear binding energy in powers of $A^{-1/3}$ and the isospin I, but then introduces further parameters like the compression coefficient K, the nuclear symmetry energy J, the effective surface stiffness Q, the symmetry anharmonicity coefficient M, and the density symmetry coefficient L. Newer versions of this model with additional improvements can be found in the 1976 and 1988 mass evaluations (Atomic and Nuclear Data Tables 17 and 39), for example, in articles by Myers [1976], von Groote et al. [1976], Möller and Nix [1988], Möller et al. [1988]. While the individual terms can also be derived with the extended Thomas–Fermi model (i.e., a microscopic approach), when expanding in powers of $A^{-1/3}$, the droplet model makes no attempt to determine these parameters from first principles. They are rather determined by fits to the properties of the experimentally known masses. If an important effect is not included correctly and explicitly in the general ansatz, it will necessarily be incorporated artificially into the other parameters. Thus, dependences on several coefficients can become confused, and extrapolations into regions of unstable nuclei become dangerous.

This is clearly seen in fig. 3.2 (fig. 5 of Haustein [1988]). Employing the mass formula of Myers

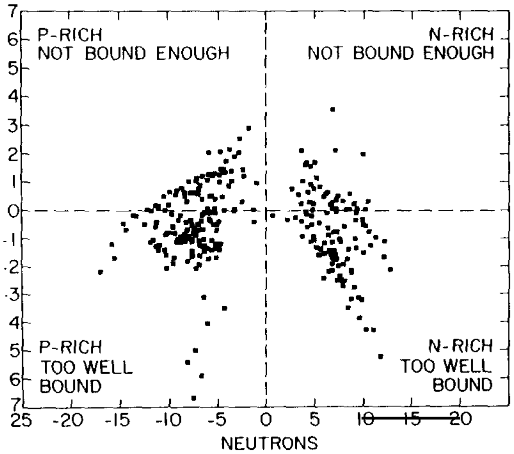

Fig. 3.2. Accuracy test for the nuclear mass formula of Myers [1976], with respect to extrapolations into neutron-rich and neutron-poor regions. Shown is the difference between predicted and experimental masses [Wapstra et al. 1988] in MeV as a function of neutron number $N - N_s$. N_s is the average neutron number for stable nuclei in each isotopic chain. The difference increases with distance from stability in the neutron-rich as well as proton-rich region, overpredicting the binding energy of these unstable nuclei.

[1976], Haustein plots the difference between experimental and predicted masses as a function of the distance from stable nuclei. This curve includes only nuclei for which the mass measurements were performed after 1976. The theoretical estimates get worse with increasing distance from stability, with nuclei far off stability predicted to be too well bound, i.e., $M_{\mathrm{exp}}-M_{\mathrm{th}}$ follows a parabola as a function of δN. In fig. 3.3, we display the same function for the mass formula of Hilf et al. [1976] which has been utilized extensively in r-process calculations. It is seen that the mean value is close to zero. However, even these predictions become increasingly uncertain for very neutron-rich nuclei. Of the new class of 1988 mass formulae, the finite-range droplet model of Möller et al. [1988] seems to give the best predictions; even at 25 units from stability, the error is less than 1 MeV (see also Howard et al. [1988] and fig. 3.4).

The results shown in fig. 3.4 reflect the improved quality of mass predictions, due both to the large number of measurements off the stability line and to an improved theoretical understanding, which has resulted from a different line of research. In principle, Hartree–Fock + BCS calculations, which make use of Skyrme-type forces, can predict nuclear masses in a consistent way, avoiding a macroscopic–microscopic approach [Tondeur 1978, 1983]. Tondeur and Berdichevsky [1985] performed Hartree–Fock + BCS calculations with a variety of Skyrme forces. The uncertainties in this approach are hidden in the choice of Skyrme force parameters. But a set which results in good agreement with experimental nuclear masses, density distributions, and fission barriers, is also expected to yield good predictions for unstable nuclei.

Tondeur and Berdichevsky [1985] concluded that macroscopic mass formulae can only give reliable extrapolations with parameter values of 30 MeV for the nuclear symmetry coefficient and 45 MeV for the effective surface stiffness. The corresponding values for the Myers [1976] formula are 36.8 and 17, the already improved Hilf et al. [1976] formula finds 30.74 and 19.5, and Möller et al. [1988] find 32.5 and 29.4. The inclusion of a finite-range dependence and higher-order compressibility terms by Möller

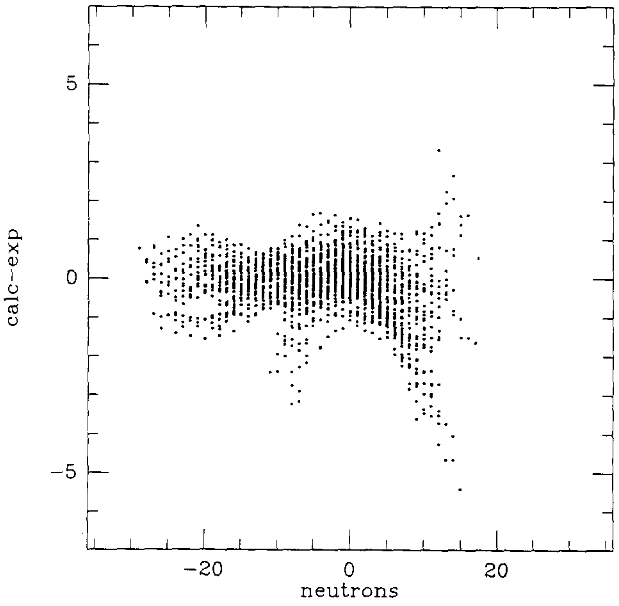

Fig. 3.3. Same as fig. 3.2 for the nuclear mass formula of Hilf et al. [1976]. While the average line stays around 0 and indicates no incorrect tendency, the uncertainties increase towards very neutron-rich nuclei.

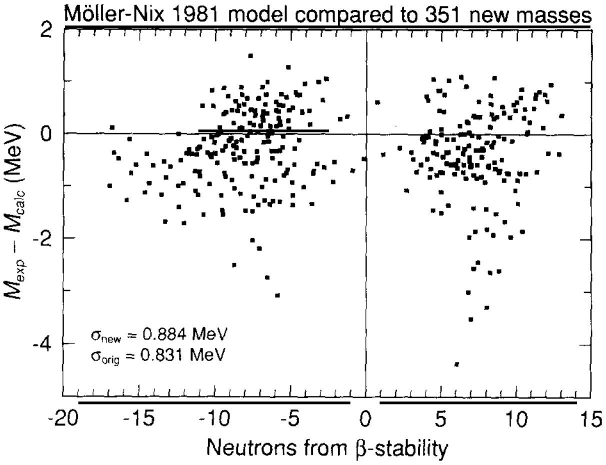

Fig. 3.4. Same as fig. 3.2 for the nuclear mass formula of Möller et al. [1988]. The average line stays around 0 and the uncertainties do not seem to increase towards very neutron-rich nuclei.

et al. reduced the symmetry coefficient and increased the effective surface stiffness by about a factor of 2 in comparison with Myers [1976], two changes necessitated by the findings of Tondeur and Berdichevsky [1985].

A complete set of nuclear masses in the Hartree–Fock + BCS formalism, including particularly values for deformed nuclei, becomes quite a computational task. Dutta et al. [1986] and Tondeur et al. [1987] developed the much faster extended Thomas–Fermi plus Strutinsky integral method (ETFSI). They could show that, even out to the neutron drip line, mass discrepancies between ETFSI and Hartree–Fock + BCS are less than 1 MeV. With this (computationally much faster) method, a complete mass table is now being generated. The interplay between the latter microscopic method and macroscopic–microscopic mass formulae, together with an increasing set of experimental nuclear masses of unstable nuclei, has led to a strong convergence in nuclear mass predictions far from stability.

There are still other recent developments in the understanding of nuclear-mass systematics, which can enhance the precision of predictions far from stability. A semi-empirical method, based on the use of the P-factor [$P = N_p N_n/(N_p + N_n)$, number of neutrons or protons in an unfilled nuclear shell], seems to indicate very smooth interpolations of nuclear masses as a function of P [Haustein et al. 1988]. For many unmeasured neutron-rich nuclei, the P-factor method operates by using interpolation among data for known nuclei rather than by extrapolation, as is common in other mass models. A fully microscopic mass formula, based on the Fermi dynamical symmetry model of nuclei [Wu et al. 1987a] has been developed by Wu et al. [1987b]. At present, predictions exist only for actinide masses, but a very promising general evaluation is in progress.

3.2. Fission barriers

Along the valley of stability, actinide and transuranic nuclei become increasingly unstable as a result of fission in their ground states. This loss of stability arises because the disruptive Coulomb force, which increases as Z^2, overcomes the cohesive surface tension, which is proportional to $A^{2/3}$. The nuclear mass (i.e., potential energy) for a given (Z, A), as a function of deformation, has a local minimum at the ground-state deformation. It first increases with increasing deformation until reaching a maximum at the saddle point, from which point onward fission is inevitable. This potential barrier (= fission barrier) can have very small tunneling transmission coefficients and therefore very long fission half-lives. The barrier is in most cases split into a double-humped barrier, due to shell effects [Strutinsky 1967, 1968]. The higher of the two peaks is denoted the fission barrier, since states beyond that excitation energy can actually fission instantaneously.

More generally, the mass (potential energy) can be evaluated not only along a unique fission (deformation) path but also as a function of several deformation parameters. One possibility is a two-dimensional display as a function of the distance r between the mass centers of the two (eventual) fragments and the fragment elongation σ. Figure 3.5 shows such a potential-energy contour plot for ^{258}Fm, from Möller et al. [1989]. Because the potential energy (= mass) as a function of deformation must be calculated for a particular choice of mass formula, the results will be dependent on the mass-formula parameters.

Figures 3.6a,b give an indication of the changes in fission barrier heights due to the improvement of mass-formula parameters from 1980 [Howard and Möller 1980] to 1989 [Meyer et al. 1989a] that were discussed in section 3.1. As in the case of nuclear masses, Hartree–Fock + BCS calculations can be used to predict fission barriers [Bartel et al. 1982; Tondeur 1985]. For economic reasons, when performing calculations for a large number of nuclei, the ETFSI method is again the method of choice [Tondeur et al. 1987]. It is interesting to note that the extended Thomas–Fermi calculations of Tondeur et al. [1989], arising from a more microscopic approach, give very similar results to those obtained with improved mass-formula parameters, chosen for a better agreement with Hartree–Fock calculations.

As discussed previously, excited states close to or above the fission barrier will have much shorter fission half-lives than ground states, and therefore processes like neutron capture or beta decay, which populate excited states of the compound nucleus or daughter nucleus, will lead to increased probabilities for fission relative to the ground state. Therefore, neutron-induced and beta-delayed fission can play an important role in astrophysics, including the r-process, where beta-delayed fission and neutron-induced fission become important for nuclei with $Z > 80$ (e.g., Thielemann et al. [1983a], Meyer et al. [1985, 1989a,b]). Beta-decay Q-values in the r-process path are of the order 13–15 MeV, much larger than the neutron-capture Q-values of 2–3 MeV. Beta decay will thus populate highly

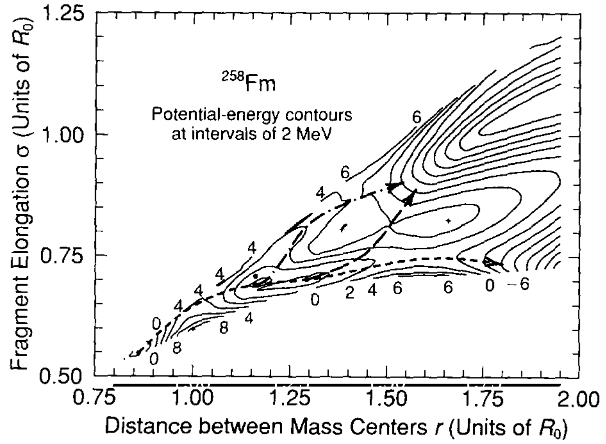

Fig. 3.5. Potential-energy contours along the fission path, as a function of the distance between the two mass centers of the eventual fission fragments and the fragment elongation. In this case, there exists no unique fission path with a double-humped barrier (after Möller et al. [1989]).

excited states above the fission barrier and, consequently, delayed fission plays a more important role than neutron-induced fission.

The only available experimental test for theoretical predictions of beta-delayed fission (which also provides a measure of the fission barrier heights of neutron-rich unstable nuclei) comes from the analysis of abundances in the products of nuclear explosions [Hoff 1986, 1987]. This analysis showed that the predicted values for beta-delayed fission were too large in the actinide region. Recent recalculations of these fission barriers, based on the improved mass formula of Möller and Nix [1988], predict fission barriers which are higher by several MeV in the r-process path [Meyer et al. 1989a], as shown in figs. 3.6a,b. A complete set of predictions which could update the existing values of Howard and Möller [1980], not only for the maximum barrier heights but also for the individual features of the double-humped barriers, is not yet available.

Fission enters into r-process calculations in three different ways. (1) Fission can terminate the r-process path at $Z \approx 92$ and prevent the r-process from producing superheavy elements in nature (see,

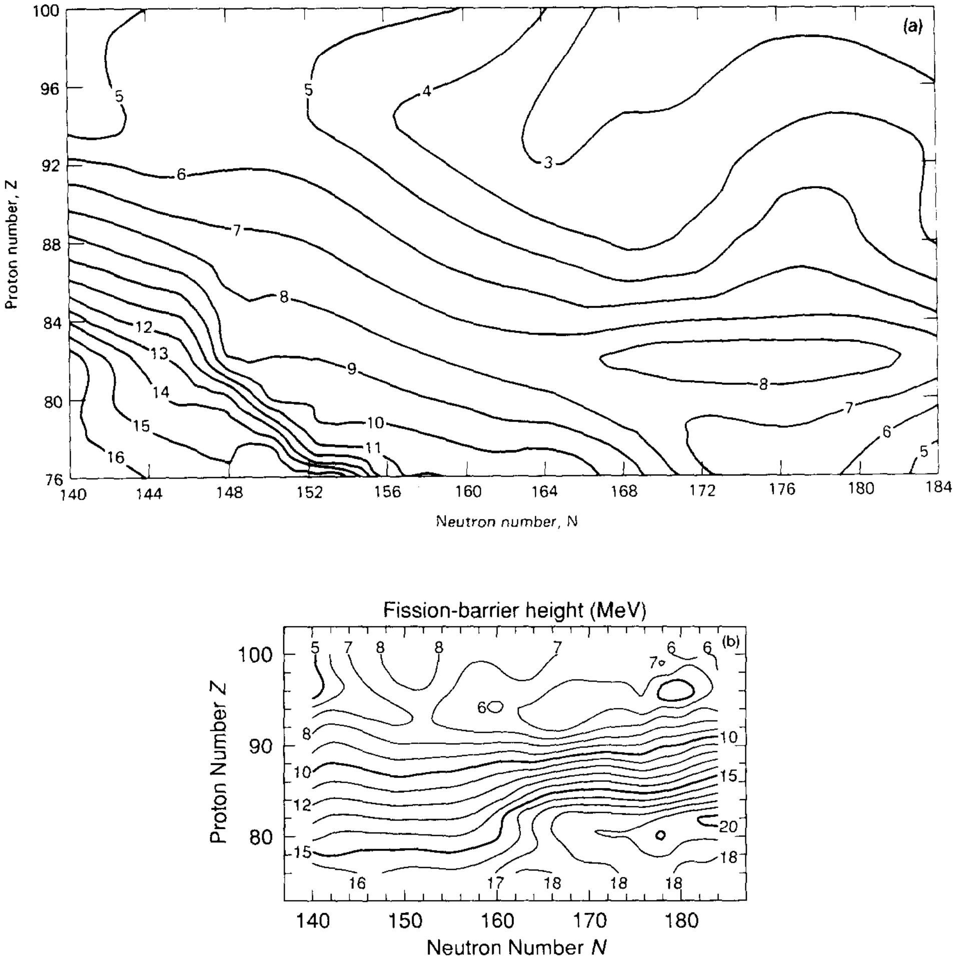

Fig. 3.6. Fission barrier heights (potential-energy maxima as a function of deformation) for two different mass formulae: (a) Howard and Möller [1980] and (b) Möller et al. [1988] as presented by Meyer et al. [1989b]. Far from stability, the more recently calculated barriers are higher by more than 3 MeV, leading to a strong reduction in beta-delayed and neutron-induced fission for these nuclei.

e.g., Howard [1974]; Thielemann et al. [1983a]). (2) After the decline of neutron densities, when the r-process freezes out, nuclei beta-decay back to the stability line. Beta-delayed fission reduces the flow along a given isobar. The resulting beta-stable nuclei will decay along alpha-decay chains and ultimately determine the abundance ratios of the very long-lived nuclei like ^{232}Th, ^{238,235}U and ^{244}Pu. The comparison of these abundance ratios in the solar system with the production ratios in the r-process (when making assumptions on galactic evolution) can be used to determine the duration of nucleosynthesis in our Galaxy and the galactic age (e.g., Cowan et al. [1987]; Fowler [1987a]; Meyer et al. [1985, 1989b]; Symbalisty and Schramm [1981]; Thielemann et al. [1983b]). (3) In environments with a long duration of neutron exposure, "fission cycling" can determine the total abundance of heavy nuclei. After fission, each of the fission fragments can capture neutrons along the r-process path, and ultimately form a heavy nucleus again with $Z > 80$, leading to renewed fission. Each cycle doubles the number of r-process nuclei (see Seeger et al. [1965]). This is of particular importance in environments characterized by a long duration of high neutron densities, and was recently suggested as relevant to primordial nucleosynthesis in neutron-rich zones of an inhomogeneous big bang [Applegate 1988].

3.3. Beta-decay half-lives

Beta decay half-lives are functions of individual transition strengths from the ground state in the parent nucleus to the ground state and excited states in the daughter nucleus. This can be expressed by

$$\lambda = \frac{\ln 2}{t_{1/2}} = \frac{1}{D'} \sum_i B(E_i, J_i, \pi_i) f_0(Z, Q_\beta - E_i) , \quad D' = \frac{2\pi^3 \hbar^7}{g_v^2 m_e^5 c^4} . \tag{3.2}$$

In this equation, g_v denotes the vector coupling constant, $f_0(E)$ the Fermi function, and $B(E_i, J_i, \pi_i)$ the reduced transition probability to a final state, with energy E_i, spin J_i, and parity π_i in the daughter nucleus. For each spin J in the final nucleus, one can perform an average that is weighted appropriately by the density of states with spin J,

$$\begin{aligned}\sum_i B(E_i, J_i, \pi_i) f_0(Z, Q_\beta - E_i) &= \int_0^{Q_\beta} \sum_J B_J(E) \rho_J(E) f_0(Z, Q_\beta - E)\, \mathrm{d}E \\ &= \int_0^{Q_\beta} S_\beta(E) f_0(Z, Q_\beta - E)\, \mathrm{d}E .\end{aligned} \tag{3.3}$$

Here $S_\beta(E)$ is also known as the beta-strength function, which governs the strength of transitions as a function of energy. The 1p1h configurations carrying the beta strength act as doorway states, spreading their strength into neighboring compound states with a typical width σ of 0.2–0.3 MeV. This can be taken into account by rewriting eq. (3.2) as

$$\begin{aligned}&\lambda = \frac{1}{D'} \int_0^{Q_\beta} \sum_i \beta_i(E, J_i, \pi_i)\, \mathrm{d}E = \frac{1}{D'} \int_0^{Q_\beta} S_\beta(E) f_0(Z, Q_\beta - E)\, \mathrm{d}E , \\ &\beta_i(E, J_i, \pi_i) = [1/\sigma_i(2\pi)^{1/2}] \exp[-(E - E_i)^2/2\sigma_i^2] B(E_i, J_i, \pi_i) f_0(Z, Q_\beta - E) .\end{aligned} \tag{3.4}$$

The populated excited states in the daughter nucleus can subsequently decay by gamma transitions to the ground state. Fermi transitions proceed to the isobaric analog state (IAS, which is located energetically above the ground state of the parent nucleus in β^- decay) and a very narrow distribution of states in the vicinity of the IAS. For more neutron-rich nuclei, this energy difference increases and Fermi transitions become negligible. Fermi transitions with $\Delta I = 0$, $\Delta\pi = 0$ and $\Delta T = 0$ can only proceed to the isobaric analog state, which is located above the available energy window ($>Q_\beta$). Therefore the decay is dominated by allowed Gamow–Teller transitions ($\Delta I = 0, 1$; not $0 \rightarrow 0$; $\Delta\pi = 0$). In a macroscopic sense, the strength function is distributed continuously with a maximum at the Gamow–Teller giant resonance.

This was also the first approach undertaken by Takahashi et al. [1973]. They assumed a continuous beta-strength function of Gaussian shape, centered at the Gamow–Teller giant resonance, which also observed the appropriate sum rules. As the beta decay includes only transitions to low-lying excited states with a small level density, such a strength function should show structures. This has been verified experimentally (see, e.g., Kratz [1984] and fig. 3.7). Klapdor et al. [1981] and Klapdor et al. [1984] calculated the beta-strength function in a microscopic approach, utilizing the Tamm–Dancoff approximation on the basis of a spherical shell model.

Based on the initial work by Krumlinde and Möller [1984], Meyer et al. [1989a] performed quasiparticle RPA calculations with an explicit treatment of nuclear deformation and a basis of deformed nuclear states. They were able to show that the beta-strength function then has a broader distribution than in the spherical case (see fig. 3.8) and that the predicted half-lives depend strongly on the nuclear deformation (see also Kratz et al. [1988]). More recently, new sets of extended compilations of beta-decay half-lives, calculated within the framework of the quasi-particle RPA model, have become available as a result of studies by Möller and Randrup [1990] and Staudt et al. [1989, 1990]. When comparing the results of all three approaches (gross theory, TDA and quasiparticle RPA), one notices that they define a range typically given by a factor of 3 between the extreme values; the initial gross theory of beta decay is generally on the slow side and the TDA calculations are on the fast side, while

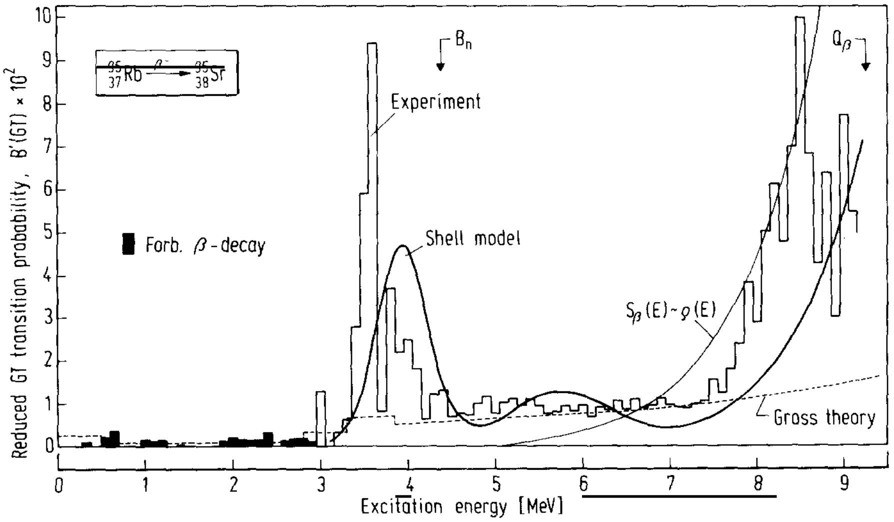

Fig. 3.7. Beta-strength function as a function of excitation energy in the daughter nucleus for the decay of ^{95}Rb (from Kratz [1984]). It can be seen that the transition probability is not smooth but reveals strong structures.

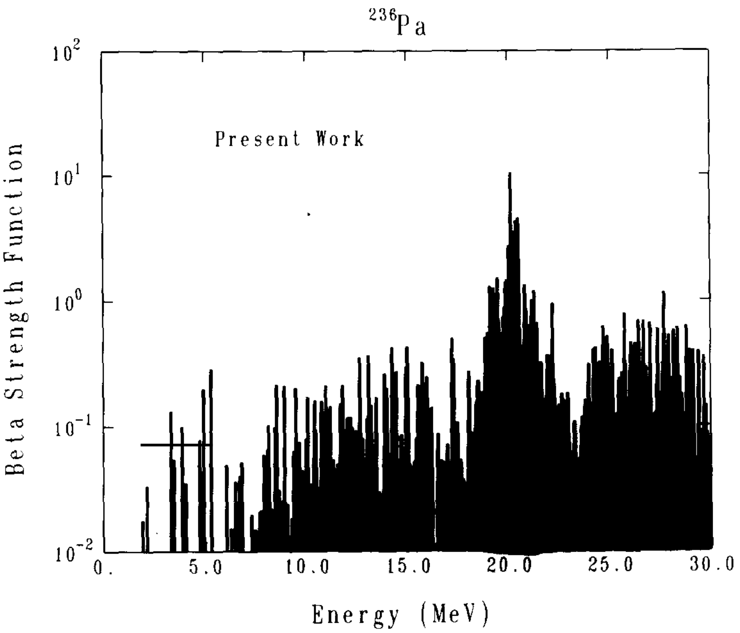

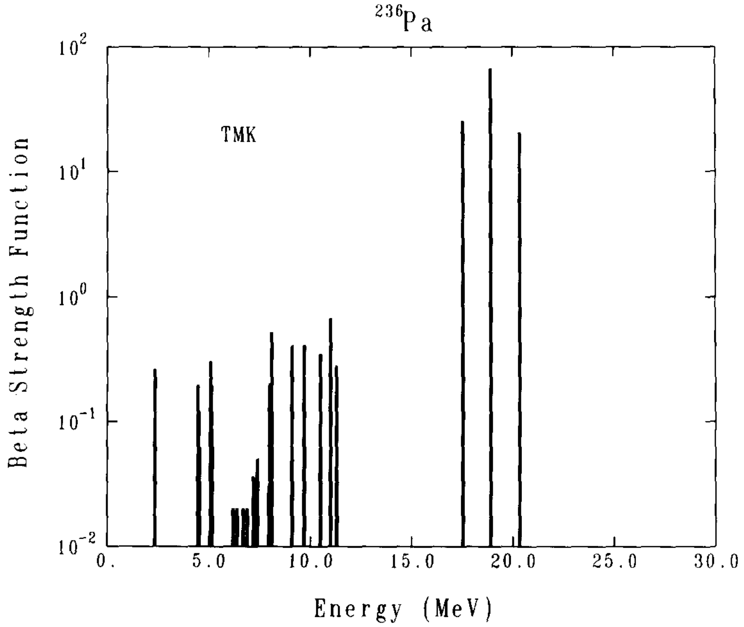

Fig. 3.8. Comparison of two calculated beta-strength distributions for ^{236}Pa (as presented in Meyer et al. [1989a]) from Meyer et al. [1989a] (top) and Thielemann et al. [1983a] (bottom). The former performed RPA calculations in a basis of deformed nuclear states. The correct treatment of deformation leads to a larger spreading of the strength distribution.

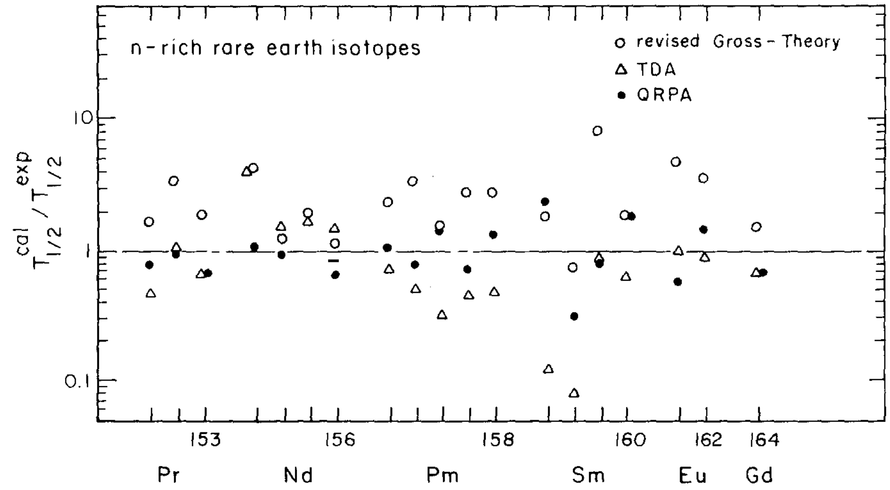

Fig. 3.9. Ratio of calculated to experimental beta-decay half-lives for the revised Gross theory [Tachibana et al. 1988], the Tamm–Dancoff approximation [Klapdor et al. 1984] and a quasiparticle RPA calculation [Staudt et al. 1989]. The gross theory generally overpredicts half-lives, while the TDA results lead to underpredictions. The QRPA seems to give the best predictions.

the QPRPA approach gives the best results (see fig. 3.9). Most recent r-process calculations have employed the rates of Klapdor et al. [1984]. The results of the quasiparticle RPA calculations, which have only recently become available for the entire set of nuclei needed for r-process calculations, have not yet been utilized.

3.4. Theoretical predictions of thermonuclear reaction rates

For two nuclear components i and j in an astrophysical plasma with number densities n_i and n_j and a Maxwell–Boltzmann distribution of relative velocities, the number of reactions, r, per (cm^3 s) is given by $r = \langle \sigma v \rangle n_i n_j$. The nuclear reaction rates $\langle \sigma v \rangle$ have the form (Fowler et al. [1967])

$$\langle \sigma v \rangle = (8/\mu\pi)^{1/2} (kT)^{-3/2} \int_0^\infty E\sigma(E) \exp(-E/kT)\, \mathrm{d}E . \tag{3.5}$$

The cross sections $\sigma(E)$ have to be determined either from experiments or theoretical predictions. The most widely used approach for the latter is the statistical model of compound nuclear reactions (Hauser–Feshbach). This approach has been employed for the calculation of thermonuclear reaction rates for astrophysical purposes by many researchers, most recently by Holmes et al. [1976], Woosley et al. [1978], and Thielemann et al. [1987, 1988]. These compilations are presently the ones utilized in large-scale applications in all subfields of nuclear astrophysics, when experimental information is unavailable.

The statistical model for compound nuclear reactions is based mainly on the assumption of a high level density in the compound nucleus, when the cross section can be described by average transmission coefficients T (for details see Mahaux and Weidenmüller [1979]). This leads to the well known expression

$$\sigma^{\mu\nu}_{jk}(E_{ij}) = \frac{\pi\hbar^2/2\mu_{ij}E_{ij}}{(2J^\mu_i+1)(2J_j+1)} \sum_{J,\pi}(2J+1)\, \frac{T^\mu_j(E, J, \pi, E^\mu_i, J^\mu_i, \pi^\mu_i)\, T^\nu_k(E, J, \pi, E^\nu_l, J^\nu_l, \pi^\nu_l)}{T_{\text{tot}}(E, J, \pi)} \tag{3.6}$$

for the reaction $i^\mu(j, k)l^\nu$ from the target state i^μ to the exited state l^ν of the final nucleus, with center of mass energy E_{ij} and reduced mass μ_{ij}. J denotes the spin, E the excitation energy, and π the parity of excited states. When these properties are used without subscripts they describe the compound nucleus, subscripts refer to states of the participating nuclei in the reaction $i^\mu(j, k)l^\nu$ and superscripts indicate the specific excited states.

While experiments measure $\Sigma_\nu\, \sigma^{0\nu}_{jk}(E_{ij})$ summed over all excited states of the final nucleus, with the target in the ground state, target states μ in an astrophysical plasma are thermally populated and the astrophysical cross section σ^*_{jk} is given by

$$\sigma^*_{jk}(E_{ij}) = \frac{\Sigma_\mu\, (2J^\mu_i+1)\exp(-E^\mu_i/kT)\, \Sigma_\nu\, \sigma^{\mu\nu}_{jk}(E_{ij})}{\Sigma_\mu\, (2J^\mu_i+1)\exp(-E^\mu_i/kT)}\ . \tag{3.7}$$

The summation over ν replaces $T^\nu_k(E, J, \pi)$ in eq. (3.6) by the total transmission coefficient

$$T_k(E, J, \pi) = \sum_{\nu=0}^{\omega} T^\nu_k(E, J, \pi, E^\nu_l, J^\nu_l, \pi^\nu_l) + \int_{E^\omega_l}^{E-S_l} \sum_{J_l, \pi_l} T_k(E, J, \pi, E_l, J_l, \pi_l)\rho(E_l, J_l, \pi_l)\, \mathrm{d}E_l\ . \tag{3.8}$$

Here S_l is the channel separation energy, and the summation over excited states above the highest experimentally known state ω is changed to an integration over the level density ρ. The summation over target states μ in eq. (3.7) has to be generalized appropriately. The important ingredients of statistical model calculations are the particle and γ transmission coefficients T and the level density of excited states. Therefore, the reliability of the result of such calculations is determined by the accuracy with which these components can be evaluated. In the following we want to discuss the methods utilized to estimate these quantities and the improvements over previous compilations.

3.4.1. *Particle transmission coefficients*

The transition from an excited state in the compound nucleus (E, J, π) to the state $(E^\mu_i, J^\mu_i, \pi^\mu_i)$ in nucleus i via the emission of a particle j is given by a summation over all quantum mechanically allowed partial waves

$$T^\mu_j(E, J, \pi, E^\mu_i, J^\mu_i, \pi^\mu_i) = \sum_{l=|J-s|}^{J+s}\ \sum_{s=|J^\mu_i - J_j|}^{J^\mu_i + J_j} T_{j_{ls}}(E^\mu_{ij})\ . \tag{3.9}$$

Here the angular momentum l and the channel spin $s = J_j + J^\mu_i$ couple to $J = l + s$. The individual transmission coefficients T_l are calculated by solving the Schrödinger equation with an optical potential for the particle–nucleus interaction. All early studies of thermonuclear reaction rates [Truran and

Cameron 1966; Michaud and Fowler 1970; Arnould 1972; Truran 1972; Holmes et al. 1976; Woosley et al. 1978] employed optical square-well potentials and made use of the black nucleus–nucleus approximation. Thielemann et al. [1987, 1988] used the optical potential for neutrons and protons given by Jeukenne et al. [1977], based on microscopic calculations, with the local density approximation. It included the corrections of the imaginary part by Fantoni et al. [1981] and Mahaux [1982].

The resulting s-wave neutron-strength function $\langle \Gamma^0/D\rangle|_{1\,\mathrm{eV}} = (1/2\pi)T_{n(l=0)}(1\,\mathrm{eV})$ was calculated by Thielemann et al. [1983a] and compared with several phenomenological optical potentials of the Woods–Saxon type (see also fig. 3.10). The equivalent square well used in earlier astrophysical applications is a straight line. The deviation from experiment at $A = 160$ is due to deformation. When

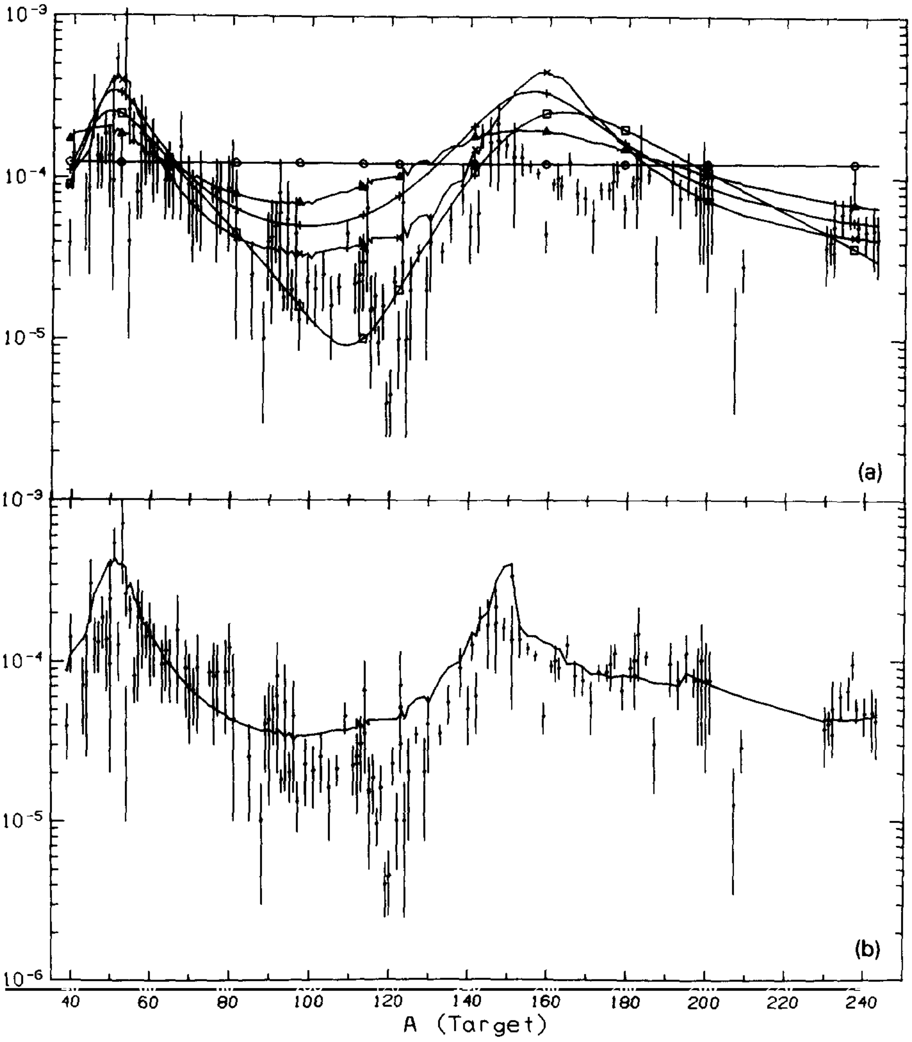

Fig. 3.10. (a) s-wave neutron strength functions [Thielemann et al. 1983a] calculated with different spherical optical potentials (circles: equivalent square well [Holmes et al. 1976; Woosley et al. 1978]; triangles: Becchetti and Greenlees [1969]; crosses: Wilmore and Hodgson [1964]; ×: Jeukenne et al. [1977]). Experimental values are from Lynn [1968]. (b) Making use of the potential of Jeukenne et al. [1977] by defining an "equivalent spherical potential" for deformed nuclei averaged over all incident projectile angles. Deformation parameters are taken from the droplet model of Hilf et al. [1976].

deformed nuclei were treated in a very simplified way (avoiding coupled-channel calculations) by using an effective spherical potential of equal volume, the result in fig. 3.10b was obtained. The effective spherical potential was based on averaging the deformed potential over all possible angles between the incoming particle and the orientation of the deformed nucleus. The purely theoretical approach gives the best fit. It is also expected to have the most reliable extrapolation properties for unstable nuclei.

Alpha particles were also treated in all earlier papers by square-well optical potentials. Thielemann et al. [1987, 1988] employed a phenomenological Woods–Saxon potential derived by Mann [1978], based on extensive data by McFadden and Satchler [1966]. For future use, for alpha particles and heavier projectiles, the best results can probably be obtained with folding potentials (e.g., Chaudhuri et al. [1985], Satchler and Love [1979]).

3.4.2. *γ-transmission coefficients*

The dominant γ-transitions (E1 and M1) have to be included in the calculation of the total photon width. The smaller, and therefore less important, M1 transitions have usually been treated with the simple single-particle approach ($T \propto E^2$ [Blatt and Weisskopf 1952]), as also discussed in Holmes et al. [1976]. The E1 transitions are usually calculated on the basis of the Lorentzian representation of the giant dipole resonance (GDR). Within this model, the E1 transmission coefficient for the transition emitting a photon of energy E_γ in a nucleus is given by

$$T_{\mathrm{E1}}(E_\gamma) = \frac{8}{3}\,\frac{NZ}{A}\,\frac{e^2}{\hbar c}\,\frac{1+\chi}{mc^2}\sum_{i=1}^{2}\frac{\mathrm{i}}{3}\,\frac{\Gamma_{\mathrm{G},i}E_\gamma^4}{(E_\gamma^2 - E_{\mathrm{G},i}^2)^2 + \Gamma_{\mathrm{G},i}^2 E_\gamma^2}\,. \tag{3.10}$$

Here $\chi(=0.2)$ accounts for the neutron–proton exchange contribution (see, e.g., Lipparini and Stringari [1989]) and the summation over i includes two terms which correspond to the split of the GDR in statically deformed nuclei, with oscillations along ($i = 1$) and perpendicular ($i = 2$) to the axis of rotational symmetry.

Many microscopic and macroscopic models have been devoted to the calculation of the GDR energies E_G and widths Γ_G (for references, see, e.g., the reviews by Lipparini and Stringari [1989], Snover [1986], Goeke and Speth [1982] and Speth and Wambach [1980]; see also the review of Eramzhyan et al. [1986] for light nuclei, where a Lorentzian approximation cannot yet be made). Experimental compilations are provided, e.g., by Berman [1975], Berman and Fultz [1975], Carlos et al. [1974], Berman et al. [1979], and Gurevich et al. [1981]. Holmes et al. [1976] and Woosley et al. [1978] used analytical fits as a function of A and Z. The (hydrodynamic) droplet-model approach for E_G by Myers et al. [1977] gives an excellent fit to the GDR energies and can also predict the split of the resonance for deformed nuclei, when making use of the deformation, calculated within the droplet model (see fig. 3.11). In that case, the two resonance energies are related to the mean value calculated in Myers et al. [1977] by the following expression given by Danos [1958]

$$E_{\mathrm{G},1} + 2E_{\mathrm{G},2} = 3E_\mathrm{G}\,, \qquad E_{\mathrm{G},2}/E_{\mathrm{G},1} = 0.911\eta + 0.089\,. \tag{3.11}$$

η is the ratio of (1) the diameter along the nuclear symmetry axis (fig. 3.11 top) to (2) the diameter perpendicular to it (fig. 3.11 bottom), and can be obtained from the experimentally known deformation or droplet-model predictions.

The width of the GDR is less understood and even modern RPA calculations can only account for a fraction of its value [Bortignon and Broglia 1981]. Macroscopic models of the hydrodynamic type

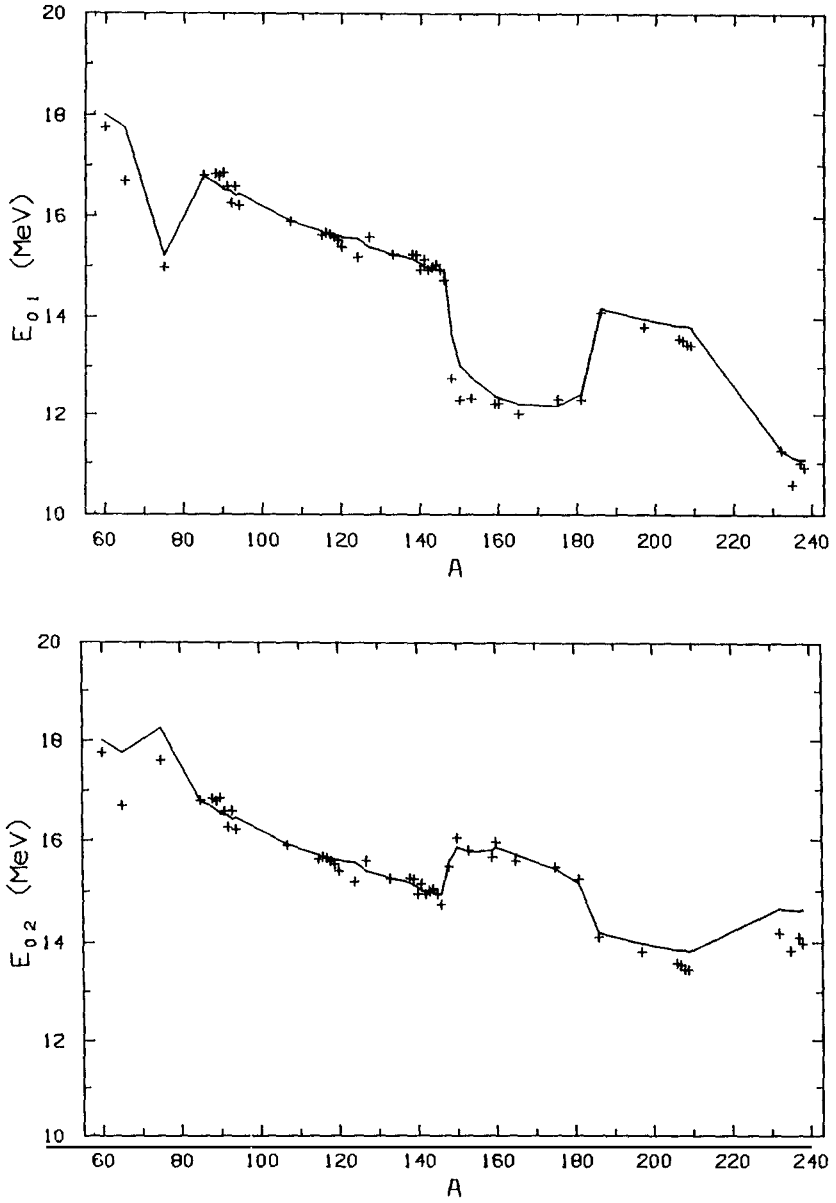

Fig. 3.11. Droplet-model predictions of the GDR energy E_G [Myers et al. 1977] in comparison with experiments, indicated by crosses [Berman and Fultz 1975]. The splitting of the GDR energies for deformed nuclei along (top) and perpendicular (bottom) to the rotational symmetry axis has been calculated with eq. (3.10) and the deformations from the droplet model of Hilf et al. [1976].

[Auerbach and Yeverechyahu 1975; Hasse and Nerud 1976] could explain more or less correctly the average trends of Γ_G variations with A, but could not account for the pronounced, observed shell effects; the widths are smaller at magic numbers. Holmes et al. [1976] and Woosley et al. [1978] used an analytical fit to simulate this behavior.

Thielemann and Arnould [1983] proposed a phenomenological model for the GDR width which satisfactorily reproduces the experimental data for spherical and deformed nuclei. Based on an older idea by Le Tourneaux [1965], the GDR width can be described as a superposition of a macroscopic width due to the viscosity of the nuclear fluid and a coupling to quadrupole surface vibrations of the nucleus. This is in agreement with more modern calculations [Gallardo et al. 1985].

Viscous damping in hydrodynamical treatments leads approximately to $\Gamma_d \propto E_G^{\delta}$ with $1 < \delta < 2$, depending upon the model [Auerbach and Yeverechyahu 1975; Hasse and Nerud 1976]. Evaluating the coupling to quadrupole surface vibrations within the Dynamic Collective Model leads to a broadening term $\Delta\Gamma$, which can be approximated by $2.35(5/8\pi)^{1/2}E_G\beta_2$, where β_2 is the root-mean-square amplitude of the quadrupole surface vibrations [Bortignon and Broglia 1981; Le Tourneaux 1965]. Thus Γ_G can be expressed in this phenomenological approximation by

$$\Gamma_G = \Gamma_d + \Delta\Gamma = \alpha E_G^{\delta} + 2.35(5/8\pi)^{1/2}E_G\beta_2 . \tag{3.12}$$

Thielemann and Arnould [1983] performed a least-squares fit to experimentally known GDR widths of spherical nuclei where E_G and β_2 were known, and found $\alpha = 0.185$ for $\delta = 1$. When E_G and β_2 are not known from experiment, droplet-model estimates of E_G and β_2 can be used accordingly. The droplet-model values for E_G by Myers et al. [1977] are in excellent agreement with experiments (see fig. 3.11). The droplet-model evaluation of β_2 is described in Thielemann and Arnould [1983]; it expresses the potential energy (mass) of the nucleus as a function of the surface deformation. Figure 3.12 shows the comparison with experimental values for different energy exponents of the damping width. The results reproduce satisfactorily the dips at magic numbers, where the coupling to surface vibrations is weak due to the "stiffness" of the nuclei.

This treatment can be extended to deformed nuclei. Because the GDR splits into two resonances, Γ_G and E_G have to be replaced by $\Gamma_{G,i}$ and $E_{G,i}$ (i has the values 1 and 2). β_2 is replaced by ζ_2, which

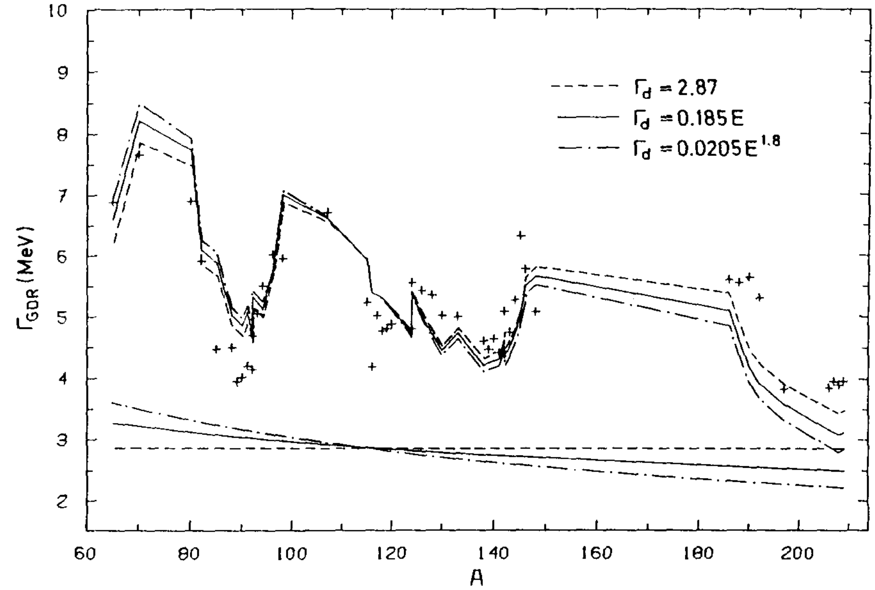

Fig. 3.12. Theoretical estimates of the width of the giant dipole resonance [Thielemann and Arnould 1983], made using eq. (3.11) and the droplet-model predictions for E_G [Myers et al. 1977] and β_2, in comparison with experiments [Berman 1975; Berman and Fultz 1975; Carlos et al. 1974; Gurevich et al. 1981]. The various curves show the effect of different assumptions for Γ_d ($\delta = 0, 1, 2$).

measures the mean amplitude of surface vibrations about the ground-state deformation. The coefficient in $\Delta\Gamma$ also becomes deformation-dependent. The combined results of Thielemann and Arnould [1983] are shown in fig. 3.13. In the region $150 < A < 180$, the experimental values from gamma-absorption cross sections [Gurevich et al. 1981] are generally higher than those derived from photoneutron cross-section experiments. Around $A \approx 75$, only photoneutron data are plotted so that the disagreement there might be artificial.

Thielemann et al. [1987, 1988] applied these predictions to eq. (3.2) and calculated the total radiation width at the neutron separation energy for all nuclei in the experimental compilation of Weigmann and Rohr [1973]. The total photon transmission coefficients for E1 radiation from a compound nucleus state with energy E, spin J and parity π is given by

$$T_\gamma(E, J, \pi) = \sum_{\nu=0}^{\omega} T_\gamma^\nu(E, J, \pi, E_l^\nu, J_l^\nu, \pi_l^\nu) + \int_{E_l^\omega}^{E} \sum_{J_l, \pi_l} T_\gamma(E, J, \pi, E_l, J_l, \pi_l)\rho(E_l, J_l, \pi_l)\, \mathrm{d}E_l\,, \tag{3.13}$$

where the first term represents a summation over the known low-lying states ν up to an excitation energy E_ω, while an integration involving the level density ρ is performed at higher excitation. This equation is fully equivalent to (3.8), as S_γ is 0. In eq. (3.13) $T_\gamma^\nu(E, J, \pi, E_l^\nu, J_l^\nu, \pi_l^\nu)$ is either zero if the E1 selection rules are violated, or equal to T_{E1} ($E_\gamma = E - E_l^\nu$) otherwise. T_{E1} is given by eq. (3.10). The average radiation width $\langle \Gamma_\gamma(E, J, \pi)\rangle$ is related to the total photon transmission coefficient by $\langle \Gamma_\gamma(E, J, \pi)\rangle = T_\gamma(E, J, \pi)/2\pi\rho(E, J, \pi)$. The most extensive sets of measured average radiation widths come from thermal s-wave neutron capture [Weigmann and Rohr 1973]. In that case, the relevant theoretical quantity to be compared with experimental data is

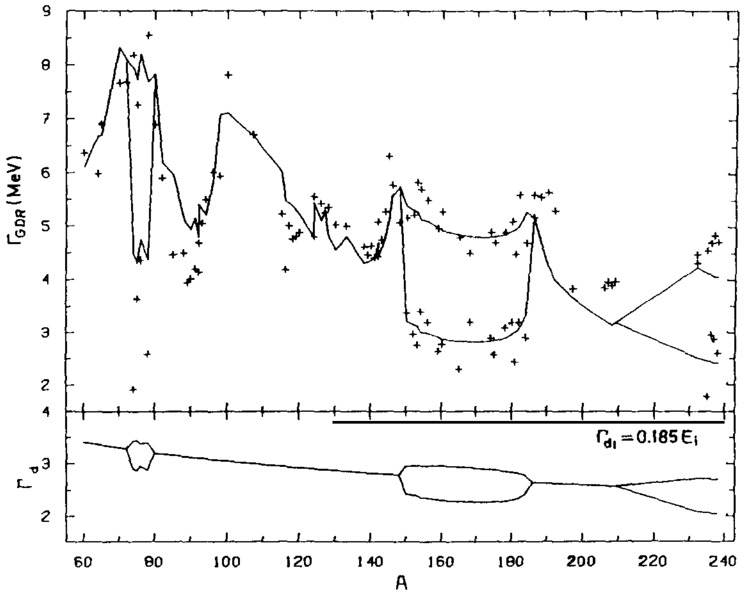

Fig. 3.13. The same as fig. 3.12 but including deformed nuclei and a generalization of (3.11) for deformed nuclei from Thielemann and Arnould [1983].

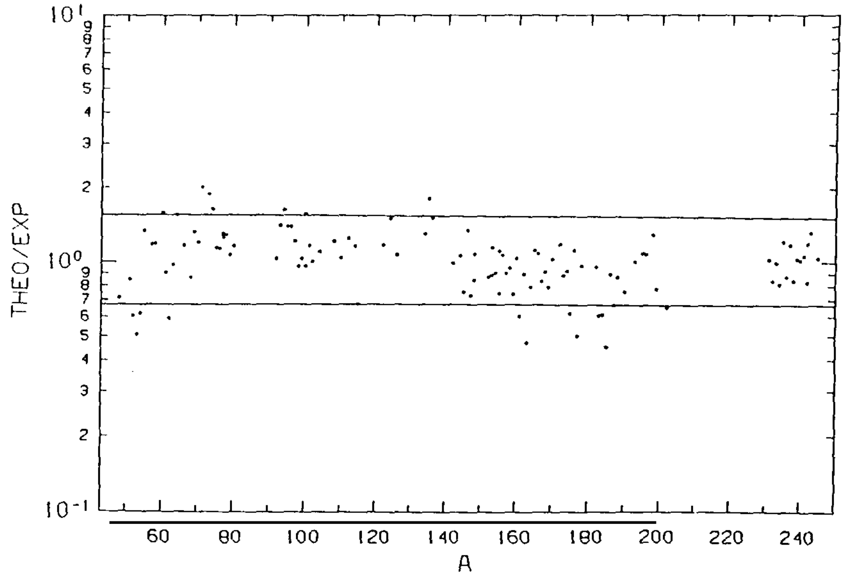

Fig. 3.14. Average radiation widths from s-wave neutron captures (from Thielemann and Arnould [1983]), calculated according to eq. (3.13), in comparison with experimental values [Weigmann and Rohr 1973]. Agreement is found to be generally within a factor of 1.5.

$$\langle \Gamma_\gamma \rangle_0 = \frac{J_i+1}{2J_i+1} \langle \Gamma_\gamma(S_n, J_i+\tfrac{1}{2}, \pi_i)\rangle + \frac{J_i}{2J_i+1} \langle \Gamma_\gamma(S_n, J_i-\tfrac{1}{2}, \pi_i)\rangle \,, \tag{3.14}$$

where S_n is the compound-nucleus neutron-separation energy and J_i (π_i) is the spin (parity) of the target nucleus.

Utilizing the methods outlined above and the level density described in section 3.4.3, Thielemann et al. [1987] found agreement generally within a factor of 1.5 (see fig. 3.14). This was an improvement over earlier attempts by Johnson [1977] and Hardy [1982]. It has been known for some time that the direct application of eq. (3.10) overestimates the radiation width by about 30% (see, e.g., McCullagh et al. [1981], Raman et al. [1981]). This is due to the fact that, for low-energy gamma transitions, the Lorentz curve is suppressed and the GDR width increases with excitation energy (e.g., Snover [1986], Draper et al. [1982]). To account for these deficiencies, various treatments have been suggested which involve the ansatz $\Gamma_G = \Gamma_G(E_\gamma)$ [McCullagh et al. 1981; Gardner and Gardner 1986; Kopecky and Chrien 1987]. The results shown in fig. 3.14 made use of the suggestion by McCullagh et al. [1981] that $\Gamma_G(E_\gamma) = \Gamma_G(E_\gamma, E_G)^{1/2}$.

3.4.3. Level densities

Most statistical model calculations use the level-density description of the backshifted Fermi gas [Gilbert and Cameron 1965]

$$\rho(U, J, \pi) = \tfrac{1}{2} f(U, J)\rho(U) \,,$$

$$\rho(U) = \frac{1}{\sqrt{2\pi}\sigma} \frac{\sqrt{\pi}}{12a^{1/4}} \frac{\exp(2\sqrt{aU})}{U^{5/4}} \,, \qquad f(U, J) = \frac{2J+1}{2\sigma^2} \exp[-J(J+1)/2\sigma^2] \,, \tag{3.15}$$

$$\sigma^2 = (\Theta_{\rm rigid}/\hbar^2)\sqrt{U/a} \,, \qquad \Theta_{\rm rigid} = \tfrac{2}{5} m_u A R^2 \,, \qquad U = E - \delta$$

(m_u is the nuclear mass unit), which assumes that positive and negative parities are evenly distributed and that the spin dependence $f(U, J)$ is determined by the spin cut-off parameter σ. The level density of a nucleus is therefore dependent only on two parameters: the level density parameter a and the backshift δ, which determines the energy of the first excited state. This backshift is related to the level spacing up to the first unoccupied state in the single-particle shell model and to the pairing gap, the energy necessary to break up a proton or neutron pair.

Of these two effects, the pairing energy dominates except in the very near vicinity of closed shells. This energy shift was not included in the initial independent-particle picture of the Fermi gas [Bethe 1936], but is accounted for in eq. (3.15) by introducing the backshifted energy $U = E - \delta$. Within this framework, the quality of level-density predictions depends on the reliability of systematic estimates of the level-density parameter a and the backshift δ. Equation (3.15) provides a valid functional form for reproducing level densities down to an excitation energy of $U = 1$–2 MeV, but it diverges for $U = 0$, i.e. $E = \delta$, if δ is a positive backshift. Ericson plots, which show the number of excited states as a function of excitation energy, reveal an almost linear behavior for $\ln N = f(E)$ with an intercept at $E = E_0 = \delta$ [Ericson 1959]; this resulted in the ansatz $\rho(U) = \exp(U/T)/T$, commonly called the constant-temperature formula. The two formulations can be combined for low and high excitation energies, with $E_0 = \delta$ and T being determined by a tangential fit to the Fermi gas formula.

Gilbert and Cameron [1965] provided the first compilation of a and δ for a large number of nuclei. They found that the backshift δ is well reproduced by experimental pairing corrections. Theoretical predictions result in $a/A \approx 1/15$ for infinite nuclear matter, but the inclusion of surface and curvature effects of finite nuclei enhances this value to 1/6–1/8 [Töke and Swiatecki 1981; Prakash et al. 1983]. While in principle a can be dependent on temperature or excitation energy, Suraud and Schuck [1985] were able to show that such a dependence is minimal for excitation energies up to $3 \times A$ MeV and thus that the zero-temperature value for a can be used up to these energies, covering all values of interest within the present context. When comparing experimentally derived values of a (e.g., Rohr [1982, 1984]) with such a simple formulation, one notices large deviations due to shell effects (nuclei near closed shells have much smaller values for a). Gilbert and Cameron [1965] were the first to identify an empirical correlation with experimental shell corrections $S(N, Z)$

$$a/A = c_0 + c_1 S(Z, N)\,, \tag{3.16}$$

where $S(N, Z)$ is negative near closed shells. Other functional dependences have been proposed (e.g., Kataria et al. [1978]) and more microscopic treatments have been carried out (e.g., Moretto [1972], Døssing and Jensen [1974], Huizenga et al. [1974a,b], Arnould and Tondeur [1982], French and Kota [1983], Lauritzen et al. [1989]), but they do not necessarily lead to better predictive power. There have been a number of compilations for a and δ, or T and E_0, based on experimental level densities (e.g., Dilg et al. [1973], Grimes et al. [1974], Woosley et al. [1978], and most recently von Egidy et al. [1986, 1988]). These should be used whenever experimental information is available. Predictions for unstable nuclei or those for which experimental information is not available have to be based on theory, including the predictions for shell and pairing corrections.

Earlier compilations for astrophysical applications still used the shell corrections $S(Z, N)$ and the pairing corrections $P(Z, N)$ from the Cameron and Elkin [1965] mass formula. When analyzing Ericson plots of excited states, taken from van Egidy et al. [1986] and the Evaluated Nuclear Data File (Karlsruhe, Brookhaven), Thielemann et al. [1987] found that the positive and negative intercepts (backshifts) can best be reproduced by

$$\delta = \Delta(Z, N) - 10/A\,, \tag{3.17}$$

where the $\Delta(Z, N)$ are the pairing corrections from a droplet-model nuclear-mass formula (e.g., Myers [1976]) and have the values 0 for odd nuclei, $12/\sqrt{A}$ for even–even nuclei and $-12/\sqrt{A}$ for odd–odd nuclei. Such a treatment differs from earlier ones in which the pairing corrections in level-density formulae had only non-negative values, but it agrees with a recent analysis by von Egidy et al. [1988] where additional corrections c_0 and c_1 were introduced in the constant-temperature and backshifted Fermi-gas formulae.

This behavior only changes within one unit of magic nucleon numbers, where the backshifts are larger. An empirical relation for those cases with $\delta_{\mathrm{tot}} = \delta + \delta_{\mathrm{shell}}$ (only for nuclei within one unit from magic numbers), and δ_{shell} having the values $-0.25S(N)$ at neutron magic numbers and $-0.18S(Z)$ at proton magic numbers, provided a good fit, when they utilized the shell corrections of the Hilf et al. [1976] or von Groote et al. [1976] mass formulae. The shell corrections for spherical nuclei are just the sum of proton and neutron shell corrections $S(Z, N) = S(Z) + S(N)$ and these corrections are negative at magic numbers. Figure 3.15 illustrates this effect. The values for δ were, however, reduced to 80% of the values described above due to the non-negligible neutron–proton pairing, which regains some energy after the breakup of neutron–neutron or proton–proton pairs.

Deformed nuclei should be treated differently, as in principle a rotational band can be associated with each excited state (see, e.g., Døssing and Jensen [1974], Huizenga et al. [1974b], Arnould and Tondeur [1982]). At high excitation energies this treatment can, however, lead to double counting. Thielemann et al. [1967] kept the same formalism as in eq. (3.16) but performed an independent

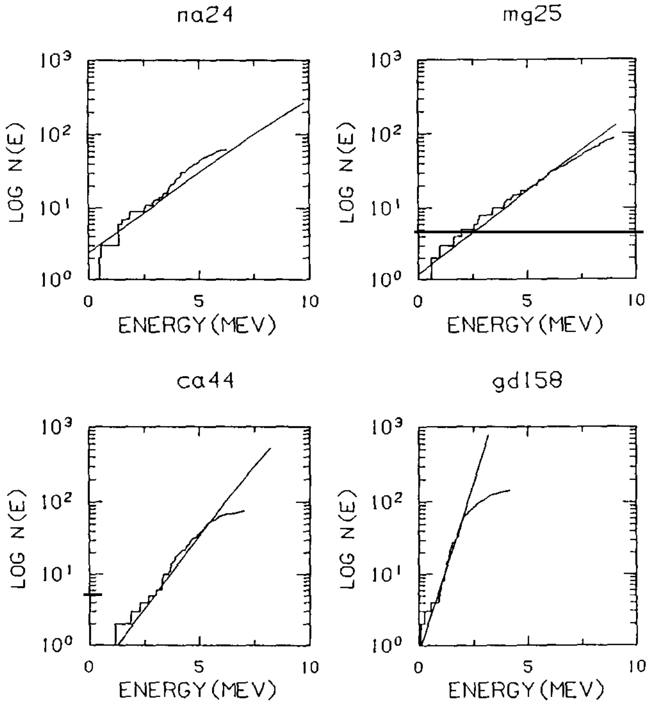

Fig. 3.15. Experimental levels as a function of excitation energy (from the Evaluated Nuclear Data File) are compared with theoretical predictions for odd–odd, odd, even–even, and deformed nuclei (from Thielemann et al. [1987]).

evaluation of the coefficients c_0 and c_1 for deformed nuclei. The intercept E_0 of the constant-temperature formula, applied at low excitation energies, was also chosen to be the energy of the first state of a rotational band on the ground state. E_0 was determined from the moment of inertia ($6 \times$ irrotational flow [Bohr and Mottelson 1975]) and the predicted deformation of the nuclear mass formula (see ^{158}Gd in fig. 3.15).

Thielemann et al. [1987, 1988] used the shell corrections of a more recent droplet-model mass formula [Hilf et al. 1976] to evaluate the coefficients in eq. (3.16) for the level-density parameter a by

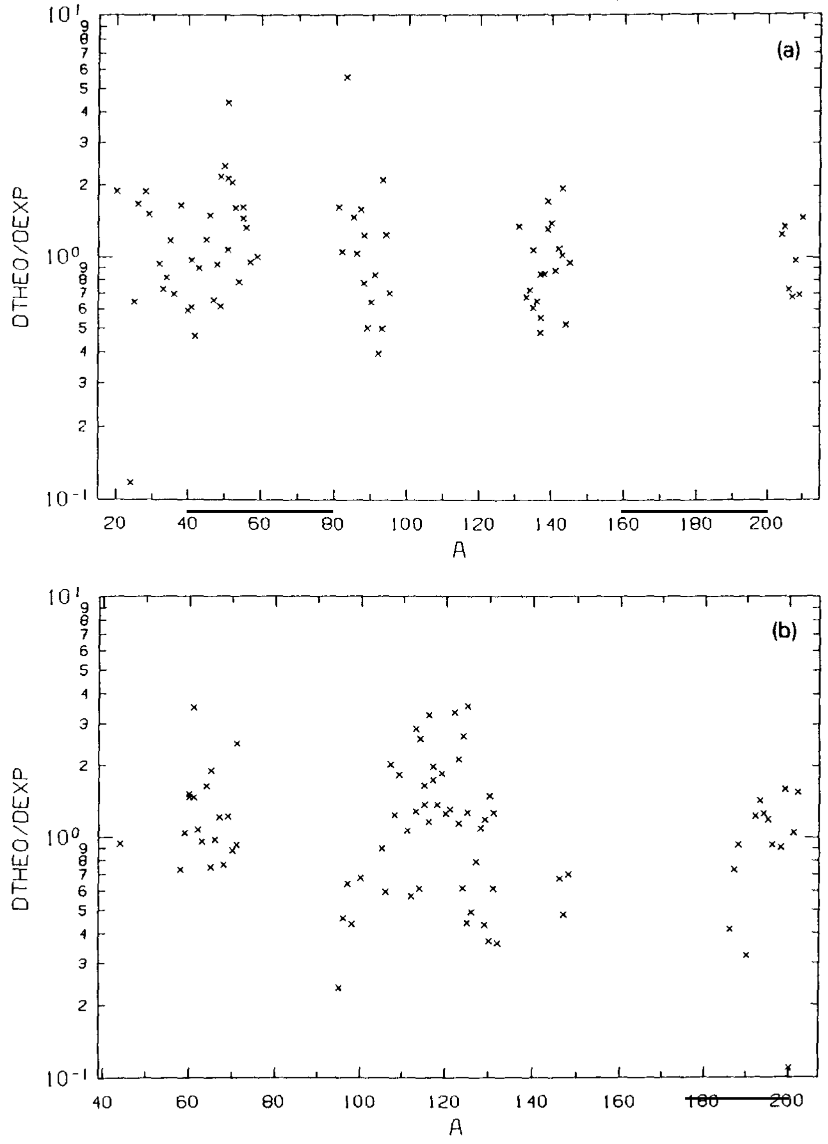

Fig. 3.16. Ratio of predicted [Thielemann et al. 1987] to experimental level spacings at the neutron separation energy [Rohr 1982, 1984] for the three cases: (a) within three units of magic numbers, (b) other spherical nuclei, (c) deformed nuclei. The deviations are still large but an improvement over Gilbert and Cameron [1965] and Woosley et al. [1978], where deviations of more than a factor of 10 occur.

performing a best fit to the experimental level densities at the neutron separation energy [Rohr 1982, 1984]. Employing only one parameter set for c_0 and c_1, they could not achieve a significantly better agreement with experimental level densities than was found by Gilbert and Cameron [1965] and Holmes et al. [1976]. These latter authors found deviations in excess of a factor of 10 in some cases. By dividing the nuclei into three classes [(a) those within three units of magic nucleon numbers; (b) other spherical nuclei; (c) deformed nuclei], they were able to obtain improved agreement (maximum deviations of a factor of 3 to 4), with the following values for c_0 and c_1 [(a) 0.119 924, $5.694\,78 \times 10^{-3}$; (b) 0.119 480, $6.319\,03 \times 10^{-3}$; (c) 0.124 8772, $6.003\,02 \times 10^{-3}$].

Figure 3.16 shows the ratios of experimental level densities to predicted level densities at the neutron separation energy for each of the three cases. This treatment remains very phenomenological and, in our opinion, is still unsatisfactory. It remains the weakest point in the present procedures for the calculation of cross sections. Future investigations should be able to improve these predictions when the microscopic shell and pairing corrections of more modern mass formulae (e.g., Möller et al. [1988], Wu et al. [1987b]) are used. Fortunately, deviations of up to a factor of 3–4 at the neutron separation energy translate into somewhat smaller deviations at the lower excitation energies which dominate the nuclear cross sections. The net uncertainties in the cross sections are in general smaller than a factor of 2.

3.4.4. Results of cross-section calculations

In addition to all the ingredients required for eq. (3.6), like the transmission coefficients for particles and photons and the level densities, width-fluctuation corrections (e.g., Tepel et al. [1974]) must also be employed. These corrections redefine the transmission coefficients in eq. (3.6) in such a manner that the total width is redistributed by enhancing the elastic channel and weak channels over the dominant one. Such a treatment has also been used by Truran [1972], and in later versions of the statistical model code by Holmes et al. [1976] and Woosley et al. [1978]. Of the presently available thermonuclear rates in the literature, this effect is only included by Thielemann et al. [1987, 1988]. While the width-

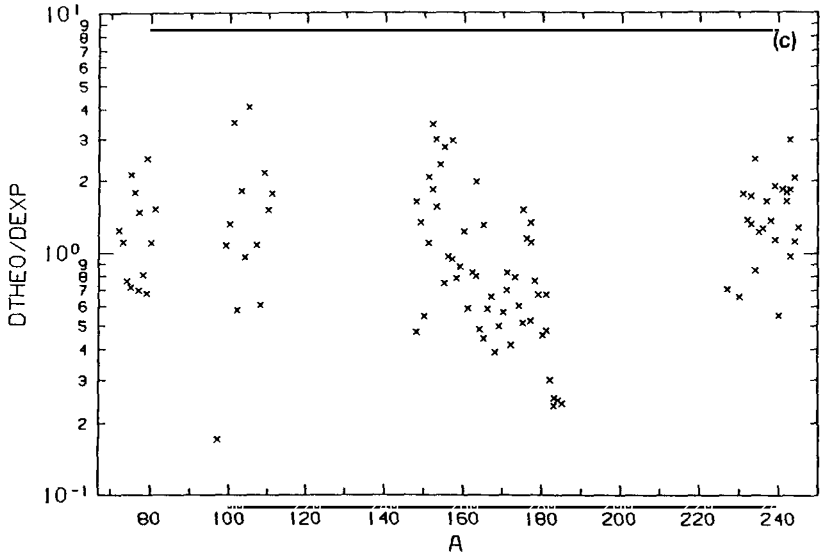

Fig. 3.16 (cont.)

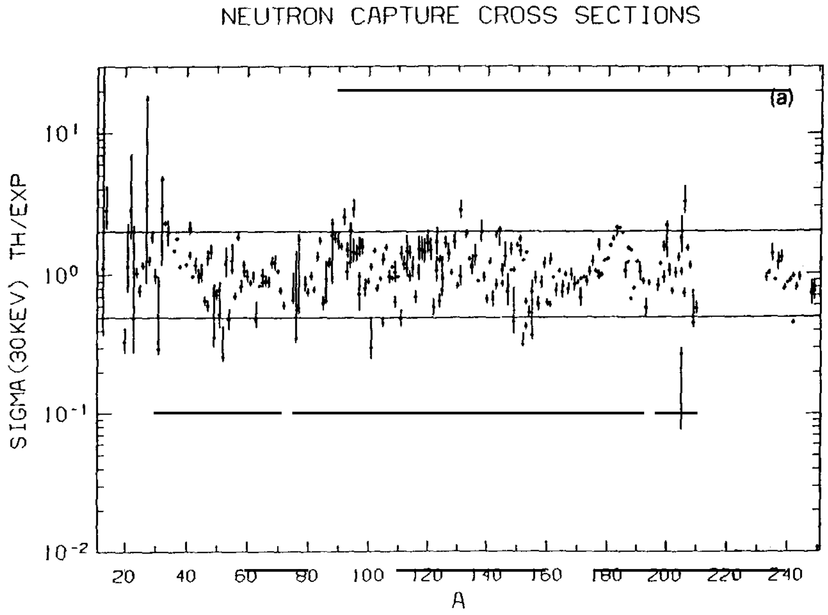

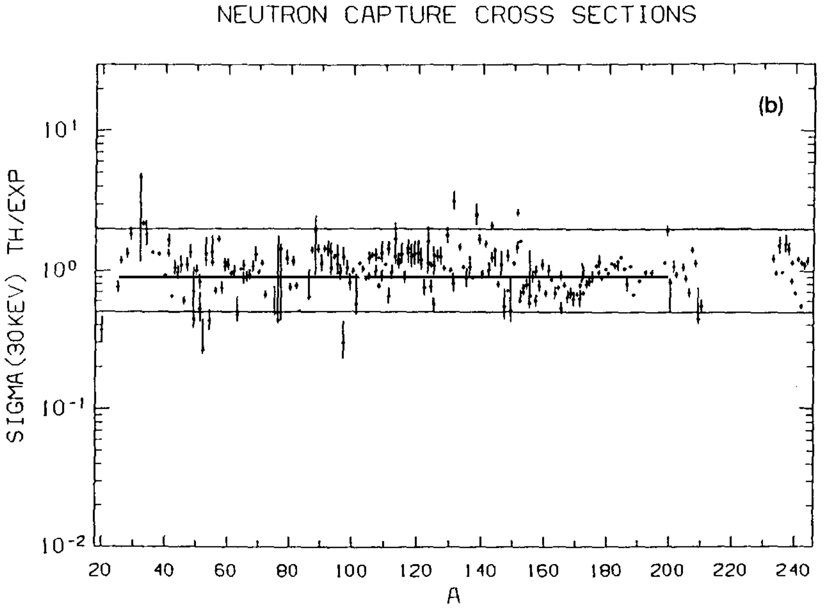

Fig. 3.17. Ratio of theoretical to experimental 30 keV neutron-capture cross sections. Experimental data from Bao and Käppeler [1987]. (a,b) from Thielemann et al. [1987]: a, employs only theoretical predictions for all involved nuclear parameters; b, makes use of experimentally determined level densities and displays only nuclei where these are known; c, results from Holmes et al. [1976] who used experimental level-density parameters where available.

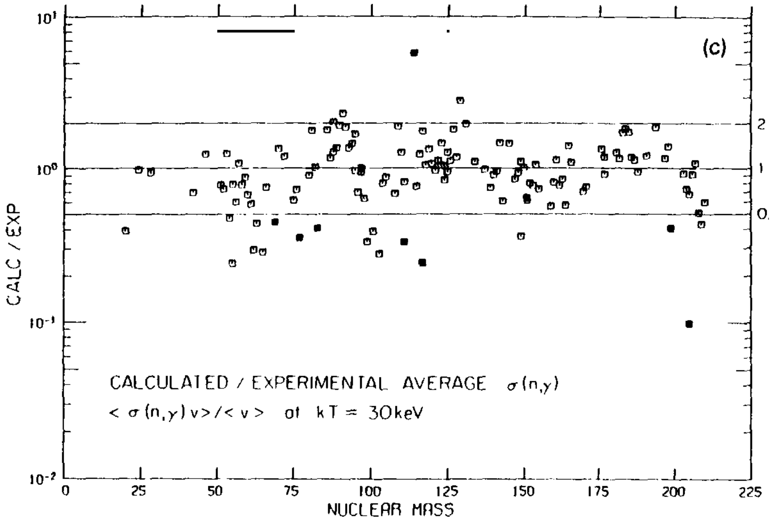

Fig. 3.17 (cont.)

fluctuation corrections of Tepel et al. [1974] are only an approximation to the correct treatment, Thomas et al. [1986] showed that they are quite adequate.

Our discussions in the previous subsections reveal that one can expect to obtain very good agreement with experiment for particle and photon transmission coefficients. On the other hand, level-density predictions, which are still based on shell correction terms and nonmicroscopic pairing terms of older generation mass formulae, show the largest statistical spread (up to a factor of 4 at the neutron separation energy). Cross sections of astrophysical importance are dominated by transitions to lower energies which reduces the influence of such uncertainties, and one might hope to obtain agreement to within a factor of 2.

This is in fact the conclusion drawn from a comparison between the results of Thielemann et al. [1987, 1988], using their code SMOKER, and experimental neutron-capture cross sections at 30 keV, for nuclei listed in the compilation of Bao and Käppeler [1987], see fig. 3.17a. A few exceptions involve nuclei located specifically at magic numbers. This is a consequence of the still imperfect predictions of nuclear level densities. Figure 3.17a makes use only of theoretical predictions for all involved nuclear quantities. Therefore, this level of agreement is also expected for unstable nuclei, as long as the adopted nuclear mass formula provides accurate predictions of nuclear deformations and reaction Q-values.

It should be noted that fig. 1 in Holmes et al. [1976] used experimentally determined level-density parameters whenever available (our fig. 3.17b). The results of Thielemann et al. [1987], who adopted the same approach and included only nuclei for which experimental level densities are available [Rohr 1982, 1984], are displayed in fig. 3.17c. This figure underscores the fact that the largest uncertainties are still associated with the level-density predictions. While such an approach is appropriate when the best possible cross-section predictions are required (as for studies of s-process nucleosynthesis involving nuclei near the beta-stable valley), it does not give a correct measure of the expected accuracy for cross-section predictions for unstable nuclei, for which no experimental information is available. This information can be deduced from fig. 3.17a, which indicates an uncertainty of approximately a factor of 2. Calculations of 30 keV neutron-capture cross sections, for all nuclei from Ne to $Z = 114$ and from stability to the neutron drip line, are tabulated in the appendix. These values, based on the mass formula of Hilf et al. [1976], provide the best available compilation for use in r-process applications.

Finally, we also want to show some energy-dependent cross-section evaluations for charged-particle reactions involving intermediate mass nuclei which play an important role in silicon burning. The results shown in fig. 3.18 verify the fact that the energy dependences and absolute values of the cross sections are also quite well reproduced, including particularly the magnitude of the cusps at the threshhold energies of channel openings. This behavior can only be reproduced when employing width fluctuation corrections [Thielemann et al. 1987, 1988]. For a more general comparison of charged-particle cross sections with statistical model calculations, for astrophysical applications, see Sargood [1982].

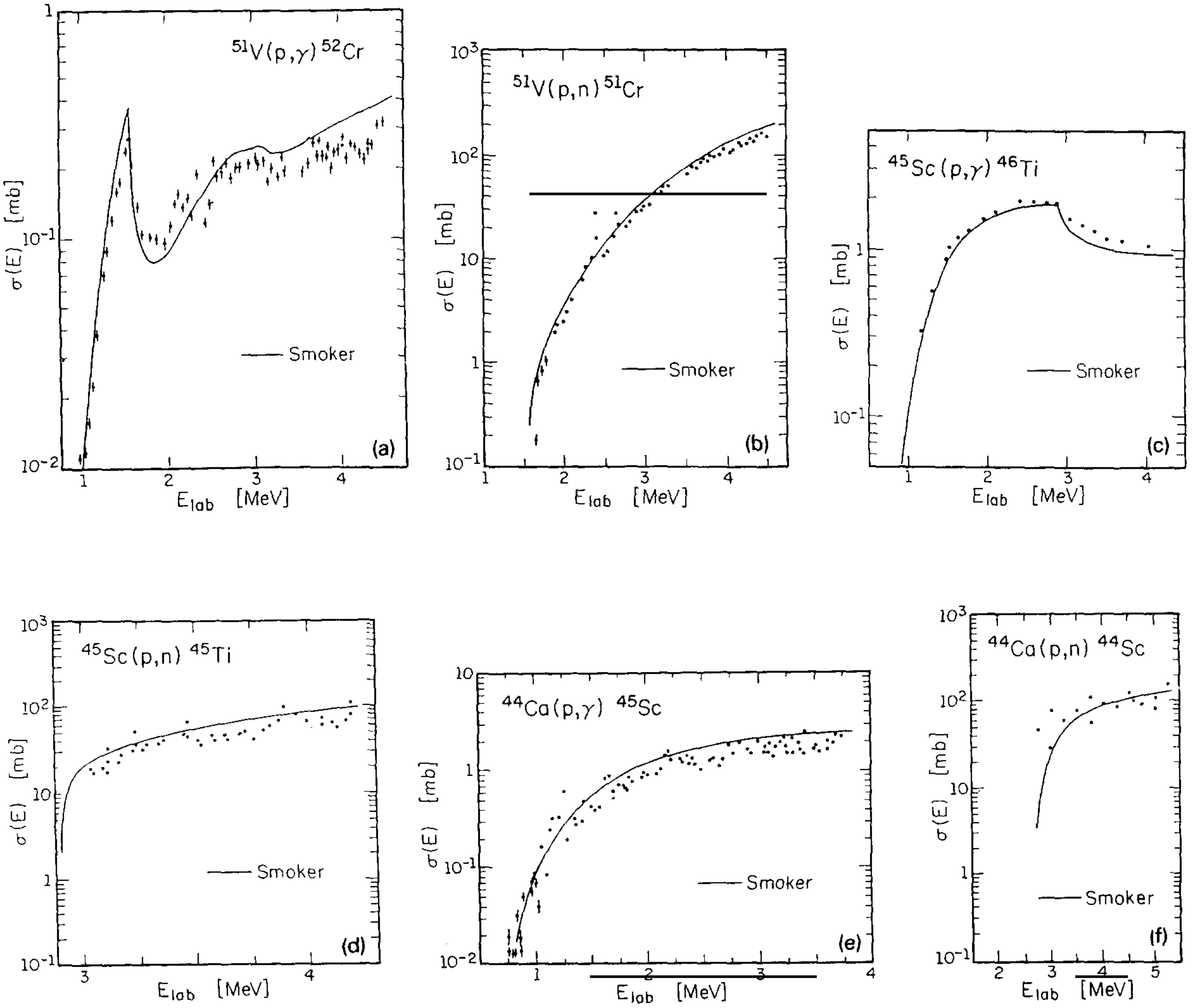

Fig. 3.18. Calculated charged-particle cross sections in comparison to experiment. Data from (a,b) Zyskind et al. [1980]; (c,d) Solomon and Sargood [1978]; (e,f) Mitchell et al. [1982]. When width-fluctuation corrections are included, the magnitude of the drop in the capture cross sections, when the neutron channel opens, can be reproduced well.

3.5. *Neutron-induced fission and beta-delayed fission*

3.5.1. *Neutron-induced fission*

The statistical model calculations of section 3.4 can be extended to include a fission channel, in order to calculate cross sections for neutron-induced fission. The cross section for a reaction $i^0(j, k)l$, from the target ground state i^0 to all excited states l^ν of a final nucleus with center of mass energy E_{ij} and reduced mass μ_{ij}, is again given by eq. (3.6), with the summation taken over all final states ν. Therefore, the sum of T_k^ν is again replaced by the expression (3.8) for T_k. The ratio going into the fission channel is then $T_k/T_{\rm tot}$ with $k = {\rm f}$, i.e., the outgoing channel is the fission channel.

When making use of a double-humped fission barrier, the fission transmission coefficients can be calculated in the limit of complete damping [Back et al. 1974; Lynn 1980; Lynn and Back 1974]. If one cannot make use of detailed information concerning the level structure in the second well, this method gives the best results and can be expressed in the form

$$\begin{aligned} P_{\rm f}(E, J, \pi) &= T_{\rm f}(E, J, \pi)/T_{\rm tot}(E, J, \pi)\,, \\ P_{\rm f}(E, J, \pi) &= \Bigg[1 + \left(\frac{\Sigma_{k\neq {\rm f}}\, T_k(E, J, \pi)}{T_{\rm eff}(E, J, \pi)}\right)^2 \\ &\quad + 2\,\frac{\Sigma_{k\neq {\rm f}}\, T_k(E, J, \pi)}{T_{\rm eff}(E, J, \pi)} \coth\{\tfrac{1}{2}[T_{\rm A}(E, J, \pi) + T_{\rm B}(E, J, \pi)]\}\Bigg]^{-1/2}\,, \\ T_{\rm eff}(E, J, \pi) &= \frac{T_{\rm A}(E, J, \pi)\, T_{\rm B}(E, J, \pi)}{T_{\rm A}(E, J, \pi) + T_{\rm B}(E, J, \pi)}\,. \end{aligned} \tag{3.18}$$

In this equation, $T_{\rm A}$ and $T_{\rm B}$ denote transmission through the first and second barriers, and can be approximated by individual parabolic Hill–Wheeler type barrier shapes, e.g.,

$$\begin{aligned} T_{\rm A}(E, J, \pi) &= \int_0^E \rho_{\rm A}(\varepsilon, J, \pi)\, T_{\rm HW}(\Delta, \hbar\omega_{\rm A})\, {\rm d}\varepsilon\,, \\ \Delta = E - E_{\rm A} - \varepsilon - (\hbar^2/2\Theta)\, l(l + 1)\,, &\qquad T_{\rm HW}(E, \hbar\omega) = [1 + \exp(-2\pi E/\hbar\omega)]^{-1}\,. \end{aligned} \tag{3.19}$$

The available energy is reduced by the rotational energy with the moment of inertia Θ deduced from $\Theta = 5\Theta_{\rm irr}$ for an irrotational flow model [Bohr and Mottelson 1975]. $\rho_{\rm A,B}$ indicates the level densities above the first and second saddle points, which show an enhancement over the level densities at ground-state deformation. This enhancement is larger for the first axially asymmetric barrier than for the second mass asymmetric (axially symmetric) barrier. In the absence of detailed calculations, standard enhancement factors of 4 and 2 can be used, respectively, over the level density at ground-state deformation [Bjørnholm and Lynn 1980; Lynn 1980]. The following relations for barrier curvatures, based on empirical evidence [Bjørnholm and Lynn 1980; Lynn 1980], seem to be reasonable: for $\hbar\omega_{\rm A}$ and $\hbar\omega_{\rm B}$, respectively, 1.04 and 0.6 (even–even), 0.8 and 0.52 (odd-A), and 0.6 and 0.45 (odd–odd).

With a value obtained for $P_{\rm f}$ and the calculated transmission coefficients T_k ($k \neq {\rm f}$) for all other

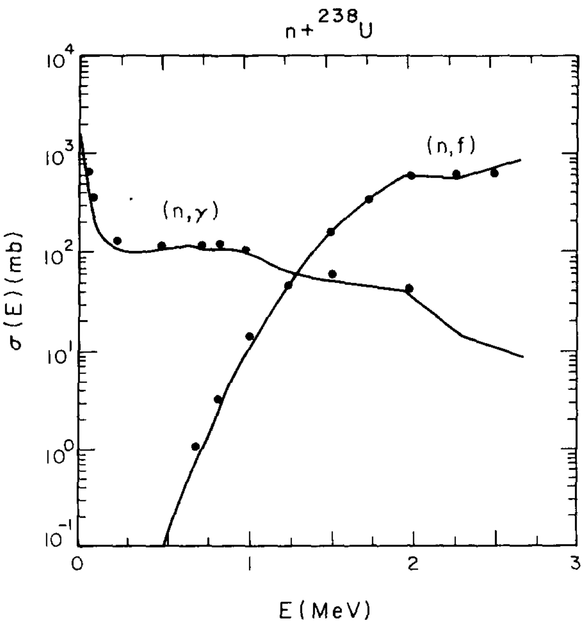

Fig. 3.19. Predicted cross sections for neutron capture and neutron-induced fission on ^{238}U (from Thielemann et al. [1989], experimental data from Bjornholm and Lynn [1980]). Only the reaction Q-values and fission barrier characteristics are taken from experiment. All other quantities, like neutron- and gamma-transmission coefficients and level densities, come from global predictions. The complete damping approximation reproduces the cross sections quite well.

channels, one can solve $P_f = T_f/(T_f + \Sigma_k T_k)$ for T_f, and width-fluctuation corrections can be included in the usual way [Tepel et al. 1974]. Using all the other parameters from global predictions, as in the original code SMOKER [Thielemann et al. 1987, 1988], and employing experimental fission barrier heights $E_{A,B}$ and curvatures $\hbar\omega_{A,B}$ from table XXXI in Bjørnholm and Lynn [1980], results in very good agreement with experimental cross sections for neutron-induced fission. This is illustrated in fig. 3.19 for ^{238}U.

3.5.2. Beta-delayed fission

Beta-delayed fission and neutron emission can be calculated in a manner similar to the procedures outlined in section 3.5.1, and has been described in detail by Thielemann et al. [1983a]. They employed the beta-strength distributions from Klapdor et al. [1984], where the beta-strength functions were calculated in the Tamm–Dancoff approximation, using a Gamow–Teller residual interaction (see section 3.3). One can again make use of the total beta-decay rate, as given in eqs. (3.2) through (3.4), keeping in mind that the excited states populated by beta decay can subsequently decay by neutron emission, fission, or gamma transitions to the ground state. The rates for fission and neutron emission are then given by

$$\lambda_f = \int_0^{Q_\beta} \sum_i \beta_i(E, J_i, \pi_i) \frac{T_f(E, J_i, \pi_i)}{T_{tot}(E, J_i, \pi_i)} \, dE \,, \qquad \lambda_n = \int_0^{Q_\beta} \sum_i \beta_i(E, J_i, \pi_i) \frac{T_n(E, J_i, \pi_i)}{T_{tot}(E, J_i, \pi_i)} \, dE \,. \tag{3.20}$$

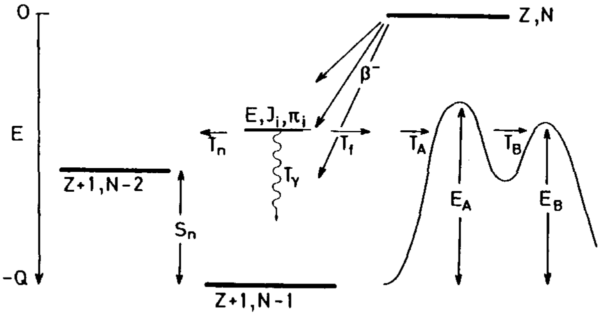

Fig. 3.20. Schematic representation and energetics of the different beta-delayed decay modes, neutron emission, gamma deexcitation and fission.

$P_f = T_f/T_{tot}$ is calculated as in eq. (3.18) for neutron-induced fission. Knowing the value of T_k ($k \neq f$), T_f and T_{tot} and, therefore, T_n/T_{tot} can be calculated accordingly. It is customary to introduce the ratios $P_n = \lambda_n/\lambda$ and $P_f = \lambda_f/\lambda$.

When employing the formalism described above for the calculation of beta-delayed and neutron-induced fission for very neutron-rich unstable nuclei, three additional physical properties are required: (1) the beta-strength function; (2) a nuclear mass formula for determining reaction or decay Q-values; and (3) fission barrier heights and curvatures. Figure 3.20 illustrates how 1, 2 and 3 influence the result. The beta-strength function gives transition strengths for decays to states in the daughter nucleus with respect to the ground-state energy of the parent nucleus. The reaction or decay Q-value then determines the corresponding excitation energy in the daughter nucleus. The fission barrier heights are measured with respect to the ground state of the daughter nucleus. In case these quantities are not known experimentally, appropriate choices are required for theoretical fission barrier heights (discussed already in section 3.2) and for a nuclear mass formula.

3.5.3. *Comparison with experiment*

We now present a few results from calculations which make use of this formalism. Table 3.1 lists the neutron-capture and neutron-induced fission cross sections (in barn), for uranium isotopes at a bombarding energy of 30 keV, as calculated by Thielemann et al. [1989]. It also lists the Q-values for the (n, γ) reaction and the maximum energy B_f of the two fission barrier heights (E_A, E_B) with respect to the ground state of the compound nucleus. Q-values [Wapstra et al. 1988] and fission barrier characteristics [Bjørnholm and Lynn 1980, table XXXI] were taken from experiment if available; otherwise the fission barriers of Howard and Möller [1980] and a nuclear mass formula [Hilf et al. 1976]

Table 3.1
Cross sections at 30 keV

Isotope	Q_n	B_f	$\sigma(n,\gamma)$	$\sigma(n,f)$	Isotope	Q_n	B_f	$\sigma(n,\gamma)$	$\sigma(n,f)$	Isotope	Q_n	B_f	$\sigma(n,\gamma)$	$\sigma(n,f)$
238	4.81	6.46	3.38-1	1.09-5	245	5.18	5.37	1.78-1	5.21-1	252	2.67	3.69	3.70-3	8.66-4
239	5.93	5.75	1.71-1	4.40-0	246	3.50	5.26	2.11-2	2.13-7	253	4.04	3.33	1.28-4	3.33-0
240	4.36	6.14	1.25-1	1.25-7	247	4.89	4.86	6.07-2	1.37-0	254	2.40	3.28	2.12-3	1.15-2
241	5.76	5.91	5.27-1	5.63-1	248	3.22	4.72	1.16-2	5.55-6	255	3.77	2.97	1.49-5	2.47-0
242	4.07	6.09	6.61-2	7.22-9	249	4.60	4.30	6.33-3	3.13-0	256	2.13	3.00	1.22-4	3.76-1
243	5.47	5.75	3.42-1	3.38-1	250	2.95	4.18	6.41-3	1.12-4	257	3.49	3.09	4.83-5	2.19-0
244	3.79	5.80	1.94-2	4.88-8	251	4.32	3.79	6.83-4	3.46-0					

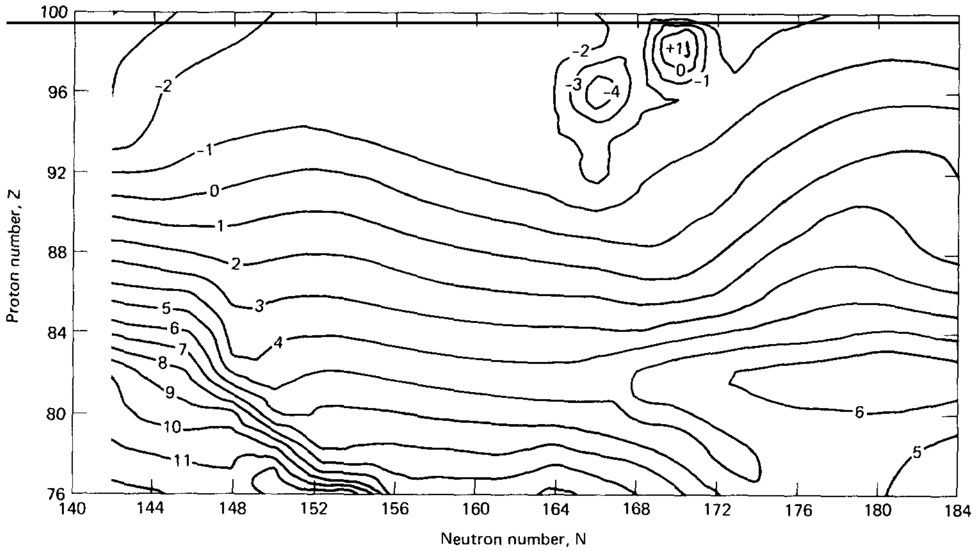

Fig. 3.21. Contour lines of the fission barrier minus the neutron separation energy, $B_f - S_n$ (in MeV), from Howard and Möller [1980]. When this quantity is negative, neutron-induced fission will occur.

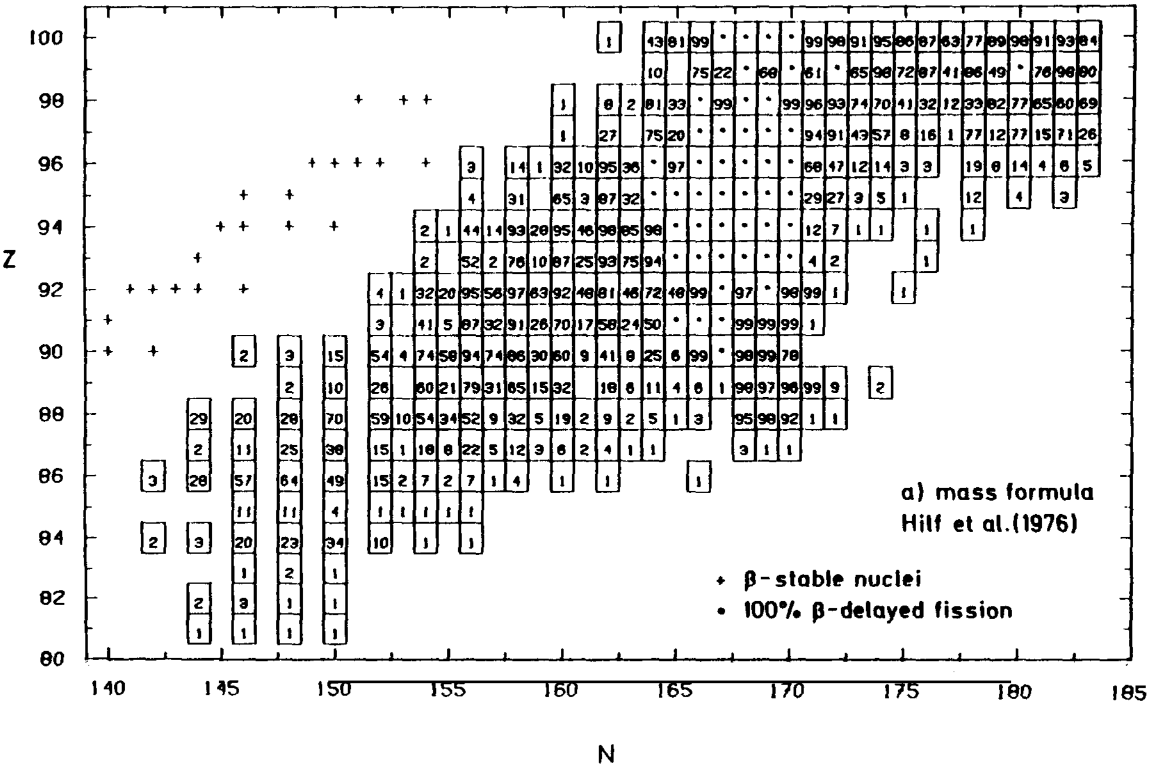

Fig. 3.22. Ratios for beta-delayed fission P_f in percent, indicated at the position of the daughter nucleus. The fission barriers by Howard and Möller [1980] are used, the Q_β-values are taken from three different mass formulas: (a) Hilf et al. [1976], (b) von Groote et al. [1976] and (c) Howard and Möller [1980]. In all cases, an area of 100% delayed fission is predicted around $Z = 94$ and $N = 168$.

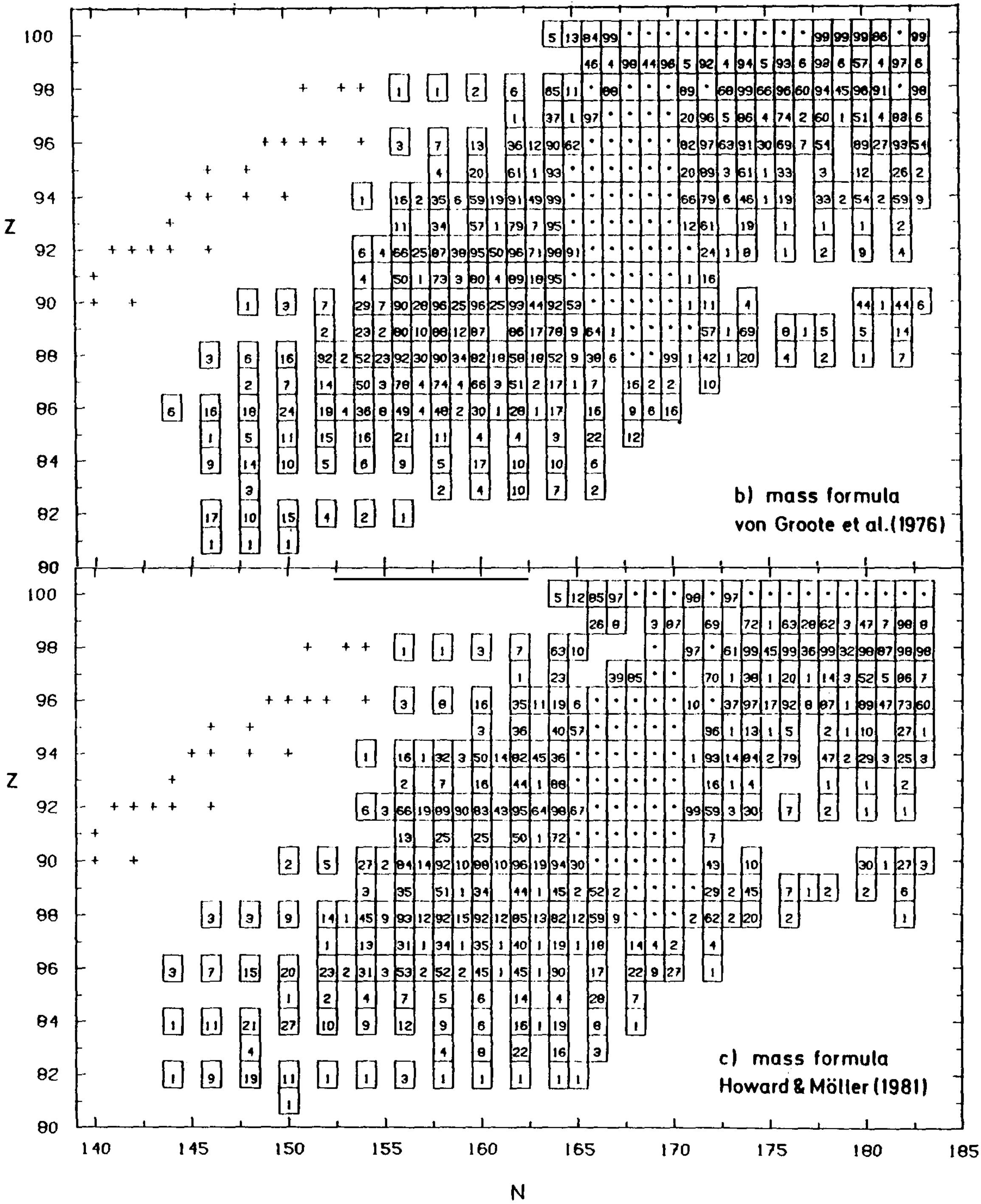
b) mass formula
von Groote et al.(1976)
c) mass formula
Howard & Möller (1981)
Z
N
100
98
96
94
92
90
88
86
84
82
80
140
145
150
155
160
165
170
175
180
185

Fig. 3.22 (cont.)

were employed. This means that, for uranium isotopes of $A > 240$, these quantities are predicted theoretically.

For the case of an effectively instantaneous exposure of ^{238}U to thermal neutrons of 20–30 keV, with a high fluence of 5×10^{24} to 2.4×10^{25} n cm^{-2} (which results in shorter neutron-capture half-lives than beta-decay half-lives even for very short-lived nuclei), one would expect a sequence of multiple-neutron captures. Such conditions were obtained in a series of thermonuclear explosions in the 1950s and 1960s [Eccles 1970; Ingley 1969; Truran and Cameron 1966]. Depending upon the design of the individual device, it has been assumed that neutron captures occur on a mixture of ^{238}U and ^{238}Pa seed nuclei with varying ratios, the latter being initially produced by high-energy neutrons in a ^{238}U(n, p)^{238}Pa reaction.

In the experiment with the highest neutron flux (Hutch), nuclei as heavy as $A = 257$ were found. If we check table 3.1 for the possibility of multiple-neutron captures, we see that there is only a 5% chance of neutron capture on ^{239}U in comparison to neutron-induced fission. There follows a series of events where neutron capture dominates for even-neutron-number targets and is comparable to induced fission for odd targets. The losses, therefore, are not larger than about 50% for every two mass numbers. But, starting from ^{247}U, induced fission dominates by two orders of magnitude on odd-neutron-number nuclei and grows steadily, so that the production of nuclei up to $A = 257$ would be inexplicable in terms of neutron captures.

Upon checking our calculations for Pa, we find a similar behavior in that isotopic chain for $A = 246$, 248, 250, etc., which leaves us with the same conclusion. These results are understandable when consulting fig. 3d of Howard and Möller [1980], see fig. 3.21, which shows contours of the neutron energies required for induced fission. At approximately ^{247}U, the energy contours turn negative, i.e., induced fission is already possible for thermal energies. Therefore, we must conclude from experimental evidence that the theoretical fission barriers employed are too low for these neutron-rich nuclei.

Thielemann et al. [1983a] calculated beta-delayed fission and neutron emission for all nuclei with $75 \leq Z \leq 100$ from stability to the neutron drip line for three different mass formulae, using the methods outlined above. We show their resulting P_{f} values in fig. 3.22. Their results are consistent with the situation depicted in fig. 3e of Howard and Möller [1980], see fig. 3.23, which shows contours of $Q_\beta - B_{\mathrm{f}}$. This quantity becomes positive for $N > 152$ and has very large values, up to 7 MeV, in an area around $163 < N < 172$ and $88 < Z < 98$.

Hoff [1986, 1987] did a very careful analysis, testing specifically whether the results of the Hutch event are compatible with the predictions for beta-delayed fission. Starting from the observed abundances of beta-stable nuclei up to $A = 257$ after the event, he extrapolated backwards to obtain the required abundances of the uranium isotopes produced in the explosion, taking into account the predicted fission losses in each isobaric chain. A reasonable agreement between predicted abundances [Eccles 1970; Ingley 1969; Truran and Cameron 1966] and experiment could only be obtained with the consistent use of the fission barriers *and* nuclear masses from Howard and Möller [1980]. Nevertheless, in this case an excessively large abundance of ^{257}U is also predicted.

Since the 1976 mass-formula evaluation, which includes formulae such as those of Myers [1976] and von Groote et al. [1976], additional knowledge about the extrapolation of nuclear masses to regions far from stability has emerged. In some regions of the nuclear chart, experimental data are now available for nuclei up to the vicinity of the r-process path (i.e., ^{130}Cd and ^{80}Zn). The general result is that a steeper slope of the "mass parabola" is indicated than in most of the 1976 mass formulae. Based on r-process studies, Hilf et al. [1976] obtained improved fits to the solar-system r-abundances, when using droplet-model parameters which led to a steeper mass parabola. The general trend they found is close to the present experimental findings and the most recent results by Möller et al. [1988] (finite-range droplet model with improved pairing corrections, treatment of nuclear deformations, etc.). The Howard

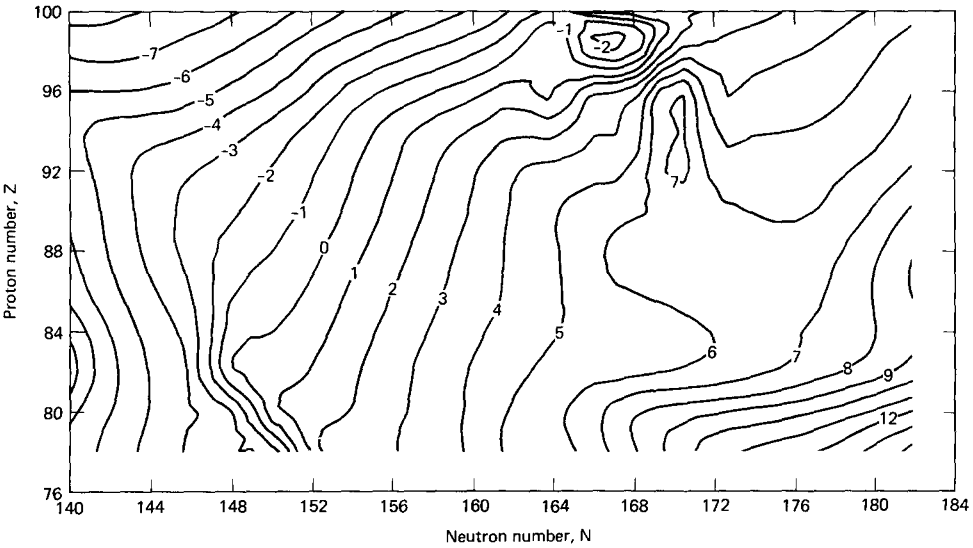

Fig. 3.23. Beta-decay minus fission-barrier energy, $Q_\beta - B_f$, contours for the mass formula of Howard and Möller [1980]. Beta-delayed fission becomes important where this difference turns positive. The contour line of 7 MeV, around $Z = 92$ and $N = 170$, indicates the area where 100% beta-delayed fission is encountered.

and Möller [1980] mass calculation still used a macroscopic model similar to the one of Myers [1976], which resulted in too shallow a mass parabola. Therefore, the predicted beta-decay Q-values are too small and neutron-capture Q-values are too large.

It is then also understandable why the P_f-values of Thielemann et al. [1983a], obtained with a more realistic but steeper mass formula with larger Q_β-values, predicted too large an amount of beta-delayed fission. Given that the nuclear masses seem to follow such a steeper slope, we must conclude – in agreement with the findings from neutron-induced fission of uranium isotopes – that larger fission barriers are needed to explain the experimental results from thermonuclear explosions. This is in agreement with the most recent calculations by Meyer et al. [1989b] which are illustrated in fig. 3.24. We note that the $Q_\beta - B_f$ values are substantially reduced, relative to the situation shown in fig. 3.23.

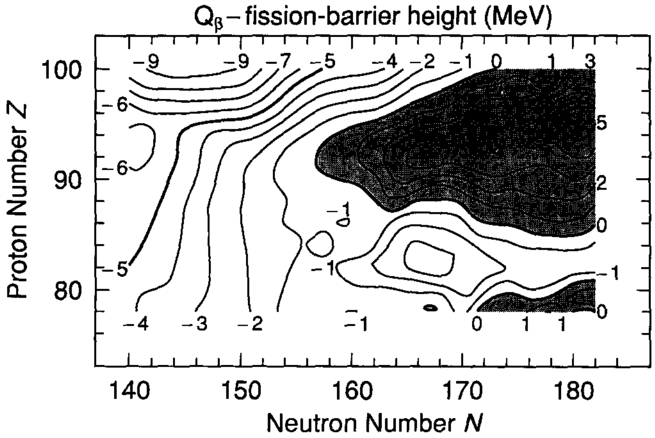

Fig. 3.24. Same as fig. 3.23 but taken from the improved calculations of Meyer et al. [1989b]. With the drastically enhanced fission barriers (see fig. 3.6), $Q_\beta - B_f$ is reduced accordingly and leads to a strong reduction in beta-delayed fission as well.

It should also be noted that the experiments mentioned above clearly established the effect of beta-delayed fission by not producing an $A = 256$ isotope nor any isotopes beyond $A = 257$, although in a series of experiments the neutron fluence was progressively increased. This effect, however, was overestimated as a result of using the previously determined (and presumably too low) fission barrier.

4. R-process calculations

4.1. Basic equations

The system of differential equations for an r-process network includes the terms for all strong, electromagnetic and weak interactions governing the nuclear transformations. These include neutron captures, neutron-induced fission, photodisintegrations, beta decays, beta-delayed neutron emission and fission. For nuclei with $Z < 80$, fission does not play any role and neutron captures, photodisintegrations and beta decays dominate. We can write a general set of N differential equations for the time rate of change of the individual nuclear abundances as (see, e.g., Clayton [1968]),

$$\dot{Y}(Z, A) = \sum_{Z',A'} \lambda_{Z',A'} Y_{Z',A'} + \sum_{Z',A'} \rho N_{\mathrm{A}} \langle \sigma v \rangle_{Z',A'} Y_{Z',A'} Y_{\mathrm{n}} , \tag{4.1}$$

where the first term on the right-hand side of eq. (4.1) includes beta decays (with all possible emission channels) and photodisintegrations. The second term includes all neutron-induced reactions. The terms can be positive or negative, depending upon whether they produce or destroy the nucleus (Z, A). For the heavy (i.e., high Z) and neutron-rich nuclei in question, only neutron-induced reactions are of importance due to the high Coulomb barriers between the particles.

Thus, only reactions involving neutrons as projectiles or emitted particles, such as (γ, n) photodisintegrations and beta-delayed neutron emission, need be considered. The number densities n are related to the abundances, Y, by

$$n = \rho N_{\mathrm{A}} Y , \tag{4.2}$$

where ρ is the mass density and N_{A} is Avogadro's number. Using this equation, we can replace $\rho N_{\mathrm{A}} Y_{\mathrm{n}}$ in eq. (4.1) by n_{n}, underlining the fact that the number density of neutrons is the important quantity for the r-process rather than the neutron abundance. Depending upon the specific conditions, either beta decays can be faster than neutron captures and photodisintegrations in an s-process, or vice versa when $(\mathrm{n}, \gamma) \rightleftarrows (\gamma, \mathrm{n})$ equilibrium exists. If the beta flow (i.e., the decay of the nuclei as a result of beta decays) from each Z-chain to $Z + 1$ is equal to the flow from $Z + 1$ to $Z + 2$ then a steady flow or beta flow equilibrium will exist. When $(\mathrm{n}, \gamma) \rightleftarrows (\gamma, \mathrm{n})$ equilibrium or a steady flow condition exists, certain simplifying assumptions can be made in solving eq. (4.1). These simplifications make it possible to avoid having to solve the general set of equations, which normally involves a linear system of the size of the nuclear network. We first discuss these special cases before considering the general case in section 4.4.

4.2. $(n, \gamma) \rightleftarrows (\gamma, n)$ *equilibrium or the waiting-point approximation*

As long as there are enough reaction partners, i.e., a high neutron density and a large high-energy photon density (= high temperatures), we can expect that strong and electromagnetic interactions occur on a much faster timescale than weak interactions (i.e., beta decays). (This will not be the case for charged particles like protons and alpha particles, because of the large charge and Coulomb barriers of the heavy nuclei involved.) In such a case, involving large neutron-capture and photodisintegration rates, the beta-decay rates become negligible in eq. (4.1) and the abundance equation for the nucleus (Z, A) is dominated by the following terms:

$$\dot{Y}(Z, A) = \lambda_\gamma(Z, A+1)Y(Z, A+1) - \langle \sigma v \rangle_{Z,A} Y_{Z,A} n_n \,. \tag{4.3}$$

The high nuclear rates will ensure an equilibrium, i.e. $\dot{Y}(Z, A) = 0$, and an abundance ratio

$$\frac{Y(Z, A+1)}{Y(Z, A)} = \frac{\langle \sigma v \rangle_{Z,A}}{\lambda_\gamma(Z, A+1)} n_n \,. \tag{4.4}$$

This condition is known as $(n, \gamma) \rightleftarrows (\gamma, n)$ equilibrium or the waiting-point approximation, where the nucleus with maximum abundance in each isotopic chain must wait for the longer beta-decay timescale.

Reaction rates for capture and photodisintegration are related by detailed balance [Fowler et al. 1967]

$$\lambda_\gamma(Z, A) = \frac{2G(Z, A)}{G(Z, A+1)} \left(\frac{A}{A+1}\right)^{3/2} \left(\frac{m_u kT}{2\pi\hbar^2}\right)^{3/2} \langle \sigma v \rangle_{Z,A} \exp[-S_n(Z, A)/kT] \,. \tag{4.5}$$

Here G denotes the partition function (m_u is the nuclear mass unit) and S_n the neutron separation energy or the neutron-capture Q-value. Equations (4.4) and (4.5) lead to a prediction for the abundance ratios which is dependent only on n_n, T and S_n,

$$\frac{Y(Z, A+1)}{Y(Z, A)} = n_n \frac{G(Z, A+1)}{2G(Z, A)} \left(\frac{A+1}{A}\right)^{3/2} \left(\frac{2\pi\hbar^2}{m_u kT}\right)^{3/2} \exp[S_n(Z, A)/kT] \,. \tag{4.6}$$

S_n introduces the dependence on nuclear masses, i.e., a nuclear mass formula for these very neutron-rich unstable nuclei. Under the assumption of $(n, \gamma) \rightleftarrows (\gamma, n)$ equilibrium (i.e., the waiting-point approximation), we do not need a detailed knowledge of neutron-capture cross sections. This is probably the main reason why many early calculations made use of this approximation. It is, however, valid for quite a number of conditions (see discussion below).

One fact which can be easily deduced from eq. (4.6), given that $A/(A+1) \approx 1$ and neglecting differences in the ratios of the partition functions, is that the abundance maxima in each isotopic chain are determined by the neutron number density n_n and the temperature. Approximating $Y(Z, A+1)/Y(Z, A)$ by one at the maximum, and all other quantities being constants, the neutron separation energy, S_n, has to be the same for all abundance maxima in each isotopic chain. The abundance flow from each isotopic chain to the next is governed by beta decays. We can introduce a total abundance in each isotopic chain $Y(Z) = \Sigma_A Y(Z, A)$, and each $Y(Z, A)$ can be expressed as $Y(Z, A) = P(Z, A)Y(Z)$. The individual population coefficients, $P(Z, A)$, are obtained from the equilibrium condition (eq. 4.6). The set of differential equations which replaces eq. (4.1) in this case is

$$\dot{Y}(Z) = Y(Z-1) \sum_A P(Z-1, A)\lambda_\beta(Z-1, A) - Y(Z) \sum_A P(Z, A)\lambda_\beta(Z, A) \,, \tag{4.7}$$

where $\lambda_\beta(Z, A)$ is the beta-decay rate of nucleus (Z, A).

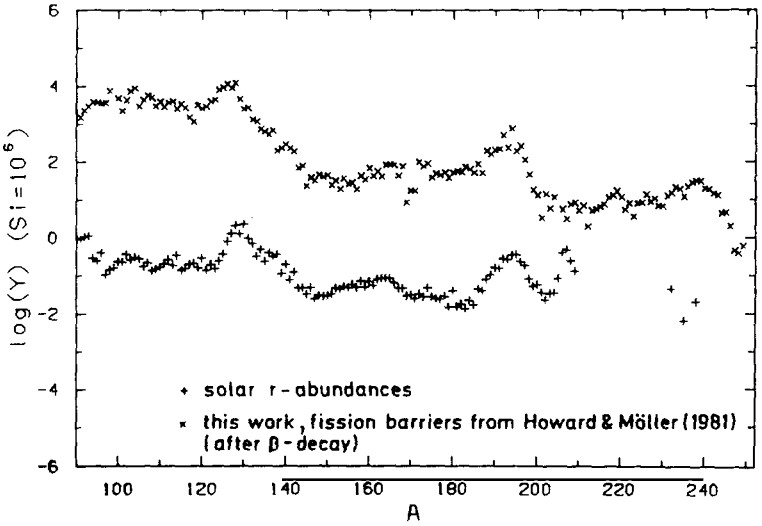

Fig. 4.1. R-process abundances after freezeout and beta decay, calculated by Thielemann et al. [1983b] (labelled as "this work"), assuming $(n,\gamma) \rightleftarrows (\gamma,n)$ equilibrium. The top curve is the observed solar-system r-process abundances from Cameron [1973].

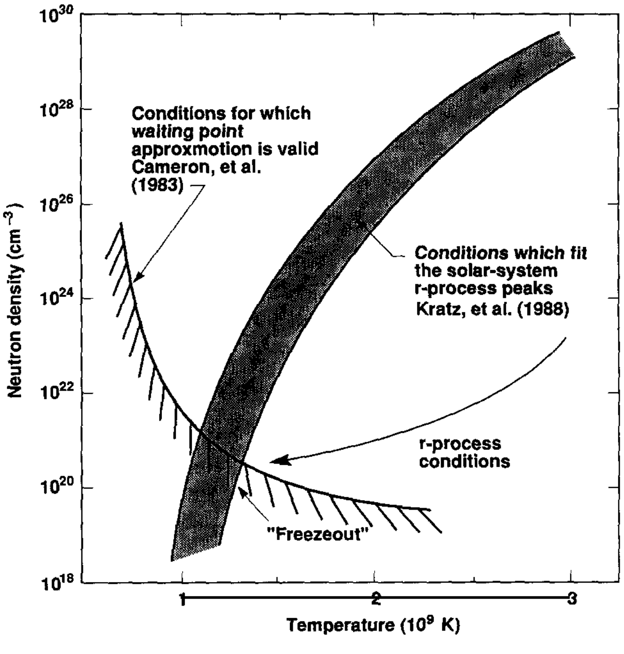

Fig. 4.2. Neutron number densities and temperatures consistent with observed r-process peaks and measured beta-decay rates [Kratz et al. 1988]. Also shown are the conditions found by Cameron et al. [1983a] for which the classical waiting-point approximation is valid. The thick arrow is a schematic illustration of the temperature and densities produced in an r-process environment before freezeout at $n_n \sim 10^{20}\,\mathrm{cm}^{-3}$ and $T \sim 10^9$ K (from Mathews and Cowan [1990]).

This means that instead of solving a system of differential equations for all individual constituents, it is sufficient to solve a system which contains only as many equations as the number of Z-chains. The individual abundances are obtained from eq. (4.6). The neutron number density is governed by the fact that the total number of nucleons, free and in nuclei, is constant in time, i.e., $Y_n(=n_n/\rho N_A) + \Sigma_{Z,A} AY(Z, A) = \text{constant}$. Results of an r-process calculation performed under the assumption of $(n,\gamma) \rightleftarrows (\gamma, n)$ equilibrium are illustrated in fig. 4.1 from Thielemann et al. [1983b].

The waiting-point approximation is only valid if either the temperature or neutron number density of the gas is very high [Cameron et al. 1983a]. If not, the flow of nuclei toward higher neutron number N, for a given proton number Z, is steadily depleted by beta decay. As a result, only a small fraction of the flow can actually reach a waiting point. This means that the waiting-point approximation is only valid for certain astrophysical conditions. Cameron et al. [1983a], using steady-flow calculations, found that for temperatures of 2×10^9 K and higher, the waiting-point approximation was valid for neutron number densities, n_n, as low as $10^{20}\,\text{cm}^{-3}$. On the other hand, they found that for lower temperatures ($\sim 10^9$ K) and high values of n_n ($\sim 10^{25}\,\text{cm}^{-3}$), the waiting-point approximation was no longer valid. Their work constrains the types of astrophysical environments that can be studied using the techniques of classical r-process calculations. Mathews and Cowan [1990] illustrate the conditions for which the waiting-point approximation is valid (fig. 4.2 and their fig. 3). It should be noted, however, that the positions of the curves in fig. 4.2 are somewhat dependent upon the mass formula employed.

4.3. *Steady flow*

Cameron et al. [1983b] examined the sensitivities of r-process yields to a number of physical quantities. Their original motivation was to examine the types of r-process conditions that might occur in the helium layer of a star undergoing a supernova explosion (see section 5), but their parameter studies were not confined to any specific astrophysical environment. In their nucleosynthesis calculations, they used the heavy-nuclei network of Truran et al. [1978a, 1978b], which contained 6033 nuclei from proton number 14 to 114. Each of these nuclei could undergo neutron capture, photodisintegration with emission of neutrons, and beta decay with the emission of up to three neutrons from the product nucleus, depending upon the excitation of that nucleus after beta decay.

To facilitate their r-process studies, Cameron et al. [1983b] used a steady-flow approximation to the r-process, which they defined in the following terms. A steady rate of input of nuclei occurs at the bottom of the network (in their case ^{28}Si), and nuclei are allowed to flow out at the top of the network. After a long enough time, and if fission cycling is neglected, then all the nuclei in the network will approach a steady-state abundance in which $\dot{Y}(Z, A) = 0$ and the rate of inflow of nuclei is equal to the rate of outflow of nuclei. The equation for each nucleus can be written as

$$\begin{aligned}
&\langle \sigma v \rangle_{Z,A-1} Y(Z, A-1) n_n + \lambda_\gamma(Z, A+1) Y(Z, A+1) \\
&\quad + \lambda_\beta(Z-1, A) Y(Z-1, A) + \lambda_{\beta n}(Z-1, A+1) Y(Z-1, A+1) \\
&\quad + \lambda_{\beta\,2n}(Z-1, A+2) Y(Z-1, A+2) + \lambda_{\beta\,3n}(Z-1, A+3) Y(Z-1, A+3) \\
&\quad = \langle \sigma v \rangle_{Z,A} Y(Z, A) n_n + \lambda_\gamma(Z, A) Y(Z, A) \\
&\qquad + [\lambda_\beta(Z, A) + \lambda_{\beta n}(Z, A), + \lambda_{\beta\,2n}(Z, A) + \lambda_{\beta\,3n}(Z, A)] Y(Z, A)\,, \qquad (4.8)
\end{aligned}$$

where $\langle \sigma v \rangle$ is the thermally averaged neutron-capture cross section, λ_γ is the photodisintegration rate,

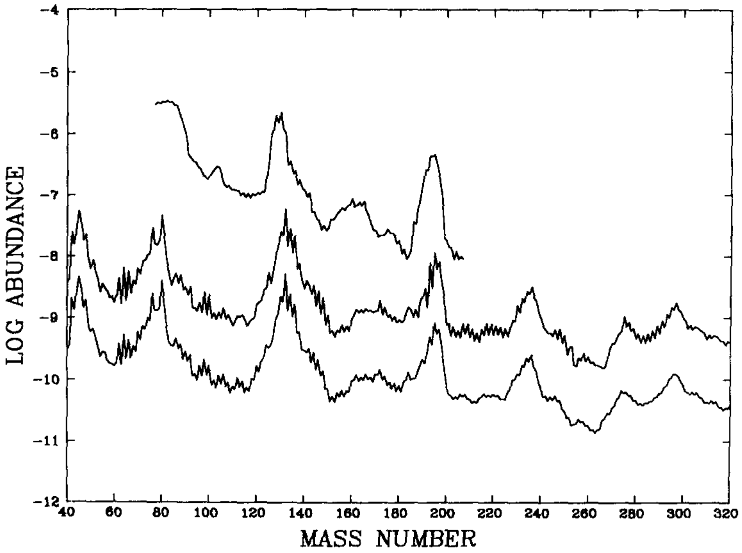

Fig. 4.3. R-process yield curves for a neutron number density of $10^{20}\ \mathrm{cm}^{-3}$ from Cameron et al. [1983b]. The top curve is the observed solar-system r-process curve from Cameron [1982a]. The middle curve is the steady-flow abundance curve, and the bottom curve is the result of letting the nuclei whose abundances are given in the middle-curve beta decay to the valley of beta stability. The vertical normalizations of the curves are arbitrary.

λ_β is the beta-decay rate, and $\lambda_{\beta n}$, $\lambda_{\beta\,2n}$, and $\lambda_{\beta\,3n}$ are the beta-decay rates with the emission of one, two and three delayed neutrons, respectively. n_n is the neutron number density, and Y is the abundance of the individual nucleus as defined in eq. (4.2).

The left-hand side of equation (4.8) represents the inflow of nuclei and the right-hand side the outflow of nuclei. This equation can be applied to all of the nuclei in the network. The ratio of each nuclear abundance to the abundance of the lightest nucleus in the network can then be determined. The steady flow is progressive such that each row of nuclei of specified Z is populated by beta decay of nuclei with $Z-1$ and is depleted as a result of beta decay to $Z+1$. Because of this progressive nature, the solution of the equations is simplified. The network is, in fact, solved one row of Z at a time once the input to it from the preceding row has been established. The results of some of the steady-flow calculations [Cameron et al. 1983b] are shown in fig. 4.3.

While the steady-flow approximation is not as applicable as a fully dynamic calculation (see section 4.4 below), it can be applied for calculations in which the neutron density only changes on time scales long in comparison to beta-decay half-lives. In that case, an equilibrium between the total abundance of nuclei with charge numbers Z and $Z+1$ is always established, without assuming an $(n,\gamma)\rightleftarrows(\gamma,n)$ equilibrium. The waiting-point approximation used in the classical (or equilibrium) r-process calculations, however, assumed that nuclei move fast towards the waiting points in each isotopic chain close to the neutron drip line. This approximation neglects the beta decays along the path before the waiting point in case of low neutron number densities and temperatures.

4.4. *Dynamic r-process calculations*

In studying various astrophysical environments it was found that there were conditions where heavy-nuclei synthesis might occur, but at neutron number densities far less than assumed in the classical r-process (see, e.g., Cameron [1973], Blake and Schramm [1976], Cowan and Rose [1977], Truran et al. [1978a]; and Thielemann et al. [1979]). To study these environments and to calculate the amount of r-process synthesis required using different techniques than had been used previously in the equilibrium models employing waiting points. As indicated above, the waiting-point approximation is only valid when the neutron number density and/or the temperature is very high. The steady-flow techniques (also described above) correctly treat the neutron-capture rates and beta decays of individual Z chains, and have the advantage of not using the waiting-point approximation. However, the steady-flow assumption ignores the effects of neutron captures and beta decays on the dynamics of the r-process. Thus, while the steady-flow approximation is useful when studying a number of different r-process conditions, it is not comparable to a full dynamic r-process calculation, particularly where the temperature and neutron number density are falling rapidly with time. Dynamic models are required for the study of r-process conditions over a wide range of neutron number densities.

The dynamic models of Cowan et al. [1983] are illustrative of the techniques needed to study nonstandard (or nonclassical) r-process environments. In these dynamic calculations, $(n, \gamma) \rightleftarrows (\gamma, n)$ equilibrium is not assumed and the steady-flow approximation is not used. Instead, the r-process path is determined by competition between the neutron captures and the beta-decay rates. The neutron-capture and beta-decay rates are determined for each nucleus as a function of temperature, density and neutron number density. If the neutron-capture rate is higher than the beta-decay rate, then a neutron is normally captured. If not, then normally a beta decay occurs. The r-process path therefore is affected both by the astrophysical conditions and by the nuclear properties of the individual nuclei.

The dynamical network used by Cowan et al. [1983] consisted of two parts. One part was a charged-particle network that was responsible for the production of neutrons, particularly as a result of (α, n) reactions on light nuclei such as ^{13}C. The second part of the dynamical network was an r-process (neutron-capture–beta-decay) code that determines the abundances of the heavy nuclei. This network extends from $Z = 14$ to 114 and contains all nuclei from the so-called "valley of beta stability" to the "neutron-drip line". Using the mass formula of Truran et al. [1970] to determine the drip line resulted in a total of 6033 nuclei in this r-process network. (Other mass formulae, which predict different drip lines, will result in a different number of nuclei. Thus, for example, using the mass formula of Hilf et al. [1976] results in 3937 nuclei in the r-process network; see the appendix.) The individual nuclear masses, the neutron-capture and beta-decay Q-values, and the shell and pairing energies were also calculated with the mass formula of Truran et al. [1970]. The neutron-capture rates were calculated with statistical model methods (see section 3.4) and the beta-decay rates were taken from the gross theory or Klapdor et al. [1984], where experimental values were not available.

These two networks are coupled together such that they both run simultaneously at each time step, and the number of neutrons produced and captured is transmitted back and forth between them. The number of neutrons captured per second per cm^3 by the heavy elements, R_n, can be written as

$$R_n = \rho N_A \dot{Y}_n = \sum_i \rho N_A Y_i \langle \sigma v \rangle n_n , \tag{4.9}$$

where Y_i is the abundance of isotope i, and $\langle \sigma v \rangle$ is the thermally averaged neutron-capture rate for isotope i. Thus at each time step, the neutrons produced by the charged-particle network are introduced into the neutron-capture–beta-decay network. The number of neutrons captured in this network is then determined, using eq. (4.9), and cycled back to the charged-particle network to ensure an accurate accounting of the number of neutrons produced and absorbed, and to ensure mass conservation.

We repeat here the description of the numerical techniques used in these dynamical calculations that was outlined in Cowan et al. [1983] (first employed by Cameron et al. [1970]). The numerical methods employed in the solution of the r-process rate equations involve the straightforward application of implicit differencing techniques. Consider the following representative segment of the nuclear reaction network:

$$\begin{array}{lllll}
(Z+1, A-2) & (Z+1, A-1) & (Z+1, A) & & \\
 & (Z, A-1) & (Z, A) & (Z, A+1) & \\
 & & (Z-1, A) & (Z-1, A+1) & (Z-1, A+2)\,.
\end{array}$$

We include all possible neutron-capture and photoneutron reactions, as well as beta decays leading to the emission of zero, one, two, or three delayed neutrons. The rate of change of the abundance of nucleus (Z, A) is then given by

$$\begin{aligned}
\dot{Y}(Z, A) = {} & n_{\mathrm{n}} Y(Z, A-1)\sigma_{A-1} + Y(Z, A+1)\lambda_{A+1} \\
& - Y(Z, A)(n_{\mathrm{n}}\sigma_A + \lambda_A + \lambda_{\beta}^{A} + \lambda_{\beta\mathrm{n}}^{A} + \lambda_{\beta\,2\mathrm{n}}^{A} + \lambda_{\beta\,3\mathrm{n}}^{A}) \\
& + Y(Z-1, A)\lambda_{\beta}^{Z-1,A} + Y(Z-1, A+1)\lambda_{\beta\mathrm{n}}^{Z-1,A+1} + Y(Z-1, A+2)\lambda_{\beta\,2\mathrm{n}}^{Z-1,A+2} \\
& + Y(Z-1, A+3)\lambda_{\beta\,3\mathrm{n}}^{Z-1,A+3}\,, \qquad (4.10)
\end{aligned}$$

where $Y(Z, A)$ is the abundance of nucleus (Z, A), n_{n} is the neutron number density, σ_{A-1} is the thermally averaged (n, γ) reaction rate $\langle \sigma v \rangle$ of nucleus $(Z, A-1)$, λ_{A+1} is the photodisintegration rate (γ, n) for nucleus $(Z, A+1)$, λ_{β}^{A} is the beta-decay rate of nucleus (Z, A), $\lambda_{\beta\mathrm{n}}^{A}$ is the rate of beta decay followed by the emission of one delayed neutron, $\lambda_{\beta\,2\mathrm{n}}^{A}$ is the rate of beta decay followed by the emission of two neutrons, and $\lambda_{\beta\,3\mathrm{n}}^{A}$ is the rate of beta decay followed by the emission of three neutrons.

In a fully implicit treatment, the stiff differential equations in eq. (4.10) can be rewritten (see, e.g., Press [1986, section 15.6]) as difference equations of the form

$$\Delta Y(Z, A)/\Delta t = f(Y(Z_i, A_i, t+\Delta t))\,, \quad Y(Z, A, t+\Delta t) = Y(Z, A, t) + \Delta Y(Z, A)\,.$$

In this treatment, all quantities on the right-hand side are evaluated at time $t + \Delta t$. If the neutron abundance $(Y_{\mathrm{n}} = n_{\mathrm{n}}/\rho N_{\mathrm{A}})$ was treated in the same manner, this would result in a set of nonlinear equations for the new abundances $Y(Z, A, t+\Delta t)$, which can be solved using a multidimensional Newton–Raphson iteration procedure. If we assume that n_{n} is constant (over a time Δt), eq. (4.10) leads to a set of linear equations for the ΔY,

$$\begin{aligned}
\Delta Y(Z, A)/\Delta t = {} & n_{\mathrm{n}}\sigma_{A-1}[Y(Z, A-1) + \Delta Y(Z, A-1)] + \lambda_{A+1}[Y(Z, A+1) + \Delta Y(Z, A+1)] \\
& - [Y(Z, A) + \Delta Y(Z, A)](n_{\mathrm{n}}\sigma_A + \lambda_A + \lambda_{\beta}^{A} + \lambda_{\beta\mathrm{n}}^{A} + \lambda_{\beta\,2\mathrm{n}}^{A} + \lambda_{\beta\,2\mathrm{n}}^{A}) \\
& + [Y(Z-1, A) + \Delta Y(Z-1, A)]\lambda_{\beta}^{Z-1,A} \\
& + [Y(Z-1, A+1) + \Delta Y(Z-1, A+1)]\lambda_{\beta\mathrm{n}}^{Z-1,A+1} \\
& + [Y(Z-1, A+2) + \Delta Y(Z-1, A+2)]\lambda_{\beta\,2\mathrm{n}}^{Z-1,A+2} \\
& + [Y(Z-1, A+3) + \Delta Y(Z-1, Z+3)]\lambda_{\beta\,3\mathrm{n}}^{Z-1,A+3}\,. \qquad (4.11)
\end{aligned}$$

Here, consistent with the implicit treatment, the derivative at time t is set equal to its value at time $t + \Delta t$. The critical assumption we have made is that the neutron number density n_n remains constant over the time interval Δt. This, as we shall see below, allows great simplicity in the algebraic solution of the difference equations.

Note that for the lowest Z occurring in the r-process network, Z_min, eq. (4.11) contains only Δ-terms for $(Z, A-1)$, (Z, A) and $(Z, A+1)$, and thus reduces to a tridiagonal matrix of the linear system. Having solved these first lines for all nuclei with $Z = Z_\mathrm{min}$, the Δ-terms in the following equations for nuclei with $Z - 1 = Z_\mathrm{min}$ are already known, and need no longer be treated as unknown variables. Then the equations for this isotopic chain also become tridiagonal for $(Z, A-1)$, (Z, A), $(Z, A+1)$, etc. Thus eq. (4.11) can be rewritten in the following form for any isotope chain:

$$\begin{aligned} &\Delta Y(Z, A)(1/\Delta t + n_\mathrm{n}\sigma_A + \lambda_A + \lambda_\beta^A + \lambda_{\beta\mathrm{n}}^A + \lambda_{\beta\,2\mathrm{n}}^A + \lambda_{\beta\,3\mathrm{n}}^A) \\ &\quad - \Delta Y(Z, A-1) n_\mathrm{n}\sigma_{A-1} - \Delta Y(Z, A+1)\lambda_{A+1} \\ &\quad = \dot{Y}(Z, A, t(Z), t + \Delta t(Z-1)) , \end{aligned} \tag{4.12}$$

where n_n, $Y(Z, A-1)$, $Y(Z, A)$ and $Y(Z, A+1)$ are evaluated at time t, and $Y(Z-1, A)$, $Y(Z-1, A+1)$, $Y(Z-1, A+2)$ and $Y(Z-1, A+3)$ are evaluated at $t = t + \Delta t$.

For each nucleus along a specified isotope chain we thus have an equation of the form

$$a_i\Delta_{i-1} + b_i\Delta_i + c_i\Delta_{i+1} = d_i , \tag{4.13}$$

where in general

$$\begin{aligned} &a_i = -n_\mathrm{n}\sigma_{A-1} , \qquad b_i = (1/\Delta t + n_\mathrm{n}\sigma_A + \lambda_A + \lambda_\beta^A + \lambda_{\beta\mathrm{n}}^A + \lambda_{\beta\,2\mathrm{n}}^A + \lambda_{\beta\,3\mathrm{n}}^A) , \\ &c_i = -\lambda_{A+1} , \qquad d_i = \dot{Y}(Z, A, t(Z), t + \Delta t(Z-1)) . \end{aligned} \tag{4.14}$$

The set of linearized equations for each isotope chain thus defines a tridiagonal matrix, the algebraic solution of which is quite straightforward.

This method of solution of the r-process network equations then proceeds as follows. Commencing with the isotope chain for Z_min, for which there is no introduction of new nuclei via beta decay, a set of linearized equations of the form (4.13) are solved for successive isotope chains. The abundances of the nuclei of lower Z, which determine the forward progression of flows via beta decay, are taken to be the values previously determined for time $t + \Delta t$. When this procedure is concluded, the neutron number density is updated consistent with the calculated gains and losses integrated over the time step, and thus with baryon conservation. One then advances to the next time step and repeats the entire procedure.

We emphasize that, subject only to the restrictions imposed by the assumed constancy of the neutron number density over the time step Δt, this method provides an exact solution to the difference equations. This procedure thus allows the advantages associated with the use of implicit techniques, even for a full r-process network containing 6033 nuclei. An example of a dynamic r-process calculation is shown in fig. 5.2.

4.5. Constraints on r-process conditions from r-abundances and nuclear properties

After having discussed all possible neutron number density and temperature conditions and the appropriate numerical methods to solve the r-process network, it might be worthwhile to ask if the isotopic abundance patterns found in solar r-process abundances together with our knowledge of nuclear properties can give a clue to the r-process conditions. Because of recent experimental and theoretical efforts in regions around $A \approx 80$ (neutron magic number $N = 50$) and $A \approx 130$ ($N = 82$), where the r-process path comes closest to stability, it is most appropriate to focus on the abundance patterns in both of these r-process peaks.

Beta-delayed neutron emission has been discussed in section 3.5. It has an impact on the final shaping of the isotopic abundances after the r-process freeze-out and during the beta decays back to stability. Figures 4.4 and 4.5 (from Kratz et al. [1988]) summarize the information in the $N = 50$ and $N = 82$ regions. P_n-values are given in % of the total beta decays of the parent nucleus. Exact numbers

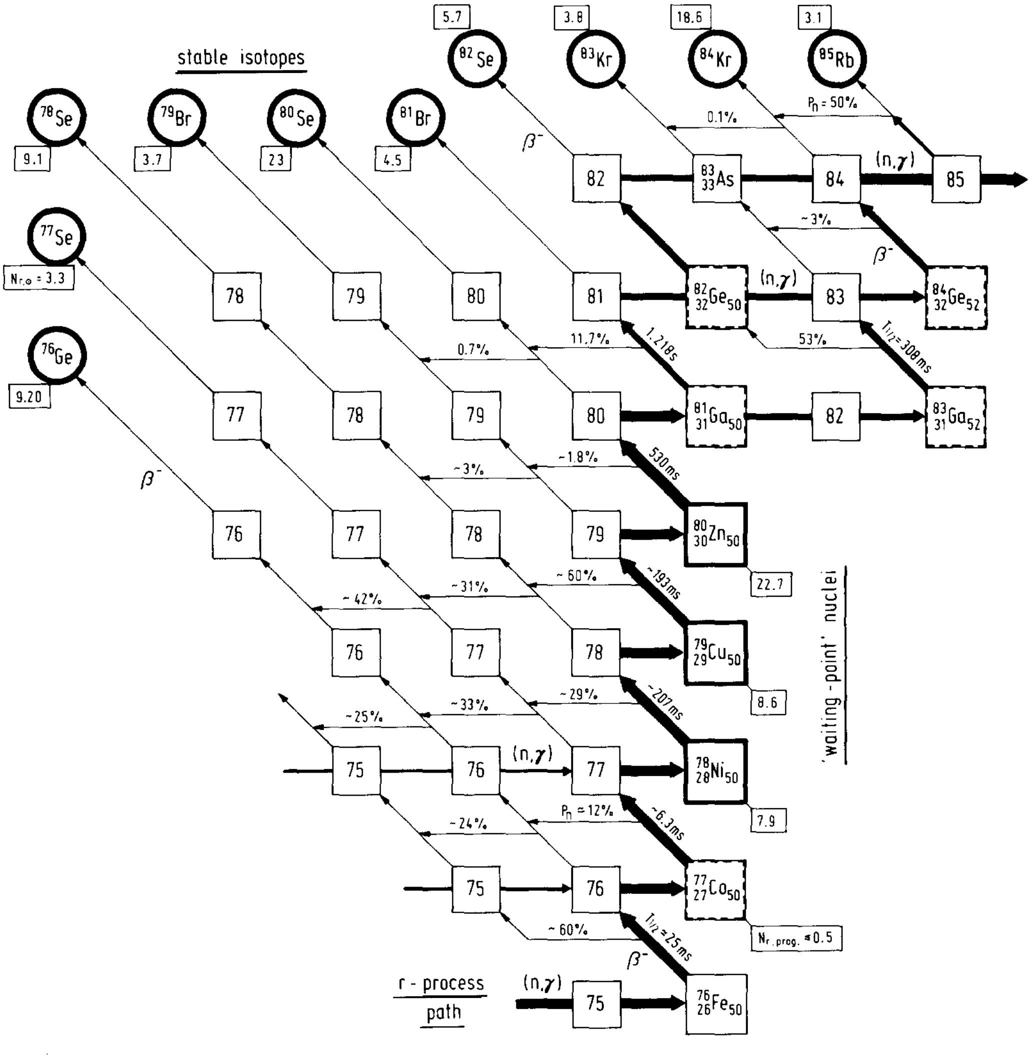

Fig. 4.4. Schematic view of the r-process path and the r-abundance features in the $A \approx 80$, $N \approx 50$ region. The $t_{1/2}$ and P_n values indicated in this figure are either experimental or, when preceded by an $\approx$ sign, RPA predictions (from Kratz et al. [1988]). The encircled isotopes are stable and are the endproducts of the r-process, after beta decay. The solar r-process abundances (normalized to $Si = 10^6$) of these stable nuclei are displayed in small boxes. The small boxes in the r-process path contain the abundances of those nuclei required to reproduce the solar values for stable isotopes.

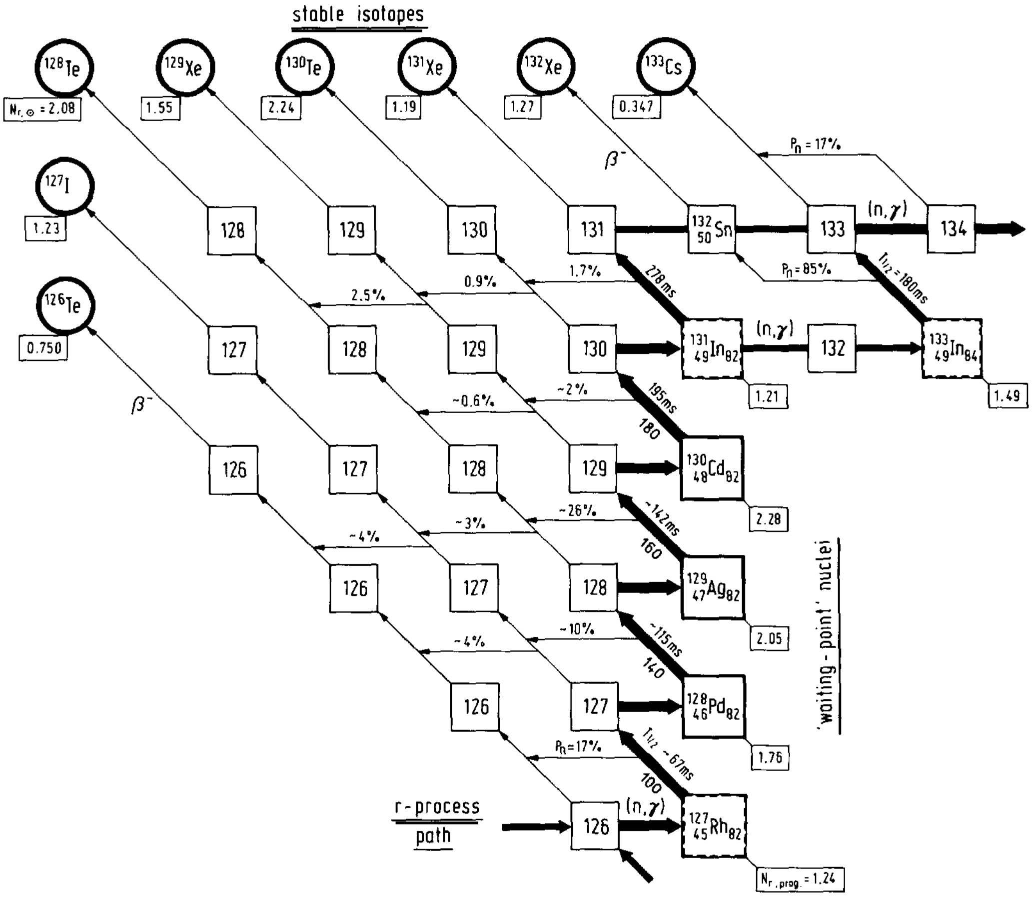

Fig. 4.5. Same as fig. 4.4 for the $A \approx 130$, $N \approx 82$ region (from Kratz et al. [1988]).

indicate experimental values, numbers preceded by a sign ≈ come from RPA calculations. With this information it is possible to predict the isotopic ratios of the final stable nuclei after decay (circles on the upper left side of the figures), provided that we know where the r-process path is located and the abundances of nuclei in the path.

Kratz et al. [1988] made the working hypothesis that the r-process abundances are produced under conditions of $(n, \gamma) \rightleftarrows (\gamma, n)$ equilibrium [see section 4.2 and eq. (4.6)]. In such a case, for a number of Z values at the neutron magic numbers $N = 50$ and 82, only one isotope contains the dominant abundance with $N = N_{\text{magic}}$. At a maximum Z, the r-process finally branches off from the magic neutron number and two even-N isotopes share the dominant abundance. In this way, the isotopic ratios of ^{131,133}In and ^{81,83}Ga are related to the abundances of the stable isotopes ^{131,132}Xe and ^{81}Br and ^{83}Kr. The beta-delayed neutron emission of ^{133}In and ^{83}Ga play an important role in these ratios, and are both experimentally determined. In order to reproduce the solar r-process ratios, certain neutron number densities and temperatures are required, as indicated in fig. 4.6. The dashed lines indicate the conditions necessary to reproduce the ^{81,83}Ga and ^{131,133}In isotopic abundance ratios, using two different mass formulae. The solid lines constrain the necessary conditions for which either ^{127}Rh, ^{128}Pd, ^{129}Ag and ^{130}Cd, or ^{77}Co, ^{78}Ni, ^{79}Cu and ^{80}Zn possess the maximum abundances in their isotopic

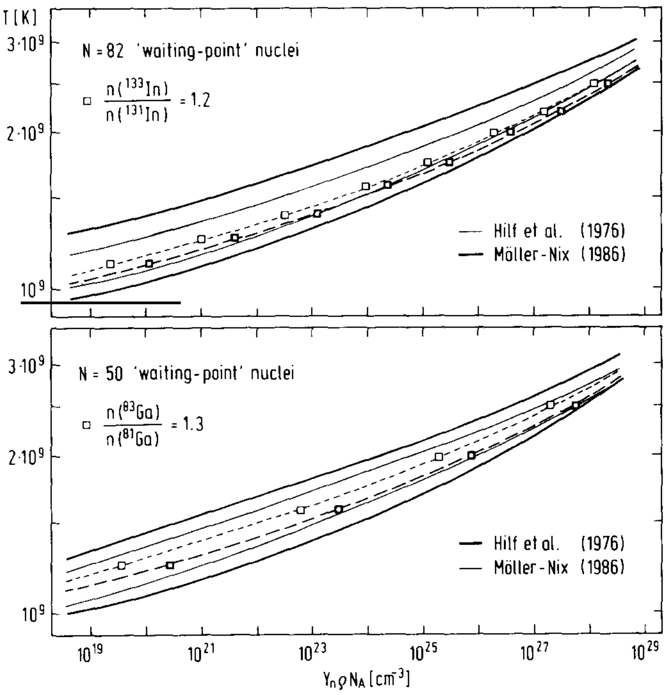

Fig. 4.6. Temperature–neutron-density ranges which give the correct r-process path through the $N = 50$ (lower part) and $N = 82$ (upper part) waiting-point nuclei, under the assumption of $(n, \gamma) \rightleftarrows (\gamma, n)$ equilibrium. The temperature and density conditions are given for two mass formulae whose behavior is similar as seen from the solid lines. The dashed lines indicate the locations at which the ^{83,81}Ga and ^{133,131}In ratios are obtained, which reproduce the solar ^{83}Kr/^{81}Br and ^{133,131}Xe ratios. The consistent temperature and density conditions found in both cases illustrated, under the assumption of $(n, \gamma) \rightleftarrows (\gamma, n)$ equilibrium, suggests that the solar-system r-process abundances resulted from a freezeout of such conditions (from Kratz et al. [1988]).

chains. One can see that these allowed regions include each other. In addition, the requirements for the $A \approx 80$ and $A \approx 130$ regions are identical. These arguments suggest that the solar r-process abundances were produced under conditions consistent with $(n, \gamma) \rightleftarrows (\gamma, n)$ equilibrium.

One can perform an additional test. When assuming that we have a steady-flow (or beta-flow) equilibrium (see section 4.3); in addition to an $(n, \gamma) \rightleftarrows (\gamma, n)$ equilibrium, we also have $\dot{Y}(Z) = 0$ in eq. (4.7). When we apply this last condition to the isotopic chains close to the $A = 80$ and 130 peaks, where only one nucleus dominates the abundance chain, the sum over A in eq. (4.7) is reduced to one term at $N = 50$ or 82. In such a case, we find $Y(Z)\lambda_\beta(Z) = \text{constant}$ along $N = 50$ or 82. From the known abundances of stable isotopes and known P_n-values for beta-delayed neutron emission, one can predict the abundances in the r-process path (c.f. boxes in figs. 4.4 and 4.5), and therefore also "predict" the beta-decay half-lives for these nuclei, provided that a steady flow existed. Table 4.1 (from Kratz et al. [1988]) indicates that the half-lives predicted in such a way agree closely with experimental or RPA values suggesting that a beta-flow or steady-flow equilibrium was achieved. If on the other hand, such an $(n, \gamma) \rightleftarrows (\gamma, n)$ and steady-flow equilibrium is assumed and the beta-decay half-lives are already known, it is possible to predict the abundance pattern in the $A \approx 80$ region. Normally, beta-delayed neutron emission is thought to smear and smooth out abundance fluctuations in the r-process path, when they occur in a statistical way. In the region $75 < A < 85$, however, the predicted beta-delayed neutron emission seems to enhance the odd–even staggering, in agreement with the observed solar r-process abundances (see fig. 4.7 from Kratz et al. [1990]).

Table 4.1
Beta-decay half-lives from Kratz et al. [1988]

	Beta-decay half-life, $T_{1/2}$ ms				Beta-decay half-life, $T_{1/2}$ ms		
Isotope	Exp.	RPA-S.M.	Beta-flow	Isotope	Exp.	RPA-S.M.	Beta-flow
^{133}In	180 ± 20	123		^{83}Ga	308 ± 4	288	
^{131}In	278 ± 3	240		^{81}Ga	1218 ± 4	1070	
^{130}Cd	195 ± 35	235	180	^{80}Zn	540 ± 30	502	750
^{129}Ag		172	160	^{79}Cu		193	200 [a]
^{128}Pd		115	140	^{78}Ni		207	185 [a]
^{127}Rh		67	100	^{77}Co		6.3	≤11.5 [a]

[a] Normalized to experimental $T_{1/2}(^{80}\mathrm{Zn})$.

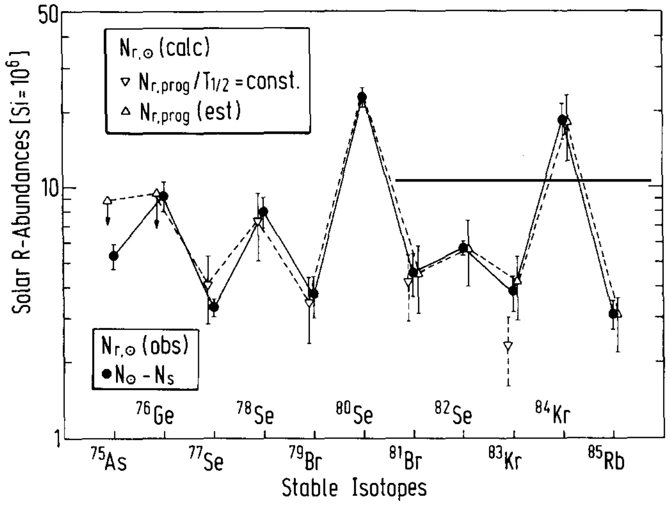

Fig. 4.7. Comparison of the solar r-process abundances in the $A \approx 80$ region with predicted abundances. The calculations employ the conditions shown in fig. 4.6 and assume $(n, \gamma) \rightleftarrows (\gamma, n)$ equilibrium in conjunction with a steady-flow (or beta-flow) equilibrium (from Kratz et al. [1990]).

While all of this is not a direct proof, it is accumulated circumstantial evidence that the solar r-process abundances originated from freeze-out abundances of an r-process with high neutron number densities and temperatures typical of $(n, \gamma) \rightleftarrows (\gamma, n)$ and steady-flow equilibrium, i.e., the conditions illustrated in fig. 4.6. This may help us to make a choice in section 5 about the most probable r-process site.

5. Astrophysical sites and models

Despite many years of effort, the site for the synthesis of the r-process nuclei remains unknown. This search has been complicated by the fact that a knowledge of both the astrophysical environments and the nuclear properties of very neutron-rich (i.e., radioactive) nuclei is required. We present here a review of the various astrophysical sites that have been suggested over the years. We also note that it is possible, although it now appears very unlikely, that more than one site could have contributed to the solar-system r-process abundances. Additional reviews dealing with the site for the r-process include those of Hillebrandt [1978], Truran [1984], Mathews and Ward [1985], Cowan et al. [1986a] and Mathews and Cowan [1990].

The astrophysical sites for the production of the r-process nuclei can be categorized into three broad classes of primary, secondary and primordial. The first part of this chapter reviews sites associated with the primary or direct production of the r-process elements, such as might occur as a result of the expansion and cooling of a neutron-rich gas. These potential sites include the regions just outside of the neutronized cores of supernovae, "bubbles" or "jets" of neutronized matter ejected from the collapse of rotating (and magnetized) stellar cores, and neutron-star–black-hole and neutron-star–neutron-star collisions. Secondary production, where the r-process elements are "built up" as a result of neutron capture on a preexisting heavy element "seed" distribution, is then reviewed. Such possible secondary production sites include the helium zones and the carbon zones of stars undergoing supernova explosions, and helium cores of low mass stars. This section is followed by a discussion of the possibility of primordial production of heavy elements. Recent work has suggested that certain big bang cosmologies might lead to such a production.

5.1. *Primary production*

5.1.1. *Supernova cores*

The short timescale (i.e., seconds) for neutron capture, and the correspondingly large neutron fluxes required, have for some time suggested an explosive astrophysical origin for the r-process. Early (and clearly unsuccessful) attempts to associate ^{254}Cf with the light curve of type I supernovae [Burbidge et al. 1956; Baade et al. 1956] led Burbidge et al. [1957] and Cameron [1957] to associate the r-process with the neutron-rich material in an exploding supernova. (We now know, of course, that it is ^{56}Ni that powers the light curves.) These works were followed by the study of Seeger et al. [1965] which was the first time-dependent, numerical study of the r-process. The r-process calculations of Seeger et al. were made under the assumption of $(n,\gamma) \rightleftarrows (\gamma,n)$ equilibrium, but also included a beta-decay reaction network. This was an improvement over the earlier r-process calculations of Burbidge et al. [1957], which assumed a steady flow. Seeger et al. [1965] also used improved nuclear data in their calculations. Burbidge et al. [1957], for example, estimated beta-decay rates by considering only the decay of the ground state of the parent nucleus to the ground state of the daughter nucleus. More accurate rates were obtained by Seeger et al. who allowed for the possibility of beta decays to lowlying excited states in the daughter nucleus. Later work indicated that these beta-decay rates were still too slow due to the neglect of additional excited states available for beta decay [Cameron et al. 1970].

Assuming an initial composition of iron and neutrons, Seeger et al. [1965] were able to fit some (but not all) of the features of the observed solar-system r-process curve. To do so, however, they had to assume that two different astrophysical environments – one of short duration ($\sim$4 s) and the other of long duration ($\geq$4 s) – were responsible for synthesizing the r-process material. They concluded that the three different solar-system r-process mass peaks could not be produced under the same set of physical conditions. Further studies of the r-process in regions just outside of the neutronized cores of supernovae were made by a number of authors, including Cameron et al. [1970], Kodama and Takahashi [1973], Schramm [1973], Sato [1974], Kodama and Takahashi [1975], Hillebrandt and Takahashi [1976], Hillebrandt et al. [1976], and Hillebrandt [1978].

The early numerical calculations regarding the r-process, such as those of Seeger et al. [1965], were static and assumed a constant temperature and neutron number density. An exploding supernova, where the r-process was believed to occur, however, would not be static. The first dynamical r-process calculations were made by Cameron et al. [1970] who studied the r-process under conditions of varying temperature and density for a number of expanding supernova envelope adiabats. However, their fit to the solar-system r-process curve was not good, due in part to the lack of adequate nuclear data (particularly beta-decay rates) at that time. Their model also did not include fission effects. Cameron et al. [1970] also did not make a detailed calculation of the freeze-out, but instead assumed a sudden freeze-out at low neutron number densities resulting in an r-process distribution displaced from the solar system curve [Hillebrandt 1978].

Schramm [1973], also employing a dynamical r-process model, demonstrated that after the majority of the neutrons had been captured in the freeze-out, $(n,\gamma)\rightleftarrows(\gamma,n)$ equilibrium was no longer valid. Schramm also showed that if nonequilibrium processes were considered, the large odd–even abundance effects created by $(n,\gamma)\rightleftarrows(\gamma,n)$ equilibrium could be smoothed out naturally during freeze-out. Previous studies had to use artificial and nonphysical means to achieve a smoothing similar to that seen in the solar system distribution. Schramm's work also suggested, in contradiction to Seeger et al. [1965], that one site could synthesize the total solar-system r-process abundances. While Schramm [1973] achieved a better fit to the solar-system r-process abundances than Cameron et al. [1970], he was still unable to reproduce all of the observed mass peaks. This was partly due to the fact that Schramm [1973] had to use the old beta-decay rates of Seeger et al. [1965] and Senbetu [1973]. There were a number of deficiencies in these early estimates of the beta-decay rates, as discussed above in section 3.3. Schramm [1973] also assumed that the initial composition for the r-process was a large quantity of neutrons and alpha particles with a few iron atoms. Detailed network calculations, however, indicate that most of the neutrons could be captured by light nuclei prior to any significant formation of the iron nuclei [Hillebrandt and Thielemann 1977]. But a more general survey of temperature and density conditions, in which the seed-nucleus production rate is compatible with r-process nucleosynthesis, was undertaken by Norman and Schramm [1979] (see also fig. 2.6).

Sato [1974] examined the r-process in conjunction with a thermodynamic equation allowing for a nonadiabatic expansion. He found that the energy released as a result of beta decays and fissions is an important factor in determining the final r-process abundances. There were several problems with this model, however. The full set of thermodynamic and hydrodynamic equations was not solved consistently, with the density expansion being represented by an analytic formula. The effects of beta-decay heating on the temperature (leading to large nonadiabatic values) were also overestimated. A correct treatment, including the effects of heating on the expansion, would have reduced the deviation from an adiabat [Hillebrandt and Takahashi 1976; Hillebrandt 1978].

Hillebrandt et al. [1976], Hillebrandt and Takahashi [1976], and Hillebrandt [1978] examined the dynamical r-process by solving the nucleosynthesis equations in conjunction with a one-dimensional hydrodynamic treatment of a supernova explosion. These models included beta-decay heating and its feedback into the hydrodynamical equations. Using a single supernova event and a timescale of approximately one second, a fair fit to the solar-system r-process curve was achieved when a range of ejected mass zones was considered with a range of neutron to proton ratios [Hillebrandt et al. 1976; Hillebrandt and Takahashi 1976]. These authors also found that odd–even abundance effects were smoothed out by delayed neutron emission after freeze-out (see fig. 5.1). Their models also predicted that the r-process terminated from a lack of free neutrons before significant neutron-induced fission could occur.

It was also found, in contrast to Sato's [1974] result, that the temperature and density of matter in the r-process followed the $\gamma=4/3$ adiabat quite closely [Hillebrandt et al. 1976]. These authors assumed that $(n,\gamma)\rightleftarrows(\gamma,n)$ equilibrium existed until the freeze-out, when the neutron flux was

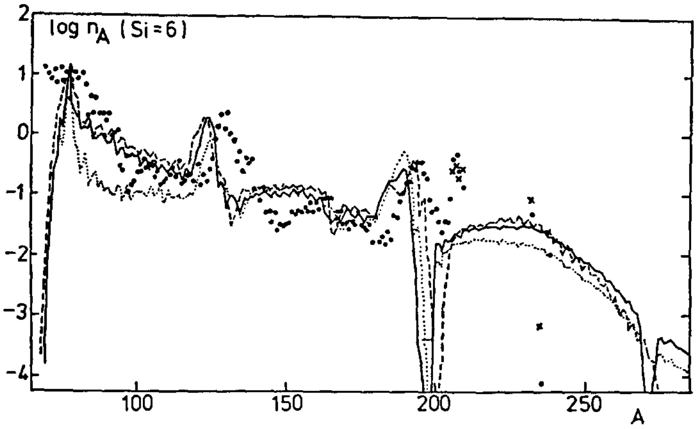

Fig. 5.1. R-process calculations from supernova-core models taken from Hillebrandt and Takahashi [1976]. The solid line is for the set of astrophysical parameters: $T_{max} = 1.2 \times 10^{10}$ K, $v_{max} = 5 \times 10^9$ cm s^{-1}, $T_{onset} = 5 \times 10^9$ K and $(n/p)_{max} = 7$. The dashed line uses $v_{max} = 4 \times 10^9$ cm s^{-1} instead of 5×10^9 cm s^{-1}. The dotted line assumes $(n/p)_{max} = 8$ rather than 7. The calculated relative abundances of $^{206-208}$Pb, ^{209}Bi, ^{232}Th and ^{235,238}U at 5×10^9 y after the event, are indicated by ×, and the observed abundances [Allen et al. 1971; Cameron 1973] are plotted as solid circles.

suddenly turned off. Such a situation is unphysical and in principle can distort the final abundance pattern. The r-process calculations of Hillebrandt et al. [1976] and Hillebrandt and Takahashi [1976] also used the initial astrophysical conditions, such as the supernova expansion velocity, as free parameters. Hillebrandt [1978], however, argues that the r-process results, in general, are not sensitive to those astrophysical conditions, with the noted exception of the initial maximum neutron to proton ratio.

A more serious problem with the model of Hillebrandt [1978], and all of the previously mentioned supernova core models, is that they predict a very large overproduction of r-process material. Hillebrandt et al. [1976], for example, find suitable conditions for r-process nucleosynthesis in at least $0.4\,M_\odot$ of the exploding supernova. In fact, such a large amount of matter, with radially varying n/p ratios, was required in order to fit the r-process abundance curve. On the other hand, only a small fraction of material per supernova is needed to reproduce the galactic r-process nucleosynthesis requirements. Depending upon the initial mass function and the assumed supernova rate, estimates range from $10^{-6}\,M_\odot$ [Truran and Cameron 1971] to $10^{-4}\,M_\odot$ [Mathews and Cowan 1990] of r-process material that must be ejected per supernova event. Core models, therefore, that predict large amounts (e.g., $0.4\,M_\odot$) of synthesized material are ejected per supernova will overproduce the observed r-process abundances by a factor of $\sim 10^3$–10^5. Thus, while most core models assume that each supernova explosion would eject the same large amount of material, the observed r-process abundances suggest that perhaps only a small subset of supernovae are responsible for synthesizing r-process material.

A second alternative is that all supernovae are responsible for r-process nucleosynthesis, but in contrast to the models mentioned above, only a small mass fraction per event is actually produced. This has not been demonstrated conclusively in any core model, however, partly due to the fact that the amount of r-process material required per supernova (i.e. $10^{-6}\,M_\odot$ to $10^{-4}\,M_\odot$) is smaller than a typical numerical zone in a supernova model. A third alternative is that while many (or all) supernovae produce r-process nuclei, only a small fraction actually eject this synthesized material. In fact, all of the models discussed above *assume* the ejection of r-process material into the interstellar medium.

We note, however, that all of these models are directly dependent upon the still unsolved type II supernova explosion mechanism, and thus are intrinsically uncertain. Only when reliable predictions are available for the prevailing conditions at the mass-cut in supernovae that form neutron stars, will it be possible to perform consistent calculations of r-process synthesis. For a general review of the current type II supernova model calculations see Bruenn [1989], Myra and Bludman [1989], Baron and Cooperstein [1991], and Mayle and Wilson [1991].

5.1.2. *Bubbles and jets*

The problems encountered by the supernova models discussed above, particularly the difficulty in ejecting the synthesized material, led to other suggested r-process sites and mechanisms for ejection. One such class is that of "bubbles" or "jets" of neutronized matter ejected from the collapse of rotating and/or magnetized stellar cores [LeBlanc and Wilson 1970; Schramm and Barkat 1972; Meier et al. 1976; Symbalisty 1984; Symbalisty et al. 1985; Mönchmeyer and Müller 1989; Hillebrandt et al. 1990]. Le Blanc and Wilson [1970] studied the magnetohydrodynamic collapse of a 7 $M_\odot$ star and found that magnetic field lines were stretched and amplified by differential rotation during the collapse. This resulted in a difference in the magnetic pressure which in turn led to the ejection (in a jet) of neutron-rich material from the core into the stellar envelope. The magnetic fields required were extremely high. Le Blanc and Wilson [1970] found that 10^{-2} $M_\odot$ of neutron-rich material was ejected from a 7 $M_\odot$ star. This presents problems since, if all core-collapse supernovae led to jet ejections typical of the Le Blanc and Wilson model, there would again be a large overproduction of r-process material in the Galaxy. Alternatively, the actual ejection of the r-process material into the interstellar medium might be a rare event.

Schramm and Barkat [1972], in a general study of the r-process in explosive environments, noted the difficulty of ejecting neutron-rich material. Depending upon their frequency of occurrence, Schramm and Barkat [1972] suggested that the magnetic jets found by Le Blanc and Wilson [1970] were the site for the r-process. Meier et al. [1976] generalized the work of Le Blanc and Wilson [1970] by considering a range of stellar core masses and initial magnetic fields. They found that matter could either be ejected violently immediately following collapse, or ejected as a result of buoyancy instabilities after a number of hydrodynamic time periods. In the first form of mass ejection [or magnetohydrodynamic (MHD) explosion] very large amounts of r-process material could be ejected, and the energy released could be comparable, in rare cases, to a supernova explosion (see also Müller and Hillebrandt [1979]). The amount of r-process material produced in this ejection ($\sim 10^3$) was much more than required to reproduce the observed solar-system abundances. In the second form of ejection (or buoyancy instability), Meier et al. [1976] found that highly magnetized, neutron-rich material near the core expands and rises into the envelope of the star. This buoyancy instability was found to occur for a wide range of conditions in cores, but only for timescales much longer than the free-fall time, and thus much longer than that considered by Le Blanc and Wilson [1970]. The study of Meier et al. [1976] was only semiquantitative, however, and the authors suggested that further numerical calculations were required to quantify their general results.

Symbalisty [1984] and Symbalisty et al. [1985] also considered collapsing rotating cores. They found, in contrast to Le Blanc and Wilson [1970], that models with rotation only (no magnetic field) could also eject neutron-rich material from the core. The different results could be explained by the improved physics (e.g. neutrino–matter coupling, an improved stellar equation of state and better presupernova evolutionary models) incorporated into the models of Symbalisty [1984] and Symbalisty et al. [1985]. The rotation-only models of these authors ejected 4×10^{-4} $M_\odot$ of neutron-rich matter per supernova.

This value is in rough agreement with their estimate of $\sim 10^{-4}\ M_{\odot}$ per supernova required to reproduce the galactic r-process abundances. The jet ejections in these rotation-only models, however, require very large rotation rates for the cores. It is not clear whether such high rotation rates are actually achieved in these collapsing cores. Furthermore, the actual abundance distribution of the matter ejected in these jets has also not been determined, and thus it is not clear whether a solar-system r-process distribution is produced. Recently Mönchmeyer and Müller [1989] and Hillebrandt et al. [1990] explored the gravitational collapse of a variety of rotating (nonmagnetic) iron cores in 2D for "realistic" rotation rates. While they do not find jets under these conditions, neutronized matter is mixed outward along the rotation axis. We note, finally, that an understanding of the core-collapse mechanism will be required to determine the viability of the models described here.

5.1.3. Neutron-star and black-hole collisions

Lattimer and Schramm [1974, 1976] studied the tidal interaction between a neutron star and a black hole in a close binary system. Gravitational radiation will cause an orbital decay, and the tidal forces of the black holes in such systems will disrupt the neutron star. Lattimer and Schramm [1974, 1976] estimated that the disruption would eject up to 5% of the neutron star into the interstellar medium. The neutron-rich ejected debris from the neutron star will form r-process nuclei during the decompression. Such a decompression, including the effects of decay heating, will lead to nonadiabatic expansion and the production of heavy nuclei along the neutron-drip line. Assuming that all of this neutron-rich material was converted into r-process nuclei and using a statistical estimate for the frequency of such events, Lattimer and Schramm [1974, 1976] suggested that neutron-star–black-hole collisions could account for some fraction of the galactic r-process material. Calculations by Lattimer et al. [1977] did indicate that the neutron-star ejecta can produce heavy neutron-rich nuclei. (See also Meyer [1989].) Detailed calculations, however, to show whether this material will produce an r-process abundance distribution similar to the solar-system distribution have not yet been made. Estimates of the frequency of neutron-star–black-hole collisions are also very uncertain. They depend not only upon the orbital parameters of the binary system but the evolutionary histories of the progenitor stars.

A variant of the neutron-star–black-hole model was suggested by Symbalisty and Schramm [1982], who noted that the evolution of the binary pulsar would eventually lead to neutron-star–neutron-star collisions. These collisions could also lead to the ejection of neutron-rich material. Since the frequency of neutron-star–neutron-star collisions might be higher than neutron-star–black-hole collisions, Symbalisty and Schramm [1982] suggested that this model might produce significant amounts of r-process material (see also Eichler et al. [1989]). This model, however, suffers from the same uncertainties as the neutron-star–black-hole model – the lack of detailed abundance studies of the ejected material and the lack of a reliable frequency estimate for the neutron-star collisions (see Clark et al. [1979]). Both models will require further study to test their validity as sites for the r-process.

5.2. Secondary production

As we noted in section 4.5, the systematics of r-process abundances and nuclear properties suggest that the r-process takes place in a high-temperature, high neutron-number density environment that would ensure an $(n,\gamma)\rightleftarrows(\gamma,n)$ equilibrium. The difficulties encountered in modeling these environments, which include supernova cores, jets or neutron-star–black-hole interactions, and the lack of conclusive results led to searches for the r-process in still other environments with typically lower temperatures and neutron number densities. We discuss in this section these various secondary production environments where neutrons are mostly produced as a result of (α, n) reactions. We conclude that, independently of the results noted in section 4.5, none of these secondary production mechanisms can, at this date, reproduce the overall r-process abundance features in a physically realistic manner.

5.2.1. Helium and carbon shells

One such studied environment was the helium zone of a star undergoing a supernova explosion. As a result of the shock wave, high temperatures and densities produce a burst of neutrons, via (α, n) reactions, in the helium zone that could drive an r-process. Similar, but independent, studies were made of this site at approximately the same time by Truran et al. [1978a,b] and Thielemann et al. [1979]. In both cases, the motivation for examining this site was, at least in part, an attempt to explain the r-process isotopic anomalies observed in the Allende meteorite. Cameron and Truran [1977] had previously suggested a supernova origin for isotopic anomalies in meteorites, but had not specifically suggested the helium zone as a site for the r-process synthesis. Additional studies of this r-process environment were made by Truran et al. [1978b], Cowan et al. [1980, 1983, 1985], Blake et al. [1981], and Klapdor et al. [1981].

In an attempt to mimic the effects of a strong supernova shock, Truran et al. [1978a] assumed a constant temperature of 8.5×10^8 K and a constant density of $10^5\ \mathrm{g\,cm^{-3}}$ in the helium zone. At this temperature neutrons were liberated by the reactions $^{18}\mathrm{O}(\alpha, n)^{21}\mathrm{Ne}$, $^{22}\mathrm{Ne}(\alpha, n)^{25}\mathrm{Mg}$ and $^{25}\mathrm{Mg}(\alpha, n)^{28}\mathrm{Si}$. The neutron flux produced as a result of the supernova shock in the helium zone – dubbed the helium-driven r-process by Truran et al. – was lower than in the classical r-process. As a result, this was not an $(n, \gamma) \rightleftarrows (\gamma, n)$ equilibrium process, but a dynamic process. In the classical r-process, it is assumed that neutron captures and photodisintegrations balance each other at neutron-rich waiting points. In the dynamic r-process, the neutron path is determined by competition between the neutron-capture rates and the beta-decay rates. This type of r-process, with neutron densities much lower than in the classical r-process, was dubbed the n process by Blake and Schramm [1976]. While Blake and Schramm [1976] noted the possibility of producing the solar r-process abundances in the n-process, they did not tie it to a specific astrophysical environment. Cowan and Rose [1977] also found that neutron densities intermediate between the s-process and the classical r-process could be produced in certain types of red giants. Cowan and Rose named this the i-process, but did not make any detailed calculations of what types of heavy elements might be produced in such an environment.

As a result of the neutron flux, heavy seed nuclei already present in the helium zone will be radiated. Truran et al. [1978a] found that heavy nuclei initially near an s-process peak (i.e. associated with a closed neutron shell) would be pushed up to the vicinity of the next r-process peak and the next higher closed neutron shell. Truran et al. [1978a] assumed that the initial distribution in the helium zone was a solar-system distribution. Later work [Truran et al. 1978b; Cowan et al. 1980] indicated that to reproduce the total solar-system r-process abundances required that the initial seed distribution be an enriched (with respect to the solar) abundance pattern. This demands prior in situ processing of the matter with an s-process flux. Such an exposure might result from the mixing of hydrogen into the helium zone, as a result of helium shell flashes, and the production of the neutron source $^{13}\mathrm{C}$ via $^{12}\mathrm{C}(p, \gamma)^{13}\mathrm{N}(\beta^+)^{13}\mathrm{C}$. Neutrons produced by $^{13}\mathrm{C}$ could then turn an initial solar-system distribution into an enhanced s-process distribution [Cowan et al. 1980]. For an appropriate initial s-process distribution, the helium-driven r-process, with neutrons produced by $^{22}\mathrm{Ne}(\alpha, n)^{25}\mathrm{Mg}$ reactions under the same physical conditions as used by Truran et al. [1978a], could approximately reproduce the solar-system r-process distribution [Cowan et al. 1980]. Klapdor et al. [1981] also found that the helium-driven r-process could reproduce the solar-system r-process distribution, provided that the initial composition consisted of solar s-process abundances. While their fit to the solar abundances was somewhat better than that of Cowan et al. [1980], Klapdor et al. [1981] assumed that $(n, \gamma) \rightleftarrows (\gamma, n)$ equilibrium existed throughout the total period of r-process nucleosynthesis. Later work [Cameron et al. 1983a] showed that for the neutron number densities and temperatures characteristic of the helium-driven r-process, such an equilibrium assumption was not always valid.

No stellar models of massive stars, the progenitors of type II supernovae, have demonstrated the mixing of hydrogen into the helium zone. In addition, these massive stars may only undergo a weak s-process, with the synthesis of s-process nuclei only up to mass $A \sim 90$ [Lamb et al. 1977]. Cowan et al. [1980] showed that either a more extensive initial s-process or a larger abundance of the neutron source, ^{13}C, are required to reproduce the solar-system r-process abundances. An initial seed distribution, with no s-process nuclei heavier than $A \sim 90$, would therefore require very large quantities of neutrons, and hence unrealistically high amounts of mixing, to reproduce the solar-system distribution. Blake et al. [1981] based their nucleosynthesis calculations on the particular evolution conditions predicted for a star of 15 $M_{\odot}$. For those particular conditions and initial seed distributions, they could not reproduce the solar-system abundance distribution. They suggested, however, that a variety of r-process nuclei are synthesized in explosive helium burning in massive stars and might be of importance in explaining isotopic anomalies found in certain meteorites.

Cowan et al. [1983] examined the helium-driven r-process under more realistic astrophysical conditions than Truran et al. [1978a] and Cowan et al. [1980]. Using the Rankine–Hugoniot jump conditions, Cowan et al. [1983] determined the shock velocities in the helium zone based on the observed supernova expansion velocities. They also allowed the temperature and density to fall adiabatically after the passage of the shock. Clearly this was more physical than the assumption of constant temperature and density made by Truran et al. [1978a] and Cowan et al. [1980]. Cowan et al. [1983] also introduced a more sophisticated accounting of the production and capture of neutrons during r-process nucleosynthesis. As a result of all of these changes, Cowan et al. [1983] found that the conditions they had previously studied [Truran et al. 1978a] no longer reproduced the solar-system distribution. In the previous studies assuming constant temperature, after the ^{22}Ne had disappeared, neutrons were produced by ^{25}Mg$(\alpha, n)^{28}$Si reactions. In the new, more physically reasonable studies where the temperature and density fall adiabatically, by the time the ^{22}Ne disappears, the temperature is too low for significant neutron production from ^{25}Mg$(\alpha, n)^{28}$Si. The neutron number density in this case falls off rapidly after $\sim 10^{-3}$ s when the ^{22}Ne vanishes. Cowan et al. [1983] suggested that the neutron number density must be $\gtrsim 10^{19}$ cm^{-3} for a one-second burning time to reproduce the solar r-process distribution. This condition was not realized for the same initial conditions and neutron sources originally studied by them.

Cowan et al. [1983] did find conditions that could reproduce the solar-system r-process abundance distribution from the helium-driven r-process. Those conditions were an initial peak temperature of 4×10^8 and an initial peak density of 10^4 g cm^{-3}. Furthermore they found that neither ^{22}Ne nor ^{18}O could produce sufficient neutrons, but ^{13}C$(\alpha, n)^{16}$O reactions could drive an r-process. Their model required the presence of ^{13}C in the helium zone and thus demanded some type of prior mixing event between the hydrogen-rich envelope and the helium zone. Although no stellar evolutionary model could demonstrate that such mixing occurred, Cowan et al. [1983] found that only 2% (by mass) of the helium zone need be ^{13}C to reproduce the solar abundance curve. This concentration, however, is very sensitive to the beta-decay rates of the nuclei. The original studies of the helium-driven r-process had employed beta-decay rates calculated on the basis of the gross theory [Takahasi and Yamada 1969]. The work of Klapdor and Oda [1980] indicated that beta-decay rates for neutron-rich nuclei calculated using the gross theory were approximately a factor of 10 too low. Using this result as a guide, Cowan et al. scaled, by up to a factor of 10, all of the beta-decay rates that had previously been calculated using the gross theory.

Cameron et al. [1983a,b], employing steady-flow calculations, independent of any particular neutron source or astrophysical model, found that the r-process curve could be reproduced under conditions very different than usually assumed in the classical r-process. They found that the solar-system r-process peaks near mass numbers 80 and 130 required a neutron number density of $\sim 10^{20}\ \mathrm{cm}^{-3}$ and a freezing time, when the neutron flux falls to a small fraction of itself (several e-folding times), comparable to or less than 0.1 s. The r-process peak near mass number 195 could be reproduced with a neutron number density of $10^{21}\ \mathrm{cm}^{-3}$ and a freezing time comparable to or less than 0.01 s.

The work of Cameron et al. [1983a,b] also emphasized the importance of the neutron-capture cross sections on the r-process path. They found that the features of the r-process yield curve, produced under the steady-flow assumptions, are determined by the neutron-capture cross sections. The beta-decay rates did not directly affect the features of the curve, but they had an indirect effect by determining the position of the flow path and hence the nuclei that would capture neutrons.

Later studies of this site [Cowan et al. 1985, 1987] employed the beta-decay rates determined using microscopic techniques by Klapdor et al. [1981, 1984], that had not been available at the time of the initial studies (see fig. 5.2). An analysis indicated that these new microscopic rates were much higher than the gross rates, but on average not by as much as a factor of 10 [Cameron et al. 1983b]. Using these [Klapdor et al. 1981] beta-decay rates, Cowan et al. [1985] found that now the required ^{13}C concentration was 5% by mass. This amount is unreasonably high, requiring extremely large amounts of mixing between the hydrogen-rich envelope and the helium zone. No stellar evolutionary model predicts such large mixing. For the currently calculated beta-decay rates, the helium-driven r-process

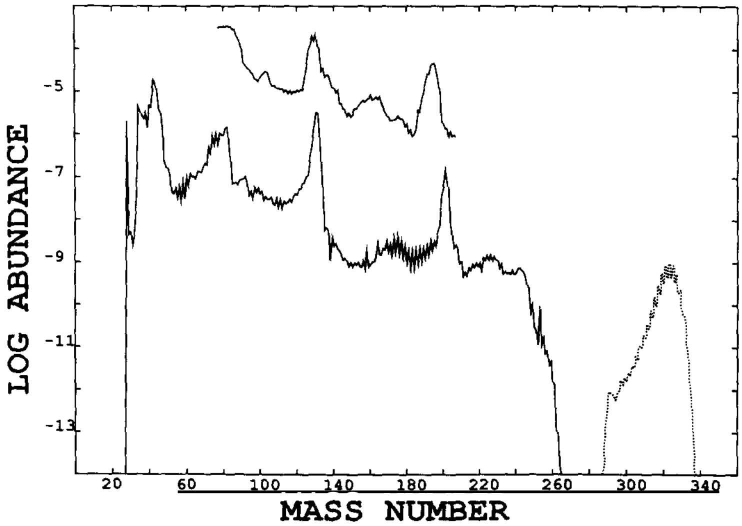

Fig. 5.2. Calculated r-process abundances as a function of mass number from Cowan et al. [1987]. The top curve is the solar system r-process abundances from Cameron [1982a]. The theoretical curve, which assumes an explosive helium-burning environment, is the result of a dynamic r-process calculation that includes beta-delayed neutron emission and fission. The dotted line for mass numbers above $A \sim 280$ indicates that the abundances of those nuclei are uncertain.

does not appear to be capable of producing the majority of the r-process nuclei [Cameron et al. 1985; Cowan et al. 1985].

Recent work has examined nucleosynthesis resulting from inelastic neutrino scattering in the helium zone of a star undergoing a core-collapse supernova [Epstein et al. 1988; Woosley and Haxton 1988]. The neutrons are produced by neutral-current excitations of ^{4}He by neutrinos (i.e., inelastic neutrino scattering), which are released by the collapsing core. Woosley and Haxton [1988] proposed that the element fluorine might be made in this manner. Epstein et al. [1988] suggested that under certain conditions an r-process could be generated. Those conditions were that the progenitor of the neutron star be metal-poor (i.e. Pop II) and/or compact. Woosley et al. [1990], however, found that the dominant neutron-production process in the helium zone resulted from explosive helium burning (as discussed above) and not from neutrino-induced reactions. Woosley et al. made careful comparisons between their calculations and those of Epstein et al., and found large discrepancies in the calculated neutron densities. These discrepancies were caused by omissions in the code of Epstein et al. [1988], which had significantly overestimated the neutron density resulting from neutrino-induced reactions [Woosley et al. 1990]. Woosley et al. [1990] concluded that while this neutrino-induced r-process might have resulted in some nucleosynthesis early in the history of the Galaxy, it could not have been responsible for r-process synthesis since that time.

Shock heating of the carbon zone as a result of a supernova was also suggested as a mechanism for producing the r-process nuclei [Lee et al. 1979]. As in the case of the helium zone, the passage of the supernova shock will produce high temperatures and densities in the carbon zone of the presupernova star. Any ^{22}Ne, produced by α captures on ^{14}N, already in the carbon zone will produce neutrons primarily as a result of ^{22}Ne(α, n)^{25}Mg reactions. These neutrons could then by captured by any preexisting heavy nuclei (i.e., "seed nuclei") in the carbon zone. Ejection of the synthesized r-process nuclei would then be a natural consequence of the supernova explosion.

The neutron fluxes produced in this explosive carbon-burning model were lower than in the classical r-process and were more typical of the n-process [Lee et al. 1979]. In addition, many of the neutrons that were produced would be captured by the products of ^{22}Ne burning. ^{25}Mg, in particular, is very effective at capturing neutrons and would act to prevent a "build up" of heavy nuclei. Studies indicate that while some neutron-rich nuclei beyond iron could be produced in explosive carbon burning (see fig.

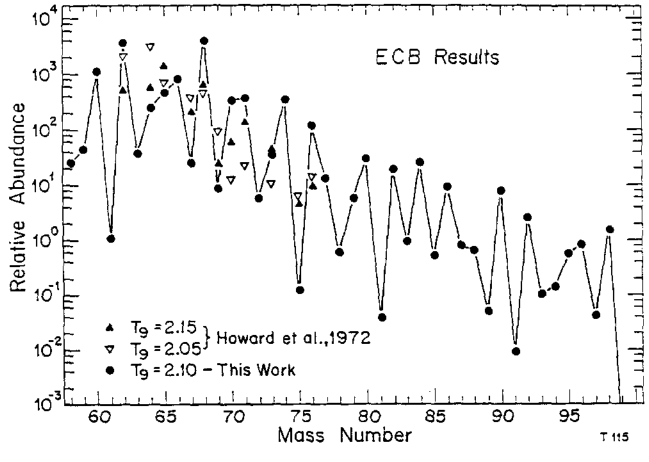

Fig. 5.3. Results of explosive carbon burning (ECB) calculations from Wefel et al. [1981] (labelled as "this work") compared to those of Howard et al. [1972]. The relative abundances are normalized to the ^{24}Mg abundance.

5.3 taken from Wefel et al. [1981]), the heavy r-process nuclei (in particular the actinides) are not produced in this process. This site, therefore, cannot be responsible for producing the majority of the r-process nuclei.

5.2.2. Helium cores

The helium cores of low-mass stars have also been suggested as a possible site for the r-process [Cowan et al. 1982, 1984]. As a result of the helium core flash in these stars, it has been suggested that hydrogen-rich material might be convectively mixed into the core (see, e.g., Deupree and Cole [1983]). This mixing could then result in the production of ^{13}C following proton capture by ^{12}C already in the core. The ^{13}C could subsequently produce neutrons via ^{13}C$(\alpha, n)^{16}$O reactions. Heavy nuclei ("seed nuclei") already in the core could capture neutrons to produce the r-process nuclei [Cowan et al. 1982]. Since low-mass stars are so common, this site would have the advantage of requiring very little r-process material per helium core flash to produce the total galactic r-process abundances. Based upon the initial mass function of Miller and Scalo [1979], Cowan et al. [1982] estimated that only 10^{-6} to 10^{-5} $M_\odot$ need be ejected per event. On the other hand, unless convection was so violent as to produce an explosion, it will be difficult for the synthesized r-process material to be ejected into the interstellar medium by these low-mass stars.

Based on the work of Klapdor and Oda [1980], the preliminary study of Cowan et al. [1982] (in a manner similar to that used in the study of the shock-heated helium zones) scaled, by up to a factor of 10, all of the beta-decay rates that had previously been calculated using the gross theory. Employing these accelerated beta-decay rates, it was found that for ^{13}C abundances as low as 3% by mass, a thermal runaway in the helium core could produce a number of features of the solar-system r-process abundance curve. These models, unlike the shock-heated helium zones of presupernova stars, were not sensitive to the initial distribution of heavier "seed nuclei" in the core. While most of the calculations assumed a solar distribution, Cowan et al. [1982] found that for sufficient neutrons, an r-process distribution could be produced starting with effectively no heavy elements at all. In a subsequent paper, these same authors employed steady-flow calculations to show that conditions that could produce neutron-rich nuclei were realized in helium core flashes [Cowan et al. 1984]. This led them to conclude that low-mass stars might be responsible for the production of some of the features of the r-process abundance curve.

Employing [Klapdor et al. 1981, 1984] beta-decay rates, Cowan et al. [1985] made detailed dynamical r-process calculations to reexamine the plausibility of the helium core as an r-process site. These authors compared the theoretical fit to the observed solar-system r-process curve as a function of ^{13}C in the core, and found for a sufficient flux of neutrons the solar-system r-process abundance distribution could be reproduced. The necessary ^{13}C depends very sensitively upon the calculated beta-decay rates. Using crude estimates for the beta-decay rates, Cowan et al. [1982] had found relatively low concentrations of ^{13}C were required. For the microscopically calculated rates of Klapdor et al., however, Cowan et al. [1985] found that the required ^{13}C concentration was 14% by mass. This concentration would demand unreasonably large amounts of mixing between the hydrogen-rich envelope and ^{12}C in the helium core, and is not predicted by any current stellar evolutionary models of low-mass stars. Even if such mixing could occur, unless the core temperature fell rapidly enough during expansion, the large amounts of H mixing into the core would probably lead to the CNO production of ^{14}N, which is a well-known neutron poison. The results indicate that unless the beta-decay rates have been underestimated significantly, the helium core flash is not a plausible r-process site [Cameron et al. 1985; Cowan et al. 1985].

5.3. Primordial production

5.3.1. Standard and inhomogeneous big bang scenarios

The standard big bang scenario assumes a homogeneous, isotropic expansion in a radiation-dominated universe without degenerate or exotic particles. During the expansion, the temperature declines below 1 MeV and eventually slows down the photodisintegration rate of ^{2}H, which is constantly produced via neutron capture on protons. Nucleosynthesis proceeds when a substantial abundance of ^{2}H at $T_{D\gamma} \approx 0.1$ MeV $\approx 1.2 \times 10^9$ K, enables further neutron, proton and light nuclei capture to form ^{3}H, ^{3}He, ^{4}He, and even heavier nuclei. However, the gaps existing among stable nuclei at mass numbers $A = 5$ and $A = 8$ inhibit the formation of nuclei beyond $A = 8$; therefore the standard big bang can produce only ^{2}H, ^{3}He, ^{4}He and ^{7}Li in appreciable amounts.

The neutron to proton ratio, which constrains primordial nucleosynthesis, is determined by the conditions during weak decoupling at $T \approx 1$ MeV, when the electrons are no longer energetic enough to ensure an equilibrium by the reaction p(e$^-$, ν)n, due to the neutron–proton mass difference of 1.3 MeV, and the positrons needed for the inverse reaction n(e$^+$, $\bar{\nu}$)p are no longer produced by pair creation. Primordial nucleosynthesis conditions are then determined by the particles remaining in thermal equilibrium, initial conditions at time t, and the global adiabatic expansion. The initial conditions are set by neutrons, protons, electrons and photons with densities n_n, n_p, n_e and $n_\gamma = 2.404/\pi^2(kT/\hbar c)^3$ [Kolb and Turner 1990; Börner 1988]. From charge neutrality it follows that $n_e = n_p$. n_p/n_n is given by the equilibrium ratio at weak freeze-out.

The strength of the standard big bang scenario is that only one free parameter must be specified, the baryon to photon ratio $\eta = n_b/n_\gamma$, to determine all of the primordial abundances, ranging over 10 orders of magnitude (see, e.g., Yang et al. [1984], Boesgaard and Steigman [1985], Kawano et al. [1988], and Olive et al. [1990]). The parameter η is related to the baryon density, $\Omega_b = \rho_b/\rho_c$, in the following way (evaluating all variables at the present time):

$$\begin{aligned} &\rho_b = n_b m_u = \eta_{10} 10^{-10} n_\gamma m_u \propto \eta_{10} T_{\gamma 0}^3 , \qquad \rho_c = 3H_0^2/8\pi G , \\ &\Omega_b/h_{50}^2 = 1.54 \times 10^{-2} (T_{\gamma 0}/2.78K)^3 \eta_{10} . \end{aligned} \tag{5.1}$$

The relation for the critical density, ρ_c, follows from the Friedmann equation for the (Hubble) expansion of the universe, $H(t)^2 = 8\pi G\rho/3 - k/R^2$ for a flat universe with $k = 0$ and therefore a critical density of the universe. $H_0 = h_{50} \times 50\,\mathrm{km\,s^{-1}\,Mpc^{-1}}$ and $T_{\gamma 0}$ denote the Hubble constant and the present temperature of the microwave background, respectively.

The abundances of individual nuclei depend on η in the following way. A high (baryon) density during the nucleosynthesis phase, i.e. a large η, gives rise to a larger number of capture reactions on ^{2}H and ^{3}He, and consequently leaves less ^{2}H and ^{3}He, but increases the ^{4}He abundance. The behavior of the ^{7}Li abundance is more complex. At low densities ^{7}Li is produced via ^{3}H(α, γ)^{7}Li, but is destroyed at higher densities by ^{7}Li(p, α)^{4}He. However, increasing densities lead also to a larger production of ^{7}Be via ^{3}He(α, γ)^{7}Be, which is preserved during the nucleosynthesis period and subsequently decays to ^{7}Li. This leads to a predicted minimum in the ^{7}Li/^{1}H ratio of about 10^{-10}, for $2 < \eta_{10} < 4$.

Primordial abundance information (see Boesgaard and Steigman [1985], and for updates Pagel [1987], Bania et al. [1987], Spite and Spite [1986], Hobbs and Duncan [1987], Hobbs and Pilachowski [1988], Rebolo et al. [1988], Olive et al. [1990], and Pagel [1991]) results in the following limits: ^{2}H/H $\geq 2 \times 10^{-5}$, ^{3}He/H $\leq 1.2 \times 10^{-5}$, (^{2}H + ^{3}He)/H $\leq 11 \times 10^{-5}$, ^{7}Li/H $\leq 2.5 \times 10^{-10}$, and $0.215 \leq$

$X_\alpha \leq 0.245$. Combining theoretical model predictions with this primordial abundance information, utilizing also the new and very precise neutron half-life measurement by Mampe et al. [1989] [$\tau_{1/2} = (10.25 \pm 0.015)$ min], leads to the following conclusions: $2.6 \leq \eta_{10} \leq 5.0$ and $0.5 \leq N_\nu \leq 3.8$. This translates to $0.040 \leq \Omega_b h_{50}^2 \leq 0.077$ and when using a Hubble constant H_0 in the range 40–100, this is equivalent to a baryon density in the universe of $0.01 \leq \Omega_b \leq 0.12$. The main difference from stellar nucleosynthesis is given by the low value of η, derived from primordial abundances, which results in low densities and does not allow for the production of heavy nuclei via the triple-alpha reaction ($3\,^4\mathrm{He} \rightarrow {}^{12}\mathrm{C}$).

The standard big bang model assumes that, during the phase of primordial nucleosynthesis, the universe has a homogeneous density distribution. There exist a number of factors which could prevent such an evolution. The most cited scenario relates to a first-order quark–hadron phase transition, occurring at $T \approx 150$ MeV and leading to supercooling, nucleation, and propagating phase boundaries, resulting in inhomogeneities of the baryon distribution. Under some conditions, these inhomogeneities can be of large enough amplitude and length scale to survive until nucleosynthesis, and can alter the abundances of the elements.

Applegate and Hogan [1985], Bonometto et al. [1985], and Sale and Mathews [1986] realized that the inhomogeneities could have dramatic consequences for primordial nucleosynthesis. Applegate and Hogan [1985] described a rich set of scenarios for inhomogeneous nucleosynthesis. The most interesting effect they considered is the differential diffusion of neutrons and protons. The neutron, being neutral, has a mean free path roughly 10^6 times that of the proton, because of smaller scattering cross sections with charged particles. Once the weak interactions – transforming neutrons into protons and vice versa via positron and electron captures – fall out of equilibrium, neutrons can diffuse to uniformity over much longer length scales than protons. This has the effect of converting density variations into variations in the local ratio of neutrons to protons. If the density variations are large enough, the neutrons, diffusing into an underdense region, can outnumber the nucleons initially there, producing an environment in which neutrons locally outnumber protons. Nucleosynthesis under neutron-rich conditions can give dramatically different results than the standard, proton-rich models. (For an in-depth treatment of this and other possible scenarios, leading to density inhomogeneities during nucleosynthesis, see Malaney and Mathews [1991].)

5.3.2. The formation of heavy elements and a primordial r-process

A most fascinating aspect of the inhomogeneous scenarios is that there appears, for the first time, to be an open window allowing the formation of nuclei beyond mass $A = 8$, in the neutron-rich regions. Reactions starting with neutron captures on protons $^1\mathrm{H}(n,\gamma)^2\mathrm{H}(n,\gamma)^3\mathrm{H}(d,n)^4\mathrm{He}(t,\gamma)^7\mathrm{Li}$ lead to the production of ^{7}Li and the sequence $^7\mathrm{Li}(n,\gamma)^8\mathrm{Li}(\alpha,n)^{11}\mathrm{B}(n,\gamma)^{12}\mathrm{B}(\beta^-)^{12}\mathrm{C}\,(n,\gamma)^{13}\mathrm{C}(n,\gamma)^{14}\mathrm{C}$ produces carbon [Malaney and Fowler 1987; Applegate et al. 1988]. An alternate branching is $^7\mathrm{Li}(\alpha,\gamma)^{11}\mathrm{B}$. Additional alternative reactions such as $^7\mathrm{Li}(t,n)^9\mathrm{Be}(t,n)^{11}\mathrm{B}$, $^8\mathrm{Li}(n,\gamma)^9\mathrm{Li}(\beta^-)^9\mathrm{Be}$, $^8\mathrm{Li}(d,p)^9\mathrm{Li}$, $^8\mathrm{Li}(d,n)^9\mathrm{Be}$, and $^8\mathrm{Li}(d,t)^7\mathrm{Li}$ might also become important [Boyd and Kajino 1989; Kajino and Boyd 1990]. At three positions (^{7}Li, ^{9}Be and ^{11}B), proton-induced reactions would prevent the build-up of heavier nuclei in a standard big bang scenario and lead to the destruction of heavy nuclei instead via $^7\mathrm{Li}(p,\alpha)^4\mathrm{He}$, $^9\mathrm{Be}(p,\alpha)^6\mathrm{Li}$, or $^{11}\mathrm{B}(p,2\alpha)^4\mathrm{He}$. There are considerable uncertainties associated with the nuclear physics as many of these reactions involve unstable nuclei, and also most of the reactions on stable targets in this region of the nuclear chart are not well determined at present [Malaney and Fowler 1989a]. Wiescher et al. [1989] remeasured the $^7\mathrm{Li}(n,\gamma)^8\mathrm{Li}$ reaction rate and found a substantial reduction in this rate and the flow to heavier nuclei with respect to previous determinations.

Applegate et al. [1988] were able to show that there are possible pathways to heavier nuclei, starting from ^{14}C: e.g., $^{14}C(\alpha,\gamma)^{18}O(n,\gamma)^{19}O(\beta^-)^{19}F(n,\gamma)^{20}F(\beta^-)^{20}Ne(n,\gamma)^{21}Ne(n,\gamma)^{22}Ne$, etc. (The reaction rate for $^{14}C(\alpha,\gamma)^{18}O$ was recently redetermined by Funck and Langanke [1989].) Wiescher et al. [1990] demonstrated, however, that the (p,γ) and (n,γ) reactions on ^{14}C are of greater importance for the build-up of heavy elements. This reaction sequence includes only reactions for which there exists some information in the literature, involving primarily neutron captures on stable nuclei. With the overwhelming abundance of neutrons in the low-density neutron-rich regions it is, however, quite feasible that neutron captures on unstable nuclei can bypass these relatively slow beta decays. For this reason, Thielemann and Wiescher [1990] have investigated neutron capture reactions on Li, Be, B, C, N, O, F and Ne isotopes, from stability to the neutron-drip line, including the effects of direct capture and all available resonance information from nuclear spectroscopy.

The build-up of heavy nuclei might not stop even at Ne. Nuclei in the neutron-rich low-density region remain embedded in a neutron bath, and Applegate [1988] speculated that a rapid neutron-capture process could form heavy nuclei. For high neutron densities, neutron captures can be faster than beta decays for unstable nuclei, and very neutron-rich isotopes can thus be produced. For neutron densities in excess of 10^{19}–10^{20} cm^{-3}, the line in the nuclear chart beyond which beta decay dominates over neutron capture would be located 15–20 mass units away from stability. Typical beta-decay half-lives of 10^{-2}–10^{-3} s are then encountered, with a few exceptions on the order 10^{-1} s. Along an r-process path at this distance from stability, Fe nuclei can be transformed to U within a few seconds. The transformation from Ne to Fe can take longer, however. The actual neutron number density found in the calculations by Thielemann et al. [1991] is shown in fig. 5.4. The mass fractions of neutrons, protons and alpha particles are displayed in fig. 5.5.

Fission in the r-process path can have a strong influence on the total abundances of heavy nuclei as a consequence of "fission cycling", whereby each of the fission fragments can capture neutrons and finally

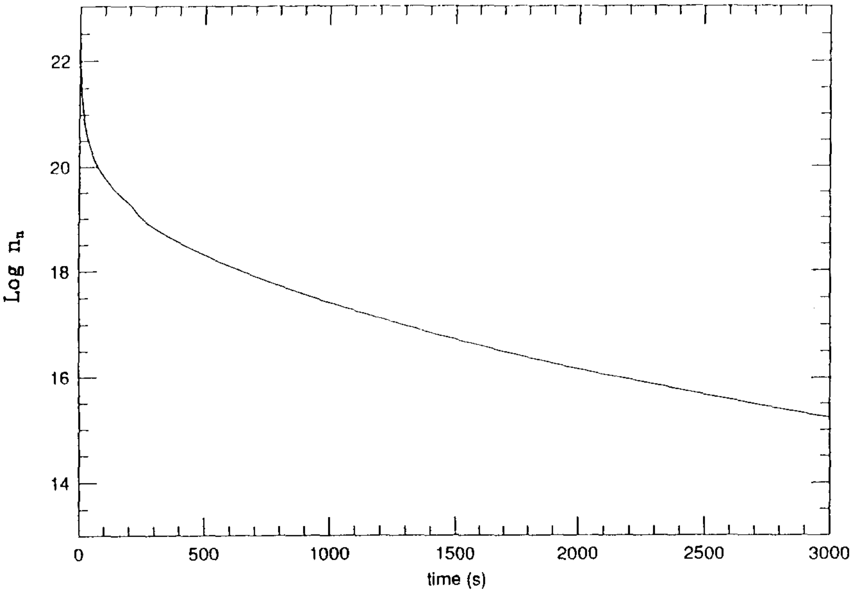

Fig. 5.4. Neutron number density in low density (neutron-rich) zones of an inhomogeneous big bang with $\Omega_b = 1$ and $R = 6$ (see Applegate [1988]). For the first 500 s the number densities are close to r-process conditions (from Thielemann et al. [1991]).

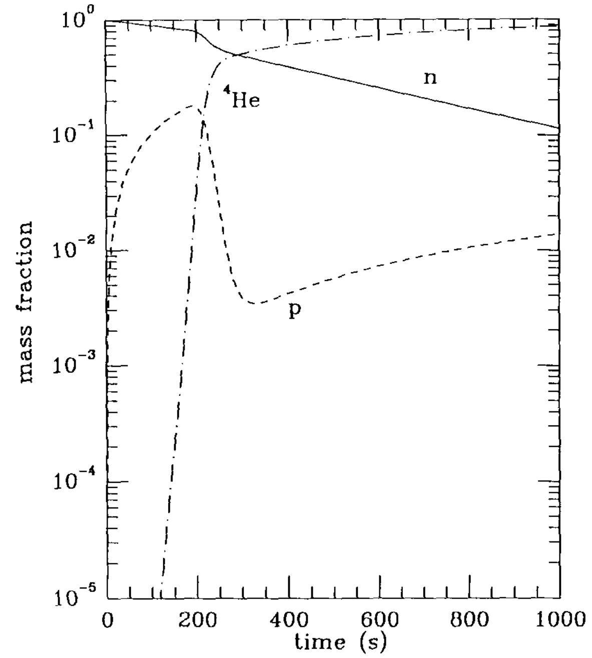

Fig. 5.5. Light-nuclei production for the same conditions shown in fig. 5.4. Only neutrons, protons and ^{4}He are displayed. Compare with fig. 2 in Applegate [1988].

form heavy nuclei which fission again [Seeger et al. 1965]. This is of particular importance in environments with a long duration of high neutron densities, and was therefore suggested as relevant to primordial nucleosynthesis in neutron-rich zones of an inhomogeneous big bang [Applegate 1988]. In contrast to the operation of the r-process in explosive stellar environments, confined to a few seconds, this possible process in the neutron-rich regions associated with an inhomogeneous big bang is only limited by the neutron half-life and can go on for an extended period of time. One of the remarkable features of an r-process with fission cycling is that the production of heavy nuclei is not limited to the r-process flow (neutron captures and beta decays) coming from light nuclei, as long as a small amount of fissionable nuclei is produced.

Applegate [1988] suggested that neutron captures in the neutron-rich regions will actually support an r-process which produces intermediate and heavy elements up to Th and U. Observations of metal-poor halo stars demonstrates the existence of real star-to-star variations in the ratio of the r-process to iron abundances [Gilroy et al. 1988]. This nonuniformity in the most metal-deficient stars clearly indicates that a primordial r-process cannot account for the major contribution to present solar-system r-abundances. It could, however, provide a base level of r-process abundances less than, but close to, the lower limit of the observed abundances in stars with metallicities of about 10^{-4}–10^{-3} × solar. For that reason, these proposed nucleosynthesis conditions were explored in detail.

The total mass fraction of heavy nuclei is doubled with each fission cycle and can thus be written as $X_r = 2^n X_{\text{seed}}$. Here, n is the number of fission cycles and the seed nuclei include all nuclei above the lightest nucleus that participates in the neutron-capture and beta-decay sequences that characterize the abundance flow. The main parameter that determines the number of fission cycles is the rate of the r-process flow, which is a function of the location of the r-process path with respect to the stability line, and thus dictates the typical beta-decay half-lives. Figure 5.6 shows the result of a calculation in the low-density (neutron-rich) region of an inhomogeneous big bang with $\Omega_b = 1$ [Thielemann and Wiescher 1990; Thielemann et al. 1991]. This calculation used a network of 655 nuclei from neutrons and protons up to krypton. Nuclei from the stability line to the neutron-drip line are included. Neutron-capture cross sections from statistical model calculations [Thielemann et al. 1987, 1988] are utilized beyond Ne. Neutron diffusion out of neutron-rich zones was not taken into account in this calculation. This calculation also does not include nuclei beyond krypton, thus neglecting the fission cycling effect discussed above; the total mass fraction of r-process nuclei is therefore underpredicted. The timescale for the build-up of nuclei up to krypton, shown in fig. 5.6, is governed by small neutron-capture cross sections and long beta-decay half-lives of lighter nuclei. The total mass fraction of 10^{-13} without fission cycling is very close to the prediction by Applegate [1988] in his eq. (3.13). Mathews et al. [1988] and Kajino et al. [1989], utilizing a network up to silicon, obtained similar results but with somewhat larger abundances. This could reflect the use of larger neutron-capture rates, in particular when they employed statistical model rates for neutron-rich light species with small Q-values.

When performing calculations with a full r-process network beyond Kr, Thielemann et al. [1991] obtained the results presented in fig. 5.7. One notices that fission cycling was indeed effective, because the final mass fraction of heavy nuclei is 1.5×10^{-11}; this is a factor of 150 larger than the mass fraction produced without the r-process network and fission. The results of these calculations differ, however, from the initial predictions of Applegate, in that the r-process abundances are about 2 orders of magnitude smaller. This is partly due to the fact that, for the first time, the reactions for nuclei above Ne and Si are included; in previous studies, their effect was only estimated (see the results for nuclei up

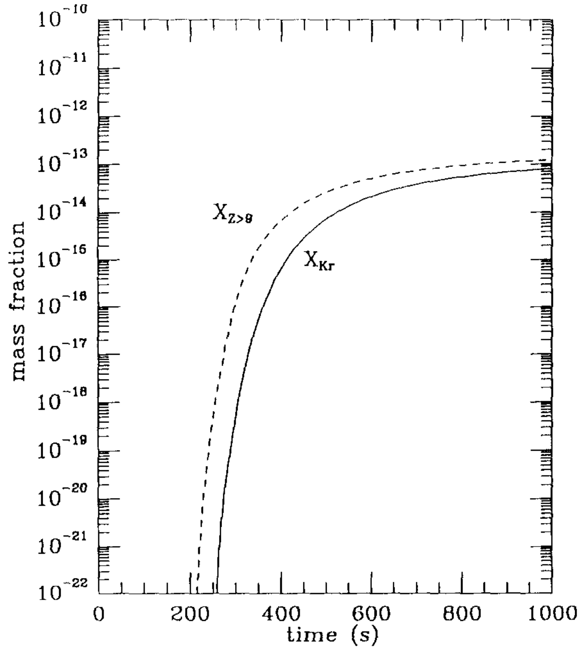

Fig. 5.6. Heavy-nuclei production in a low-density (neutron-rich) zone of an inhomogeneous big bang. The calculation includes only nuclei up to Kr and does not allow for any further processing (from Thielemann et al. [1991]). The shift in the two curves, which contain nuclei heavier than Ne and Kr (the end of the network), indicates that about 50 s are needed to process nuclei from Ne to Kr via neutron captures and beta decay. In total, a mass fraction of 10^{-13} is produced.

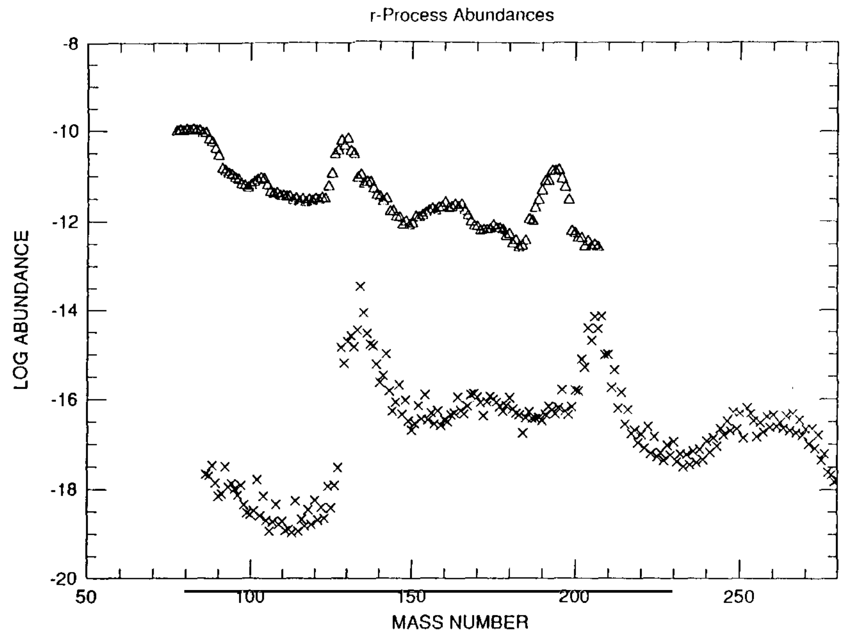

Fig. 5.7. Full r-process calculation coupled to the light and intermediate nuclei network used in figs. 5.5 and 5.6. The effect of fission cycling is that a total mass fraction of 1.5×10^{-11} is produced from the seed mass fraction of 10^{-13} displayed in fig. 5.6, i.e. a multiplication by 150 or approximately 7 cycles. This is, however, not sufficient to explain the r-process abundances in the oldest, most metal-deficient stars. In addition, the low neutron number densities at the end of an inhomogeneous big bang lead to a path very close to stability and therefore to shifted peaks that almost coincide with s-process peaks (from Thielemann et al. [1991]).

to Kr, in Thielemann and Wiescher [1990]). In addition, the amount of fission cycling was overestimated in earlier work. For an initial neutron density of $10^{19}\,\mathrm{g\,cm^{-3}}$, the r-process path closely approximates a path reproducing the solar r-process abundance pattern. Such a path has a cycle time due to fast beta-decay half-lives of about 4–5 s. However, during the subsequent expansion the neutron density decreases as well, resulting in an r-process path closer to stability. When an average is taken over the total duration of big bang nucleosynthesis, one obtains a cycle time of 50–70 s rather than the much shorter initial estimates. Since the abundances are proportional to 2^n, with n denoting the number of fission cycles, the change to longer cycle times leads to much smaller abundance predictions.

The calculation described here represents the most optimistic case with $\Omega_b = 1$ and neutron diffusion neglected. Based on that calculation, it thus appears questionable whether an r-process abundance level, that would be observationally detectable, was produced in an inhomogeneous big bang. In addition, it is clear from fig. 5.7 that these calculated primordial abundances do not even follow an r-process pattern. The small neutron densities at late time led to a path very close to stability and abundance maxima close to the s-process, rather than the r-process, peaks.

6. Chemical evolution of r-process abundances

The general features of the neutron-capture processes, which are primarily responsible for the formation of the heavy-element $A > 60$ abundance patterns observed in galactic matter, were established in the important early papers by Burbidge et al. [1957] and Cameron [1957]. Nevertheless, there remain many unanswered questions concerning both the specific stellar or supernova environments, in which they occur, and the timescales and histories of their enrichment of the Galaxy. In this regard, our rapidly increasing knowledge of the heavy-element abundance patterns in stars as a function of their ages (metallicities, population, etc.) is serving to provide critical constraints on the chemical evolution of r-process and s-process abundances over the course of galactic history. A general review of abundance ratios as a function of metallicity has recently been presented by Wheeler et al. [1989]; see also Spite and Spite [1985] and Gehren [1988]. We will first reexamine specifically the abundance trends involving the products of s-process and r-process nucleosynthesis in section 6.1 and explore their implications both for galactic chemical evolution and for the ranges of stellar mass with which these processes are to be associated. In section 6.2, we explore chemical trends for specific r-process sites. We then, in section 6.3, formulate a simplified chemical evolution model that will be utilized in section 7 to determine the duration of galactic r-process nucleosynthesis, making use of different chronometric pairs.

6.1. Observational overview

The fact that there exist real and systematic depletions in the abundances of many heavy elements relative to iron, in stars of low [Fe/H], has been recognized for many years [Wallerstein et al. 1963; Pagel 1965; Danziger 1966; Pagel 1968]. More recent observational investigations of these "anomalous" abundance patterns have been provided by a number of researchers [Peterson 1976; Spite and Spite 1978; Sneden and Parthasarathy 1983; Luck and Bond 1985; Sneden and Pilachowski 1985; Gilroy et al. 1988; Magain 1989]. The anomalous heavy-element abundance patterns found to characterize the most iron-deficient stars include both [Sr–Y–Zr/Fe] ~ -0.5 and [Ba/Fe] ~ -1.0 ($[x/y]$ denotes the $\log_{10}(x/y)_{\mathrm{star}} - \log_{10}(x/y)_{\odot}$).

Interpretation of these trends in the context of nucleosynthesis theory can at first seem quite straightforward. The bulk (~90%) of the nuclei in both the Sr–Y–Zr and the barium abundance peaks in solar-system matter are certainly attributable to s-process nucleosynthesis. Since the s-process nuclei represent secondary nucleosynthesis products, in the sense that their production in a star demands the presence of concentrations of seed (iron peak) elements formed in prior generations of stars, it is to be expected that their abundance levels in the earliest generations of stars formed in our Galaxy should lag behind that of the seed iron nuclei. The most straightforward interpretation would be that stars containing s-process nuclei represent at least third generation objects: first-generation (pure hydrogen and helium) stars formed the elements carbon-to-iron by charged-particle reaction mechanisms, while second-generation processing yielded s-process elements which in turn were incorporated into the presently observed metal-poor stars. Truran and Iben [1977] (see also Truran [1980]) pointed out that the relative depletion factors quoted above, showing a deficiency in barium relative to strontium–yttrium–zirconium, are consistent with their having been produced during core helium burning in massive stars [Lamb et al. 1977; Prantzos et al. 1990]. This environment produces smaller neutron fluxes than are found in helium shell flashes of less massive stars. This "weak" component of the s-process produces nuclei only up to masses $A \sim 90$–100. The shorter lifetimes of these more massive stars made this an attractive alternative.

While this zeroth-order agreement of observation and theory at first seemed encouraging, Tinsley [1979] voiced concern with the fact that the time-dependent trends in [Y/Fe] and [Ba/Fe] were apparently inconsistent with the generic "theoretical" behavior for the evolution of secondary elements.

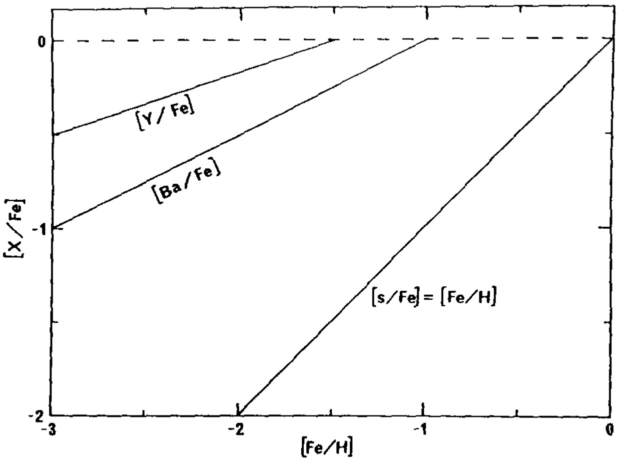

Fig. 6.1. Observed trends in the variations of [Y/Fe] and [Ba/Fe] with [Fe/H] are illustrated (from Truran [1980]). ([Fe/H] = $\log_{10}(\mathrm{Fe/H})_{\mathrm{star}}/\log_{10}(\mathrm{Fe/H})_{\odot}$). The theoretical relation [s/Fe] = [Fe/H], where s designates some arbitrary s-process nucleus is shown for comparison.

This apparent discrepancy is illustrated in fig. 6.1. Here the trends in [Y/Fe] and [Ba/Fe] with [Fe/H], as reflected in the observations of Spite and Spite [1978] of a sample of metal-deficient stars, are compared with the "expected" evolution of secondary elements defined by the relation [s/Fe] = [Fe/H].

The critical clue to the nature of these abundance patterns was that provided by the result of Spite and Spite [1978] that europium, an element whose abundance in nature is dominated by its r-process component, is present in roughly solar proportions relative to iron even in the most metal-deficient stars. This alone confirmed that r-process nucleosynthesis had occurred in the very earliest stages of our Galaxy's evolution. Since the nuclear species most crucial to the determination of the age of our Galaxy by nuclear cosmochronology (^{235}U, ^{238}U and ^{232}Th) are products of r-process synthesis, it is extremely important to have such evidence that their synthesis dates back to the very earliest stages of the Galaxy's evolution. It was also recognized [Truran 1981] that the low levels of nuclei in the strontium and barium "s-process" peaks could be explained in this context; that is, the heavy-element abundance patterns characteristic of the most iron-deficient stars ([Eu/Fe] ~ 0; [Y/Fe] ~ −0.5; [Ba/Fe] ~ −1.0) are entirely compatible with their having a pure r-process origin in that early stage of galactic evolution.

The view that the abundances of these elements (collectively) in extreme halo population stars are exclusively r-process products has been strongly supported by recent detailed abundance analyses for many metal-poor stars [Sneden and Parthasarathy 1983; Sneden and Pilachowski 1985; Gilroy et al. 1988]. The abundance pattern obtained by Sneden and Pilachowski [1985] for the famous metal-poor star HD 110184 is shown in fig. 6.2. For purposes of comparison, this figure also illustrates the (scaled) solar-system r-process distribution from Cameron [1982b] and a theoretical s-process distribution from Cowley and Downs [1980]. A composite abundance diagram, showing the abundance distribution characteristic of stars in the metallicity range $-2.5 < [\mathrm{Fe/H}] < -2.0$, is shown in fig. 6.3 (from Wheeler et al. [1989]). These data reflect averages for five stars studied by Gilroy et al. [1988]. Figure 6.3 also illustrates the solar-system r-process abundance patterns as inferred by Cameron [1982b]. A theoretical s-process curve from Malaney [1987] and a theoretical r-process curve, based on the calculations of Cowan et al. [1985], is also shown in this figure.

Recent improvements have been made in the laboratory measurements of transition probabilities for several of the rare earth elements. Using these new oscillator values, Sneden [1990] has reevaluated the

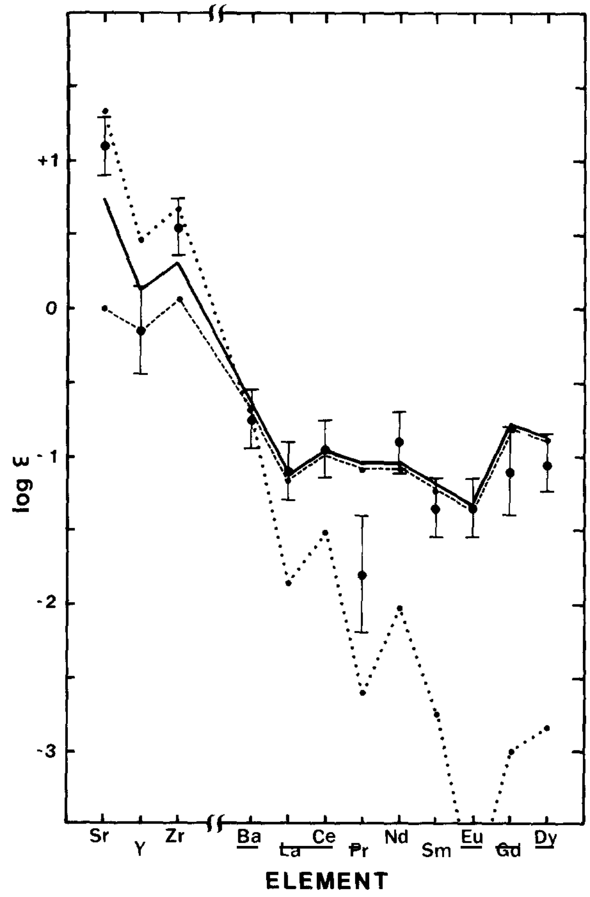

Fig. 6.2. The heavy-element abundances of the metal-poor star HD 110184 and abundance distribution curves of the s- and r-process (from Sneden and Pilachowski [1985]). Filled circles are the observed abundances. The dotted line illustrates a theoretical s-process abundance distribution, the dashed line is a scaled, solar-system r-process distribution (from Cameron [1982b]), and the solid line illustrates the same r-process distribution with a small addition of some s-processing to increase the abundances of Sr and Zr.

abundances in six stars, with metallicity $-2.5 < [\mathrm{Fe/H}] < -2.0$, from the data of Gilroy et al. [1988]. Figure 6.4 illustrates the data for these stars along with a theoretical s-process curve from Malaney [1987]. Sneden [1990] notes that this is one of the better s-process fits to the rare-earth data, but the same calculation does not fit the Sr–Y–Zr data. Also shown in fig. 6.4 is a theoretical r-process curve, where the elemental abundances have been determined from the calculations of Cowan et al. [1987]. These same calculations are also shown in fig. 5.2. It is interesting to note that the theoretical curve that gives a good fit to the total, observed solar-system r-process abundance distribution, also gives an excellent fit to the average abundances of the rare-earth elements in six metal-poor halo stars.

Two features of these comparisons, illustrated in figs. 6.2–6.4, are particularly important to emphasize with respect to the history of r-process nucleosynthesis. In the first place, it is immediately apparent that the observed abundance patterns are much more consistent with an r-process than an s-process origin, confirming that contributions from the r-process dominated at the earliest stages of Galactic history. Perhaps more significant is the fact that the solar-system r-process mass fractions fit the data extremely well, suggesting that the basic mechanism of r-process nucleosynthesis has not changed significantly over the history of the Galaxy.

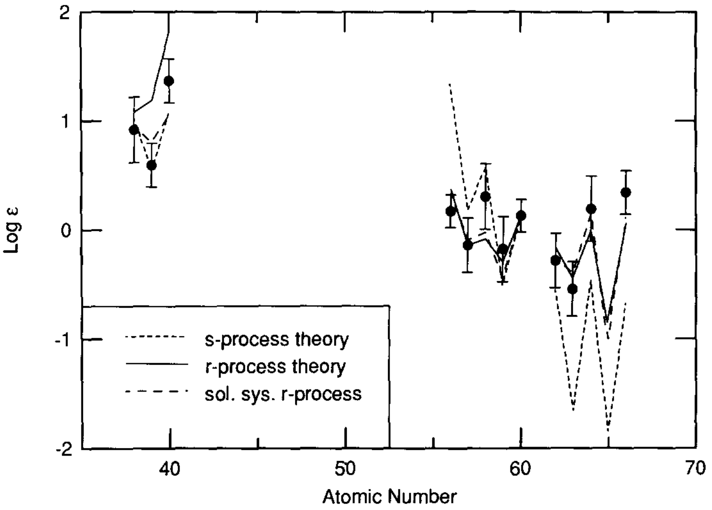

Fig. 6.3. Average abundances of five metal-poor halo stars taken from the data of Gilroy et al. [1988] (as shown in Wheeler et al. [1989]). Also shown for comparison is the observed solar-system r-process abundance distribution (dashed line) from Cameron [1982b], and a theoretical s- and r-process distribution (see text for details).

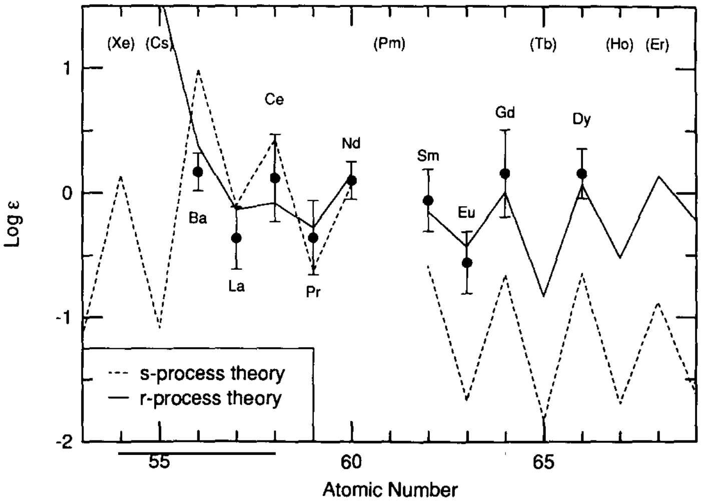

Fig. 6.4. Averages of the rare-earth elements for six metal-poor halo stars taken from the data of Gilroy et al. [1988] (as shown in Sneden [1990]). Also shown for comparison is a theoretical s-process curve from Malaney [1987], and a theoretical r-process curve based on the calculations of Cowan et al. [1987].

The timescales of the variations of these heavy-element abundance ratios with respect to iron can potentially be utilized to extract further information concerning both the stage at which significant s-process contributions first appear and (more important for our present purposes) the range in stellar mass of the dominant contributors to the r-process. The variations in [Sr/Fe], [Ba/Fe] and [Eu/Fe] with respect to [Fe/H] are illustrated in figs. 6.5, 6.6 and 6.7, respectively. These data seem to suggest that, in the most extremely metal-poor stars ($[\mathrm{Fe/H}] < -2.5$), all of the heavy elements may be significantly depleted with respect to iron. This trend seems somewhat more apparent for both strontium and barium than it does for europium. (This may be due to the larger scatter in the Eu data.) The observed

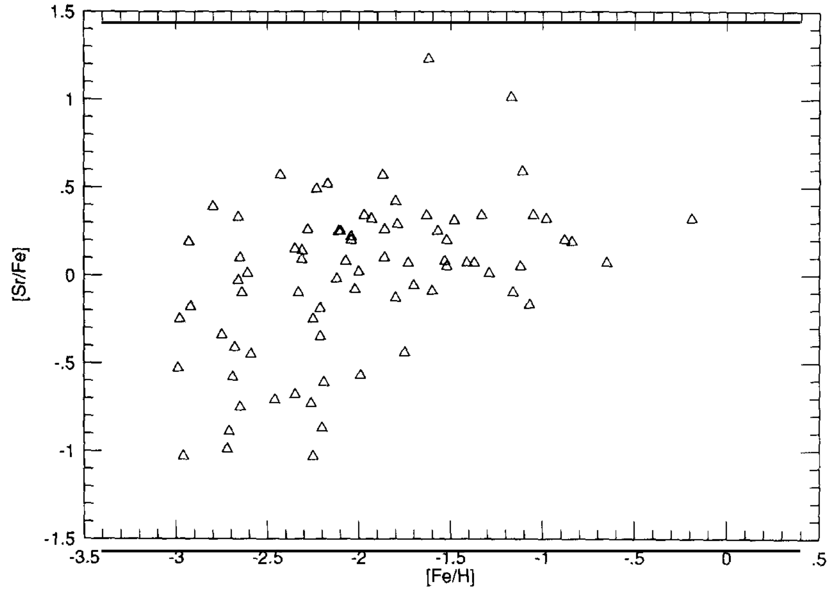

Fig. 6.5. The variation in [Sr/Fe] with respect to [Fe/H]. The data are taken from Sneden and Parathasarathy [1983], Luck and Bond [1985], Gilroy et al. [1988], Gratton and Sneden [1988], Hartmann and Gehren [1988] and Magain [1989]. The error bars are not plotted, but for the most part are comparable to the scatter in the data.

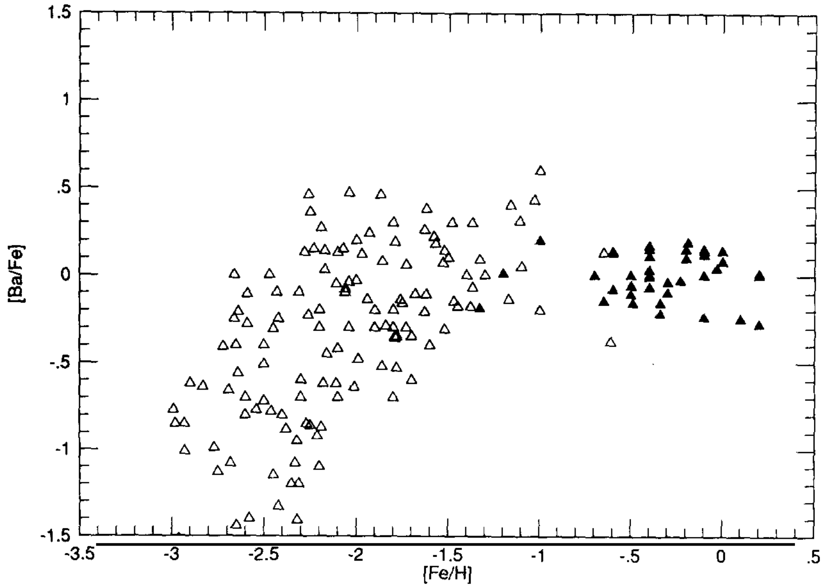

Fig. 6.6. Variation in [Ba/Fe] as a function of metallicity [Fe/H] (from Mathews et al. [1991]). The solid triangles are disk stars with near-solar metallicities [Butcher 1975]. The rest of the data, open triangles, are taken from da Silva et al. [1989], Gilroy et al. [1988], Gratton [1983], Gratton and Sneden [1988], Hartmann and Gehren [1988], Lepp and Wallerstein [1981], Luck and Bond [1985], Magain [1989], Peterson et al. [1990], Sneden and Parthasarathy [1983], Spite and Spite [1978] and Steenbock [1983]. The error bars are not plotted, but for the most part are comparable to the scatter in the data.

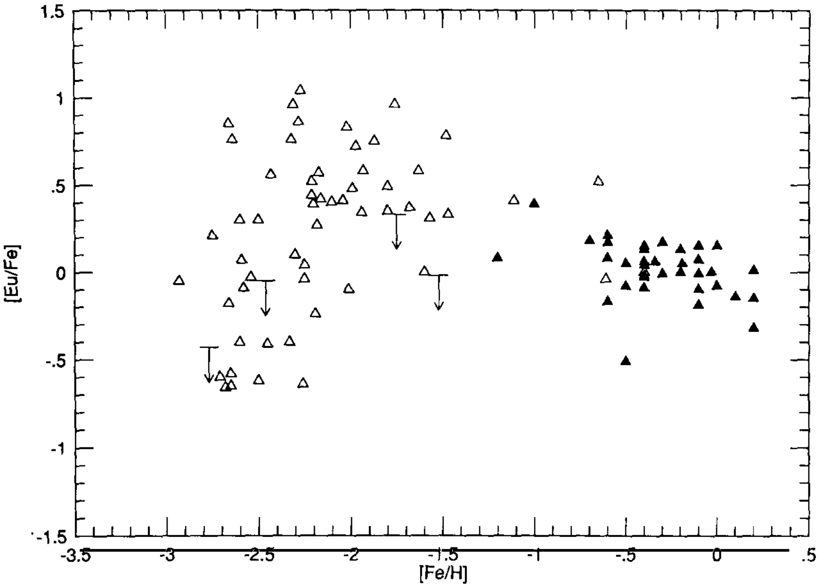

Fig. 6.7. Variation in [Eu/Fe] as a function of metallicity [Fe/H] (from Mathews et al. [1991]). The solid triangles are disk stars with near-solar metallicities [Butcher 1975]. The rest of the data, open triangles and inverted arrows (= upper limits), are taken from da Silva et al. [1989], Gilroy et al. [1988], Luck and Bond [1985], Magain [1989], Sneden and Parthasarathy [1983], and Spite and Spite [1978]. The error bars are not plotted, but for the most part are comparable to the scatter in the data.

variations in the ratios [Sr/Eu] and [Ba/Eu] indicate that the onset of significant contributions from the s-process occurs at approximately [Fe/H] ~ −2.0 (see, e.g., Gilroy et al. [1988]), from which point onward in time (or [Fe/H]) it becomes necessary to consider both s-process and r-process contaminations.

It also seems appropriate, in our present discussion of galactic chemical evolutionary effects, to call attention to the potentially important recent studies of the evolution of the thorium to neodymium ratio in the Galactic disk [Butcher 1987, 1988]. The use of such variations to provide an independent measure of the age of the disk is complicated by the fact that the abundance of Nd in the Galaxy includes contributions from both the s-process and the r-process. We will return to this issue in our subsequent discussion of nucleocosmochronology.

6.2. R-process sites and their abundance histories

As we have seen in the previous section, observations of metal-poor halo stars indicate the presence of r-process nucleosynthesis early in the history of the Galaxy. In particular, abundances of Eu, which is considered to be an r-process element, have been determined in stars with metallicities of [Fe/H] < −2, as shown in fig. 6.7. Furthermore, the r-process abundance distribution in these metal-poor halo stars is very similar to the solar-system abundances, as shown in figs. 6.2–6.4 and discussed above. This suggests that the solar-system r-process abundances could not be the average of r-process products from a number of different environments. Instead, it implies that there is only one r-process site.

Recently Mathews and Cowan [1990] have attempted to identify the site of the r-process based on a comparison between galactic, chemical evolution models and abundance observations of the very metal-poor stars. They used the observations of Butcher [1975], Luck and Bond [1985] and Gilroy et al.

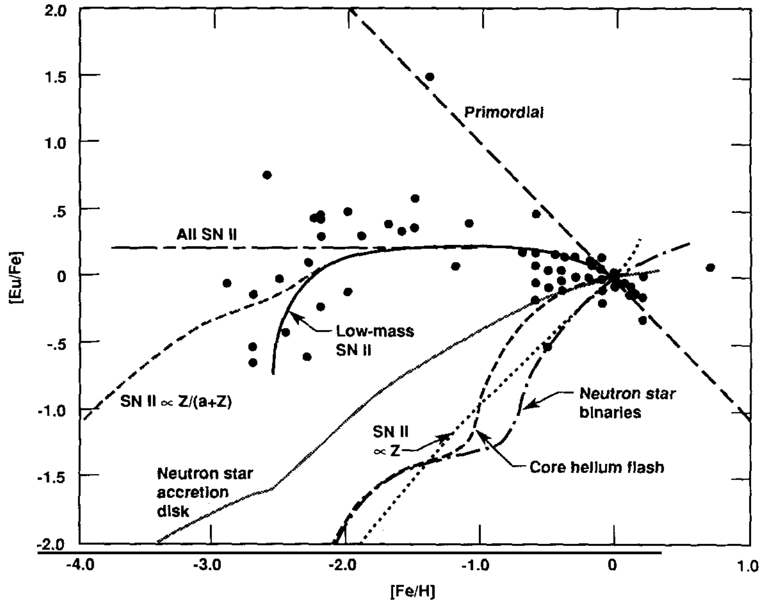

Fig. 6.8. Comparisons of galactic chemical evolution predictions from proposed r-process sites with observations of [Eu/Fe] as a function of metallicity [Fe/H] (from Mathews and Cowan [1990]). The data are from Butcher [1975], Luck and Bond [1985] and Gilroy et al. [1988]. The curve labeled "Primordial" corresponds to an r-process occurring before the galactic production of iron. The curves labeled: "All SN II" corresponding to a primary r-process occurring in all type II supernovae, "Low-mass SN II" corresponding to the case for a primary r-process occurring in stars of 10–11 $M_\odot$, "SN II $\propto Z$" corresponds to a secondary r-process with yields proportional to the star's initial metallicity, and "SN II $\propto Z/(a+Z)$" is for a secondary r-process which depends upon the initial metallicity but has a primary neutron source. The other three curves are for a core-helium-flash r-process in low-mass stars, an r-process occurring in neutron-star binary coalescence, and neutron-star accretion disks. (See text for discussion.)

[1988]. Figure 6.8 shows the results of Mathews and Cowan [1990]. Evolution models which assume that the r-process occurs in (1) the helium cores of low-mass stars, (2) primordial synthesis, or (3) neutron-star binary coalescence do not give a good fit to the time dependence ([Fe/H]) of the data. It is also seen in fig. 6.8 that the evolution model assuming neutron-star accretion disks, suggested as an r-process site by Hogan and Applegate [1987], does not fit the data. Purely primordial contributions would lead to a decline in [r/Fe] with time, as the iron fraction increases due to type II and, later, type I supernovae, while the r-component would remain at its primordial value. Helium core flashes of low-mass stars would take too long, due to their long evolutionary times, to match the observed production of r-process material early in the galactic history.

Similar arguments can be made about neutron-star binaries as an r-process site. The formation of neutron stars by Type II supernovae explosions will occur on short timescales, but the coalescence of the binary system as a result of gravitational wave radiation is expected to take approximately 10^8 y or $[\mathrm{Fe/H}] \approx -1$ (see also Eichler et al. [1989]). However, if the binary is formed in a high eccentricity orbit (perhaps by capture rather than by a common envelope phase), the orbital decay lifetime could be more than an order of magnitude less [Fajardo and Lattimer 1990]. The binary pulsar 1913 + 16 does in fact have a highly eccentric orbit, and gravitational damping is not expected to circularize the orbits until near the final merging. As shown in fig. 6.8, the best fits to the data are achieved with models that assume a supernova origin for the r-process. (Assuming a rapid merging timescale as a result of high eccentricity, neutron-star binary systems could also give a consistent fit to the observational data as shown by Mathews et al. [1991].)

On the other hand, if *all* type II supernovae produced a similar ratio of r-process elements to iron, Mathews and Cowan [1990] find that [Eu/Fe] would be relatively constant with time. As shown in fig. 6.8 (labeled "All SN II") such an assumption does not fit the data, particularly at low metallicity. Mathews and Cowan [1990] also argue that the apparent decline in [Eu/Fe] at very low metallicity, illustrated in fig. 6.7, can be explained by a delay in the production of r-process elements. Since iron presumably was formed first in the most massive progenitors, Mathews and Cowan [1990] suggest that these data imply a lower mass range for stars responsible for the production of the r-process elements. They, therefore, conclude that the cores of low-mass type II supernovae are the most likely site for the r-process. Mathews and Cowan [1990] note, however, that the actual mass range is uncertain.

6.3. Chemical evolution and age determinations

There exists an extensive literature regarding galactic chemical evolution (for a general review see Tinsley [1980]). Age determinations within the framework of cosmochronology, utilizing the r-process chronometer pairs ^{232}Th/^{238}U, ^{235}U/^{238}U and ^{244}Pu/^{238}U have been performed by Fowler and Hoyle [1960], Schramm and Wasserburg [1970], Truran and Cameron [1971], Fowler [1972, 1977, 1987a], Tinsley [1975, 1977], Hainebach and Schramm [1977], Reeves [1979], Symbalisty and Schramm [1981], Thielemann et al. [1983b], Clayton [1985a,b], Thielemann and Truran [1986], Cowan et al. [1986b, 1987], Clayton [1988], and Pagel [1989, 1990]. Other age determinations have been made using the pairs ^{187}Re/^{187}Os, ^{87}Rb/^{87}Sr and ^{207}Pb/^{235}U rather than the actinide chronometers [Woosley and Fowler 1979; Yokoi et al. 1983; Arnould et al. 1984; Beer and Walter 1984; Beer and Macklin 1985; Käppeler et al. 1989; Beer 1990].

All of these calculations start from the basic equation for the gas mass in the galactic disk,

$$\mathrm{d}M_\mathrm{G}/\mathrm{d}t = -\Psi + R\Psi + f - o\,, \tag{6.1}$$

where M_G denotes the mass of gas in the galactic disk, Ψ is the star-formation rate (SFR), i.e., the mass of gas turned into stars per unit time, R is the fractional mass ejected by stars during and at the end of their evolution (stellar winds, supernovae, etc.), f describes the infalling gas into the disk from the galactic halo, and o denotes a possible outflow into the galactic halo. The form used above already includes the instantaneous recycling approximation. In principle, the reejection R occurs after a period of stellar evolution and Ψ should not be evaluated at the same time for both terms in eq. (6.1). The time delay of ejection $\Psi(t - t_\mathrm{ev})$ is a function of the mass of a star and generally demands the use of a more general equation (see Tinsley [1980]). Fortunately, for the purposes of our present discussion, a more general treatment is not required. The elements and isotopes which are of concern here are produced in the r-process, which, as we have seen, is most likely associated with type II supernovae, and they involve massive stars with short evolutionary timescales, where the instantaneous recycling approximation is well founded.

Based on eq. (6.1), one can write an equation for the rate of change of the number of nuclei of species A which reads

$$\frac{\mathrm{d}N_\mathrm{A}}{\mathrm{d}t} = P_\mathrm{A}\Psi - \frac{1-R}{M_\mathrm{G}}\Psi N_\mathrm{A} + \frac{f}{M_\mathrm{G}}\frac{Z_f}{Z}N_\mathrm{A} - \frac{o}{M_\mathrm{G}}N_\mathrm{A} - \lambda_\mathrm{A}N_\mathrm{A}\,. \tag{6.2}$$

The term including $(1-R)\Psi$ is the same as in eq. (6.1). The infall term has to be modified here because the contribution of the infalling gas to the abundance of a heavy nucleus A is reduced according to its lower metallicity Z_f, in comparison with the disk metallicity Z; this is not the case for outflow. Besides the pure reejection of unprocessed gas in the outer envelope of stars R, there is a term (denoted by $P_A \Psi$) which describes the number of nuclei A being newly synthesized in material processed during stellar evolution and explosive processing. This number is not dependent upon metallicity for a primary production mechanism, as we concluded in sections 5, 6.1 and 6.2. We will therefore assume that P_A is a constant in the following derivation. The term λ_A in eq. (6.1) is the decay rate of radioactive nucleus A. A general solution to this equation, when abbreviated as $\dot{N}_A = P_A \Psi - \omega N_A - \lambda_A N_A$, has been given for $N_A(t)$ by Tinsley [1975] as

$$\nu(t) = \int_0^t \omega(t')\,\mathrm{d}t' , \qquad \omega = \frac{1-R}{M_G}\Psi - \frac{f}{M_G}\frac{Z_f}{Z} + \frac{o}{M_G} , \tag{6.3}$$

$$N_A(t) = N_A(0)\exp\{-[\lambda_A t + \nu(t)]\} + \exp\{-[\lambda_A t + \nu(t)]\}\int_0^t P_A \Psi(t')\exp[\lambda_A t' + \nu(t')]\,\mathrm{d}t' . \tag{6.4}$$

This marks the point of departure for the different approaches undertaken by different authors. They all depend upon the relation between the gas mass, M_G, the star formation rate (SFR), Ψ, and the amount and time dependence of the infall f. The result is determined by the time dependence of the function $\Psi(t)\,e^{\nu}$ in the integrand, also referred to as the "effective nucleosynthesis rate". Schramm and Wasserburg [1970] and Meyer and Schramm [1986] expand the integral in terms of moments of $\Psi\, e^{\nu}$. Other approaches assume a linear dependence between the star-formation rate and the total gas mass, $(1-R)\Psi = \alpha M_G$ (see, e.g., Clayton [1985a,b]). Note that, for vanishing infall and outflow, α equals ω, and for α = constant, eq. (6.1) would then result in an exponential decrease in time for the gas mass as well as for the star-formation rate [Schmidt 1963]. If a nonvanishing infall is taken into account, realistic assumptions for its amount and time dependence are necessary and solutions to eqs. (6.1) and (6.2) can be found numerically (e.g., Tinsley [1977], Yokoi et al. [1983]) or analytically for special functional forms of $f(t)$ [Clayton 1985a,b, 1988].

Here we want to perform as general a derivation as possible and to introduce assumptions of functional forms only in the final result. Introducing the abbreviation $\alpha(t) = (1-R)\Psi/M_G$ (note that α can be variable in time), eq. (6.1) may be written as

$$\mathrm{d}M_G/\mathrm{d}t = -(\alpha - f/M_G + o/M_G)M_G , \tag{6.5}$$

and has the general solution

$$M_G(t) = M_{G,0}\exp\left[-\int_0^t \left(\alpha - \frac{f}{M_G} + \frac{o}{M_G}\right)\mathrm{d}t'\right] . \tag{6.6}$$

Equation (6.1), together with the definition of α, also leads to

$$\frac{\mathrm{d}\Psi}{\mathrm{d}t} = -\left(\alpha - \frac{1}{\alpha}\frac{\mathrm{d}\alpha}{\mathrm{d}t} - \frac{f}{M_G} + \frac{o}{M_G}\right)\Psi , \qquad \Psi(t) = \Psi_0\exp\left[-\int_0^t \left(\alpha - \frac{1}{\alpha}\frac{\mathrm{d}\alpha}{\mathrm{d}t} - \frac{f}{M_G} + \frac{o}{M_G}\right)\mathrm{d}t'\right] . \tag{6.7}$$

For $\alpha =$ constant, the star-formation rate is linearly proportional to the gas mass, by definition, and therefore also has the same time behavior. Using this result for $\Psi(t)$ and the definition of $\nu(t)$ from eq. (6.3), the effective nucleosynthesis rate $\Psi\, \mathrm{e}^{\nu}$ becomes

$$\Psi\, \mathrm{e}^{\nu} = \Psi_0 \exp\left\{ - \int_0^t \left[\frac{f}{M_\mathrm{G}} \left(\frac{Z_f}{Z} - 1 \right) - \frac{1}{\alpha} \frac{\mathrm{d}\alpha}{\mathrm{d}t'} \right] \mathrm{d}t' \right\} \equiv \Psi_0 \exp\left(- \int_0^t \lambda_R \, \mathrm{d}t' \right) . \tag{6.8}$$

Thus the general result for the abundance of nuclei of species A becomes

$$\begin{aligned} N_\mathrm{A}(t) &= N_\mathrm{A}(0) \exp\{-[\lambda_\mathrm{A} t + \nu(t)]\} \\ &\quad + \exp\{-[\lambda_\mathrm{A} t + \nu(t)]\} \int_0^t P_\mathrm{A}\, \Psi_0 \exp\left(- \int_0^{t'} \lambda_R \, \mathrm{d}\tau \right) \exp(\lambda_\mathrm{A} t')\, \mathrm{d}t' . \end{aligned} \tag{6.9}$$

We want to describe the initial enrichment $N_\mathrm{A}(0)$ in such a way that its contribution to the total abundance of a stable nucleus A at time $t = \Delta$ is equal to a given value $S_0\ (<1)$. This leads to

$$N_\mathrm{A}(0) = \frac{S_0}{1 - S_0} P_\mathrm{A}\, \Psi_0 \int_0^\Delta \exp\left(- \int_0^{t'} \lambda_R \, \mathrm{d}\tau \right) \mathrm{d}t' . \tag{6.10}$$

For the ratio of the abundances of two nuclei A and B at the time of the formation of the solar system, i.e., after a nucleosynthesis epoch of duration $t = \Delta$, we find from eqs. (6.9) and (6.10),

$$N_\mathrm{A}(\Delta)/N_\mathrm{B}(\Delta) = (P_\mathrm{A}/P_\mathrm{B}) f(\lambda_\mathrm{A}, \lambda_\mathrm{B}, S_0, \lambda_R, \Delta) . \tag{6.11}$$

The ratio of the two radioactive nuclei $N_\mathrm{A}/N_\mathrm{B}$ is then a function of the unknowns λ_R, S_0 and Δ, as Ψ_0 and $\mathrm{e}^{-\nu(t)}$ cancel out. Given knowledge of the production ratio $P_\mathrm{A}/P_\mathrm{B}$ in a nucleosynthesis process and the abundance ratio $N_\mathrm{A}/N_\mathrm{B}$ at the time of the formation of meteorites in the solar system, i.e., 4.6×10^9 y prior to today, these three unknowns can be determined, if for three chronometric pairs A/B, the production ratios and meteoritic ratios are known. This is, however, only the case if we treat λ_R, to first approximation, as a constant. Such an approximation corresponds to the exponential model for $\Psi\, \mathrm{e}^{\nu}$, which was initially introduced by Fowler [1972]. This approximation turns the simple model of galactic chemical evolution into a "Mickey Mouse model" [Pagel 1990], and one should be aware of the resulting uncertainties in using such a model. In this simplified case, eqs. (6.9) and (6.10) become

$$N_\mathrm{A}(\Delta) = \Psi_0\, \mathrm{e}^{-\nu(\Delta)} P_\mathrm{A} \left(\frac{1}{\lambda_R - \lambda_\mathrm{A}} (\mathrm{e}^{-\lambda_\mathrm{A}\Delta} - \mathrm{e}^{-\lambda_R \Delta}) + \frac{S_0/(1 - S_0)}{\lambda_R} (1 - \mathrm{e}^{-\lambda_R \Delta})\, \mathrm{e}^{-\lambda_\mathrm{A}\Delta} \right) , \tag{6.12}$$

with S_0 indicating the fraction of stable r-process material present at solar-system formation resulting from the initial enrichment.

It is possible to argue against this simple exponential model (i.e., $\lambda_R =$ constant), but all more elaborate models also introduce assumptions about the relation between the gas mass, the star formation rate, and the amount and time dependence of infall. Thus, new uncertainties are introduced which could again affect the model in terms of the galactic age. Thus, we still employ the exponential model, but examine in detail how the results for λ_R, S_0 and t_G are compatible with observational information and the general model derived in eqs. (6.1) through (6.10).

One should be aware of the most important shortcoming of the simple exponential model – forcing f/M_G to be constant in time. This assumption is true for a closed model with $f = 0$ [Schmidt 1963]. In order to satisfy the observational constraints for the metallicity distribution of stars [Pagel and Patchett 1975] and the age metallicity relation [Twarog 1980] when $f = 0$, it is necessary to assume an initial enrichment in metals at the beginning of the galactic disk evolution of the order $Z_0/Z_{sol} = 0.1$–0.3 [Lynden-Bell 1975; Tinsley 1980] (see also Yokoi et al. [1983]). This will be the same value as S_0, if the initial r-process enrichment is the same as the initial metal enrichment.

An initial enrichment can be avoided and the metallicity distribution can be naturally explained if one allows for infall. In the early stages of disk evolution, the gas mass is then dominated by infall from the collapsing galactic halo and the gas mass, as well as the star-formation rate, reach a maximum before they start to decline in time. This first rise and burst of star formation is able to reproduce all observed quantities. While the declining phase of f and M_G with comparable timescales might be approximated by a constant ratio, the first rise and burst of star formation can be included as a separate term in eq. (6.8) by performing the integral over two intervals in time. Technically, such a term corresponds to an initial enrichment. When treating the problem in this way one should be aware of the fact that the results give lower limits to the age of the Galaxy, because the duration of the initial burst of star formation is not included. While this duration time might be as short as $\sim 2 \times 10^8$ y, it could be as long as $(2$–$3) \times 10^9$ y (see, e.g., Clayton [1985a,b, 1988]).

7. Nuclear chronometers, production ratios and ages

Nucleochronology, employing radioactive nuclei with very long half-lives, can be used to determine the age of the Galaxy and hence provide a lower limit upon the age of the universe. Particularly useful for these age determinations are the long-lived r-process nuclear chronometers (see table 7.1): ^{187}Re, ^{232}Th, ^{238}U and ^{235}U. Nuclei with shorter half-lives, such as ^{244}Pu and ^{129}I, can be used to provide a measure of the rate of galactic nucleosynthesis close to the time of the formation of the solar system. This chapter reviews the various r-process chronometers and their associated production ratios. Using these ratios, together with a knowledge (from meteoritic abundances) of the isotopic abundances at the time of the formation of the solar system and the history of chemical evolution discussed above, galactic age determinations can be made.

While there are a number of nuclear species that can be utilized to estimate the galactic age, there is clearly an advantage to be gained by restricting oneself only to nuclear species produced in a single astrophysical process (environment). This approach can help to reduce some of the uncertainties in the calculations. The emphasis in this paper is on the r-process, and we thus confine our attention here

Table 7.1
Nuclear chronometers

Nucleus	Decay product	Half-life (y)	Nucleus	Decay product	Half-life (y)
^{147}Sm	^{143}Nd	1.06×10^{11}	^{238}U	^{206}Pb	4.47×10^{9}
^{87}Rb	^{87}Sr	4.89×10^{10}	^{235}U	^{207}Pb	7.04×10^{8}
^{187}Re	^{187}Os	4.5×10^{10}	^{244}Pu	^{208}Pb	8.2×10^{7}
^{232}Th	^{208}Pb	1.40×10^{10}	^{129}I	^{129}Xe	1.6×10^{7}

primarily to r-process chronometers. A forthcoming discussion of age determinations, which includes various s-process chronometers, will appear in Cowan et al. [1991].

7.1. Th, U and Pu chronology

7.1.1. Production ratios

The r-process is entirely responsible for the synthesis of ^{187}Re, ^{232}Th, ^{235}U, ^{238}U and ^{244}Pu. There is no s-process contribution to the production of any of these nuclei, with the possible exception of Re (see section 7.2.1). In the r-process, the final abundances of all these long-lived isotopes, except ^{187}Re, involve summations over the abundances of a number of short-lived progenitors in alpha-decay chains, viz,

^{232}Th: ^{232}Th, ^{236}U, ^{240}Pu, ^{244}Pu, ^{248}Cm, ^{252}Cf
^{235}U: ^{235}U, ^{239}Pu, ^{243}Am, ^{247}Cm, ^{251}Cf, ^{255}Fm
^{238}U: ^{238}U, ^{242}Pu, ^{246}Cm, ^{250}Cf
^{244}Pu: ^{244}Pu, ^{248}Cm, ^{252}Cf.

Performing the indicated summations allows the calculation of the production ratios of the actinide pairs ^{232}Th/^{238}U, ^{235}U/^{238}U and ^{244}Pu/^{238}U. (The ^{187}Re chronometer is discussed below in section 7.2.) Particularly useful are the first two pairs. The very short half-life of ^{244}Pu, which can only provide information near the time of the formation of the solar system, makes the ratio of ^{244}Pu/^{238}U relatively useless for age determinations. It should also be noted that the summation over the short-lived progenitors reduces the uncertainties associated with the production of any individual isotope.

In each of these summations, the number of progenitors is constrained by a line, beyond which spontaneous fission dominates all other modes of decay. On this basis alone, we see that the isotopes ^{232}Th, ^{235}U, ^{238}U and ^{244}Pu have 6, 6, 4 and 3 progenitors, respectively. It is also necessary to take into account the fission losses experienced by the listed progenitors, which reduces the "effective" number of progenitors. For ^{232}Th, the six identified progenitors become 5.9; for ^{235}U, the six progenitors remain six; for ^{238}U, the four progenitors are reduced to 3.35 effective progenitors; and for ^{244}Pu, the three become 2.85. These numbers may be used directly to provide a zeroth-order estimate of the production ratios of these isotopes, based on the assumption that the various progenitors are produced in equal abundances in the r-process. In this case, the corresponding production ratios are

$$^{232}\mathrm{Th}/^{238}\mathrm{U} = 1.73\,, \qquad ^{235}\mathrm{U}/^{238}\mathrm{U} = 1.79\,, \qquad ^{244}\mathrm{Pu}/^{238}\mathrm{U} = 0.82\,.$$

The assumption that the progenitors of these long-lived isotopes are formed in equal abundance is not consistent with the results of detailed calculations of r-process nucleosynthesis. For purposes of illustration, we list in table 7.2 the values obtained by various authors, utilizing both different sources of input nuclear physics (e.g., mass formulae) and quite different assumptions concerning the r-process nucleosynthesis conditions (see section 5). The critical piece of information to be drawn from this compilation is the breadth of the range of predicted values for the production ratios. Note specifically that the predicted production ratios for ^{232}Th/^{238}U take values in the range 1.40 to 1.90; those for ^{235}U/^{238}U have allowed values of 0.89 to 1.89; and those for ^{244}Pu/^{238}U range from 0.12 to 0.96. These ranges clearly reflect the substantial uncertainties associated both with the nuclear physics and with the astrophysical conditions. They also clearly introduce a significant uncertainty into calculations of nucleocosmochronology.

Table 7.2
Production ratios from r-process calculations

^{232}Th/^{238}U	^{235}U/^{238}U	^{244}Pu/^{238}U	Reference
1.65	1.42	0.90	Seeger et al. [1965], Fowler [1972]
1.90	1.89	0.96	Seeger and Schramm [1970]
1.70	0.89	0.53	Wene and Johansson [1976]
1.80	1.42	0.90	Fowler [1977]
1.90	1.50	0.90	Symbalisty and Schramm [1981]
1.50	1.10	0.40	Krumlinde et al. [1981]
1.40	1.24	0.12	Thielemann et al. [1983a,b]
1.71	1.34	0.66	Fowler and Meisl [1986], Fowler [1987a]
1.60	1.16	0.40	Cowan et al. [1987] with β-delayed fission
1.53	1.26	0.49	Thielemann et al. [1989] without β-delayed fission
1.73	1.79	0.82	equal abundances assumed

The variations in production ratios are a consequence of the fact that the identified neutron-rich progenitors of ^{232}Th, ^{235}U, ^{238}U and ^{244}Pu are not formed in equal concentrations. There are two basic reasons for this behavior:

(1) The nuclear-reaction properties of individual nuclei in these regions – the (n, γ) cross sections and β^- decay lifetimes – introduce a significant amount of local structure along the r-process capture path. The levels of production are thus expected both to differ from equality and to be a function of specific choices of the nuclear physics parameters. For example, all calculations based upon the use of the Klapdor et al. [1984] beta-decay rates show structure in the abundance distribution around the $A = 238$ mass region (see fig. 7.1), in contrast to the case of constant progenitor abundances. The influence of these various nuclear properties on the production ratios is also dependent upon the detailed temperature and density history of matter at the r-process site, hence we might expect to obtain different results for different environments even when we use the same mass-formula predictions and neutron-capture and beta-decay properties.

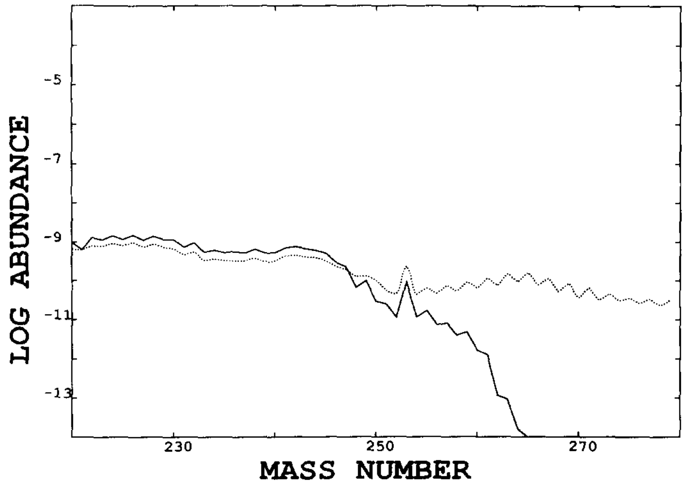

Fig. 7.1. Calculated r-process abundances of heavy nuclei in the range $220 \leq A \leq 280$ from Cowan et al. [1987]. (The total abundance curve is shown in fig. 5.2.) The dotted line shows the calculated abundances for the same astrophysical conditions, but without the effects of fission.

(2) An additional feature is the fact that the abundances of the neutron-rich progenitors can be further depleted by beta-delayed fission, as indicated in the extreme by calculations of Thielemann et al. [1983a,b]. As we have discussed in section 3, however, the use of a more consistent data set largely eliminates this strong dependence on beta-delayed fission [Thielemann et al. 1989].

Our personal view in this matter has been guided by the philosophy that we can expect to obtain more reliable estimates of these critical production ratios for cosmochronology in the context of calculations which, independently of the astrophysical site, tend to best reproduce the gross features of the solar-system r-process distributions. Thielemann et al. [1983a,b], for example, performed a number of detailed r-process calculations that included the effects of beta-delayed neutron emission and beta-delayed fission. Their calculated abundance curve showed good agreement with the observed solar-system r-process abundance curve [Cameron 1982a; Käppeler et al. 1989]. Using the same calculated abundances, Thielemann et al. [1983a,b] found the production ratios to be $^{232}\mathrm{Th}/^{238}\mathrm{U} = 1.40$, $^{235}\mathrm{U}/^{238}\mathrm{U} = 1.24$, and $^{244}\mathrm{Pu}/^{238}\mathrm{U} = 0.12$. Although their calculations assumed conditions typical of explosive helium burning, they noted that "this abundance distribution in the r-process path has to be produced by any event which can reproduce the solar r-abundances". In other words, the production ratios they determine should be substantially independent of the assumed site, as long as the conditions in that site reproduce the solar-system abundances.

Cowan et al. [1987] similarly used calculations which provided a good a fit to the solar system to determine the production ratios. Their calculations were different in a number of important ways, however, which resulted in very different values of the chronometric production ratios (see table 7.2). Different neutron-capture cross sections, based on different nuclear mass formulae, were used by the two groups. Furthermore, their estimates of the beta-delayed fission and beta-delayed neutron-emission rates were very different; the values used by Cowan et al. [1987] were lower than those of Thielemann et al. [1983a,b]. Finally, Thielemann et al. [1983a,b] assumed equilibrium conditions for their r-process calculations, while Cowan et al. [1987] performed dynamic r-process calculations. (The different assumptions made in these types of calculations are described in detail in section 4.) Using their best calculated fit to the solar r-process curve, Cowan et al. [1987] determined the production ratios to be $^{232}\mathrm{Th}/^{238}\mathrm{U} = 1.60$, $^{235}\mathrm{U}/^{238}\mathrm{U} = 1.16$, and $^{244}\mathrm{Pu}/^{238}\mathrm{U} = 0.40$. They also attempted to estimate the uncertainties associated with these ratios. Uncertainties in the nuclear data yielded a spread of 0.1 in the $^{232}\mathrm{Th}/^{238}\mathrm{U}$ ratio and 0.05 in that for $^{244}\mathrm{Pu}/^{238}\mathrm{U}$. (These authors did not find any difference in the $^{235}\mathrm{U}/^{238}\mathrm{U}$ ratio based on the two sets of calculations they performed.)

Cowan et al. [1987] and Thielemann et al. [1983a,b] both used conditions for their r-process calculations that were typical of explosive helium-burning environments. As noted above in section 5, this does not seem, at this time, to be a plausible site for the r-process. Cowan et al. [1987], however, reiterated the point made by Thielemann et al. [1983a,b] that, if the calculations can reproduce the solar-system r-process curve, then the r-process path in the N–Z plane must be in approximately the right position. It should follow that, under these circumstances, the different mass numbers will be produced in the correct proportions. This argument is equivalent to the statement that the r-process is a unique event, which always produces an abundance distribution similar to that found in the solar system. As noted in section 6, observations of extremely metal-poor stars, which show a solar r-process distribution, support this argument [Mathews and Cowan 1990]. It was estimated that the uncertainty in the production ratios resulting from the fit to the solar curve was of the same magnitude as produced by nuclear uncertainties, or 0.1 in $^{232}\mathrm{Th}/^{238}\mathrm{U}$ [Cowan et al. 1987].

The fact that Thielemann et al. [1983a] and Cowan et al. [1987] got different production ratios, even though they both fit the observed solar-system curve, is attributable to the uncertainties in the nuclear physics, particularly earlier estimates of the rates of beta-delayed fission in the mass range of $A = 240$. The influence of fission on the determination of the r-process production ratios is beginning to be better understood. Some early estimates of these ratios ignored the effects of beta-delayed fission [Seeger et al. 1965; Fowler 1972; Seeger and Schramm 1970]. Other authors attempted to include fission by assuming constant nuclear abundances as a function of mass number [Wene and Johansson 1976; Krumlinde et al. 1981; Meyer et al. 1985]. This latter approach ignored the details of the abundance distribution along the r-process path.

Thielemann et al. [1983a,b] explicitly included the effects of beta-delayed fission in their calculations, based on the fission barrier height determinations of Howard and Möller [1980]. These calculated fission probabilities strongly affected the predicted values of the production ratios. There are indications, however, that Thielemann et al. [1983a,b] overestimated the fission rates, due to the fact that the fission barrier heights are larger than they had assumed [Meyer et al. 1989b]. Smaller percentages of beta-delayed fission were found when using a more consistent nuclear data set (see discussion in section 3), but one that still relied on the Howard and Möller [1980] fission barrier heights [Cowan et al. 1987]. Since these predicted barrier heights are also too low (see section 3.2), the calculated beta-delayed fission rates may still be too large.

Thielemann et al. [1989] repeated the dynamic calculations of Cowan et al. [1987] in an attempt to examine the effect of the fission results on the production ratios. In these new calculations, Thielemann et al. [1989] set the fission probabilities equal to zero, corresponding to infinitely high fission barrier heights. This clearly represents a limiting case. Their calculated production ratios are listed in table 7.2; as can be seen, they are little different from those found by Cowan et al. [1987]. It appears, therefore, that beta-delayed fission has little influence on the actinide chronometer ratios.

The values presented in table 7.2 make clear that there is a wide range of possible values of the r-process production ratios. More work will be needed to constrain these ratios. Particularly important will be calculations that use consistent nuclear data bases, for which all of the relevant theoretical parameters will be calculated using the same (presumably reliable) nuclear mass formula.

7.1.2. Meteoritic abundances

The calculated production ratios can then be compared with the measured isotopic ratios in solar-system material, to obtain the duration of nucleosynthesis from the time of formation of the Galaxy until the time of formation of the solar system. The $^{232}\mathrm{Th}/^{238}\mathrm{U}$ ratio is difficult to determine, because of the chemical differences between the two different elements. Fowler [1977] noted that the ratio varies in terrestrial material, possibly as a result of chemical fractionation. For this reason, Fowler [1977] adopted $^{232}\mathrm{Th}/^{238}\mathrm{U} = 4.0 \pm 0.2$ based on a weighted average of meteorites and moon rocks, with heavy emphasis on the "expensive" Apollo results. This number corresponds to the value for this ratio at the current time. Using the relative lifetimes for decay, Fowler [1977] then determined $^{232}\mathrm{Th}/^{238}\mathrm{U} = 2.50 \pm 0.2$ at the time of the formation of the solar system. Anders and Ebihara [1982] and Anders and Grevesse [1989], using various meteorite samples, found the present day value of Th/U to be 3.6, which translates into $^{232}\mathrm{Th}/^{238}\mathrm{U} = 2.32$ at the time of the formation of the solar system. They note that their abundances are typically accurate to between 5% and 10%; in particular, Th and U are uncertain by 5% and 11% respectively. Cameron [1982a] also lists the current value of Th/U as 3.6, but finds a slightly different value of the isotopic ratio $^{232}\mathrm{Th}/^{238}\mathrm{U} = 2.22$.

There is good agreement on the $^{235}\mathrm{U}/^{238}\mathrm{U}$ ratio. Fowler [1977] lists a ratio $7.25 \pm 0.01 \times 10^{-3}$ for the current value which translates into 0.313 ± 0.001 at the formation of the solar system. The same value is used by Symbalisty and Schramm [1981]. Anders and Ebihara [1982] and Anders and Grevesse [1989] find $^{235}U/^{238}U = 0.317$ when the solar system formed. Cameron [1982a] finds a similar value of 0.315, while Fowler [1987a] uses a somewhat higher value of 0.330. Note that the uncertainties in the elemental abundances of (5–10%), as a result of chemical fractionation effects, do not enter into the isotopic ratios.

7.1.3. Galactic ages

Using the calculated production ratios in section 7.1.1, the meteoritic abundance ratios from section 7.1.2 and a model for galactic chemical evolution (section 6.3), chronometric age determinations can be made. Depending upon the various choices for these parameters, a variety of age estimates have resulted. One can adopt the simple exponential model for determining the duration of galactic nucleosynthesis (Δ) before the formation of the meteorites and the solar system, 4.6×10^9 y ago, by utilizing eq. (6.11). The needed quantities for each chronometer pair are the production ratios P_A/P_B and the meteoritic abundance ratios $N_A(\Delta)/N_B(\Delta)$. As long as the simple chemical evolution model is defined by three parameters, the initial enrichment S_0, the time change of r-process nucleosynthesis λ_R and its duration Δ, three chronometer pairs are needed as well. When making use only of $^{232}Th/^{238}U$ and $^{235}U/^{238}U$, one parameter has to be fixed. In the following, we discuss various age estimates appearing in the literature for different choices of production ratios and chemical evolution models. As noted in sections 7.1.1 and 7.1.2, the uncertainties in the meteoritic ratios and the production ratios are comparable.

Fowler and Meisl [1986] and Fowler [1987a] assumed a constant effective nucleosynthesis rate, i.e., $\lambda_R = 0$. With the production ratios ($^{232}Th/^{238}U = 1.71$, $^{235}U/^{238}U = 1.34$) and meteoritic ratios ($^{232}Th/^{238}U = 2.305$, $^{235}U/^{238}U = 0.330$). Fowler finds a galactic age of $t_G = 10.0 \pm 1.6$ Gy.

Cowan et al. [1987] also adopted the simple model. They varied the initial r-element enrichment S_0 between 0.1 and 0.3. This corresponds to the initial metal enrichment needed in evolution models without infall, and results in values for λ_R and Δ. With meteoritic abundance ratios of 0.317 for $^{235}U/^{238}U$ and 2.32 for $^{232}Th/^{238}U$ (see discussion above in section 7.1.2), and their production ratios of 1.16 and 1.60, Cowan et al. [1987] found values ranging from 7.8×10^9 y to 10.1×10^9 y for Δ, depending upon S_0. These values translate into ages of the Galaxy of 12.4×10^9 y to 14.7×10^9 y, after adding the age of the solar system (i.e., 4.6×10^9 y). These ages did not include the duration of galactic evolution which produced the initial enrichment. As discussed previously, more complex evolution models, which start with a small gas mass in the disk and have an increasing star-formation rate during the early infall period, can result in a duration of galactic nucleosynthesis which is larger by as much as $(2–3) \times 10^9$ y. Cowan et al. [1987] also estimated the effects of uncertainties in nuclear data. Variations within the range of 0.10 for the Th/U production ratio led to an increased age uncertainty of approximately 2×10^9 y.

Earlier evaluations within the exponential model also included the short-lived chronometers $^{244}Pu/^{238}U$ and $^{129}I/^{127}I$ and additional parameters like a last nucleosynthesis spike before the formation of the solar system. Such a parametrization might be somewhat questionable and can lead to artificial results. Thielemann et al. [1983a,b] were the first to include explicitly the beta-delayed neutron emission and fission in their r-process calculations. They made use, however, of an inconsistent set of mass formula and fission barrier heights (see discussion in section 3) which maximized the beta-delayed fission rate and led to very small Th/U production ratios: $^{232}Th/^{238}U = 1.39$ and $^{235}U/^{238}U = 1.24$. The resulting galactic age was 20.8^{+2}_{-4} Gy.

Fowler [1977] used a four-parameter exponential model for the galactic chemical evolution with an early spike in nucleosynthesis. Using $^{232}\mathrm{Th}/^{238}\mathrm{U} = 1.80$, $^{235}\mathrm{U}/^{238}\mathrm{U} = 1.42$ and $^{244}\mathrm{Pu}/^{238}\mathrm{U} = 0.90$ he found the galactic age to be $t_G = 12^{+3}_{-2}$ Gy and the duration of nucleosynthesis, $\Delta = 6.1 \pm 2.3$ Gy.

The use of the simple exponential model is probably only meaningful if its time behavior obeys observational constraints and the uncertainties in short-lived chronometers do not force the parameters into purely mathematical, but physically questionable, solutions. Thielemann and Truran [1986] noted that a reduced $^{235}\mathrm{U}/^{238}\mathrm{U}$ production ratio forces the value of λ_R to be slightly negative, in contrast to earlier studies [Fowler 1972, 1977]. They argued, on the basis of observational evidence for the rate of the decline of the star-formation rate and the value of the gas-depletion timescale, that λ_R had to be equal to or less than zero. From the definition of λ_R in eq. (6.8), we can see that for the case of nonvanishing infall, λ_R has to be negative, if $\alpha = \text{constant}$ (i.e., when the star-formation rate is proportional to the gas mass). In a closed model λ_R would be zero and the effective nucleosynthesis rate constant. A negative λ_R, resulting in a time dependence of the effective nucleosynthesis rate which agrees with observational constraints, can only be achieved with a low $^{235}\mathrm{U}/^{238}\mathrm{U}$ production ratio. This is illustrated in fig. 7.2. Note also the large variation in Δ with the change in the Th/U production ratio.

Clayton [1988], instead of making use of the simplest, analytically solvable model with $\lambda_R = \text{constant}$, parametrized the infall to gas mass ratio in two different ways: $f(t)/M_G(t) = k/(t + \Delta)$ or $f(t) = \omega_f M_{G0}\, e^{-\omega' t}$. Such a parametrization also leads to analytical solutions, but with the appropriate choice of k and Δ or ω_f and ω', can mimic the more complex behavior of infall models at early times. Figure 7.3 shows the allowed range of galactic ages, deduced from the Th/U chronometer pair with a ratio of 1.71, for a family of parameters [Clayton 1988]. For that ratio, Clayton's [1988] results indicate $8 < T_G < 13$ Gy for closed (i.e., no infall) models, but much larger ages may be possible with infall. Smaller production ratios would also lead to larger ages.

Yokoi et al. [1983] performed a very general galactic chemical evolution calculation, without any simplifications which might lead to analytical solutions. Their main emphasis was to try to reproduce the

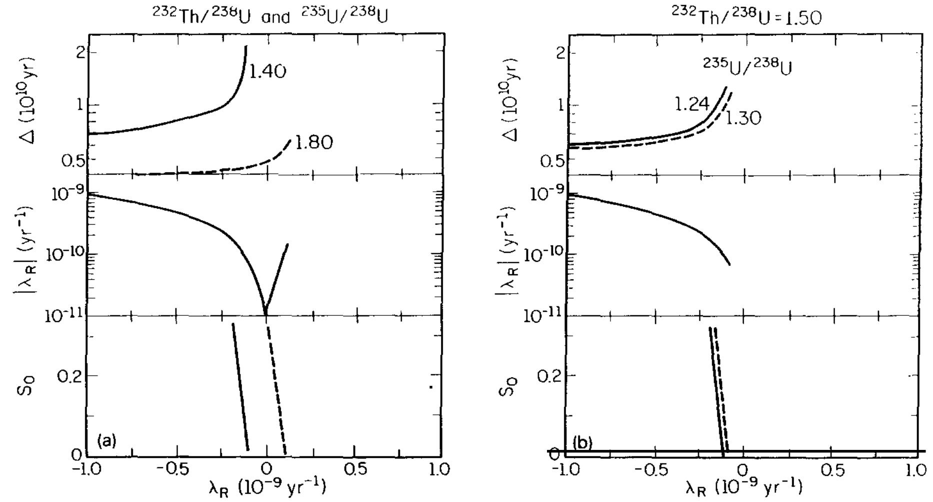

Fig. 7.2. Using the two chronometric pairs, $^{232}\mathrm{Th}/^{238}\mathrm{U}$ and $^{235}\mathrm{U}/^{238}\mathrm{U}$, the values of Δ (duration of galactic nucleosynthesis before the formation of the solar system) are presented as a function of λ_R, which governs the time dependence of the effective nucleosynthesis rate $[= \Psi_0 \exp(-\lambda_R t) = \Psi(t)\exp(\omega t)]$. The absolute value of λ_R is also displayed on a logarithmic scale. (a) Two cases with production ratios of $^{232}\mathrm{Th}/^{238}\mathrm{U} = 1.40$ and $^{235}\mathrm{U}/^{238}\mathrm{U} = 1.24$ or 1.80 and 1.42, respectively. The latter ratios do not allow solutions with $\lambda_R \leq 0$ for $S_0 \leq 0.3$. Larger values of S_0 result in shorter galactic ages. (b) The results for $^{232}\mathrm{Th}/^{238}\mathrm{U} = 1.50$ and $^{235}\mathrm{U}/^{238}\mathrm{U} = 1.24$ or 1.30. In comparison with a, it is seen that the shift of $S_0(\lambda_R)$ is due mostly to the $^{235}\mathrm{U}/^{238}\mathrm{U}$ ratio.

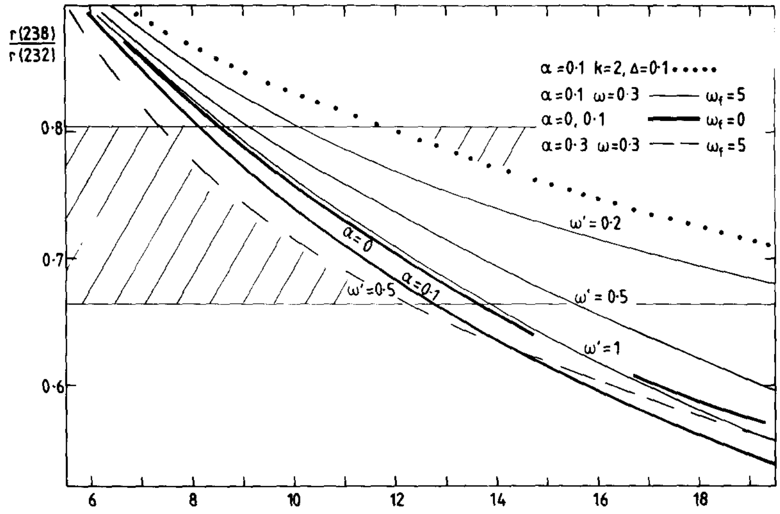

Fig. 7.3. The allowed range of galactic ages for a family of evolution parameters (including initial metallicity, α, gas consumption rate, ω, and rate of infall) from Clayton [1988]. All of the models assume an r-process production ratio for ^{232}Th/^{238}U of 1.71.

available astronomical constraints. Figure 7.4 displays the results of their numerical integrations, based upon these models for calculating the time evolution of the chronometer pairs. From the figure, it can be seen that production ratios between 1.1 and 1.3 are needed for the U-pair and that ratios larger than 1.7 are required for the Th/U pair, to obtain galactic ages lower than 15×10^9 y.

Meyer and Schramm [1986] made use of the so-called "model independent" approach [Schramm and Wasserburg 1970], by expanding the integral in eq. (6.4) in moments of $\Psi\,e^{\nu}$. For small values of the Th/U production ratio, one has to expand to higher moments and the result becomes rather model-dependent. Meyer and Schramm [1986] give a range for the age of the Galaxy of $9–27 \times 10^9$ y.

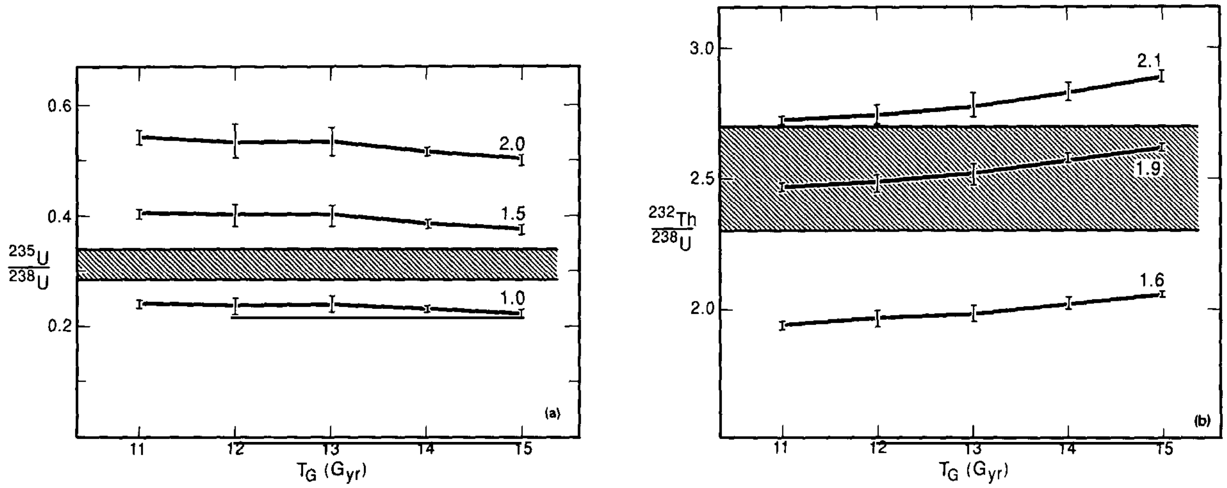

Fig. 7.4(a). Abundance ratio ^{235}U/^{238}U at $T + \Delta$ for three choices of the r-process production ratio (from Yokoi et al. [1983]). The observed ratio with its uncertainty (shaded area) and the α-decay rates are from Symbalisty and Schramm [1981]. (b) Same as a for ^{232}Th/^{238}U (from Yokoi et al. [1983]).

Malaney et al. [1989] recently found that high-energy photons, from CNO reactions in stellar hydrogen burning, can lead to photofission of actinides. Because of a lower fission barrier, ^{238}U is more sensitive to this effect than ^{232}Th. This would cause a further complication in the evolutionary models discussed above, but in a simplified model, photofission would enhance the Th/U production ratio relative to the pure r-process predictions. This effect might also alter the conclusion of Yokoi et al. [1983], that Th/U ratios larger than 1.7 are required to fit astronomical constraints of galactic evolution models, and allow their result to be in accord with smaller production ratios (<1.6) found in most r-process predictions, based on more recent nuclear data.

7.2. Mixed r- and s-process chronologies

The chronometers discussed in section 7.1 are the only pure r-process chronometers where both components are made in the r-process. Our emphasis, therefore, in this review has been on these chronometers. There exist a number of other chronometers, however, where at least one of the components has an r-process contribution. These will be discussed here in a more cursory way. For a deeper discussion and analysis of pure s-process chronometers see Clayton [1988], Arnould and Takahashi [1990] and our forthcoming review [Cowan et al. 1991].

The mixed chronometers include the ^{187}Re/^{187}Os pair. ^{187}Re is produced in the r-process, and ^{187}Os results from both the long-term decay of the r-process nucleus ^{187}Re and an intrinsic s-process contribution. It is important to subtract this s-process component in order to utilize the remaining cosmoradiogenic osmium, ^{187}Os$_c$, along with the ^{187}Re for age determinations. The case of ^{87}Rb/^{87}Sr is similar, except that ^{87}Rb might also have an s-process contribution. Other pairs like ^{206}Pb/^{238}U or ^{207}Pb/^{235}U have still a third component. For example, ^{206}Pb is produced in the s-process. It also has an r-process component, including the decay of all short-lived nuclei between Pb and Th, which are produced in the r-process but decay to ^{206}Pb. And finally, there is the r-process component of ^{238}U, which decays on long timescales to ^{206}Pb, leading again to a cosmoradiogenic component. The same argument holds for the ^{207}Pb/^{235}U pair. In both of these cases, it is important to determine the cosmoradiogenic component.

In addition to the pairs mentioned above, which were first introduced into cosmochronology by Clayton [1964], the elemental pair Th/Nd has recently been suggested as a chronometer [Butcher 1987]. In the following subsections we discuss all of these chronometers pairs in more detail.

7.2.1. Re/Os

There are a number of uncertainties involved in using this chronometer. The stellar beta-decay rate of ^{187}Re may be affected by a number of factors, which make it very different from the laboratory decay rate. Clayton [1969] noted that thermal effects in the star should excite and ionize the ^{187}Re. Beta decay would then be enhanced (i.e. the lifetime greatly decreased with respect to the value listed in table 7.1), as shown by Takahashi and Yokoi [1983]. Beta decay of excited bound states in ^{187}Re to the 9.75 keV state in ^{187}Os will occur [Arnould et al. 1984], and more low-lying nuclear states will be populated at higher temperatures. The inverse process, electron capture on ^{187}Os, can also occur, however. The net result of these factors will significantly increase the rate of beta decay of ^{187}Re [Cosner and Truran 1981].

Another uncertainty with this chronometer involves the s-process contribution to ^{187}Os. This is normally determined by using the local approximation for the s-process,

$$n_s(^{187}\mathrm{Os})\langle\sigma v\rangle_{187} = n_s(^{186}\mathrm{Os})\langle\sigma v\rangle_{186}\,,$$

where n_s is the s-process abundance and $\langle\sigma v\rangle$ is the thermally averaged neutron-capture cross section for the indicated nucleus. In using this approximation to determine the s-process contribution to ^{187}Os production, the neutron cross sections need to be well determined. In addition, Arnould et al. [1984] suggested that this local approximation is not valid due to s-process branching in this mass region. Both of these latter problems seem to be resolved now (see Käppeler et al. [1990] and references therein), allowing the determination of the cosmoradiogenic ratio, $r = {}^{187}\mathrm{Os_c}/{}^{187}\mathrm{Re}$, at the time of the formation of the meteorites. The remaining task is to include the temperature-dependent half-life correctly in galactic evolution calculations.

Thielemann and Truran [1986] tried to treat the Re/Os chronometer pair as a third equation together with the Th/U and U/U pairs in the simple exponential model of galactic chemical evolution. The equivalent equation to (6.11) for cosmoradiogenic pairs leads to a different function f on the right-hand side and cancellation of the production ratio P_A/P_A. In such a case, all three free parameters of the exponential model with initial spike can be determined. Assuming a long half-life for the ground state of ^{187}Re, however, resulted in solutions requiring small Th/U production ratios (and large galactic ages) for the uncertainty range r defined above. On the other hand, one can again make an assumption for S_0 and ask what average half-life (in stars and the interstellar medium) is required to make all three chronometers consistent. The results for both cases are displayed in fig. 7.5. With a value of Th/U = 1.5, an effective half-life of $2.5–4 \times 10^9$ y is required for such consistency.

Yokoi et al. [1983] also found that only the proper inclusion of a decreased half-life into their numerical evolution model could make this chronometer concordant with astronomical constraints of the evolution model, suggesting a galactic age range of $11\,\mathrm{Gy} < t_G < 15\,\mathrm{Gy}$. Clayton [1988] did not

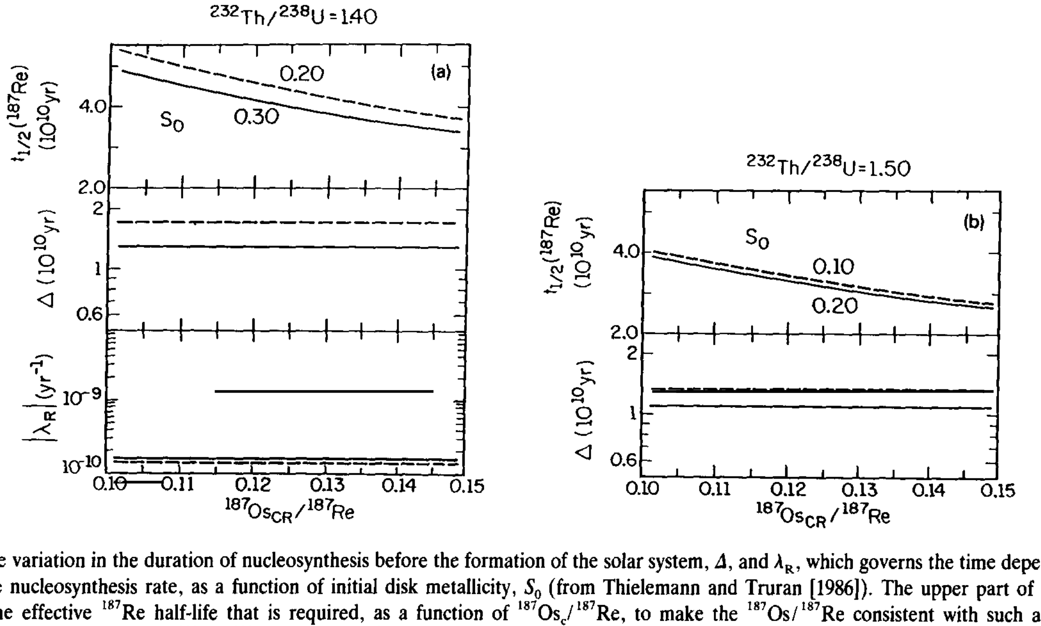

Fig. 7.5. The variation in the duration of nucleosynthesis before the formation of the solar system, Δ, and λ_R, which governs the time dependence of the effective nucleosynthesis rate, as a function of initial disk metallicity, S_0 (from Thielemann and Truran [1986]). The upper part of the figure illustrates the effective ^{187}Re half-life that is required, as a function of $^{187}\mathrm{Os_c}/^{187}\mathrm{Re}$, to make the $^{187}\mathrm{Os}/^{187}\mathrm{Re}$ consistent with such a solution. Assume a production ratio of (a) $^{232}\mathrm{Th}/^{238}\mathrm{U} = 1.40$; (b) $^{232}\mathrm{Th}/^{238}\mathrm{U} = 1.50$, illustrating that a larger production ratio requires shorter effective ^{187}Re half-lives (and also results in smaller galactic ages).

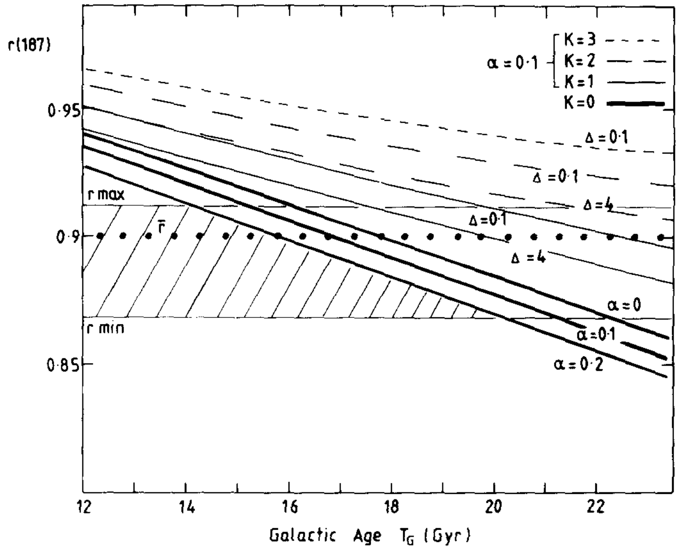

Fig. 7.6. The ^{187}Re remainder at $t = t_\odot$ for a range of galactic evolution model parameters, as a function of galactic age T_G (from Clayton [1988]). The results show that increased infall yields an increased galactic age. The horizontal band indicates the value of the remainder required by the abundances. The dotted line at $r(187) = 0.90$, based on the terrestrial decay rate $\lambda_\beta(187)$, suggests an age of T_G = 16–18 Gy for closed models, but much larger ages for models with infall.

include this effect in his family of analytic models, and finds, therefore, longer ages (see fig. 7.6). He states that only in evolution models without infall can galactic ages be as low as 10–12 Gy. With galactic infall (which he strongly argues for), he suggests a range of $14\,\mathrm{Gy} < t_G < 20\,\mathrm{Gy}$, with a most probable value of 16 Gy. Ultimately, to determine the effective beta-decay rate of this chronometer will require a detailed knowledge of the thermal history of ^{187}Re in stars.

7.2.2. *Rb and Sm chronology*

The long half-life of the isotope ^{87}Rb (see table 7.1) would seem to make it a good chronometer for estimating the age of the Galaxy. Unfortunately, this nucleus is produced by a combination of the s- and the r-process which makes it more difficult to use as a chronometer [Beer and Walter 1984]. Beer and Walter developed a formalism to separate the two different contributions to the production of ^{87}Rb, but uncertainties in the current data prevent a reliable decomposition of ^{87}Rb into the s- and r-process components. Improved cross sections and solar-abundance measurements will be needed before accurate age determinations can be made. In addition, Käppeler et al. [1989] note that the problem is further complicated by the likely enhancement of the stellar beta-decay rate for this isotope, as shown by Takahashi and Yokoi [1987].

^{147}Sm has the same problems as a chronometer that ^{87}Rb has. That is, ^{147}Sm, despite its very long half-life, is made by a combination of the s- and the r-processes. Furthermore, it is not possible at the present time to separate those contributions [Beer and Walter 1984].

7.2.3. *^{207}Pb/^{235}U and ^{206}Pb/^{238}U chronologies*

The principle of these chronologies has been explained in section 7.2. The essence again lies in the extraction of the cosmoradiogenic components $^{206,207}\mathrm{Pb}_c$ by subtracting the s- and r-process contributions. This is not an easy task. The s-process is rather complicated in this nuclear mass range where it terminates, so that its analysis requires rather accurate determinations of neutron-capture cross sections. At present these chronometers do not appear to give very reliable results. Using these chronometers, Clayton [1988] finds only ages larger than 20 Gy for the Galaxy. Beer [1990], however, with a new analysis of the s-process component, finds ages of $T_G > 12$ Gy to be acceptable.

7.2.4. *Th/Nd chronology*

Butcher [1987] has measured the strength of the Th and Nd lines in a sample of nearby (mostly dwarf) stars. He finds that the abundance ratio of Th/Nd is virtually the same in all of the stars regardless of age. Based on these results, he then argues that the lack of noticeable decay in Th with respect to Nd reflects a very young age for the Galaxy, and suggests an upper limit of 9.6 Gy. Mathews and Schramm [1988] argue that Butcher's age result is model-dependent and pointed out that Th is typically an r-process element while Nd is principally produced in the s-process. Using Butcher's data, Mathews and Schramm [1988] find a range of galactic ages for various chemical evolution models, with an upper limit of 20 Gy.

Clayton [1987] also suggests that an upper limit of 20 Gy for the Galaxy is not inconsistent with Butcher's data, and stresses the importance of properly treating the time rate of change of the s- and r-processes in determining the galactic age. In particular, there is the possibility that the s-process in thermally pulsating AGB stars behaves like a primary component. The same neutron flux from the $^{13}C(\alpha, n)$ source, but with a smaller amount of heavy neutron poisons in lower metallicity stars, will result in a larger irradiation and thus a larger ratio of s-process to r-process nuclei (i.e. Nd to Th) will occur during that period of galactic evolution. Clayton [1988] shows that the explicit inclusion of these s-process contributions in a model of chemical evolution leads to galactic ages older than suggested by Butcher [1987], see also fig. 7.7.

On the other hand, Fowler [1987b] and Malaney and Fowler [1989b], using a simple exponential

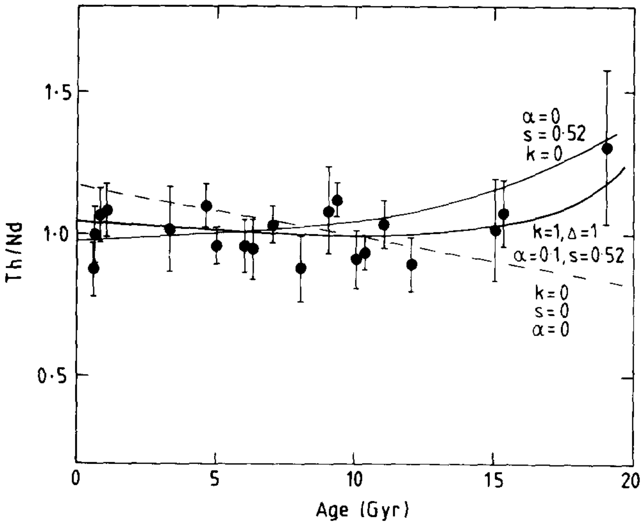

Fig. 7.7. Model fits from Clayton [1988] to the Th/Nd stellar data obtained by Butcher [1987]. The top curve ($\alpha = 0$), a closed model from Clayton [1987], assumes a secondary s-process production for Nd. The dashed line is for the same galactic evolution model but without a secondary contribution to Nd. The middle curve assumes moderate infall.

model that assumes an early spike in galactic nucleosynthesis, find an upper limit of 12 Gy using the Th/Nd data. They argue that the Butcher [1987] data, when interpreted within their cosmochronological model, confirm the relatively young galactic age of 10 Gy previously derived by Fowler and Meisl [1986] and Fowler [1987a].

Butcher [1988] also responds that the models of Clayton [1987] and Mathews and Schramm [1988], while adequately reproducing the Th/Nd data, are inconsistent with the Eu/Ba abundances [Butcher 1975] for some of the same stars. The Eu/Ba ratio is constant for all stars measured by Butcher [1975], which have metallicities in excess of 3% solar. Pagel [1989] uses these Eu/Ba ratios to derive the r-process ratio Th/Eu, and finds this ratio to be constant in all (11) of the stars for which both Th/Nd and Eu/Ba ratios have been measured. Pagel [1989] argues therefore that including the relative s-process contribution to Nd in the Th/Nd ratios, as suggested by Clayton [1987] and Mathews and Schramm [1988], will not lead to ages significantly longer than suggested by Butcher [1987]. In contrast, recent work by Malaney et al. [1989] suggests that the results of photofission of the actinides during normal stellar evolution will affect the abundance of Th. They argue, therefore, that the Th/Nd ratio will predict longer ages (up to 13 Gy) for the Galaxy than found by Butcher [1987].

There are still questions that need to be resolved in using the Th/Nd ratio as a chronometer. Butcher [1988] has pointed out the problem of identifying the Th line, noting the possibility of contamination with CoII. Butcher notes that a contamination of more than approximately 10% would make the Th line unusable as a chronometer. There is also still the question of how the galactic s-process and r-process nucleosynthesis histories will affect the age determination. Observations of very metal-poor halo stars (clearly very old stars with metallicities less than 3% solar) do show wide variations in the Eu/Ba ratio [Sneden and Parthasarathy 1983; Sneden and Pilachowski 1985; Gilroy et al. 1988]. These data indicate that the r-process occurred prior to the s-process (at least in the halo) early in the history of the Galaxy. These data also indicate that elements normally thought to be produced in the s-process, such as Ba and Nd, were first synthesized in the halo by the r-process [Truran 1981; Gilroy et al. 1988]. It is still not clear, however, how these metal-poor halo stars and their ages relate to the results of Butcher [1987] for disk stars. Observations of Th with respect to Eu or Nd in the halo stars would help greatly in determining the age of the Galaxy.

8. Summary and conclusions

The r-process is responsible for the production of roughly one half of all heavy elements beyond Fe. Its principal mechanism, as a fast neutron-capture process, running through highly unstable nuclei on the very neutron-rich side of the valley of stability, is well understood. The abundance peaks determine at which charge number, Z, the neutron magic numbers $N = 50$, 82 and 126 are encountered, as the long beta-decay half-lives (and correspondingly small neutron-capture cross sections) cause a bottleneck at these locations. While experimental data for nuclei actually in the r-process path are very scarce (essentially ^{80}Zn, ^{81,83}Ga, ^{130}Cd and ^{131,133}In), an increasing number of neutron-rich unstable nuclei are being produced at a variety of laboratories (CERN, GANIL, GSI, ILL, BNL, Studsvik). These new experimental data will provide more realistic extrapolations into unstable regions. Theoretical predictions of atomic masses, beta-decay half-lives, and fission barrier heights have also improved and seem to be giving consistently reliable results.

While constant improvements have been evident in nuclear physics, the astrophysical site of the r-process is still not clearly established. There are at least four possible r-process environments.

(1) A recently hypothesized primordial r-process in neutron-rich zones of inhomogeneous big bang scenarios. The most recent calculations show that, even if such scenarios exist, they would only produce a negligible contribution to the present solar-system r-process abundances.

(2) The outer shells of supernovae (He or C) or He-core flashes in low mass stars. In these cases, the neutrons are produced by (α, n)-reactions during the sudden temperature increase resulting from the supernova shocks or the helium core flashes. All present calculations show that for realistic stellar models, not enough neutrons are produced in these environments to allow an r-process which can reproduce the observed solar-system abundance pattern.

(3) Neutron-star collisions, where binary systems of neutron stars coalesce and cause the ejection of neutron-rich matter, which can then form r-process nuclei during the decompression phase. Detailed nucleosynthesis calculations of this scenario have not been performed as yet, and it is still not clear whether these collisions would occur often enough to provide for the total galactic r-process abundances.

(4) Ejection of highly neutronized matter from collapsed stellar cores during a type II supernova explosion. This could occur either in a spherical ring or in jets, if rotation (or magnetic fields) play an important part in the supernova mechanism. Observational and theoretical evidence indicates that this is a most promising site. One such piece of theoretical evidence that supernovae cores are a likely site comes from individual isotopic ratios in the observed r-process abundance curve. Using the most recent nuclear data, these features are most easily explained as the result of a freeze-out from an $(n, \gamma) \rightleftarrows (\gamma, n)$ equilibrium. This equilibrium only occurs in sites where high temperatures ($>10^9$ K) and neutron densities ($>10^{20}\,\mathrm{cm}^{-3}$) are encountered, such as in the cores of exploding supernovae. We note, however, that while this is a most promising site, a thorough understanding of the type II supernova explosion mechanism has not yet been achieved.

The observations of the heavy-element abundances in low-metallicity stars, as a function of [Fe/H] $[=\log_{10}(\mathrm{Fe/H})_{\mathrm{star}}/\log_{10}(\mathrm{Fe/H})_{\odot}]$, can be explained by constantly improving models of the chemical evolution of our Galaxy. Within the uncertainties, it seems possible to transform [Fe/H] into a timescale of galactic evolution. Several trends can be detected in the data. The observations of the most metal-poor halo stars, [Fe/H] = −2, indicate that the heavy elements in these stars were formed solely by the r-process very early in the history of the Galaxy. The stellar abundances further indicate that a change in $[x/\mathrm{Fe}]$ (x being O, Mg, Si, S, Ca) from ~0.3–0.5 to 0.0 (i.e., solar) occurs at approximately [Fe/H] = −1. This change can be interpreted as the result of the increased iron production from type Ia supernovae, which form from intermediate-mass binary systems and therefore begin to appear only after a long time delay. The trends in the data, when integrated within a framework of chemical evolution, can be used to constrain the site for the r-process. For example, the data seem to exclude single intermediate-mass stars as r-process production sites due to the long evolutionary delay. In other words, these stars could not contribute to r-process nucleosynthesis at very low metallicities, and presumably very early times in the history of the Galaxy.

Within the uncertainties of models of chemical evolution, coalescing neutron stars in binary systems also do not appear to fit the time-dependent behavior of the heavy-element data. The formation time for the neutron star and the long period required for gravitational radiation to shrink the binary orbit, both of which have to precede a neutron-star collision, seem to require too long a delay in the onset of r-process nucleosynthesis, although neutron-star pairs formed in highly eccentric orbits could shorten this delay time drastically. Sites like the outer shells of type II supernovae, where the neutron captures occur on heavy nuclei (produced in earlier generations of stars) already in these zones (i.e., secondary sites), would show a functional dependence of [r/Fe] increasing with the metallicity [Fe/H]. The rather constant behavior in the stellar data down to $[\mathrm{Fe/H}] = -2.5$ also seems to exclude these sites. (Other arguments, including a lack of sufficient neutrons in realistic stellar models, had earlier suggested these were not the site of the r-process.) Models assuming type II supernova sites (primary sites) do seem to fit the data, and the evidence points to the inner neutronized cores. It is hoped that the final emergence of a type II supernova mechanism will thus also provide an identification of this r-process site.

There is one further complication. Observations seem to show a downturn in $[r/\mathrm{Fe}]$ at about $[\mathrm{Fe/H}] = -2.7$. If additional high-quality observations continue to show this trend, it would support the contention that a delay is also required for the r-process production in galactic evolution. This would exclude the most massive type II supernovae, as r-process sites, and only stars less massive than about $11\ M_\odot$ would seem to be likely contributors. If there really exists some minimum lower level in the heavy element abundances for stars with very low metallicities ($[\mathrm{Fe/H}] \lesssim -3$), a primordial r-process contribution (inhomogeneous big bang) is not excluded.

The r-process also produces very long-lived nuclei like ^{187}Re, ^{232}Th, ^{238}U and ^{235}U, with half-lives ranging from several times 10^{10} y to 10^{8} y, and a few other nuclei with half-lives longer than 10^{7} y. The longest of these are comparable to the age of the Galaxy and can be utilized as galactic chronometers, i.e., to measure the duration of r-process nucleosynthesis in the Galaxy and therefore also provide a lower limit to the age of the universe. A knowledge of the production ratios of these isotopes in an r-process event, the time dependence of r-process nucleosynthesis in galactic evolution, and the isotopic ratios found in primitive meteorites (which do not show elemental fractionation) going back to the formation of the solar system, can be utilized to determine the time duration of nucleosynthesis in our Galaxy. This age determination has been performed mostly using very simple models of galactic evolution.

Recent galactic evolution models, however, have taken account of the observations of the light- and medium-mass elements. These models can also be utilized in age determinations employing the r-process chronometers, with the added benefit of automatically including astronomical constraints on the calculations. The calculated chronometric ages reflect the still remaining uncertainties in the predictions of production ratios from the r-process and our knowledge of galactic evolution. When beta-delayed fission was first introduced into r-process calculations, it caused a large change in the actinide production ratios. The improvement in mass formulae and fission barrier predictions makes its influence rather negligible now for the chronometer production ratios, but not for other effects such as fission cycling. Present chronometric age predictions for the Galaxy seem to lie mostly in the range of $12\text{–}15 \times 10^{9}$ y. Including all nuclear and galactic evolution uncertainties in the chronometric age determinations, the Galaxy could be as young as 10 Gy or as old as 20 Gy. These estimates fall in the same range as globular cluster ages or ages determined from cosmology.

We end by noting that there has been much recent progress in understanding the r-process, including recent observational and theoretical evidence that strongly reaffirms an association of the r-process with type II supernovae cores. An understanding of the r-process is, however, linked to many other subfields, including nuclear physics, stellar physics, stellar observations and the chemical evolution of galaxies. While progress has been significant in all of these fields, further improvement in our understanding of the r-process will require that our colleagues solve the type II supernova explosion problem and discover the mechanism that will then also lead to the ejection of this neutron-rich material into the interstellar medium.

Acknowledgements

This review spans a wide range of topics involved in the explanation of the r-process, including the nuclear physics input, the nucleosynthesis calculations, stellar models and supernova explosions, chemical evolution of galaxies, the observations of elemental abundances in low-metallicity stars, and the meteoritic-abundance determinations. It would not have been possible to write this paper without discussions, advice and communications, prior to publication, from many colleagues. In this regard, we wish to thank the following: J. Applegate, M. Arnould, G. Bazan, H. Beer, A.G.W. Cameron, D.D. Clayton, W.A. Fowler, W. Hillebrandt, R. Hoff, F. Käppeler, H.-V. Klapdor, K.-L. Kratz, J. Lattimer, G. Mathews, B. Meyer, P. Möller, B. Pagel, J.M. Pearson, D.N. Schramm, C. Sneden, K. Takahashi and M. Wiescher. This research was supported in part by NSF (at the University of Oklahoma, at Harvard University and at the University of Illinois), and by NASA (at Harvard University). We also thank the National Center for Supercomputing Applications at the University of Illinois for supplying computer time used in some of the calculations. J.J.C. thanks the University of Oklahoma Research Council for partial support.

Appendix. Neutron-capture cross sections

This appendix includes thermonuclear reaction rates $\langle \sigma v \rangle$, in $cm^3\,s^{-1}$, for neutron captures on nuclei included in the r-process network. These reaction rates were calculated with the code SMOKER [Thielemann et al. 1987, 1988]. The properties and parameters of this code have been discussed at length in sections 3.4 and 3.5. The rates given here can be regarded as independent of temperature, as long as s-waves dominate and the cross section, σ, behaves like $1/v$. In such a case, the resulting reaction rate is equal to the product $\sigma(E)v(E)$ at any bombarding energy and, therefore, independent of the energy at which it is evaluated. The calculations were made assuming an energy of 30 keV. The corresponding cross section is displayed in column 4 for nuclei of charge Z, mass number A and neutron number N.

It should be noted, however, that since the reaction rates were calculated at only one bombarding energy, they are therefore approximations to the actual rate values. This simplification, however, allowed us to perform cross-section calculations for several thousand nuclei, and the calculated values are reasonably accurate with an approximate uncertainty of only a factor of several. The mass formula used in these calculations is the one of Hilf et al. [1976], which predicts the neutron separation energy for cases where no experimental values exist. (See section 3.1 for further discussion regarding this mass formula.)

We add one additional word of caution. The cross sections in this table result from statistical model calculations, i.e., they reflect the contribution from resonances. For very neutron-rich nuclei, with small neutron separation energies, the contribution from resonances can be smaller than the cross section due to direct capture, particularly near closed shells. In those cases, the value given here is only a lower limit to the total cross section, and the direct capture contribution has to be added to obtain the correct rate (see, e.g., Mathews et al. [1983].)

We will make the following table available in electronic form to any interested parties. The code SMOKER has also been utilized to calculate charged-particle reaction rates for targets from $Z = 20$ to 36, for isotopes from the proton to neutron-drip line. A table of these rates is also available (from the second author) in electronic form.

Table A.1

Z	A	N	$\langle \sigma v \rangle$ (cm^3 s^{-1})
10	20	10	4.0142E − 19
10	21	11	1.0718E − 18
10	22	12	1.1241E − 19
10	23	13	2.2470E − 19
10	24	14	6.4091E − 20
10	25	15	2.2067E − 20
10	26	16	4.1490E − 21
10	27	17	2.3413E − 20
10	28	18	1.0296E − 23
10	29	19	5.5460E − 21
11	23	12	5.8481E − 19
11	24	13	4.5853E − 19
11	25	14	1.5965E − 19
11	26	15	1.8417E − 19
11	27	16	3.0161E − 20
11	28	17	2.2389E − 20
11	29	18	8.0200E − 21
11	30	19	2.4561E − 20
11	31	20	2.5891E − 20
11	32	21	6.8657E − 21
11	33	22	1.5399E − 20
11	34	23	4.9580E − 21
12	24	12	7.8413E − 19
12	25	13	1.8623E − 18
12	26	14	3.6911E − 19
12	27	15	4.6932E − 19
12	28	16	4.6947E − 20
12	29	17	6.8598E − 20
12	30	18	1.4640E − 20
12	31	19	4.9330E − 20
12	32	20	1.0340E − 20
12	33	21	2.7262E − 20
12	34	22	2.4696E − 21
12	35	23	1.4383E − 20
12	36	24	1.2254E − 23
12	37	25	6.7343E − 21
13	27	14	1.1650E − 18
13	28	15	1.6579E − 18
13	29	16	2.2784E − 19
13	30	17	3.5836E − 19
13	31	18	6.0373E − 20
13	32	19	1.4746E − 19
13	33	20	2.2184E − 20
13	34	21	8.1852E − 20
13	35	22	1.4641E − 20
13	36	23	6.7689E − 20
13	37	24	2.9670E − 21
13	38	25	3.3185E − 20
13	39	26	6.8578E − 22
13	40	27	1.0446E − 20
14	28	14	1.3055E − 18
14	29	15	1.8686E − 18
14	30	16	4.5688E − 19
14	31	17	5.5140E − 19
14	32	18	9.2638E − 20
14	33	19	1.5819E − 19
14	34	20	1.7306E − 20
14	35	21	9.4943E − 20
14	36	22	1.0320E − 20
14	37	23	5.5445E − 20
14	38	24	8.5238E − 21
14	39	25	5.3672E − 20
14	40	26	3.0633E − 21
14	41	27	1.7837E − 20
15	31	16	1.9942E − 18
15	32	17	3.8273E − 18
15	33	18	5.7470E − 19
15	34	19	1.6053E − 18
15	35	20	7.5454E − 20
15	36	21	2.9052E − 19
15	37	22	5.4688E − 20
15	38	23	1.7369E − 19
15	39	24	3.8527E − 20
15	40	25	2.5090E − 19
15	41	26	1.8901E − 20
15	42	27	8.2908E − 20
15	43	28	9.3295E − 23
15	44	29	6.4516E − 21
16	32	16	2.6095E − 18
16	33	17	3.4268E − 18
16	34	18	7.8743E − 19
16	35	19	1.0983E − 18
16	36	20	8.8214E − 20
16	37	21	4.5026E − 19
16	38	22	1.1506E − 19
16	39	23	4.3231E − 19
16	40	24	4.6594E − 20
16	41	25	1.6273E − 19
16	42	26	3.8188E − 20
16	43	27	1.0752E − 19
16	44	28	8.4766E − 22
16	45	29	1.1640E − 20
16	46	30	1.0077E − 23
16	47	31	3.6843E − 21
17	35	18	3.7467E − 18
17	36	19	6.7283E − 18
17	37	20	6.2592E − 19
17	38	21	2.6165E − 18
17	39	22	7.8755E − 19
17	40	23	2.3457E − 18
17	41	24	3.5487E − 19
17	42	25	6.0382E − 19
17	43	26	1.8734E − 19
17	44	27	4.7523E − 19
17	45	28	7.4782E − 21
17	46	29	6.9682E − 20
17	47	30	1.8240E − 21
17	48	31	2.7237E − 20
17	49	32	1.3560E − 22
17	50	33	8.9486E − 21
18	36	18	3.6984E − 18
18	37	19	2.7549E − 18
18	38	20	6.4356E − 19
18	39	21	2.3499E − 18
18	40	22	7.7738E − 19
18	41	23	1.8339E − 18
18	42	24	5.4911E − 19
18	43	25	1.0353E − 18
18	44	26	1.9307E − 19
18	45	27	2.1784E − 19
18	46	28	1.9234E − 20
18	47	29	9.2197E − 20
18	48	30	7.1173E − 21
18	49	31	3.7698E − 20
18	50	32	1.2089E − 21
18	51	33	1.4786E − 20
18	52	34	3.1136E − 23
18	53	35	4.5601E − 21
19	39	20	3.6158E − 18
19	40	21	7.6447E − 18
19	41	22	5.1413E − 18
19	42	23	1.2677E − 17
19	43	24	3.8263E − 18
19	44	25	5.7047E − 18
19	45	26	1.2873E − 18
19	46	27	1.9469E − 18
19	47	28	1.6759E − 19
19	48	29	1.0097E − 18
19	49	30	4.1223E − 20
19	50	31	2.2899E − 19
19	51	32	1.2310E − 20
19	52	33	1.0472E − 19
19	53	34	2.3183E − 21
19	54	35	4.0332E − 20
19	55	36	1.8363E − 22
19	56	37	1.1276E − 20
19	57	38	4.0892E − 26
19	58	39	4.6413E − 21
20	40	20	3.6939E − 18
20	41	21	1.0943E − 17
20	42	22	4.3608E − 18
20	43	23	1.2089E − 17
20	44	24	2.2025E − 18
20	45	25	5.2608E − 18
20	46	26	9.4339E − 19

Table A.1 (cont.)

Z	A	N	$\langle \sigma v \rangle$ (cm^3 s^{-1})
20	47	27	8.1202E − 19
20	48	28	1.6587E − 19
20	49	29	2.2907E − 19
20	50	30	2.3764E − 19
20	51	31	2.8935E − 19
20	52	32	2.9800E − 20
20	53	33	1.3315E − 19
20	54	34	8.5088E − 21
20	55	35	5.3901E − 20
20	56	36	1.4265E − 21
20	57	37	1.9522E − 20
20	58	38	9.4473E − 23
20	59	39	9.4126E − 21
21	45	24	1.4218E − 17
21	46	25	2.0291E − 17
21	47	26	5.1453E − 18
21	48	27	1.9868E − 18
21	49	28	7.0086E − 19
21	50	29	5.3635E − 19
21	51	30	4.1243E − 19
21	52	31	1.4556E − 18
21	53	32	1.6413E − 19
21	54	33	7.7107E − 19
21	55	34	6.3512E − 20
21	56	35	3.4106E − 19
21	57	36	1.7590E − 20
21	58	37	1.6787E − 19
21	59	38	4.5443E − 21
21	60	39	8.3739E − 20
21	61	40	7.0257E − 22
21	62	41	3.3733E − 20
21	63	42	4.5890E − 23
21	64	43	1.1871E − 20
22	46	24	8.3277E − 18
22	47	25	2.2252E − 17
22	48	26	3.1102E − 18
22	49	27	5.4050E − 18
22	50	28	8.2993E − 19
22	51	29	1.4212E − 18
22	52	30	7.6615E − 19
22	53	31	5.2569E − 19
22	54	32	2.4799E − 19
22	55	33	8.9470E − 19
22	56	34	1.0824E − 19
22	57	35	4.4649E − 19
22	58	36	3.5376E − 20
22	59	37	1.9420E − 19
22	60	38	1.1176E − 20
22	61	39	1.0050E − 19
22	62	40	2.8670E − 21
22	63	41	4.3180E − 20
22	64	42	5.4868E − 22
22	65	43	1.6157E − 20
22	66	44	2.0417E − 23
22	67	45	5.5588E − 21
22	68	46	1.6737E − 23
22	69	47	4.6478E − 21
22	70	48	9.2188E − 26
22	71	49	1.6747E − 21
23	50	27	7.9695E − 18
23	51	28	3.3439E − 18
23	52	29	4.9116E − 18
23	53	30	1.8456E − 18
23	54	31	3.3590E − 18
23	55	32	8.0443E − 19
23	56	33	3.9702E − 18
23	57	34	5.9333E − 19
23	58	35	2.4121E − 18
23	59	36	2.5085E − 19
23	60	37	1.3400E − 18
23	61	38	9.4139E − 20
23	62	39	6.1392E − 19
23	63	40	2.7162E − 20
23	64	41	2.8834E − 19
23	65	42	8.2895E − 21
23	66	43	1.2368E − 19
23	67	44	2.1346E − 21
23	68	45	7.3171E − 20
23	69	46	1.8916E − 21
23	70	47	4.9075E − 20
23	71	48	4.3771E − 22
23	72	49	9.6436E − 21
24	50	26	7.6007E − 18
24	51	27	1.5756E − 17
24	52	28	3.4333E − 18
24	53	29	6.7674E − 18
24	54	30	2.1128E − 18
24	55	31	2.9897E − 18
24	56	32	1.2087E − 18
24	57	33	1.8371E − 18
24	58	34	6.4778E − 19
24	59	35	2.3001E − 18
24	60	36	3.0283E − 19
24	61	37	1.1959E − 18
24	62	38	1.1761E − 19
24	63	39	5.5774E − 19
24	64	40	4.0582E − 20
24	65	41	2.9210E − 19
24	66	42	1.7831E − 20
24	67	43	1.4012E − 19
24	68	44	6.9587E − 21
24	69	45	8.5060E − 20
24	70	46	5.4776E − 21
24	71	47	5.2105E − 20
24	72	48	1.9198E − 21
24	73	49	1.1180E − 20
25	55	30	6.7716E − 18
25	56	31	9.0925E − 18
25	57	32	4.1654E − 18
25	58	33	6.6327E − 18
25	59	34	2.3869E − 18
25	60	35	8.4280E − 18
25	61	36	1.4850E − 18
25	62	37	5.2719E − 18
25	63	38	6.8941E − 19
25	64	39	3.1671E − 18
25	65	40	2.6772E − 19
25	66	41	1.6030E − 18
25	67	42	1.4717E − 19
25	68	43	9.9503E − 19
25	69	44	8.0542E − 20
25	70	45	6.9400E − 19
25	71	46	4.2233E − 20
25	72	47	3.0818E − 19
25	73	48	1.0953E − 20
25	74	49	7.4597E − 20
26	54	28	8.5909E − 18
26	55	29	1.9220E − 17
26	56	30	5.8537E − 18
26	57	31	6.9966E − 18
26	58	32	3.3265E − 18
26	59	33	6.1292E − 18
26	60	34	1.5621E − 18
26	61	35	4.1025E − 18
26	62	36	5.2583E − 19
26	63	37	3.9567E − 18
26	64	38	6.2312E − 19
26	65	39	2.2861E − 18
26	66	40	2.4528E − 19
26	67	41	1.4529E − 18
26	68	42	1.7607E − 19
26	69	43	9.2427E − 19
26	70	44	1.1086E − 19
26	71	45	5.8345E − 19
26	72	46	5.7000E − 20
26	73	47	2.4894E − 19
26	74	48	2.1357E − 20
26	75	49	5.5573E − 20
27	59	32	8.8388E − 18
27	60	33	1.2950E − 17
27	61	34	5.1602E − 18
27	62	35	1.2695E − 17
27	63	36	3.5234E − 18
27	64	37	7.5455E − 18
27	65	38	2.4824E − 18
27	66	39	8.2851E − 18
27	67	40	1.2513E − 18
27	68	41	5.7785E − 18
27	69	42	9.7677E − 19

Table A.1 (cont.)

Z	A	N	$\langle \sigma v \rangle$ (cm^3 s^{-1})	Z	A	N	$\langle \sigma v \rangle$ (cm^3 s^{-1})	Z	A	N	$\langle \sigma v \rangle$ (cm^3 s^{-1})
27	70	43	4.3451E − 18	29	83	54	1.6105E − 22	31	88	57	2.2108E − 19
27	71	44	5.8839E − 19	29	84	55	2.1392E − 20	31	89	58	4.3618E − 21
27	72	45	2.4575E − 18	29	85	56	1.6670E − 22	31	90	59	8.7019E − 20
27	73	46	2.8137E − 19	29	86	57	2.4414E − 20	31	91	60	7.1275E − 22
27	74	47	1.2089E − 18	29	87	58	2.6528E − 23	31	92	61	3.0307E − 20
27	75	48	7.8167E − 20	29	88	59	1.0330E − 20	31	93	62	3.5406E − 23
27	76	49	2.7273E − 19					31	94	63	9.1974E − 21
27	77	50	6.5938E − 24	30	64	34	1.1926E − 17				
27	78	51	6.1725E − 21	30	65	35	5.3772E − 17	32	70	38	1.5125E − 17
				30	66	36	7.0742E − 18	32	71	39	8.8431E − 17
28	58	30	1.0421E − 17	30	67	37	4.2082E − 17	32	72	40	1.0872E − 17
28	59	31	2.2353E − 17	30	68	38	5.3230E − 18	32	73	41	7.5796E − 17
28	60	32	6.3597E − 18	30	69	39	2.1498E − 17	32	74	42	8.4927E − 18
28	61	33	1.8512E − 17	30	70	40	3.8944E − 18	32	75	43	4.6027E − 17
28	62	34	3.9420E − 18	30	71	41	2.1062E − 17	32	76	44	6.6710E − 18
28	63	35	1.0730E − 17	30	72	42	2.3282E − 18	32	77	45	2.6081E − 17
28	64	36	2.3879E − 18	30	73	43	1.4189E − 17	32	78	46	3.0140E − 18
28	65	37	7.7916E − 18	30	74	44	1.5881E − 18	32	79	47	7.1236E − 18
28	66	38	2.0501E − 18	30	75	45	6.9616E − 18	32	80	48	6.7343E − 19
28	67	39	4.1078E − 18	30	76	46	6.4710E − 19	32	81	49	1.0099E − 18
28	68	40	1.2030E − 18	30	77	47	2.3189E − 18	32	82	50	1.9703E − 19
28	69	41	3.8285E − 18	30	78	48	4.2577E − 19	32	83	51	3.1418E − 19
28	70	42	6.8917E − 19	30	79	49	8.7420E − 19	32	84	52	3.4818E − 20
28	71	43	2.7720E − 18	30	80	50	4.9642E − 21	32	85	53	2.8257E − 19
28	72	44	4.4341E − 19	30	81	51	5.4260E − 20	32	86	54	2.6969E − 20
28	73	45	1.6757E − 18	30	82	52	2.8402E − 21	32	87	55	3.6536E − 19
28	74	46	2.5360E − 19	30	83	53	3.8580E − 20	32	88	56	3.1970E − 20
28	75	47	8.2112E − 19	30	84	54	9.4210E − 22	32	89	57	2.0536E − 19
28	76	48	1.0031E − 19	30	85	55	3.6308E − 20	32	90	58	1.4577E − 20
28	77	49	1.2061E − 19	30	86	56	1.7328E − 21	32	91	59	8.4262E − 20
28	78	50	1.3771E − 22	30	87	57	3.5366E − 20	32	92	60	4.4447E − 21
28	79	51	5.2371E − 21	30	88	58	5.4889E − 22	32	93	61	3.0911E − 20
28	80	52	6.4027E − 24	30	89	59	1.3954E − 20	32	94	62	6.8921E − 22
28	81	53	3.5614E − 21	30	90	60	1.6808E − 23	32	95	63	1.0988E − 20
				30	91	61	4.8589E − 21	32	96	64	1.4155E − 23
29	63	34	1.8021E − 17					32	97	65	3.7546E − 21
29	64	35	3.4908E − 17	31	69	38	3.5190E − 17				
29	65	36	1.1059E − 17	31	70	39	6.8791E − 17	33	75	42	4.7732E − 17
29	66	37	2.9300E − 17	31	71	40	1.7475E − 17	33	76	43	1.5052E − 16
29	67	38	7.2277E − 18	31	72	41	7.6983E − 17	33	77	44	4.2831E − 17
29	68	39	1.9448E − 17	31	73	42	1.8281E − 17	33	78	45	8.6357E − 17
29	69	40	3.4687E − 18	31	74	43	5.6084E − 17	33	79	46	1.9014E − 17
29	70	41	1.8488E − 17	31	75	44	1.1587E − 17	33	80	47	3.2405E − 17
29	71	42	4.0738E − 18	31	76	45	3.0996E − 17	33	81	48	2.6310E − 18
29	72	43	1.4886E − 17	31	77	46	2.9173E − 18	33	82	49	8.3525E − 18
29	73	44	2.5972E − 18	31	78	47	1.0180E − 17	33	83	50	4.6409E − 19
29	74	45	8.6396E − 18	31	79	48	6.9092E − 19	33	84	51	2.4084E − 18
29	75	46	1.3340E − 18	31	80	49	1.8506E − 18	33	85	52	2.4309E − 19
29	76	47	4.3891E − 18	31	81	50	2.3476E − 20	33	86	53	1.9864E − 18
29	77	48	4.0057E − 19	31	82	51	3.9344E − 19	33	87	54	2.4346E − 19
29	78	49	1.0420E − 18	31	83	52	2.3784E − 20	33	88	55	2.2956E − 18
29	79	50	1.7712E − 21	31	84	53	3.2557E − 19	33	89	56	1.7095E − 19
29	80	51	5.5719E − 20	31	85	54	1.4962E − 20	33	90	57	1.2091E − 18
29	81	52	7.6239E − 22	31	86	55	3.7352E − 19	33	91	58	5.7879E − 20
29	82	53	3.5662E − 20	31	87	56	1.6087E − 20	33	92	59	5.0683E − 19

Table A.1 (cont.)

Z	A	N	$\langle\sigma v\rangle$ (cm^3 s^{-1})
33	93	60	1.5398E − 20
33	94	61	1.9656E − 19
33	95	62	3.3056E − 21
33	96	63	7.2910E − 20
33	97	64	4.9017E − 22
33	98	65	2.5589E − 20
33	99	66	2.2285E − 23
33	100	67	8.0474E − 21
34	74	40	3.5511E − 17
34	75	41	1.7794E − 16
34	76	42	2.3465E − 17
34	77	43	1.1825E − 16
34	78	44	1.9560E − 17
34	79	45	1.0180E − 16
34	80	46	1.0014E − 17
34	81	47	2.9946E − 17
34	82	48	1.5839E − 18
34	83	49	6.2786E − 18
34	84	50	4.0023E − 19
34	85	51	1.6941E − 18
34	86	52	7.2760E − 19
34	87	53	1.5930E − 18
34	88	54	2.0729E − 19
34	89	55	1.6981E − 18
34	90	56	1.7834E − 19
34	91	57	9.1260E − 19
34	92	58	9.4004E − 20
34	93	59	3.9905E − 19
34	94	60	4.1172E − 20
34	95	61	1.6911E − 19
34	96	62	1.4511E − 20
34	97	63	6.9756E − 20
34	98	64	3.6166E − 21
34	99	65	2.6597E − 20
34	100	66	4.7833E − 22
34	101	67	9.6319E − 21
34	102	68	6.1032E − 24
34	103	69	3.2858E − 21
35	79	44	1.1285E − 16
35	80	45	2.0100E − 16
35	81	46	5.6893E − 17
35	82	47	1.0154E − 16
35	83	48	1.2129E − 17
35	84	49	2.6436E − 17
35	85	50	1.7714E − 18
35	86	51	7.1579E − 18
35	87	52	4.3723E − 18
35	88	53	6.8296E − 18
35	89	54	1.2697E − 18
35	90	55	1.0500E − 17
35	91	56	1.0076E − 18
35	92	57	5.5499E − 18
35	93	58	4.1225E − 19
35	94	59	2.4548E − 18
35	95	60	1.4860E − 19
35	96	61	1.0422E − 18
35	97	62	4.7257E − 20
35	98	63	4.3245E − 19
35	99	64	1.3006E − 20
35	100	65	1.7132E − 19
35	101	66	2.8323E − 21
35	102	67	6.5083E − 20
35	103	68	4.5745E − 22
35	104	69	2.3184E − 20
35	105	70	1.3511E − 23
35	106	71	7.4571E − 21
36	78	42	6.8786E − 17
36	79	43	2.4580E − 16
36	80	44	5.6568E − 17
36	81	45	2.2836E − 16
36	82	46	2.4500E − 17
36	83	47	9.3481E − 17
36	84	48	7.3095E − 18
36	85	49	2.4829E − 17
36	86	50	1.5642E − 18
36	87	51	5.6847E − 18
36	88	52	2.3111E − 18
36	89	53	4.1452E − 18
36	90	54	1.2424E − 18
36	91	55	9.6593E − 19
36	92	56	3.0839E − 19
36	93	57	3.5411E − 18
36	94	58	3.7452E − 19
36	95	59	1.7517E − 18
36	96	60	1.7772E − 19
36	97	61	7.8092E − 19
36	98	62	7.9050E − 20
36	99	63	3.4703E − 19
36	100	64	3.1496E − 20
36	101	65	1.5156E − 19
36	102	66	1.0530E − 20
36	103	67	6.2323E − 20
36	104	68	2.6089E − 21
36	105	69	2.4150E − 20
36	106	70	3.2802E − 22
36	107	71	8.7766E − 21
36	108	72	2.8784E − 24
36	109	73	3.0747E − 21
37	85	48	7.4813E − 17
37	86	49	6.7621E − 17
37	87	50	7.0414E − 18
37	88	51	1.9987E − 17
37	89	52	1.3407E − 17
37	90	53	1.8609E − 17
37	91	54	9.5997E − 18
37	92	55	9.6635E − 18
37	93	56	1.3810E − 18
37	94	57	3.4532E − 18
37	95	58	4.3056E − 19
37	96	59	2.5488E − 18
37	97	60	8.7805E − 19
37	98	61	1.5452E − 18
37	99	62	3.5232E − 19
37	100	63	2.1088E − 18
37	101	64	1.2914E − 19
37	102	65	9.2559E − 19
37	103	66	4.1252E − 20
37	104	67	3.9829E − 19
37	105	68	1.1229E − 20
37	106	69	1.6324E − 19
37	107	70	2.3993E − 21
37	108	71	6.4079E − 20
37	109	72	3.8459E − 22
37	110	73	2.3910E − 20
37	111	74	1.2331E − 23
37	112	75	8.6406E − 21
38	84	46	6.1222E − 17
38	85	47	2.0887E − 16
38	86	48	2.6537E − 17
38	87	49	7.7457E − 17
38	88	50	3.4310E − 18
38	89	51	1.4160E − 17
38	90	52	6.0904E − 18
38	91	53	1.8666E − 17
38	92	54	4.4350E − 18
38	93	55	9.0649E − 18
38	94	56	1.0499E − 18
38	95	57	2.2315E − 18
38	96	58	5.9827E − 19
38	97	59	2.0951E − 18
38	98	60	4.1815E − 19
38	99	61	2.0225E − 18
38	100	62	3.0984E − 19
38	101	63	1.4789E − 18
38	102	64	1.4267E − 19
38	103	65	6.8457E − 19
38	104	66	6.3058E − 20
38	105	67	3.1601E − 19
38	106	68	2.5152E − 20
38	107	69	1.4189E − 19
38	108	70	8.4470E − 21
38	109	71	6.0321E − 20
38	110	72	2.1774E − 21
38	111	73	2.4375E − 20
38	112	74	3.2460E − 22
38	113	75	9.7877E − 21
38	114	76	1.1981E − 23
38	115	77	4.5160E − 21
38	116	78	2.7397E − 25
38	117	79	2.9283E − 21

Table A.1 (cont.)

Z	A	N	$\langle \sigma v \rangle$ (cm^3 s^{-1})
39	89	50	1.2158E − 17
39	90	51	4.4914E − 17
39	91	52	3.1163E − 17
39	92	53	5.9583E − 17
39	93	54	4.5251E − 17
39	94	55	4.8400E − 17
39	95	56	8.4723E − 18
39	96	57	1.1720E − 17
39	97	58	1.8994E − 18
39	98	59	6.6854E − 18
39	99	60	3.3600E − 18
39	100	61	6.9200E − 18
39	101	62	1.8440E − 18
39	102	63	9.2036E − 18
39	103	64	7.7639E − 19
39	104	65	4.3470E − 18
39	105	66	3.1694E − 19
39	106	67	2.0365E − 18
39	107	68	1.2082E − 19
39	108	69	9.4189E − 19
39	109	70	4.0035E − 20
39	110	71	4.2851E − 19
39	111	72	1.1562E − 20
39	112	73	1.8931E − 19
39	113	74	2.8963E − 21
39	114	75	8.6237E − 20
39	115	76	8.2363E − 22
39	116	77	4.6982E − 20
39	117	78	6.1422E − 22
39	118	79	2.8341E − 20
39	119	80	7.4513E − 23
39	120	81	5.2376E − 21
40	90	50	8.1998E − 18
40	91	51	3.6453E − 17
40	92	52	1.7922E − 17
40	93	53	4.7273E − 17
40	94	54	2.3292E − 17
40	95	55	5.1221E − 17
40	96	56	6.9160E − 18
40	97	57	5.3773E − 18
40	98	58	1.6282E − 18
40	99	59	1.0918E − 17
40	100	60	1.4810E − 18
40	101	61	9.0356E − 18
40	102	62	5.8931E − 19
40	103	63	6.1018E − 18
40	104	64	5.7078E − 19
40	105	65	2.9136E − 18
40	106	66	2.7154E − 19
40	107	67	1.4124E − 18
40	108	68	1.2766E − 19
40	109	69	6.8800E − 19
40	110	70	5.7856E − 20
40	111	71	3.3476E − 19
40	112	72	2.4293E − 20
40	113	73	1.6147E − 19
40	114	74	9.4003E − 21
40	115	75	8.0057E − 20
40	116	76	3.9068E − 21
40	117	77	4.9856E − 20
40	118	78	3.4341E − 21
40	119	79	2.1716E − 20
40	120	80	5.8914E − 22
40	121	81	5.1650E − 21
41	93	52	7.9180E − 17
41	94	53	1.3682E − 16
41	95	54	1.1014E − 16
41	96	55	1.8198E − 16
41	97	56	4.8618E − 17
41	98	57	4.1630E − 17
41	99	58	2.7000E − 17
41	100	59	4.9845E − 17
41	101	60	1.7717E − 17
41	102	61	3.9969E − 17
41	103	62	6.2991E − 18
41	104	63	2.3106E − 17
41	105	64	3.7768E − 18
41	106	65	1.7753E − 17
41	107	66	1.7107E − 18
41	108	67	9.0968E − 18
41	109	68	7.6745E − 19
41	110	69	4.6665E − 18
41	111	70	3.3591E − 19
41	112	71	2.3817E − 18
41	113	72	1.4083E − 19
41	114	73	1.2443E − 18
41	115	74	5.7265E − 20
41	116	75	7.1764E − 19
41	117	76	3.2617E − 20
41	118	77	5.8311E − 19
41	119	78	2.2508E − 20
41	120	79	1.6375E − 19
41	121	80	2.7408E − 21
41	122	81	3.3456E − 20
42	92	50	2.3040E − 17
42	93	51	1.0096E − 16
42	94	52	3.6548E − 17
42	95	53	1.2859E − 16
42	96	54	3.9095E − 17
42	97	55	1.4833E − 16
42	98	56	1.9792E − 17
42	99	57	8.0409E − 17
42	100	58	6.8441E − 18
42	101	59	3.5106E − 17
42	102	60	4.0848E − 18
42	103	61	4.9121E − 17
42	104	62	2.2038E − 18
42	105	63	2.3938E − 17
42	106	64	9.5677E − 19
42	107	65	1.1424E − 17
42	108	66	1.0889E − 18
42	109	67	5.8785E − 18
42	110	68	5.4179E − 19
42	111	69	3.0159E − 18
42	112	70	2.7114E − 19
42	113	71	1.6035E − 18
42	114	72	1.3708E − 19
42	115	73	8.8260E − 19
42	116	74	7.2572E − 20
42	117	75	5.3454E − 19
42	118	76	5.1032E − 20
42	119	77	4.0018E − 19
42	120	78	2.8080E − 20
42	121	79	1.1090E − 19
42	122	80	7.1607E − 21
42	123	81	2.5015E − 20
43	97	54	1.5259E − 16
43	98	55	3.4987E − 16
43	99	56	1.6907E − 16
43	100	57	2.5364E − 16
43	101	58	5.8578E − 17
43	102	59	1.4531E − 16
43	103	60	4.4068E − 17
43	104	61	1.1812E − 16
43	105	62	2.1893E − 17
43	106	63	8.4185E − 17
43	107	64	1.1631E − 17
43	108	65	5.7360E − 17
43	109	66	7.9505E − 18
43	110	67	3.4213E − 17
43	111	68	3.9667E − 18
43	112	69	1.9965E − 17
43	113	70	1.9959E − 18
43	114	71	1.1518E − 17
43	115	72	1.0445E − 18
43	116	73	7.3630E − 18
43	117	74	6.4155E − 19
43	118	75	6.2587E − 18
43	119	76	4.8497E − 19
43	120	77	2.9478E − 18
43	121	78	1.6256E − 19
43	122	79	7.1563E − 19
43	123	80	2.3453E − 20
43	124	81	1.4572E − 19
43	125	82	3.5942E − 24
43	126	83	4.8554E − 21
44	96	52	6.4236E − 17
44	97	53	2.6449E − 16
44	98	54	6.5720E − 17
44	99	55	3.2124E − 16

Table A.1 (cont.)

Z	A	N	$\langle \sigma v \rangle$ (cm^3 s^{-1})
44	100	56	5.6199E − 17
44	101	57	3.5139E − 16
44	102	58	3.4492E − 17
44	103	59	1.2667E − 16
44	104	60	1.6871E − 17
44	105	61	8.7015E − 17
44	106	62	7.7575E − 18
44	107	63	6.6891E − 17
44	108	64	5.3344E − 18
44	109	65	3.9993E − 17
44	110	66	2.5544E − 18
44	111	67	2.3431E − 17
44	112	68	2.3123E − 18
44	113	69	1.3237E − 17
44	114	70	1.2478E − 18
44	115	71	7.9261E − 18
44	116	72	7.1508E − 19
44	117	73	5.2716E − 18
44	118	74	5.2469E − 19
44	119	75	3.8426E − 18
44	120	76	2.8008E − 19
44	121	77	1.4556E − 18
44	122	78	1.1967E − 19
44	123	79	4.0821E − 19
44	124	80	3.4152E − 20
44	125	81	9.0478E − 20
44	126	82	7.3555E − 23
44	127	83	4.6946E − 21
44	128	84	3.3508E − 24
44	129	85	2.0973E − 21
45	103	58	1.9185E − 16
45	104	59	3.5776E − 16
45	105	60	1.2078E − 16
45	106	61	2.2098E − 16
45	107	62	8.3760E − 17
45	108	63	1.7147E − 16
45	109	64	6.0256E − 17
45	110	65	1.1333E − 16
45	111	66	2.7425E − 17
45	112	67	9.3355E − 17
45	113	68	1.8412E − 17
45	114	69	7.0294E − 17
45	115	70	1.1150E − 17
45	116	71	5.1364E − 17
45	117	72	7.8052E − 18
45	118	73	4.6050E − 17
45	119	74	4.9296E − 18
45	120	75	2.2342E − 17
45	121	76	1.8250E − 18
45	122	77	8.7754E − 18
45	123	78	6.8501E − 19
45	124	79	2.2922E − 18
45	125	80	1.1228E − 19
45	126	81	4.8972E − 19
45	127	82	8.4757E − 22
45	128	83	3.4325E − 20
45	129	84	2.4479E − 22
45	130	85	1.8266E − 20
45	131	86	4.0793E − 23
45	132	87	1.3069E − 20
45	133	88	3.2196E − 23
45	134	89	1.8003E − 20
45	135	90	7.5794E − 24
45	136	91	8.6781E − 21
46	102	56	1.0378E − 16
46	103	57	4.3769E − 16
46	104	58	8.7217E − 17
46	105	59	4.1184E − 16
46	106	60	5.6891E − 17
46	107	61	2.6131E − 16
46	108	62	2.9293E − 17
46	109	63	1.8329E − 16
46	110	64	1.6224E − 17
46	111	65	1.3398E − 16
46	112	66	1.0451E − 17
46	113	67	9.4616E − 17
46	114	68	6.4952E − 18
46	115	69	7.4628E − 17
46	116	70	6.8749E − 18
46	117	71	4.2057E − 17
46	118	72	4.3653E − 18
46	119	73	2.4360E − 17
46	120	74	1.9862E − 18
46	121	75	1.0184E − 17
46	122	76	8.4752E − 19
46	123	77	4.0328E − 18
46	124	78	3.8831E − 19
46	125	79	1.1382E − 18
46	126	80	1.1050E − 19
46	127	81	2.5413E − 19
46	128	82	2.1993E − 21
46	129	83	2.2616E − 20
46	130	84	1.1465E − 21
46	131	85	1.2472E − 20
46	132	86	3.5746E − 22
46	133	87	8.7972E − 21
46	134	88	5.1422E − 23
46	135	89	1.0918E − 20
46	136	90	8.0589E − 23
46	137	91	7.0650E − 21
46	138	92	3.2006E − 24
46	139	93	3.1261E − 21
47	107	60	2.0034E − 16
47	108	61	4.4426E − 16
47	109	62	1.6436E − 16
47	110	63	2.8547E − 16
47	111	64	1.0014E − 16
47	112	65	2.7118E − 16
47	113	66	6.4682E − 17
47	114	67	1.9772E − 16
47	115	68	5.7606E − 17
47	116	69	1.9786E − 16
47	117	70	3.2361E − 17
47	118	71	1.2001E − 16
47	119	72	2.7355E − 17
47	120	73	7.8451E − 17
47	121	74	1.1846E − 17
47	122	75	4.2643E − 17
47	123	76	4.8139E − 18
47	124	77	1.8913E − 17
47	125	78	2.0059E − 18
47	126	79	5.3588E − 18
47	127	80	3.4278E − 19
47	128	81	1.2161E − 18
47	129	82	7.6978E − 21
47	130	83	1.4701E − 19
47	131	84	5.2689E − 21
47	132	85	9.2071E − 20
47	133	86	3.0086E − 21
47	134	87	8.2627E − 20
47	135	88	1.0354E − 21
47	136	89	4.8576E − 20
47	137	90	5.0146E − 22
47	138	91	4.6556E − 20
47	139	92	2.0235E − 22
47	140	93	2.1660E − 20
47	141	94	9.7541E − 24
47	142	95	8.2212E − 21
48	106	58	1.2229E − 16
48	107	59	4.3055E − 16
48	108	60	9.5334E − 17
48	109	61	3.9394E − 16
48	110	62	7.9306E − 17
48	111	63	2.6485E − 16
48	112	64	5.5145E − 17
48	113	65	2.1788E − 16
48	114	66	3.7783E − 17
48	115	67	1.6961E − 16
48	116	68	2.2073E − 17
48	117	69	1.2335E − 16
48	118	70	1.0131E − 17
48	119	71	7.8053E − 17
48	120	72	5.5188E − 18
48	121	73	5.5291E − 17
48	122	74	3.0930E − 18
48	123	75	1.9508E − 17
48	124	76	2.0549E − 18
48	125	77	8.3877E − 18
48	126	78	1.0056E − 18
48	127	79	2.4373E − 18
48	128	80	2.8411E − 19

Table A.1 (cont.)

Z	A	N	$\langle \sigma v \rangle$ (cm^3 s^{-1})
48	129	81	5.8357E − 19
48	130	82	1.2998E − 20
48	131	83	7.9038E − 20
48	132	84	9.7007E − 21
48	133	85	5.6324E − 20
48	134	86	5.5455E − 21
48	135	87	4.8068E − 20
48	136	88	2.5013E − 21
48	137	89	3.0108E − 20
48	138	90	9.0896E − 22
48	139	91	1.5906E − 20
48	140	92	4.8893E − 22
48	141	93	1.6009E − 20
48	142	94	1.2486E − 22
48	143	95	7.0437E − 21
48	144	96	1.9973E − 24
48	145	97	2.7895E − 21
49	113	64	1.9098E − 16
49	114	65	2.8914E − 16
49	115	66	1.3217E − 16
49	116	67	2.4487E − 16
49	117	68	1.0539E − 16
49	118	69	1.7815E − 16
49	119	70	6.0862E − 17
49	120	71	1.6500E − 16
49	121	72	3.4759E − 17
49	122	73	1.2130E − 16
49	123	74	2.4276E − 17
49	124	75	6.3747E − 17
49	125	76	1.2746E − 17
49	126	77	3.9671E − 17
49	127	78	5.5714E − 18
49	128	79	1.4555E − 17
49	129	80	1.8341E − 18
49	130	81	4.5842E − 18
49	131	82	2.8412E − 20
49	132	83	3.1019E − 19
49	133	84	2.8803E − 20
49	134	85	2.3245E − 19
49	135	86	2.3594E − 20
49	136	87	2.5478E − 19
49	137	88	1.3519E − 20
49	138	89	1.7355E − 19
49	139	90	6.5423E − 21
49	140	91	1.0667E − 19
49	141	92	2.4922E − 21
49	142	93	5.9583E − 20
49	143	94	1.0511E − 21
49	144	95	3.8744E − 20
49	145	96	1.6158E − 22
49	146	97	1.5743E − 20
49	147	98	5.7716E − 24
49	148	99	5.9023E − 21
50	112	62	7.9554E − 17
50	113	63	2.5756E − 16
50	114	64	7.1958E − 17
50	115	65	1.7585E − 16
50	116	66	4.1797E − 17
50	117	67	1.4983E − 16
50	118	68	2.5449E − 17
50	119	69	1.0751E − 16
50	120	70	1.6099E − 17
50	121	71	1.0056E − 16
50	122	72	1.0870E − 17
50	123	73	7.4566E − 17
50	124	74	6.2196E − 18
50	125	75	4.3589E − 17
50	126	76	4.0444E − 18
50	127	77	2.2143E − 17
50	128	78	2.8652E − 18
50	129	79	6.5008E − 18
50	130	80	1.1033E − 18
50	131	81	9.2682E − 19
50	132	82	4.0644E − 21
50	133	83	1.5723E − 19
50	134	84	3.2997E − 20
50	135	85	1.2134E − 19
50	136	86	2.2616E − 20
50	137	87	1.1594E − 19
50	138	88	1.2983E − 20
50	139	89	9.0824E − 20
50	140	90	6.9063E − 21
50	141	91	5.1712E − 20
50	142	92	3.0924E − 21
50	143	93	3.4827E − 20
50	144	94	1.2520E − 21
50	145	95	1.7893E − 20
50	146	96	3.4264E − 22
50	147	97	8.9643E − 21
50	148	98	6.2749E − 23
50	149	99	3.8214E − 21
50	150	100	1.4346E − 24
50	151	101	1.3132E − 21
51	121	70	1.1195E − 16
51	122	71	2.5217E − 16
51	123	72	7.5999E − 17
51	124	73	2.0053E − 16
51	125	74	4.6704E − 17
51	126	75	1.1562E − 16
51	127	76	2.5349E − 17
51	128	77	6.9881E − 17
51	129	78	1.6750E − 17
51	130	79	2.4991E − 17
51	131	80	5.0973E − 18
51	132	81	7.8640E − 18
51	133	82	9.0631E − 20
51	134	83	4.9943E − 19
51	135	84	1.2913E − 19
51	136	85	8.5404E − 19
51	137	86	1.3232E − 19
51	138	87	1.1435E − 18
51	139	88	9.4663E − 20
51	140	89	8.9824E − 19
51	141	90	5.9736E − 20
51	142	91	6.1875E − 19
51	143	92	3.2847E − 20
51	144	93	3.7291E − 19
51	145	94	1.5855E − 20
51	146	95	2.2938E − 19
51	147	96	6.2989E − 21
51	148	97	1.0797E − 19
51	149	98	1.2689E − 21
51	150	99	4.0371E − 20
51	151	100	2.1161E − 22
51	152	101	1.4125E − 20
51	153	102	7.9377E − 24
51	154	103	5.3052E − 21
52	120	68	9.9978E − 17
52	121	69	2.8392E − 16
52	122	70	6.8359E − 17
52	123	71	2.1344E − 16
52	124	72	4.1451E − 17
52	125	73	1.5406E − 16
52	126	74	2.4961E − 17
52	127	75	1.2036E − 16
52	128	76	1.4897E − 17
52	129	77	6.7574E − 17
52	130	78	1.0009E − 17
52	131	79	2.4183E − 17
52	132	80	2.9729E − 18
52	133	81	5.2610E − 18
52	134	82	1.7955E − 19
52	135	83	2.9098E − 19
52	136	84	1.3029E − 19
52	137	85	8.4770E − 19
52	138	86	1.5724E − 19
52	139	87	1.0219E − 18
52	140	88	1.1332E − 19
52	141	89	8.3438E − 19
52	142	90	7.5098E − 20
52	143	91	6.0910E − 19
52	144	92	4.3738E − 20
52	145	93	4.8242E − 19
52	146	94	3.0014E − 20
52	147	95	2.4665E − 19
52	148	96	1.3075E − 20
52	149	97	1.1080E − 19
52	150	98	4.3877E − 21
52	151	99	4.3964E − 20
52	152	100	1.1903E − 21
52	153	101	1.6994E − 20

Table A.1 (cont.)

Z	A	N	$\langle \sigma v \rangle$ (cm^3 s^{-1})
52	154	102	1.5538E − 22
52	155	103	5.8122E − 21
52	156	104	2.9685E − 24
52	157	105	2.1817E − 21
53	127	74	1.3770E − 16
53	128	75	2.1958E − 16
53	129	76	7.9770E − 17
53	130	77	2.1512E − 16
53	131	78	5.8837E − 17
53	132	79	9.1572E − 17
53	133	80	1.3670E − 17
53	134	81	3.3880E − 17
53	135	82	1.5989E − 19
53	136	83	2.6701E − 18
53	137	84	1.5792E − 18
53	138	85	1.9233E − 18
53	139	86	1.1237E − 18
53	140	87	8.5756E − 18
53	141	88	9.4527E − 19
53	142	89	7.7875E − 18
53	143	90	7.0742E − 19
53	144	91	6.5045E − 18
53	145	92	5.7750E − 19
53	146	93	3.9431E − 18
53	147	94	2.3478E − 19
53	148	95	1.3630E − 18
53	149	96	8.7415E − 20
53	150	97	5.4838E − 19
53	151	98	2.5518E − 20
53	152	99	2.2725E − 19
53	153	100	7.0265E − 21
53	154	101	8.6036E − 20
53	155	102	1.1304E − 21
53	156	103	3.0345E − 20
53	157	104	2.2296E − 22
53	158	105	1.2114E − 20
53	159	106	1.0584E − 23
53	160	107	4.8992E − 21
53	161	108	7.5304E − 26
53	162	109	3.5860E − 21
54	124	70	1.6109E − 16
54	125	71	3.5854E − 16
54	126	72	1.0815E − 16
54	127	73	2.6985E − 16
54	128	74	6.6076E − 17
54	129	75	1.9093E − 16
54	130	76	3.7878E − 17
54	131	77	1.4999E − 16
54	132	78	2.4478E − 17
54	133	79	5.7387E − 17
54	134	80	9.1259E − 18
54	135	81	1.4617E − 17
54	136	82	3.5347E − 19
54	137	83	3.0751E − 18
54	138	84	5.0813E − 19
54	139	85	2.4567E − 18
54	140	86	5.7084E − 19
54	141	87	4.9378E − 18
54	142	88	6.1522E − 19
54	143	89	4.6566E − 18
54	144	90	4.7829E − 19
54	145	91	4.4258E − 18
54	146	92	4.5577E − 19
54	147	93	2.7155E − 18
54	148	94	2.4088E − 19
54	149	95	1.3372E − 18
54	150	96	1.0106E − 19
54	151	97	5.2633E − 19
54	152	98	3.7835E − 20
54	153	99	2.5197E − 19
54	154	100	1.2975E − 20
54	155	101	1.1365E − 19
54	156	102	3.5409E − 21
54	157	103	4.0341E − 20
54	158	104	9.3929E − 22
54	159	105	1.7376E − 20
54	160	106	1.3628E − 22
54	161	107	7.1722E − 21
54	162	108	5.9147E − 24
54	163	109	2.1744E − 21
54	164	110	1.0226E − 24
54	165	111	1.3463E − 21
55	133	78	1.3915E − 16
55	134	79	1.8564E − 16
55	135	80	4.1542E − 17
55	136	81	7.0249E − 17
55	137	82	2.0075E − 18
55	138	83	1.1037E − 17
55	139	84	5.2118E − 18
55	140	85	5.8962E − 18
55	141	86	9.1522E − 18
55	142	87	2.3203E − 17
55	143	88	5.9945E − 18
55	144	89	1.9391E − 17
55	145	90	4.3560E − 18
55	146	91	1.0227E − 17
55	147	92	2.4582E − 18
55	148	93	1.3880E − 17
55	149	94	1.5573E − 18
55	150	95	6.6769E − 18
55	151	96	5.9464E − 19
55	152	97	3.2422E − 18
55	153	98	2.4057E − 19
55	154	99	1.2134E − 18
55	155	100	8.9589E − 20
55	156	101	5.8721E − 19
55	157	102	2.0569E − 20
55	158	103	2.3273E − 19
55	159	104	6.1600E − 21
55	160	105	1.0273E − 19
55	161	106	1.5663E − 21
55	162	107	4.4481E − 20
55	163	108	2.5467E − 22
55	164	109	2.0027E − 20
55	165	110	5.5125E − 23
55	166	111	9.0349E − 21
55	167	112	1.4397E − 23
55	168	113	6.7437E − 21
55	169	114	2.0820E − 26
55	170	115	1.9112E − 21
56	130	74	1.4600E − 16
56	131	75	3.3622E − 16
56	132	76	8.7681E − 17
56	133	77	2.0369E − 16
56	134	78	5.5543E − 17
56	135	79	1.3176E − 16
56	136	80	1.8525E − 17
56	137	81	3.8749E − 17
56	138	82	1.1358E − 18
56	139	83	1.1551E − 17
56	140	84	2.5296E − 18
56	141	85	1.1385E − 17
56	142	86	3.1712E − 18
56	143	87	2.0628E − 17
56	144	88	5.5478E − 18
56	145	89	6.1453E − 18
56	146	90	5.4009E − 18
56	147	91	8.7420E − 18
56	148	92	5.6450E − 19
56	149	93	1.0343E − 17
56	150	94	1.1801E − 18
56	151	95	5.6724E − 18
56	152	96	5.3483E − 19
56	153	97	2.8722E − 18
56	154	98	2.2016E − 19
56	155	99	1.3632E − 18
56	156	100	8.5505E − 20
56	157	101	6.1953E − 19
56	158	102	2.5989E − 20
56	159	103	2.0349E − 19
56	160	104	9.2730E − 21
56	161	105	9.2326E − 20
56	162	106	2.9950E − 21
56	163	107	4.1033E − 20
56	164	108	8.7179E − 22
56	165	109	1.9439E − 20
56	166	110	2.2766E − 22
56	167	111	7.5887E − 21
56	168	112	1.8689E − 22
56	169	113	4.9122E − 21
56	170	114	1.5096E − 23

Table A.1 (cont.)

Z	A	N	$\langle \sigma v \rangle$ (cm^3 s^{-1})	Z	A	N	$\langle \sigma v \rangle$ (cm^3 s^{-1})	Z	A	N	$\langle \sigma v \rangle$ (cm^3 s^{-1})
56	171	115	1.9386E − 21	58	149	91	3.8500E − 17	59	164	105	2.3824E − 18
				58	150	92	1.4816E − 17	59	165	106	1.3990E − 19
57	138	81	1.4937E − 16	58	151	93	2.9764E − 17	59	166	107	1.2138E − 18
57	139	82	9.2015E − 18	58	152	94	4.3667E − 18	59	167	108	5.5669E − 20
57	140	83	5.6582E − 17	58	153	95	1.7783E − 17	59	168	109	5.4468E − 19
57	141	84	2.2426E − 17	58	154	96	2.2023E − 18	59	169	110	2.2368E − 20
57	142	85	4.9935E − 17	58	155	97	9.8657E − 18	59	170	111	3.2406E − 19
57	143	86	2.1346E − 17	58	156	98	1.0039E − 18	59	171	112	1.3049E − 20
57	144	87	1.1219E − 16	58	157	99	5.0933E − 18	59	172	113	4.6223E − 19
57	145	88	2.4158E − 17	58	158	100	4.3239E − 19	59	173	114	1.3159E − 20
57	146	89	5.1981E − 17	58	159	101	2.4970E − 18	59	174	115	1.1417E − 19
57	147	90	4.8815E − 17	58	160	102	1.3694E − 19	59	175	116	3.0493E − 21
57	148	91	3.1960E − 17	58	161	103	8.3973E − 19	59	176	117	4.5768E − 20
57	149	92	3.3286E − 17	58	162	104	5.6597E − 20	59	177	118	6.4335E − 22
57	150	93	4.5471E − 17	58	163	105	4.0519E − 19	59	178	119	2.2972E − 20
57	151	94	6.9670E − 18	58	164	106	2.2394E − 20	59	179	120	9.4578E − 23
57	152	95	2.5477E − 17	58	165	107	1.8948E − 19	59	180	121	8.5541E − 21
57	153	96	3.3827E − 18	58	166	108	8.5596E − 21	59	181	122	6.9013E − 24
57	154	97	1.3843E − 17	58	167	109	9.3872E − 20	59	182	123	3.3462E − 21
57	155	98	1.4934E − 18	58	168	110	3.2890E − 21				
57	156	99	7.1764E − 18	58	169	111	5.1917E − 20	60	142	82	1.2454E − 17
57	157	100	5.8125E − 19	58	170	112	1.9342E − 21	60	143	83	1.1131E − 16
57	158	101	3.5359E − 18	58	171	113	4.7087E − 20	60	144	84	2.0551E − 17
57	159	102	1.5252E − 19	58	172	114	1.3220E − 21	60	145	85	1.4405E − 16
57	160	103	1.2565E − 18	58	173	115	1.4723E − 20	60	146	86	2.5917E − 17
57	161	104	5.7957E − 20	58	174	116	3.4192E − 22	60	147	87	2.1334E − 16
57	162	105	5.2758E − 19	58	175	117	5.3467E − 21	60	148	88	1.9732E − 17
57	163	106	1.9376E − 20	58	176	118	4.8256E − 23	60	149	89	2.1438E − 16
57	164	107	2.5363E − 19	58	177	119	2.1981E − 21	60	150	90	6.0918E − 17
57	165	108	5.9772E − 21	58	178	120	7.2668E − 25	60	151	91	1.0672E − 16
57	166	109	1.2024E − 19	58	179	121	8.5595E − 22	60	152	92	2.7708E − 17
57	167	110	1.8401E − 21					60	153	93	4.9747E − 17
57	168	111	6.8200E − 20	59	141	82	2.6954E − 17	60	154	94	1.1796E − 17
57	169	112	1.5789E − 21	59	142	83	9.9319E − 17	60	155	95	4.0898E − 17
57	170	113	4.5516E − 20	59	143	84	6.7995E − 17	60	156	96	6.6391E − 18
57	171	114	4.5233E − 22	59	144	85	8.2733E − 17	60	157	97	2.4468E − 17
57	172	115	1.7785E − 20	59	145	86	6.6090E − 17	60	158	98	3.4816E − 18
57	173	116	4.8351E − 23	59	146	87	2.2250E − 16	60	159	99	1.4178E − 17
57	174	117	6.6759E − 21	59	147	88	6.9294E − 17	60	160	100	1.7205E − 18
57	175	118	1.3503E − 24	59	148	89	1.4429E − 16	60	161	101	7.8974E − 18
57	176	119	2.5943E − 21	59	149	90	1.4248E − 16	60	162	102	5.7990E − 19
				59	150	91	2.0440E − 16	60	163	103	2.8771E − 18
58	136	78	1.1229E − 16	59	151	92	8.4887E − 17	60	164	104	2.6821E − 19
58	137	79	2.6919E − 16	59	152	93	1.1703E − 16	60	165	105	1.4918E − 18
58	138	80	3.8733E − 17	59	153	94	2.1222E − 17	60	166	106	1.2026E − 19
58	139	81	9.0398E − 17	59	154	95	7.0319E − 17	60	167	107	7.9208E − 19
58	140	82	3.9568E − 18	59	155	96	1.1618E − 17	60	168	108	5.2805E − 20
58	141	83	4.1278E − 17	59	156	97	4.1096E − 17	60	169	109	4.1824E − 19
58	142	84	7.7171E − 18	59	157	98	5.8723E − 18	60	170	110	2.3618E − 20
58	143	85	3.6010E − 17	59	158	99	2.3285E − 17	60	171	111	2.4168E − 19
58	144	86	9.8923E − 18	59	159	100	2.7635E − 18	60	172	112	1.2989E − 20
58	145	87	8.4302E − 17	59	160	101	1.2617E − 17	60	173	113	2.6395E − 19
58	146	88	8.1479E − 18	59	161	102	7.9166E − 19	60	174	114	1.3930E − 20
58	147	89	4.2467E − 17	59	162	103	4.6181E − 18	60	175	115	1.1920E − 19
58	148	90	1.6690E − 17	59	163	104	3.5242E − 19	60	176	116	4.7906E − 21

Table A.1 (cont.)

Z	A	N	$\langle \sigma v \rangle$ (cm^3 s^{-1})	Z	A	N	$\langle \sigma v \rangle$ (cm^3 s^{-1})	Z	A	N	$\langle \sigma v \rangle$ (cm^3 s^{-1})
60	177	117	4.1348E − 20	62	146	84	4.6639E − 17	63	163	100	2.2428E − 17
60	178	118	1.6614E − 21	62	147	85	3.3664E − 16	63	164	101	7.9296E − 17
60	179	119	1.4184E − 20	62	148	86	6.2426E − 17	63	165	102	8.7554E − 18
60	180	120	5.0646E − 22	62	149	87	5.5408E − 16	63	166	103	3.4503E − 17
60	181	121	5.0996E − 21	62	150	88	1.7792E − 16	63	167	104	5.1034E − 18
60	182	122	1.0333E − 22	62	151	89	5.6106E − 16	63	168	105	2.2060E − 17
60	183	123	2.3511E − 21	62	152	90	5.5502E − 17	63	169	106	2.8687E − 18
60	184	124	6.0079E − 24	62	153	91	2.5039E − 16	63	170	107	1.3913E − 17
60	185	125	8.7698E − 22	62	154	92	4.9216E − 17	63	171	108	1.5326E − 18
				62	155	93	1.3188E − 16	63	172	109	8.6386E − 18
61	145	84	1.3632E − 16	62	156	94	3.6097E − 17	63	173	110	8.7476E − 19
61	146	85	3.8458E − 16	62	157	95	4.4719E − 17	63	174	111	5.9461E − 18
61	147	86	2.7711E − 16	62	158	96	1.4970E − 17	63	175	112	5.8741E − 19
61	148	87	4.1436E − 16	62	159	97	5.1916E − 17	63	176	113	9.4155E − 18
61	149	88	1.6741E − 16	62	160	98	8.7776E − 18	63	177	114	1.0857E − 18
61	150	89	1.0076E − 15	62	161	99	3.1892E − 17	63	178	115	5.8172E − 18
61	151	90	2.0834E − 16	62	162	100	4.9683E − 18	63	179	116	3.5246E − 19
61	152	91	3.8911E − 16	62	163	101	1.9518E − 17	63	180	117	2.1953E − 18
61	153	92	1.7423E − 16	62	164	102	1.9268E − 18	63	181	118	1.0481E − 19
61	154	93	2.0842E − 16	62	165	103	7.9599E − 18	63	182	119	7.9607E − 19
61	155	94	8.0101E − 17	62	166	104	1.0164E − 18	63	183	120	2.9841E − 20
61	156	95	1.5727E − 16	62	167	105	4.7140E − 18	63	184	121	2.5835E − 19
61	157	96	2.8344E − 17	62	168	106	5.1832E − 19	63	185	122	9.2676E − 21
61	158	97	9.3351E − 17	62	169	107	2.7154E − 18	63	186	123	1.1296E − 19
61	159	98	1.6289E − 17	62	170	108	2.5732E − 19	63	187	124	1.0932E − 21
61	160	99	5.7174E − 17	62	171	109	1.5972E − 18	63	188	125	1.2283E − 20
61	161	100	8.9566E − 18	62	172	110	1.2932E − 19				
61	162	101	3.4667E − 17	62	173	111	9.9944E − 19	64	152	88	9.3178E − 17
61	163	102	3.0287E − 18	62	174	112	7.6000E − 20	64	153	89	9.3755E − 16
61	164	103	1.3853E − 17	62	175	113	1.3205E − 18	64	154	90	1.0416E − 16
61	165	104	1.5457E − 18	62	176	114	1.0414E − 19	64	155	91	5.8247E − 16
61	166	105	7.9838E − 18	62	177	115	7.9708E − 19	64	156	92	8.7553E − 17
61	167	106	7.4315E − 19	62	178	116	3.5686E − 20	64	157	93	2.9838E − 16
61	168	107	4.2348E − 18	62	179	117	2.6487E − 19	64	158	94	5.3974E − 17
61	169	108	3.4887E − 19	62	180	118	1.3213E − 20	64	159	95	1.6845E − 16
61	170	109	2.5411E − 18	62	181	119	8.6082E − 20	64	160	96	3.7393E − 17
61	171	110	1.6671E − 19	62	182	120	5.1186E − 21	64	161	97	9.2649E − 17
61	172	111	1.5701E − 18	62	183	121	3.0666E − 20	64	162	98	1.8690E − 17
61	173	112	9.6335E − 20	62	184	122	2.0022E − 21	64	163	99	6.9473E − 17
61	174	113	2.1842E − 18	62	185	123	1.2352E − 20	64	164	100	1.1652E − 17
61	175	114	1.5934E − 19	62	186	124	5.5875E − 22	64	165	101	4.4273E − 17
61	176	115	8.3650E − 19	62	187	125	3.1642E − 21	64	166	102	4.9767E − 18
61	177	116	4.3283E − 20					64	167	103	1.8819E − 17
61	178	117	3.4125E − 19	63	151	88	3.1819E − 16	64	168	104	2.9533E − 18
61	179	118	1.1615E − 20	63	152	89	1.5908E − 15	64	169	105	1.2131E − 17
61	180	119	1.3355E − 19	63	153	90	3.8768E − 16	64	170	106	1.7259E − 18
61	181	120	2.8475E − 21	63	154	91	9.8726E − 16	64	171	107	7.8087E − 18
61	182	121	5.0995E − 20	63	155	92	3.0471E − 16	64	172	108	9.8873E − 19
61	183	122	7.6207E − 22	63	156	93	2.6475E − 16	64	173	109	5.0515E − 18
61	184	123	2.1937E − 20	63	157	94	1.6078E − 16	64	174	110	5.7186E − 19
61	185	124	8.6518E − 23	63	158	95	1.7010E − 16	64	175	111	3.4850E − 18
61	186	125	3.2251E − 21	63	159	96	9.6552E − 17	64	176	112	3.7975E − 19
				63	160	97	1.1242E − 16	64	177	113	5.1491E − 18
62	144	82	2.9832E − 17	63	161	98	3.7069E − 17	64	178	114	5.9815E − 19
62	145	83	2.5380E − 16	63	162	99	1.2668E − 16	64	179	115	3.8639E − 18

Table A.1 (cont.)

Z	A	N	$\langle\sigma v\rangle$ (cm^3 s^{-1})	Z	A	N	$\langle\sigma v\rangle$ (cm^3 s^{-1})	Z	A	N	$\langle\sigma v\rangle$ (cm^3 s^{-1})
64	180	116	2.2086E − 19	66	167	101	7.6612E − 17	67	192	125	1.3852E − 19
64	181	117	1.3475E − 18	66	168	102	1.1347E − 17	67	193	126	3.6440E − 23
64	182	118	7.8159E − 20	66	169	103	4.2537E − 17	67	194	127	8.7818E − 21
64	183	119	4.5024E − 19	66	170	104	7.3222E − 18	67	195	128	4.3781E − 24
64	184	120	2.9726E − 20	66	171	105	2.8844E − 17	67	196	129	4.0299E − 21
64	185	121	1.5087E − 19	66	172	106	4.6551E − 18				
64	186	122	1.2802E − 20	66	173	107	1.9764E − 17	68	162	94	1.6702E − 16
64	187	123	5.9733E − 20	66	174	108	2.9553E − 18	68	163	95	6.6784E − 16
64	188	124	3.9797E − 21	66	175	109	1.3847E − 17	68	164	96	1.2513E − 16
64	189	125	9.2968E − 21	66	176	110	1.9472E − 18	68	165	97	5.1437E − 16
				66	177	111	1.0516E − 17	68	166	98	1.0157E − 16
65	159	94	2.4960E − 16	66	178	112	1.5078E − 18	68	167	99	3.2647E − 16
65	160	95	5.3486E − 16	66	179	113	1.6991E − 17	68	168	100	6.5906E − 17
65	161	96	2.1278E − 16	66	180	114	2.5507E − 18	68	169	101	1.2937E − 16
65	162	97	2.2804E − 16	66	181	115	1.2440E − 17	68	170	102	3.2581E − 17
65	163	98	8.8679E − 17	66	182	116	1.0705E − 18	68	171	103	8.6636E − 17
65	164	99	2.7057E − 16	66	183	117	5.0164E − 18	68	172	104	2.3396E − 17
65	165	100	5.1523E − 17	66	184	118	3.8496E − 19	68	173	105	8.8052E − 17
65	166	101	1.7205E − 16	66	185	119	1.8528E − 18	68	174	106	1.1344E − 17
65	167	102	2.1283E − 17	66	186	120	1.4077E − 19	68	175	107	4.7801E − 17
65	168	103	7.5948E − 17	66	187	121	6.3292E − 19	68	176	108	7.8386E − 18
65	169	104	1.3507E − 17	66	188	122	6.0083E − 20	68	177	109	3.5564E − 17
65	170	105	5.3009E − 17	66	189	123	2.5219E − 19	68	178	110	5.6525E − 18
65	171	106	8.5085E − 18	66	190	124	1.5809E − 20	68	179	111	2.9112E − 17
65	172	107	3.6453E − 17	66	191	125	2.5593E − 20	68	180	112	5.0440E − 18
65	173	108	5.3323E − 18	66	192	126	1.2854E − 25	68	181	113	4.5741E − 17
65	174	109	2.5469E − 17	66	193	127	8.5510E − 22	68	182	114	8.1384E − 18
65	175	110	3.4254E − 18					68	183	115	2.8761E − 17
65	176	111	1.8811E − 17	67	165	98	2.8079E − 16	68	184	116	3.5470E − 18
65	177	112	2.6527E − 18	67	166	99	2.2820E − 16	68	185	117	1.3032E − 17
65	178	113	3.1031E − 17	67	167	100	2.3812E − 16	68	186	118	1.4420E − 18
65	179	114	4.8993E − 18	67	168	101	2.0576E − 16	68	187	119	5.4681E − 18
65	180	115	2.1481E − 17	67	169	102	9.2510E − 17	68	188	120	5.4872E − 19
65	181	116	1.9438E − 18	67	170	103	1.5879E − 16	68	189	121	2.0569E − 18
65	182	117	8.7364E − 18	67	171	104	3.2713E − 17	68	190	122	2.3688E − 19
65	183	118	6.3218E − 19	67	172	105	1.1633E − 16	68	191	123	8.8241E − 19
65	184	119	3.2991E − 18	67	173	106	2.2072E − 17	68	192	124	4.8629E − 20
65	185	120	1.9277E − 19	67	174	107	8.5822E − 17	68	193	125	7.1336E − 20
65	186	121	1.1697E − 18	67	175	108	1.5056E − 17	68	194	126	2.5413E − 22
65	187	122	6.5860E − 20	67	176	109	6.4143E − 17	68	195	127	4.4128E − 21
65	188	123	4.8232E − 19	67	177	110	1.0763E − 17	68	196	128	6.9694E − 23
65	189	124	6.4480E − 21	67	178	111	5.2465E − 17	68	197	129	2.4851E − 21
65	190	125	4.2360E − 20	67	179	112	9.3728E − 18	68	198	130	5.2861E − 24
				67	180	113	9.4991E − 17	68	199	131	1.2731E − 21
66	156	90	1.9226E − 16	67	181	114	1.5999E − 17				
66	157	91	8.2947E − 16	67	182	115	5.4505E − 17	69	169	100	2.0942E − 16
66	158	92	1.5113E − 16	67	183	116	6.9276E − 18	69	170	101	3.5680E − 16
66	159	93	5.3034E − 16	67	184	117	2.4926E − 17	69	171	102	9.6834E − 17
66	160	94	9.6864E − 17	67	185	118	2.6030E − 18	69	172	103	2.0651E − 16
66	161	95	4.1482E − 16	67	186	119	1.0364E − 17	69	173	104	5.3691E − 17
66	162	96	7.7882E − 17	67	187	120	8.7740E − 19	69	174	105	1.7260E − 16
66	163	97	2.5916E − 16	67	188	121	3.9109E − 18	69	175	106	6.1160E − 17
66	164	98	4.2822E − 17	67	189	122	3.2957E − 19	69	176	107	1.8523E − 16
66	165	99	1.4958E − 16	67	190	123	1.6865E − 18	69	177	108	3.9203E − 17
66	166	100	3.0757E − 17	67	191	124	2.8373E − 20	69	178	109	1.4400E − 16

Table A.1 (cont.)

Z	A	N	$\langle\sigma v\rangle$ (cm^3 s^{-1})	Z	A	N	$\langle\sigma v\rangle$ (cm^3 s^{-1})	Z	A	N	$\langle\sigma v\rangle$ (cm^3 s^{-1})
69	179	110	3.0408E − 17	70	196	126	2.2810E − 21	72	175	103	3.6414E − 16
69	180	111	1.2933E − 16	70	197	127	1.9418E − 20	72	176	104	9.7804E − 17
69	181	112	3.0673E − 17	70	198	128	1.4848E − 21	72	177	105	2.8421E − 16
69	182	113	1.9740E − 16	70	199	129	1.2269E − 20	72	178	106	8.1119E − 17
69	183	114	3.7457E − 17	70	200	130	6.1728E − 22	72	179	107	2.6750E − 16
69	184	115	1.1831E − 16	70	201	131	7.4220E − 21	72	180	108	5.8704E − 17
69	185	116	1.7085E − 17	70	202	132	1.8574E − 22	72	181	109	9.7040E − 17
69	186	117	5.4846E − 17	70	203	133	4.5361E − 21	72	182	110	4.2348E − 17
69	187	118	7.3407E − 18	70	204	134	2.8311E − 23	72	183	111	9.1550E − 17
69	188	119	2.4480E − 17	70	205	135	2.1526E − 21	72	184	112	3.6128E − 17
69	189	120	2.8362E − 18	70	206	136	4.8366E − 25	72	185	113	2.2959E − 16
69	190	121	9.7817E − 18	70	207	137	1.2035E − 21	72	186	114	3.0905E − 17
69	191	122	1.1942E − 18					72	187	115	1.1399E − 16
69	192	123	4.7129E − 18	71	175	104	2.6273E − 16	72	188	116	1.6281E − 17
69	193	124	1.0577E − 19	71	176	105	3.1078E − 16	72	189	117	5.3583E − 17
69	194	125	4.1391E − 19	71	177	106	2.2651E − 16	72	190	118	8.0179E − 18
69	195	126	6.8581E − 22	71	178	107	2.0883E − 16	72	191	119	2.4062E − 17
69	196	127	4.4161E − 20	71	179	108	1.7698E − 16	72	192	120	3.6365E − 18
69	197	128	5.3822E − 22	71	180	109	2.7260E − 16	72	193	121	1.0216E − 17
69	198	129	2.4151E − 20	71	181	110	1.0658E − 16	72	194	122	1.8646E − 18
69	199	130	1.5078E − 22	71	182	111	2.7386E − 16	72	195	123	5.1577E − 18
69	200	131	1.5653E − 20	71	183	112	7.9159E − 17	72	196	124	3.2478E − 19
69	201	132	2.4219E − 23	71	184	113	4.2969E − 16	72	197	125	5.3742E − 19
69	202	133	8.6234E − 21	71	185	114	7.6450E − 17	72	198	126	9.7654E − 21
69	203	134	7.5467E − 25	71	186	115	2.2484E − 16	72	199	127	7.3749E − 20
69	204	135	4.2043E − 21	71	187	116	3.5671E − 17	72	200	128	9.0164E − 21
				71	188	117	1.0746E − 16	72	201	129	5.1533E − 20
70	168	98	1.7462E − 16	71	189	118	1.6102E − 17	72	202	130	4.9981E − 21
70	169	99	5.4864E − 16	71	190	119	4.9008E − 17	72	203	131	3.7374E − 20
70	170	100	1.4086E − 16	71	191	120	6.7748E − 18	72	204	132	2.5768E − 21
70	171	101	2.8212E − 16	71	192	121	2.0971E − 17	72	205	133	2.6128E − 20
70	172	102	7.6808E − 17	71	193	122	3.1859E − 18	72	206	134	1.1485E − 21
70	173	103	1.9089E − 16	71	194	123	1.0444E − 17	72	207	135	1.4668E − 20
70	174	104	4.5775E − 17	71	195	124	3.2693E − 19	72	208	136	4.0914E − 22
70	175	105	1.2551E − 16	71	196	125	1.0672E − 18	72	209	137	8.5517E − 21
70	176	106	3.7616E − 17	71	197	126	4.0017E − 21	72	210	138	9.1033E − 23
70	177	107	1.3379E − 16	71	198	127	1.7535E − 19	72	211	139	4.6034E − 21
70	178	108	1.8898E − 17	71	199	128	5.9387E − 21	72	212	140	1.5096E − 23
70	179	109	8.6058E − 17	71	200	129	1.0363E − 19	72	213	141	7.8478E − 21
70	180	110	1.4988E − 17	71	201	130	2.9699E − 21	72	214	142	1.5614E − 23
70	181	111	7.8241E − 17	71	202	131	8.3917E − 20	72	215	143	3.8694E − 21
70	182	112	1.5902E − 17	71	203	132	1.4131E − 21				
70	183	113	1.1827E − 16	71	204	133	5.5322E − 20	73	180	107	4.7786E − 16
70	184	114	1.7092E − 17	71	205	134	4.7844E − 22	73	181	108	2.7658E − 16
70	185	115	5.9793E − 17	71	206	135	3.2564E − 20	73	182	109	3.5989E − 16
70	186	116	8.3740E − 18	71	207	136	9.9910E − 23	73	183	110	2.3666E − 16
70	187	117	2.7660E − 17	71	208	137	1.7171E − 20	73	184	111	3.3258E − 16
70	188	118	3.8065E − 18	71	209	138	7.8524E − 24	73	185	112	1.5572E − 16
70	189	119	1.2318E − 17	71	210	139	8.6457E − 21	73	186	113	5.7751E − 16
70	190	120	1.6186E − 18	71	211	140	4.3562E − 24	73	187	114	1.4067E − 16
70	191	121	5.0723E − 18	71	212	141	1.1540E − 20	73	188	115	3.4444E − 16
70	192	122	7.5631E − 19	71	213	142	2.9433E − 25	73	189	116	6.7985E − 17
70	193	123	2.3845E − 18	71	214	143	5.0054E − 21	73	190	117	1.8474E − 16
70	194	124	1.3120E − 19					73	191	118	3.1039E − 17
70	195	125	2.1848E − 19	72	174	102	1.2638E − 16	73	192	119	8.8202E − 17

Table A.1 (cont.)

Z	A	N	$\langle\sigma v\rangle$ (cm^3 s^{-1})
73	193	120	1.3397E − 17
73	194	121	3.7928E − 17
73	195	122	6.7582E − 18
73	196	123	1.9977E − 17
73	197	124	8.5289E − 19
73	198	125	2.3468E − 18
73	199	126	1.5905E − 20
73	200	127	5.4639E − 19
73	201	128	3.5869E − 20
73	202	129	3.7679E − 19
73	203	130	2.2788E − 20
73	204	131	3.2875E − 19
73	205	132	1.4667E − 20
73	206	133	2.6497E − 19
73	207	134	7.9267E − 21
73	208	135	1.8039E − 19
73	209	136	3.5557E − 21
73	210	137	1.1042E − 19
73	211	138	1.2934E − 21
73	212	139	6.3918E − 20
73	213	140	3.1860E − 22
73	214	141	5.0109E − 20
73	215	142	3.0482E − 22
73	216	143	3.3586E − 20
73	217	144	4.1171E − 23
73	218	145	1.3741E − 20
73	219	146	3.6136E − 25
73	220	147	4.5773E − 21
74	180	106	1.7115E − 16
74	181	107	4.6147E − 16
74	182	108	1.2142E − 16
74	183	109	2.2842E − 16
74	184	110	9.2269E − 17
74	185	111	2.1596E − 16
74	186	112	4.5868E − 17
74	187	113	1.9055E − 16
74	188	114	2.4334E − 17
74	189	115	1.3830E − 16
74	190	116	2.7961E − 17
74	191	117	9.3899E − 17
74	192	118	1.4438E − 17
74	193	119	4.2737E − 17
74	194	120	6.9203E − 18
74	195	121	1.8197E − 17
74	196	122	3.7542E − 18
74	197	123	9.5970E − 18
74	198	124	7.2545E − 19
74	199	125	1.1460E − 18
74	200	126	3.0212E − 20
74	201	127	2.3141E − 19
74	202	128	3.6768E − 20
74	203	129	1.8087E − 19
74	204	130	2.3519E − 20
74	205	131	1.5401E − 19
74	206	132	1.4966E − 20
74	207	133	1.2049E − 19
74	208	134	8.5700E − 21
74	209	135	8.4809E − 20
74	210	136	4.4521E − 21
74	211	137	5.2969E − 20
74	212	138	2.0487E − 21
74	213	139	3.0962E − 20
74	214	140	8.0017E − 22
74	215	141	1.5133E − 20
74	216	142	4.9260E − 22
74	217	143	2.0574E − 20
74	218	144	2.5913E − 22
74	219	145	9.6944E − 21
74	220	146	2.2486E − 23
74	221	147	3.5885E − 21
75	185	110	3.4406E − 16
75	186	111	4.5234E − 16
75	187	112	2.3074E − 16
75	188	113	3.7801E − 16
75	189	114	1.9979E − 16
75	190	115	3.0462E − 16
75	191	116	1.0049E − 16
75	192	117	2.6609E − 16
75	193	118	5.4186E − 17
75	194	119	1.3746E − 16
75	195	120	2.3547E − 17
75	196	121	6.1808E − 17
75	197	122	1.2418E − 17
75	198	123	3.3928E − 17
75	199	124	1.8270E − 18
75	200	125	4.4538E − 18
75	201	126	5.0859E − 20
75	202	127	1.3642E − 18
75	203	128	1.4821E − 19
75	204	129	1.0977E − 18
75	205	130	1.0586E − 19
75	206	131	1.0846E − 18
75	207	132	8.3513E − 20
75	208	133	9.3475E − 19
75	209	134	5.8609E − 20
75	210	135	7.1251E − 19
75	211	136	3.5317E − 20
75	212	137	4.8585E − 19
75	213	138	1.7832E − 20
75	214	139	3.3911E − 19
75	215	140	8.0333E − 21
75	216	141	1.9421E − 19
75	217	142	2.8208E − 21
75	218	143	1.4860E − 19
75	219	144	2.0263E − 21
75	220	145	8.2661E − 20
75	221	146	4.3351E − 22
75	222	147	3.3871E − 20
75	223	148	3.0990E − 23
75	224	149	1.2218E − 20
75	225	150	7.9112E − 26
75	226	151	3.8570E − 21
76	184	108	2.2405E − 16
76	185	109	4.2710E − 16
76	186	110	1.3760E − 16
76	187	111	2.8512E − 16
76	188	112	6.7696E − 17
76	189	113	4.0990E − 16
76	190	114	6.5170E − 17
76	191	115	3.3672E − 16
76	192	116	3.8701E − 17
76	193	117	1.1056E − 16
76	194	118	1.9153E − 17
76	195	119	4.1471E − 17
76	196	120	1.1521E − 17
76	197	121	2.9275E − 17
76	198	122	6.6332E − 18
76	199	123	1.6032E − 17
76	200	124	1.4156E − 18
76	201	125	2.1309E − 18
76	202	126	7.8113E − 20
76	203	127	5.8401E − 19
76	204	128	1.1914E − 19
76	205	129	5.0806E − 19
76	206	130	8.3853E − 20
76	207	131	5.0372E − 19
76	208	132	6.1922E − 20
76	209	133	4.3609E − 19
76	210	134	4.1809E − 20
76	211	135	3.4584E − 19
76	212	136	2.5731E − 20
76	213	137	2.4348E − 19
76	214	138	1.4522E − 20
76	215	139	1.6330E − 19
76	216	140	7.3987E − 21
76	217	141	9.5713E − 20
76	218	142	3.4825E − 21
76	219	143	5.0166E − 20
76	220	144	1.7041E − 21
76	221	145	4.8515E − 20
76	222	146	1.2422E − 21
76	223	147	2.1332E − 20
76	224	148	2.4970E − 22
76	225	149	8.6253E − 21
76	226	150	1.4095E − 23
76	227	151	3.0440E − 21
77	191	114	2.5862E − 16
77	192	115	5.5846E − 16
77	193	116	1.6241E − 16
77	194	117	2.0391E − 16
77	195	118	8.2225E − 17

Table A.1 (cont.)

Z	A	N	$\langle \sigma v \rangle$ (cm^3 s^{-1})
77	196	119	7.9106E − 17
77	197	120	4.2907E − 17
77	198	121	8.8975E − 17
77	199	122	2.0519E − 17
77	200	123	5.1506E − 17
77	201	124	3.2952E − 18
77	202	125	7.4489E − 18
77	203	126	1.3633E − 19
77	204	127	2.8485E − 18
77	205	128	4.4531E − 19
77	206	129	2.5311E − 18
77	207	130	3.5049E − 19
77	208	131	2.8112E − 18
77	209	132	3.2123E − 19
77	210	133	2.7067E − 18
77	211	134	2.6136E − 19
77	212	135	2.3593E − 18
77	213	136	1.8810E − 19
77	214	137	1.8304E − 18
77	215	138	1.2223E − 19
77	216	139	1.2909E − 18
77	217	140	6.9581E − 20
77	218	141	8.4063E − 19
77	219	142	3.2930E − 20
77	220	143	5.5725E − 19
77	221	144	1.4613E − 20
77	222	145	2.7747E − 19
77	223	146	6.6109E − 21
77	224	147	1.8939E − 19
77	225	148	2.1302E − 21
77	226	149	8.0739E − 20
77	227	150	3.4465E − 22
77	228	151	3.1018E − 20
77	229	152	1.9434E − 23
77	230	153	1.1118E − 20
77	231	154	1.0318E − 26
77	232	155	3.6486E − 21
78	190	112	1.0374E − 16
78	191	113	5.7006E − 16
78	192	114	9.5808E − 17
78	193	115	2.7631E − 16
78	194	116	5.9209E − 17
78	195	117	1.6405E − 16
78	196	118	3.1763E − 17
78	197	119	7.7758E − 17
78	198	120	1.3169E − 17
78	199	121	4.9490E − 17
78	200	122	6.8858E − 18
78	201	123	2.9442E − 17
78	202	124	2.4257E − 18
78	203	125	3.5100E − 18
78	204	126	1.7806E − 19
78	205	127	1.2156E − 18
78	206	128	3.1374E − 19
78	207	129	1.1250E − 18
78	208	130	2.3918E − 19
78	209	131	1.2266E − 18
78	210	132	2.0071E − 19
78	211	133	1.1942E − 18
78	212	134	1.5466E − 19
78	213	135	1.0579E − 18
78	214	136	1.0924E − 19
78	215	137	8.4315E − 19
78	216	138	7.0307E − 20
78	217	139	6.1686E − 19
78	218	140	4.1246E − 20
78	219	141	4.0983E − 19
78	220	142	2.2712E − 20
78	221	143	2.5990E − 19
78	222	144	1.1408E − 20
78	223	145	1.4305E − 19
78	224	146	5.2506E − 21
78	225	147	7.1820E − 20
78	226	148	2.0037E − 21
78	227	149	4.1336E − 20
78	228	150	9.6632E − 22
78	229	151	1.8924E − 20
78	230	152	1.8889E − 22
78	231	153	7.1132E − 21
78	232	154	1.4488E − 23
78	233	155	2.1022E − 21
78	234	156	8.7426E − 26
78	235	157	9.7458E − 22
79	197	118	1.4280E − 16
79	198	119	1.8929E − 16
79	199	120	6.6837E − 17
79	200	121	6.3169E − 17
79	201	122	3.9172E − 17
79	202	123	3.4536E − 17
79	203	124	2.9725E − 18
79	204	125	1.0379E − 17
79	205	126	3.0666E − 19
79	206	127	5.1250E − 18
79	207	128	1.0161E − 18
79	208	129	4.7229E − 18
79	209	130	8.5770E − 19
79	210	131	5.7668E − 18
79	211	132	8.8199E − 19
79	212	133	6.1994E − 18
79	213	134	8.1189E − 19
79	214	135	6.0106E − 18
79	215	136	6.7376E − 19
79	216	137	5.2752E − 18
79	217	138	4.9897E − 19
79	218	139	4.1545E − 18
79	219	140	3.3532E − 19
79	220	141	2.9809E − 18
79	221	142	2.0526E − 19
79	222	143	1.9575E − 18
79	223	144	1.1095E − 19
79	224	145	1.1931E − 18
79	225	146	4.9990E − 20
79	226	147	6.3366E − 19
79	227	148	2.0157E − 20
79	228	149	6.5300E − 19
79	229	150	3.2522E − 21
79	230	151	3.8736E − 19
79	231	152	4.0507E − 22
79	232	153	1.7555E − 19
79	233	154	1.0903E − 22
79	234	155	1.3348E − 19
79	235	156	6.4722E − 24
79	236	157	5.9046E − 20
79	237	158	6.5410E − 25
79	238	159	2.6187E − 20
80	196	116	9.9247E − 17
80	197	117	2.1336E − 16
80	198	118	5.7003E − 17
80	199	119	1.2145E − 16
80	200	120	2.6267E − 17
80	201	121	4.4028E − 17
80	202	122	1.6576E − 17
80	203	123	3.9432E − 17
80	204	124	3.7257E − 18
80	205	125	3.7166E − 18
80	206	126	3.5655E − 20
80	207	127	2.9146E − 18
80	208	128	6.7193E − 19
80	209	129	2.0430E − 18
80	210	130	5.4450E − 19
80	211	131	2.4140E − 18
80	212	132	5.0572E − 19
80	213	133	2.5666E − 18
80	214	134	4.3561E − 19
80	215	135	2.4845E − 18
80	216	136	3.4623E − 19
80	217	137	2.1812E − 18
80	218	138	2.5311E − 19
80	219	139	1.7664E − 18
80	220	140	1.6951E − 19
80	221	141	1.3101E − 18
80	222	142	1.0489E − 19
80	223	143	8.9513E − 19
80	224	144	5.9043E − 20
80	225	145	5.6056E − 19
80	226	146	3.1487E − 20
80	227	147	3.3253E − 19
80	228	148	1.5366E − 20
80	229	149	1.6986E − 19
80	230	150	7.0989E − 21
80	231	151	8.2790E − 20
80	232	152	2.9939E − 21

Table A.1 (cont.)

Z	A	N	$\langle \sigma v \rangle$ (cm^3 s^{-1})
80	233	153	3.7262E − 20
80	234	154	1.0724E − 21
80	235	155	1.4706E − 20
80	236	156	2.9235E − 22
80	237	157	6.2450E − 21
80	238	158	4.6364E − 23
80	239	159	2.2730E − 21
80	240	160	1.8820E − 24
80	241	161	1.0502E − 21
81	203	122	4.2169E − 17
81	204	123	6.2377E − 17
81	205	124	1.4023E − 17
81	206	125	7.2650E − 18
81	207	126	2.5202E − 19
81	208	127	2.9088E − 18
81	209	128	7.0387E − 19
81	210	129	6.5488E − 18
81	211	130	1.1872E − 18
81	212	131	7.5031E − 18
81	213	132	1.2976E − 18
81	214	133	8.6026E − 18
81	215	134	1.2786E − 18
81	216	135	8.9466E − 18
81	217	136	1.1459E − 18
81	218	137	8.4798E − 18
81	219	138	9.3499E − 19
81	220	139	7.3000E − 18
81	221	140	6.9971E − 19
81	222	141	5.7759E − 18
81	223	142	4.8032E − 19
81	224	143	4.1667E − 18
81	225	144	3.0151E − 19
81	226	145	2.7613E − 18
81	227	146	1.7223E − 19
81	228	147	1.6853E − 18
81	229	148	8.8621E − 20
81	230	149	9.5064E − 19
81	231	150	4.1697E − 20
81	232	151	5.1545E − 19
81	233	152	1.7277E − 20
81	234	153	2.4789E − 19
81	235	154	6.6860E − 21
81	236	155	1.1046E − 19
81	237	156	2.1618E − 21
81	238	157	4.7441E − 20
81	239	158	6.0787E − 22
81	240	159	1.9529E − 20
81	241	160	1.1088E − 22
81	242	161	7.6198E − 21
81	243	162	9.6935E − 24
81	244	163	3.0411E − 21
81	245	164	2.8340E − 26
81	246	165	1.0998E − 21
82	204	122	2.4081E − 17
82	205	123	4.7406E − 17
82	206	124	7.7252E − 18
82	207	125	3.0445E − 18
82	208	126	8.4040E − 20
82	209	127	1.2914E − 18
82	210	128	2.5423E − 19
82	211	129	1.5007E − 18
82	212	130	6.7208E − 19
82	213	131	1.7617E − 18
82	214	132	7.6138E − 19
82	215	133	3.2464E − 18
82	216	134	6.8814E − 19
82	217	135	3.3081E − 18
82	218	136	5.7810E − 19
82	219	137	3.0719E − 18
82	220	138	4.5348E − 19
82	221	139	2.6164E − 18
82	222	140	3.2784E − 19
82	223	141	2.0403E − 18
82	224	142	2.2156E − 19
82	225	143	1.4814E − 18
82	226	144	1.3847E − 19
82	227	145	9.9284E − 19
82	228	146	8.1213E − 20
82	229	147	6.2457E − 19
82	230	148	4.4310E − 20
82	231	149	3.6366E − 19
82	232	150	2.3637E − 20
82	233	151	1.9947E − 19
82	234	152	1.2089E − 20
82	235	153	1.0338E − 19
82	236	154	5.6255E − 21
82	237	155	4.9516E − 20
82	238	156	2.6053E − 21
82	239	157	2.3883E − 20
82	240	158	9.5813E − 22
82	241	159	1.0707E − 20
82	242	160	3.2966E − 22
82	243	161	5.1897E − 21
82	244	162	7.5855E − 23
82	245	163	2.2231E − 21
82	246	164	7.2092E − 24
82	247	165	1.1228E − 21
83	209	126	2.3806E − 18
83	210	127	3.5188E − 18
83	211	128	5.4740E − 18
83	212	129	5.0850E − 18
83	213	130	4.2688E − 18
83	214	131	9.3233E − 18
83	215	132	3.5531E − 18
83	216	133	2.9103E − 17
83	217	134	4.9619E − 18
83	218	135	3.1543E − 17
83	219	136	4.7579E − 18
83	220	137	3.1759E − 17
83	221	138	4.1714E − 18
83	222	139	2.9327E − 17
83	223	140	3.3591E − 18
83	224	141	2.4683E − 17
83	225	142	2.4880E − 18
83	226	143	1.9469E − 17
83	227	144	1.7104E − 18
83	228	145	1.4233E − 17
83	229	146	1.0915E − 18
83	230	147	9.4982E − 18
83	231	148	6.4220E − 19
83	232	149	5.8505E − 18
83	233	150	3.4960E − 19
83	234	151	3.2616E − 18
83	235	152	1.7006E − 19
83	236	153	1.6650E − 18
83	237	154	7.5672E − 20
83	238	155	7.7882E − 19
83	239	156	2.9703E − 20
83	240	157	3.6657E − 19
83	241	158	1.1133E − 20
83	242	159	1.5479E − 19
83	243	160	3.7145E − 21
83	244	161	6.2703E − 20
83	245	162	1.0324E − 21
83	246	163	2.3891E − 20
83	247	164	2.1334E − 22
83	248	165	9.5143E − 21
83	249	166	2.5573E − 23
83	250	167	3.7687E − 21
83	251	168	7.5554E − 25
83	252	169	1.3787E − 21
84	210	126	8.5289E − 19
84	211	127	1.6216E − 17
84	212	128	2.8733E − 18
84	213	129	1.8767E − 17
84	214	130	2.6184E − 18
84	215	131	2.9921E − 17
84	216	132	3.8169E − 18
84	217	133	2.3799E − 17
84	218	134	4.6948E − 18
84	219	135	2.9045E − 17
84	220	136	4.3200E − 18
84	221	137	2.8585E − 17
84	222	138	3.6818E − 18
84	223	139	2.6206E − 17
84	224	140	2.9240E − 18
84	225	141	2.2508E − 17
84	226	142	2.2067E − 18
84	227	143	1.8113E − 17
84	228	144	1.5093E − 18
84	229	145	1.4864E − 17

Table A.1 (cont.)

Z	A	N	$\langle\sigma v\rangle$ (cm^3 s^{-1})
84	230	146	1.1495E − 18
84	231	147	1.0107E − 17
84	232	148	6.7867E − 19
84	233	149	5.0444E − 18
84	234	150	3.6932E − 19
84	235	151	2.3332E − 18
84	236	152	1.9070E − 19
84	237	153	1.0514E − 18
84	238	154	9.1184E − 20
84	239	155	4.8838E − 19
84	240	156	4.0876E − 20
84	241	157	2.3509E − 19
84	242	158	1.7162E − 20
84	243	159	1.6277E − 19
84	244	160	6.5530E − 21
84	245	161	6.4717E − 20
84	246	162	2.3397E − 21
84	247	163	2.2961E − 20
84	248	164	7.5998E − 22
84	249	165	9.1827E − 21
84	250	166	1.7855E − 22
84	251	167	4.7107E − 21
84	252	168	2.3547E − 23
84	253	169	1.4787E − 21
84	254	170	3.9445E − 25
84	255	171	7.2391E − 22
85	211	126	7.8713E − 18
85	212	127	3.8381E − 17
85	213	128	4.0140E − 17
85	214	129	7.2972E − 17
85	215	130	3.6706E − 17
85	216	131	8.4703E − 17
85	217	132	4.3737E − 17
85	218	133	1.2896E − 16
85	219	134	4.2549E − 17
85	220	135	1.6267E − 16
85	221	136	3.8617E − 17
85	222	137	1.6648E − 16
85	223	138	3.6814E − 17
85	224	139	1.6513E − 16
85	225	140	3.2716E − 17
85	226	141	1.6793E − 16
85	227	142	3.7205E − 17
85	228	143	2.0003E − 16
85	229	144	2.3447E − 17
85	230	145	1.3415E − 16
85	231	146	1.1473E − 17
85	232	147	7.3135E − 17
85	233	148	5.1401E − 18
85	234	149	3.6472E − 17
85	235	150	2.2116E − 18
85	236	151	1.7332E − 17
85	237	152	9.0757E − 19
85	238	153	8.0802E − 18
85	239	154	3.6301E − 19
85	240	155	3.7314E − 18
85	241	156	1.3966E − 19
85	242	157	1.7220E − 18
85	243	158	5.0756E − 20
85	244	159	8.0867E − 19
85	245	160	1.8453E − 20
85	246	161	4.5113E − 19
85	247	162	1.2438E − 20
85	248	163	3.9075E − 19
85	249	164	7.3016E − 21
85	250	165	1.4266E − 19
85	251	166	1.7480E − 21
85	252	167	5.3264E − 20
85	253	168	3.4869E − 22
85	254	169	1.9481E − 20
85	255	170	4.8795E − 23
85	256	171	7.0954E − 21
85	257	172	2.8479E − 24
85	258	173	2.7468E − 21
86	217	131	1.7111E − 16
86	218	132	1.7789E − 17
86	219	133	1.2954E − 16
86	220	134	1.8003E − 17
86	221	135	2.0811E − 16
86	222	136	2.2769E − 17
86	223	137	1.3272E − 16
86	224	138	2.3761E − 17
86	225	139	1.7024E − 16
86	226	140	2.8640E − 17
86	227	141	1.8378E − 16
86	228	142	1.6544E − 17
86	229	143	1.1667E − 16
86	230	144	8.2517E − 18
86	231	145	6.2093E − 17
86	232	146	4.0818E − 18
86	233	147	3.0737E − 17
86	234	148	2.0910E − 18
86	235	149	1.4712E − 17
86	236	150	1.1055E − 18
86	237	151	6.9461E − 18
86	238	152	5.9658E − 19
86	239	153	3.2332E − 18
86	240	154	3.1286E − 19
86	241	155	1.4886E − 18
86	242	156	1.5366E − 19
86	243	157	6.9912E − 19
86	244	158	7.0361E − 20
86	245	159	3.1761E − 19
86	246	160	2.8714E − 20
86	247	161	1.4378E − 19
86	248	162	1.0559E − 20
86	249	163	7.0566E − 20
86	250	164	4.4296E − 21
86	251	165	5.6159E − 20
86	252	166	3.8131E − 21
86	253	167	3.2710E − 20
86	254	168	1.1861E − 21
86	255	169	1.2169E − 20
86	256	170	3.0855E − 22
86	257	171	4.8442E − 21
86	258	172	5.2471E − 23
86	259	173	1.7828E − 21
86	260	174	2.9639E − 24
86	261	175	8.8593E − 22
87	221	134	2.1474E − 16
87	222	135	3.8287E − 16
87	223	136	2.4808E − 16
87	224	137	4.4531E − 16
87	225	138	3.1119E − 16
87	226	139	6.0786E − 16
87	227	140	2.5569E − 16
87	228	141	7.0885E − 16
87	229	142	1.3013E − 16
87	230	143	5.0903E − 16
87	231	144	6.7310E − 17
87	232	145	3.1545E − 16
87	233	146	3.2541E − 17
87	234	147	1.7810E − 16
87	235	148	1.5331E − 17
87	236	149	9.4220E − 17
87	237	150	7.1263E − 18
87	238	151	4.7336E − 17
87	239	152	3.2320E − 18
87	240	153	2.3996E − 17
87	241	154	1.4297E − 18
87	242	155	1.1721E − 17
87	243	156	6.0887E − 19
87	244	157	5.7250E − 18
87	245	158	2.5500E − 19
87	246	159	2.6899E − 18
87	247	160	9.8090E − 20
87	248	161	1.2590E − 18
87	249	162	3.4480E − 20
87	250	163	5.9420E − 19
87	251	164	1.1419E − 20
87	252	165	2.8987E − 19
87	253	166	4.5156E − 21
87	254	167	2.9009E − 19
87	255	168	1.0924E − 20
87	256	169	1.8599E − 19
87	257	170	2.5227E − 21
87	258	171	6.5891E − 20
87	259	172	5.4260E − 22
87	260	173	2.3225E − 20
87	261	174	8.7654E − 23
87	262	175	8.3430E − 21
87	263	176	7.6431E − 24

Table A.1 (cont.)

Z	A	N	$\langle \sigma v \rangle$ ($cm^3 s^{-1}$)
87	264	177	3.1917E − 21
87	265	178	6.4990E − 26
87	266	179	1.2339E − 21
88	222	134	1.3938E − 16
88	223	135	2.9983E − 16
88	224	136	1.5657E − 16
88	225	137	5.7828E − 16
88	226	138	8.7854E − 17
88	227	139	5.8790E − 16
88	228	140	7.6476E − 17
88	229	141	4.4028E − 16
88	230	142	4.5470E − 17
88	231	143	2.5160E − 16
88	232	144	2.1862E − 17
88	233	145	1.4019E − 16
88	234	146	1.0641E − 17
88	235	147	7.3820E − 17
88	236	148	5.3256E − 18
88	237	149	3.7923E − 17
88	238	150	2.7700E − 18
88	239	151	1.9076E − 17
88	240	152	1.4749E − 18
88	241	153	9.5488E − 18
88	242	154	8.0630E − 19
88	243	155	4.7135E − 18
88	244	156	4.3727E − 19
88	245	157	2.3080E − 18
88	246	158	2.2852E − 19
88	247	159	1.1167E − 18
88	248	160	1.1076E − 19
88	249	161	5.4501E − 19
88	250	162	5.0076E − 20
88	251	163	2.5157E − 19
88	252	164	2.0270E − 20
88	253	165	1.1637E − 19
88	254	166	7.2487E − 21
88	255	167	5.6190E − 20
88	256	168	3.2280E − 21
88	257	169	6.4660E − 20
88	258	170	5.3123E − 21
88	259	171	4.1559E − 20
88	260	172	1.6773E − 21
88	261	173	1.3765E − 20
88	262	174	4.7732E − 22
88	263	175	5.4240E − 21
88	264	176	9.7829E − 23
88	265	177	2.0288E − 21
88	266	178	9.7336E − 24
88	267	179	1.0281E − 21
89	225	136	7.5448E − 16
89	226	137	1.1431E − 15
89	227	138	5.0870E − 16
89	228	139	1.1679E − 15
89	229	140	3.6967E − 16
89	230	141	6.6998E − 16
89	231	142	2.7123E − 16
89	232	143	8.1543E − 16
89	233	144	1.4736E − 16
89	234	145	5.4127E − 16
89	235	146	7.7981E − 17
89	236	147	3.3806E − 16
89	237	148	3.9612E − 17
89	238	149	2.0089E − 16
89	239	150	1.9807E − 17
89	240	151	1.1477E − 16
89	241	152	9.7703E − 18
89	242	153	6.2846E − 17
89	243	154	4.7495E − 18
89	244	155	3.2849E − 17
89	245	156	2.2622E − 18
89	246	157	1.7266E − 17
89	247	158	1.0459E − 18
89	248	159	8.7679E − 18
89	249	160	4.5559E − 19
89	250	161	4.3900E − 18
89	251	162	1.9703E − 19
89	252	163	2.1952E − 18
89	253	164	7.6388E − 20
89	254	165	1.0381E − 18
89	255	166	2.6826E − 20
89	256	167	4.9405E − 19
89	257	168	8.9351E − 21
89	258	169	2.6313E − 19
89	259	170	6.5723E − 21
89	260	171	6.0079E − 19
89	261	172	1.2599E − 20
89	262	173	1.9903E − 19
89	263	174	3.0930E − 21
89	264	175	6.8884E − 20
89	265	176	6.5011E − 22
89	266	177	2.4181E − 20
89	267	178	1.2503E − 22
89	268	179	8.5814E − 21
89	269	180	1.5774E − 23
89	270	181	3.6652E − 21
89	271	182	4.5994E − 25
89	272	183	9.4215E − 22
90	226	136	3.9931E − 16
90	227	137	1.2521E − 15
90	228	138	2.7583E − 16
90	229	139	4.5044E − 16
90	230	140	2.1041E − 16
90	231	141	3.0403E − 16
90	232	142	1.0400E − 16
90	233	143	2.0730E − 16
90	234	144	4.4714E − 17
90	235	145	2.2161E − 16
90	236	146	2.6248E − 17
90	237	147	1.5193E − 16
90	238	148	1.3262E − 17
90	239	149	8.5731E − 17
90	240	150	6.8743E − 18
90	241	151	4.6596E − 17
90	242	152	3.6557E − 18
90	243	153	2.4987E − 17
90	244	154	1.9900E − 18
90	245	155	1.3213E − 17
90	246	156	1.1003E − 18
90	247	157	6.9151E − 18
90	248	158	6.1456E − 19
90	249	159	3.5336E − 18
90	250	160	3.3630E − 19
90	251	161	1.6787E − 18
90	252	162	1.7536E − 19
90	253	163	7.1421E − 19
90	254	164	8.4499E − 20
90	255	165	3.1471E − 19
90	256	166	3.7992E − 20
90	257	167	2.1344E − 19
90	258	168	1.5443E − 20
90	259	169	1.0324E − 19
90	260	170	5.9493E − 21
90	261	171	6.2975E − 20
90	262	172	1.5834E − 20
90	263	173	1.1394E − 19
90	264	174	6.5752E − 21
90	265	175	3.9943E − 20
90	266	176	2.1759E − 21
90	267	177	1.2902E − 20
90	268	178	6.7369E − 22
90	269	179	5.4572E − 21
90	270	180	1.6256E − 22
90	271	181	3.1677E − 21
90	272	182	2.0709E − 23
90	273	183	1.0110E − 21
91	231	140	7.5188E − 16
91	232	141	9.6401E − 17
91	233	142	4.5589E − 16
91	234	143	5.5663E − 16
91	235	144	2.3783E − 16
91	236	145	3.7442E − 16
91	237	146	1.1800E − 16
91	238	147	5.0355E − 16
91	239	148	8.8968E − 17
91	240	149	3.4234E − 16
91	241	150	4.8645E − 17
91	242	151	2.2172E − 16
91	243	152	2.5887E − 17
91	244	153	1.3672E − 16
91	245	154	1.3548E − 17
91	246	155	7.6134E − 17

Table A.1 (cont.)

Z	A	N	$\langle \sigma v \rangle$ (cm^3 s^{-1})
91	247	156	7.0902E − 18
91	248	157	2.0896E − 17
91	249	158	3.5667E − 18
91	250	159	2.2928E − 18
91	251	160	1.7580E − 18
91	252	161	1.4851E − 19
91	253	162	8.3282E − 19
91	254	163	2.0587E − 20
91	255	164	3.9232E − 19
91	256	165	3.2134E − 19
91	257	166	1.6367E − 19
91	258	167	1.7771E − 18
91	259	168	6.3765E − 20
91	260	169	9.2442E − 19
91	261	170	2.2854E − 20
91	262	171	4.7149E − 19
91	263	172	1.0778E − 20
91	264	173	9.7386E − 19
91	265	174	4.4617E − 20
91	266	175	5.3402E − 19
91	267	176	1.1985E − 20
91	268	177	1.7809E − 19
91	269	178	3.0853E − 21
91	270	179	5.9778E − 20
91	271	180	7.6460E − 22
91	272	181	2.4449E − 20
91	273	182	7.3897E − 23
91	274	183	3.4240E − 21
92	232	140	1.0806E − 16
92	233	141	7.2546E − 18
92	234	142	2.1827E − 16
92	235	143	1.1409E − 17
92	236	144	1.5651E − 16
92	237	145	3.1163E − 17
92	238	146	8.4449E − 17
92	239	147	4.1667E − 17
92	240	148	3.1876E − 17
92	241	149	1.3515E − 16
92	242	150	1.6917E − 17
92	243	151	8.6089E − 17
92	244	152	9.1251E − 18
92	245	153	4.5496E − 17
92	246	154	4.9853E − 18
92	247	155	1.5437E − 17
92	248	156	2.7833E − 18
92	249	157	1.5738E − 18
92	250	158	1.5655E − 18
92	251	159	1.6477E − 19
92	252	160	8.8729E − 19
92	253	161	3.0985E − 20
92	254	162	5.0060E − 19
92	255	163	5.1135E − 21
92	256	164	2.0444E − 19
92	257	165	3.4680E − 20
92	258	166	1.4200E − 19
92	259	167	3.7546E − 19
92	260	168	6.8696E − 20
92	261	169	3.1349E − 19
92	262	170	3.0550E − 20
92	263	171	1.3102E − 19
92	264	172	1.3385E − 20
92	265	173	1.1892E − 19
92	266	174	3.2054E − 20
92	267	175	2.6423E − 19
92	268	176	2.0235E − 20
92	269	177	9.6743E − 20
92	270	178	7.4006E − 21
92	271	179	3.4221E − 20
92	272	180	2.7142E − 21
92	273	181	1.3245E − 20
92	274	182	6.7676E − 22
92	275	183	3.0830E − 21
93	237	144	6.1633E − 16
93	238	145	2.4586E − 17
93	239	146	4.2308E − 16
93	240	147	2.0966E − 17
93	241	148	2.9882E − 16
93	242	149	5.1802E − 17
93	243	150	1.0311E − 16
93	244	151	1.1462E − 17
93	245	152	6.0596E − 17
93	246	153	3.0382E − 18
93	247	154	3.4656E − 17
93	248	155	4.7145E − 19
93	249	156	1.9053E − 17
93	250	157	8.6179E − 20
93	251	158	7.9804E − 18
93	252	159	2.3757E − 20
93	253	160	1.9424E − 18
93	254	161	8.8692E − 21
93	255	162	2.5863E − 19
93	256	163	2.1404E − 21
93	257	164	1.0438E − 18
93	258	165	1.2957E − 20
93	259	166	7.2168E − 19
93	260	167	8.1352E − 20
93	261	168	3.3053E − 19
93	262	169	6.9171E − 19
93	263	170	1.4554E − 19
93	264	171	6.1698E − 19
93	265	172	5.7399E − 20
93	266	173	9.0403E − 19
93	267	174	3.1557E − 20
93	268	175	2.6119E − 18
93	269	176	1.3374E − 19
93	270	177	1.2342E − 18
93	271	178	3.8413E − 20
93	272	179	4.0794E − 19
93	273	180	1.1868E − 20
93	274	181	1.5641E − 19
93	275	182	7.3215E − 22
93	276	183	9.8730E − 21
94	238	144	2.5242E − 16
94	239	145	2.7917E − 18
94	240	146	1.4949E − 16
94	241	147	3.6574E − 18
94	242	148	1.0708E − 16
94	243	149	3.4141E − 18
94	244	150	5.7424E − 17
94	245	151	2.9724E − 18
94	246	152	2.2132E − 17
94	247	153	6.0512E − 19
94	248	154	1.1787E − 17
94	249	155	1.2829E − 19
94	250	156	3.3975E − 18
94	251	157	3.4634E − 20
94	252	158	8.0873E − 19
94	253	159	1.3118E − 20
94	254	160	2.4670E − 19
94	255	161	5.2677E − 21
94	256	162	5.1448E − 20
94	257	163	1.3913E − 21
94	258	164	6.5205E − 20
94	259	165	4.6024E − 21
94	260	166	2.6091E − 19
94	261	167	1.5796E − 20
94	262	168	2.3233E − 19
94	263	169	6.3598E − 20
94	264	170	5.9971E − 20
94	265	171	4.7229E − 20
94	266	172	5.9315E − 20
94	267	173	1.9607E − 19
94	268	174	2.9003E − 20
94	269	175	2.1102E − 19
94	270	176	1.3198E − 19
94	271	177	5.0492E − 19
94	272	178	5.1222E − 20
94	273	179	1.7516E − 19
94	274	180	2.0379E − 20
94	275	181	6.5597E − 20
94	276	182	4.5683E − 21
94	277	183	7.8013E − 21
95	241	146	5.3828E − 16
95	242	147	1.5760E − 17
95	243	148	4.4458E − 16
95	244	149	1.7410E − 16
95	245	150	1.5709E − 16
95	246	151	6.7136E − 17
95	247	152	1.3078E − 17
95	248	153	2.0121E − 19
95	249	154	8.4168E − 19

Table A.1 (cont.)

Z	A	N	$\langle \sigma v \rangle$ (cm^3 s^{-1})
95	250	155	4.9875E − 20
95	251	156	3.3154E − 19
95	252	157	2.0380E − 20
95	253	158	2.8135E − 19
95	254	159	9.9547E − 21
95	255	160	1.9330E − 19
95	256	161	4.2695E − 21
95	257	162	2.1658E − 20
95	258	163	1.0448E − 21
95	259	164	1.5292E − 20
95	260	165	4.0036E − 21
95	261	166	1.5042E − 18
95	262	167	9.2604E − 21
95	263	168	1.3772E − 18
95	264	169	1.6321E − 20
95	265	170	4.5674E − 19
95	266	171	1.6158E − 20
95	267	172	3.2666E − 19
95	268	173	3.8973E − 19
95	269	174	1.4608E − 19
95	270	175	1.6513E − 18
95	271	176	2.5633E − 19
95	272	177	2.4222E − 18
95	273	178	3.2652E − 19
95	274	179	1.4786E − 18
95	275	180	1.1143E − 19
95	276	181	5.6186E − 19
95	277	182	3.5734E − 21
95	278	183	1.9996E − 20
96	242	146	1.7289E − 17
96	243	147	1.0438E − 18
96	244	148	1.8138E − 17
96	245	149	1.0110E − 18
96	246	150	1.8815E − 17
96	247	151	6.0629E − 19
96	248	152	4.4305E − 18
96	249	153	1.1494E − 19
96	250	154	3.2357E − 17
96	251	155	1.5308E − 17
96	252	156	1.7612E − 17
96	253	157	2.9878E − 17
96	254	158	1.0361E − 17
96	255	159	3.1574E − 17
96	256	160	6.0838E − 18
96	257	161	3.5359E − 17
96	258	162	3.5883E − 18
96	259	163	1.5567E − 17
96	260	164	4.0833E − 21
96	261	165	1.6766E − 21
96	262	166	3.2006E − 20
96	263	167	3.4010E − 21
96	264	168	2.1519E − 19
96	265	169	3.8096E − 21
96	266	170	4.1932E − 20
96	267	171	3.4902E − 21
96	268	172	1.0285E − 19
96	269	173	2.9562E − 20
96	270	174	9.7542E − 20
96	271	175	1.3175E − 19
96	272	176	7.1222E − 20
96	273	177	1.9955E − 19
96	274	178	1.8006E − 19
96	275	179	3.1583E − 19
96	276	180	9.0554E − 20
96	277	181	1.1857E − 19
96	278	182	1.5817E − 20
96	279	183	1.4507E − 20
96	280	184	2.4942E − 24
96	281	185	1.1441E − 21
97	247	150	1.8242E − 17
97	248	151	4.4303E − 17
97	249	152	2.7774E − 16
97	250	153	1.6815E − 19
97	251	154	1.3480E − 18
97	252	155	9.1548E − 20
97	253	156	2.9575E − 18
97	254	157	6.4832E − 20
97	255	158	5.2598E − 18
97	256	159	4.6682E − 20
97	257	160	3.2184E − 18
97	258	161	1.9483E − 20
97	259	162	3.0965E − 19
97	260	163	4.4314E − 21
97	261	164	7.1862E − 21
97	262	165	5.8065E − 22
97	263	166	7.2092E − 21
97	264	167	2.2029E − 21
97	265	168	4.4794E − 20
97	266	169	2.4380E − 21
97	267	170	1.8819E − 20
97	268	171	2.1697E − 21
97	269	172	7.2628E − 19
97	270	173	8.8654E − 21
97	271	174	6.7578E − 19
97	272	175	4.0779E − 20
97	273	176	3.8412E − 19
97	274	177	2.6912E − 20
97	275	178	1.5578E − 18
97	276	179	2.8233E − 20
97	277	180	5.0853E − 19
97	278	181	9.5192E − 21
97	279	182	1.1750E − 20
97	280	183	6.8273E − 21
97	281	184	4.3182E − 23
97	282	185	2.4227E − 20
97	283	186	6.1396E − 24
97	284	187	4.9158E − 21
98	248	150	3.8879E − 18
98	249	151	1.5200E − 18
98	250	152	2.3270E − 18
98	251	153	1.9058E − 19
98	252	154	2.1657E − 17
98	253	155	1.7198E − 19
98	254	156	3.4360E − 18
98	255	157	1.0664E − 19
98	256	158	4.4909E − 18
98	257	159	8.3692E − 20
98	258	160	3.2861E − 18
98	259	161	3.7462E − 20
98	260	162	5.4626E − 19
98	261	163	8.3089E − 21
98	262	164	1.6996E − 20
98	263	165	1.0679E − 21
98	264	166	9.0590E − 22
98	265	167	1.7957E − 22
98	266	168	2.4528E − 21
98	267	169	3.5794E − 22
98	268	170	3.1988E − 21
98	269	171	1.0187E − 21
98	270	172	6.2102E − 20
98	271	173	2.9911E − 21
98	272	174	1.2216E − 19
98	273	175	7.4638E − 21
98	274	176	1.0631E − 19
98	275	177	7.4095E − 20
98	276	178	1.9602E − 19
98	277	179	1.2332E − 20
98	278	180	1.1531E − 19
98	279	181	4.2840E − 21
98	280	182	2.1759E − 20
98	281	183	1.8241E − 20
98	282	184	2.9046E − 22
98	283	185	1.0295E − 20
98	284	186	7.2799E − 23
98	285	187	2.5001E − 21
98	286	188	4.7307E − 24
98	287	189	1.3527E − 21
99	253	154	2.2347E − 17
99	254	155	9.2399E − 19
99	255	156	1.4605E − 17
99	256	157	2.1400E − 19
99	257	158	4.6751E − 17
99	258	159	2.1045E − 19
99	259	160	3.3670E − 17
99	260	161	9.7397E − 20
99	261	162	4.7828E − 18
99	262	163	2.1009E − 20
99	263	164	4.8514E − 20
99	264	165	2.7556E − 21
99	265	166	1.5696E − 21
99	266	167	5.0530E − 22

Table A.1 (cont.)

Z	A	N	$\langle \sigma v \rangle$ (cm^3 s^{-1})
99	267	168	9.9246E - 22
99	268	169	7.5213E - 22
99	269	170	5.0399E - 21
99	270	171	1.5675E - 21
99	271	172	3.8541E - 20
99	272	173	1.8414E - 21
99	273	174	1.5879E - 19
99	274	175	2.9716E - 21
99	275	176	5.7002E - 19
99	276	177	7.5899E - 21
99	277	178	6.1691E - 20
99	278	179	2.0238E - 21
99	279	180	2.2765E - 20
99	280	181	1.4270E - 21
99	281	182	2.0292E - 20
99	282	183	5.3050E - 21
99	283	184	6.2259E - 22
99	284	185	1.4198E - 19
99	285	186	7.3681E - 22
99	286	187	3.8817E - 20
99	287	188	1.5144E - 22
99	288	189	2.1560E - 20
99	289	190	1.2973E - 23
99	290	191	9.3522E - 21
99	291	192	4.3931E - 26
99	292	193	3.5129E - 21
100	254	154	6.8008E - 18
100	255	155	4.6163E - 19
100	256	156	1.2326E - 17
100	257	157	5.0566E - 19
100	258	158	2.0513E - 17
100	259	159	3.2479E - 19
100	260	160	1.6172E - 17
100	261	161	1.6705E - 19
100	262	162	3.8692E - 18
100	263	163	3.6088E - 20
100	264	164	1.0994E - 19
100	265	165	4.5568E - 21
100	266	166	3.5317E - 21
100	267	167	4.5293E - 22
100	268	168	9.0002E - 22
100	269	169	6.0339E - 22
100	270	170	3.4829E - 21
100	271	171	1.2613E - 21
100	272	172	1.3854E - 20
100	273	173	1.6442E - 21
100	274	174	1.6138E - 20
100	275	175	1.3981E - 21
100	276	176	4.3718E - 20
100	277	177	2.2415E - 21
100	278	178	2.2803E - 20
100	279	179	1.9401E - 21
100	280	180	2.0418E - 20
100	281	181	1.6880E - 21
100	282	182	2.4375E - 20
100	283	183	1.1795E - 20
100	284	184	2.5650E - 21
100	285	185	4.6799E - 20
100	286	186	1.6973E - 21
100	287	187	1.8387E - 20
100	288	188	5.3005E - 22
100	289	189	1.1929E - 20
100	290	190	1.0425E - 22
100	291	191	4.0063E - 21
100	292	192	7.6693E - 24
100	293	193	1.7977E - 21
101	257	156	3.8593E - 16
101	258	157	5.7877E - 16
101	259	158	2.8865E - 16
101	260	159	4.8263E - 16
101	261	160	1.7251E - 16
101	262	161	4.1814E - 16
101	263	162	1.2785E - 16
101	264	163	3.5497E - 16
101	265	164	9.2197E - 17
101	266	165	2.9409E - 16
101	267	166	6.4410E - 17
101	268	167	2.3948E - 16
101	269	168	4.3682E - 17
101	270	169	1.8900E - 16
101	271	170	2.8582E - 17
101	272	171	1.4438E - 16
101	273	172	1.8138E - 17
101	274	173	1.0595E - 16
101	275	174	1.1097E - 17
101	276	175	7.4717E - 17
101	277	176	6.5162E - 18
101	278	177	5.1769E - 17
101	279	178	6.3160E - 18
101	280	179	1.8674E - 16
101	281	180	1.4097E - 17
101	282	181	7.5966E - 17
101	283	182	2.4986E - 19
101	284	183	1.4211E - 18
101	285	184	3.5349E - 21
101	286	185	6.5226E - 19
101	287	186	1.2023E - 20
101	288	187	2.4811E - 19
101	289	188	4.4259E - 21
101	290	189	1.5966E - 19
101	291	190	1.4878E - 21
101	292	191	8.1318E - 20
101	293	192	3.0911E - 22
101	294	193	3.6950E - 20
101	295	194	2.7163E - 23
101	296	195	6.6795E - 16
101	297	196	2.4468E - 21
101	298	197	8.1240E - 20
101	299	198	3.5227E - 22
101	300	199	2.9826E - 20
101	301	200	2.7358E - 23
101	302	201	1.0621E - 20
101	303	202	2.6506E - 25
101	304	203	3.5317E - 21
102	258	156	1.8072E - 16
102	259	157	4.9536E - 16
102	260	158	1.0997E - 16
102	261	159	3.3751E - 16
102	262	160	7.8980E - 17
102	263	161	2.7646E - 16
102	264	162	5.5482E - 17
102	265	163	2.2175E - 16
102	266	164	3.8145E - 17
102	267	165	1.7429E - 16
102	268	166	2.5562E - 17
102	269	167	1.3343E - 16
102	270	168	1.6702E - 17
102	271	169	9.9242E - 17
102	272	170	1.0714E - 17
102	273	171	7.1579E - 17
102	274	172	6.7138E - 18
102	275	173	5.0122E - 17
102	276	174	4.1715E - 18
102	277	175	3.3706E - 17
102	278	176	2.5845E - 18
102	279	177	2.2604E - 17
102	280	178	1.7727E - 18
102	281	179	9.0199E - 17
102	282	180	4.9404E - 18
102	283	181	3.3286E - 17
102	284	182	2.4885E - 19
102	285	183	5.6037E - 19
102	286	184	9.8415E - 21
102	287	185	2.2420E - 19
102	288	186	1.3546E - 20
102	289	187	1.1283E - 19
102	290	188	6.4428E - 21
102	291	189	8.0438E - 20
102	292	190	2.3221E - 21
102	293	191	3.5897E - 20
102	294	192	7.0433E - 22
102	295	193	1.8987E - 20
102	296	194	1.3844E - 22
102	297	195	6.3278E - 16
102	298	196	5.0252E - 21
102	299	197	4.3751E - 20
102	300	198	1.4044E - 21
102	301	199	1.8452E - 20
102	302	200	2.4243E - 22
102	303	201	6.8842E - 21
102	304	202	1.6960E - 23
102	305	203	2.6597E - 21

Table A.1 (cont.)

Z	A	N	$\langle \sigma v \rangle$ (cm^{3} s^{-1})	Z	A	N	$\langle \sigma v \rangle$ (cm^{3} s^{-1})	Z	A	N	$\langle \sigma v \rangle$ (cm^{3} s^{-1})
103	259	156	4.7937E − 16	104	262	158	1.9205E − 16	105	267	162	3.5857E − 16
103	260	157	6.2852E − 16	104	263	159	4.6524E − 16	105	268	163	6.0064E − 16
103	261	158	3.4744E − 16	104	264	160	1.4699E − 16	105	269	164	3.0231E − 16
103	262	159	5.8455E − 16	104	265	161	4.0523E − 16	105	270	165	5.6182E − 16
103	263	160	2.8476E − 16	104	266	162	1.1048E − 16	105	271	166	2.5015E − 16
103	264	161	5.3608E − 16	104	267	163	3.4737E − 16	105	272	167	5.1834E − 16
103	265	162	2.2875E − 16	104	268	164	8.1737E − 17	105	273	168	2.0262E − 16
103	266	163	4.8385E − 16	104	269	165	2.9275E − 16	105	274	169	4.7095E − 16
103	267	164	1.7967E − 16	104	270	166	5.9240E − 17	105	275	170	1.6037E − 16
103	268	165	4.2930E − 16	104	271	167	2.4231E − 16	105	276	171	4.2264E − 16
103	269	166	1.3742E − 16	104	272	168	4.2075E − 17	105	277	172	1.2256E − 16
103	270	167	3.7399E − 16	104	273	169	1.9615E − 16	105	278	173	3.6735E − 16
103	271	168	1.0186E − 16	104	274	170	2.9053E − 17	105	279	174	9.1943E − 17
103	272	169	3.1737E − 16	104	275	171	1.5496E − 16	105	280	175	3.1949E − 16
103	273	170	7.3689E − 17	104	276	172	1.9601E − 17	105	281	176	6.7289E − 17
103	274	171	2.6670E − 16	104	277	173	1.1942E − 16	105	282	177	2.6779E − 16
103	275	172	5.1517E − 17	104	278	174	1.2845E − 17	105	283	178	4.5781E − 17
103	276	173	2.1746E − 16	104	279	175	8.9369E − 17	105	284	179	5.9050E − 16
103	277	174	3.4827E − 17	104	280	176	8.3503E − 18	105	285	180	1.2547E − 16
103	278	175	1.7200E − 16	104	281	177	6.5220E − 17	105	286	181	3.5928E − 16
103	279	176	2.2994E − 17	104	282	178	4.9052E − 18	105	287	182	3.0065E − 18
103	280	177	1.3212E − 16	104	283	179	2.1414E − 16	105	288	183	1.5748E − 17
103	281	178	1.6992E − 17	104	284	180	1.6511E − 17	105	289	184	3.9350E − 20
103	282	179	2.7713E − 16	104	285	181	9.3165E − 17	105	290	185	9.3427E − 18
103	283	180	4.8770E − 17	104	286	182	6.1665E − 19	105	291	186	5.1399E − 19
103	284	181	1.9564E − 16	104	287	183	1.7560E − 18	105	292	187	5.5984E − 18
103	285	182	9.1449E − 19	104	288	184	2.6408E − 20	105	293	188	3.4275E − 19
103	286	183	4.9421E − 18	104	289	185	8.5768E − 19	105	294	189	4.5735E − 18
103	287	184	1.1452E − 20	104	290	186	6.7268E − 20	105	295	190	2.0990E − 19
103	288	185	2.6097E − 18	104	291	187	5.7659E − 19	105	296	191	3.0131E − 18
103	289	186	1.0291E − 19	104	292	188	3.9591E − 20	105	297	192	1.0773E − 19
103	290	187	1.2839E − 18	104	293	189	4.0093E − 19	105	298	193	1.7088E − 18
103	291	188	5.4176E − 20	104	294	190	2.0167E − 20	105	299	194	4.7533E − 20
103	292	189	9.1874E − 19	104	295	191	2.5522E − 19	105	300	195	9.7059E − 19
103	293	190	2.5476E − 20	104	296	192	8.9141E − 21	105	301	196	6.0197E − 16
103	294	191	5.3656E − 19	104	297	193	1.4285E − 19	105	302	197	1.8693E − 18
103	295	192	8.3155E − 21	104	298	194	2.8661E − 21	105	303	198	6.2925E − 20
103	296	193	2.9160E − 19	104	299	195	6.1623E − 20	105	304	199	7.4244E − 19
103	297	194	2.7208E − 21	104	300	196	5.9055E − 16	105	305	200	1.8859E − 20
103	298	195	6.3914E − 16	104	301	197	2.2937E − 19	105	306	201	2.9477E − 19
103	299	196	2.6820E − 20	104	302	198	1.1006E − 20	105	307	202	5.2690E − 21
103	300	197	4.0781E − 19	104	303	199	8.8978E − 20	105	308	203	1.1730E − 19
103	301	198	7.0576E − 21	104	304	200	3.8312E − 21	105	309	204	1.1747E − 21
103	302	199	1.5683E − 19	104	305	201	3.5940E − 20	105	310	205	4.5746E − 20
103	303	200	1.6683E − 21	104	306	202	1.0444E − 21	105	311	206	1.6467E − 22
103	304	201	5.9693E − 20	104	307	203	1.3895E − 20	105	312	207	1.7612E − 20
103	305	202	2.4775E − 22	104	308	204	1.7154E − 22	105	313	208	9.2307E − 24
103	306	203	2.2564E − 20	104	309	205	5.5760E − 21	105	314	209	6.4050E − 21
103	307	204	1.6054E − 23	104	310	206	6.8850E − 24	105	315	210	6.4113E − 27
103	308	205	8.0770E − 21	104	311	207	2.1981E − 21	105	316	211	2.2127E − 21
103	309	206	3.9248E − 26								
103	310	207	2.7718E − 21	105	263	158	4.7969E − 16	106	264	158	3.0412E − 16
				105	264	159	6.6425E − 16	106	265	159	5.8931E − 16
104	260	156	2.7949E − 16	105	265	160	4.1814E − 16	106	266	160	2.4857E − 16
104	261	157	5.2539E − 16	105	266	161	6.3469E − 16	106	267	161	5.4109E − 16

Table A.1 (cont.)

Z	A	N	$\langle \sigma v \rangle$ (cm^3 s^{-1})	Z	A	N	$\langle \sigma v \rangle$ (cm^3 s^{-1})	Z	A	N	$\langle \sigma v \rangle$ (cm^3 s^{-1})
106	268	162	1.9935E − 16	107	271	164	4.5291E − 16	108	272	164	2.7162E − 16
106	269	163	4.8979E − 16	107	272	165	6.7933E − 16	108	273	165	5.9672E − 16
106	270	164	1.5681E − 16	107	273	166	3.9838E − 16	108	274	166	2.2477E − 16
106	271	165	4.3706E − 16	107	274	167	6.5962E − 16	108	275	167	5.5621E − 16
106	272	166	1.2101E − 16	107	275	168	3.4650E − 16	108	276	168	1.8183E − 16
106	273	167	3.8440E − 16	107	276	169	6.3057E − 16	108	277	169	5.0902E − 16
106	274	168	9.1842E − 17	107	277	170	2.9527E − 16	108	278	170	1.4415E − 16
106	275	169	3.3432E − 16	107	278	171	5.9618E − 16	108	279	171	4.6020E − 16
106	276	170	6.8511E − 17	107	279	172	2.4695E − 16	108	280	172	1.1248E − 16
106	277	171	2.8489E − 16	107	280	173	5.5706E − 16	108	281	173	4.1191E − 16
106	278	172	5.0154E − 17	107	281	174	2.0297E − 16	108	282	174	8.7034E − 17
106	279	173	2.3827E − 16	107	282	175	5.1642E − 16	108	283	175	3.6761E − 16
106	280	174	3.5933E − 17	107	283	176	1.6261E − 16	108	284	176	4.1013E − 18
106	281	175	1.9612E − 16	107	284	177	2.2594E − 16	108	285	177	7.1177E − 16
106	282	176	2.5399E − 17	107	285	178	4.4073E − 16	108	286	178	2.1811E − 16
106	283	177	1.5605E − 16	107	286	179	6.9304E − 16	108	287	179	5.0548E − 16
106	284	178	1.9865E − 17	107	287	180	2.3909E − 16	108	288	180	1.0298E − 16
106	285	179	3.6999E − 16	107	288	181	5.0759E − 16	108	289	181	3.1241E − 16
106	286	180	4.7141E − 17	107	289	182	8.8904E − 18	108	290	182	3.5593E − 18
106	287	181	1.9331E − 16	107	290	183	4.2094E − 17	108	291	183	1.4124E − 17
106	288	182	1.4927E − 18	107	291	184	1.3252E − 19	108	292	184	1.3907E − 19
106	289	183	5.2457E − 18	107	292	185	2.8252E − 17	108	293	185	8.7995E − 18
106	290	184	6.3523E − 20	107	293	186	2.0030E − 18	108	294	186	7.8414E − 19
106	291	185	2.9177E − 18	107	294	187	1.9675E − 17	108	295	187	6.9759E − 18
106	292	186	2.5813E − 19	107	295	188	1.5014E − 18	108	296	188	5.7157E − 19
106	293	187	2.1796E − 18	107	296	189	1.7569E − 17	108	297	189	6.2425E − 18
106	294	188	1.7129E − 19	107	297	190	1.1038E − 18	108	298	190	4.2270E − 19
106	295	189	1.7733E − 18	107	298	191	1.2621E − 17	108	299	191	4.7564E − 18
106	296	190	1.0722E − 19	107	299	192	7.0507E − 19	108	300	192	2.7133E − 19
106	297	191	1.2367E − 18	107	300	193	8.7866E − 18	108	301	193	3.3544E − 18
106	298	192	5.8239E − 20	107	301	194	4.0054E − 19	108	302	194	1.5756E − 19
106	299	193	7.7088E − 19	107	302	195	5.3722E − 18	108	303	195	2.2160E − 18
106	300	194	2.7940E − 20	107	303	196	1.9010E − 19	108	304	196	8.1761E − 20
106	301	195	4.4045E − 19	107	304	197	2.9831E − 18	108	305	197	1.2993E − 18
106	302	196	1.1842E − 20	107	305	198	5.7351E − 16	108	306	198	3.7342E − 20
106	303	197	5.8643E − 16	107	306	199	3.3267E − 18	108	307	199	5.6475E − 16
106	304	198	5.9545E − 20	107	307	200	1.4298E − 19	108	308	200	1.1569E − 19
106	305	199	4.2271E − 19	107	308	201	1.3405E − 18	108	309	201	8.0351E − 19
106	306	200	2.2628E − 20	107	309	202	4.5847E − 20	108	310	202	4.5772E − 20
106	307	201	1.7150E − 19	107	310	203	5.5067E − 19	108	311	203	3.2731E − 19
106	308	202	8.5660E − 21	107	311	204	1.3966E − 20	108	312	204	1.8023E − 20
106	309	203	6.9567E − 20	107	312	205	2.2321E − 19	108	313	205	1.3726E − 19
106	310	204	3.0258E − 21	107	313	206	3.9516E − 21	108	314	206	6.9464E − 21
106	311	205	2.8873E − 20	107	314	207	9.0658E − 20	108	315	207	5.6910E − 20
106	312	206	7.9759E − 22	107	315	208	8.5222E − 22	108	316	208	2.4592E − 21
106	313	207	1.1395E − 20	107	316	209	3.5939E − 20	108	317	209	2.4088E − 20
106	314	208	1.2317E − 22	107	317	210	1.1181E − 22	108	318	210	6.2461E − 22
106	315	209	4.6575E − 21	107	318	211	1.3995E − 20	108	319	211	9.6494E − 21
106	316	210	5.4071E − 24	107	319	212	5.4069E − 24	108	320	212	8.8120E − 23
106	317	211	1.6343E − 21	107	320	213	5.1348E − 21	108	321	213	3.9965E − 21
								108	322	214	2.8619E − 24
107	267	160	5.6010E − 16	108	268	160	3.7882E − 16	108	323	215	1.4164E − 21
107	268	161	7.1555E − 16	108	269	161	6.6998E − 16				
107	269	162	5.0745E − 16	108	270	162	3.2331E − 16	109	271	162	6.6146E − 16
107	270	163	6.9912E − 16	108	271	163	6.3588E − 16	109	272	163	7.8642E − 16

Table A.1 (cont.)

Z	A	N	$\langle \sigma v \rangle$ (cm^3 s^{-1})
109	273	164	6.2160E − 16
109	274	165	7.8889E − 16
109	275	166	5.8007E − 16
109	276	167	7.8409E − 16
109	277	168	5.3112E − 16
109	278	169	7.7741E − 16
109	279	170	4.8036E − 16
109	280	171	7.6872E − 16
109	281	172	4.3013E − 16
109	282	173	7.5984E − 16
109	283	174	3.8568E − 16
109	284	175	7.6852E − 16
109	285	176	5.7856E − 17
109	286	177	8.0086E − 16
109	287	178	5.5821E − 16
109	288	179	7.1811E − 16
109	289	180	3.6123E − 16
109	290	181	5.9687E − 16
109	291	182	2.3017E − 17
109	292	183	8.9139E − 17
109	293	184	4.1606E − 19
109	294	185	6.7538E − 17
109	295	186	6.1382E − 18
109	296	187	5.2517E − 17
109	297	188	4.8539E − 18
109	298	189	5.0554E − 17
109	299	190	4.0712E − 18
109	300	191	4.3323E − 17
109	301	192	2.9731E − 18
109	302	193	3.2948E − 17
109	303	194	1.9681E − 18
109	304	195	2.2946E − 17
109	305	196	1.2044E − 18
109	306	197	1.4535E − 17
109	307	198	6.6145E − 19
109	308	199	7.6907E − 18
109	309	200	2.8116E − 19
109	310	201	5.5354E − 16
109	311	202	3.1683E − 19
109	312	203	2.4336E − 18
109	313	204	1.0801E − 19
109	314	205	1.0108E − 18
109	315	206	3.5410E − 20
109	316	207	4.1915E − 19
109	317	208	1.0808E − 20
109	318	209	1.7374E − 19
109	319	210	3.0659E − 21
109	320	211	7.1535E − 20
109	321	212	6.3680E − 22
109	322	213	2.8657E − 20
109	323	214	7.7590E − 23
109	324	215	1.1232E − 20
109	325	216	3.1691E − 24
109	326	217	4.1405E − 21
110	272	162	4.8073E − 16
110	273	163	7.7702E − 16
110	274	164	4.2689E − 16
110	275	165	7.6020E − 16
110	276	166	3.7318E − 16
110	277	167	7.3863E − 16
110	278	168	3.2219E − 16
110	279	169	7.1239E − 16
110	280	170	2.7455E − 16
110	281	171	6.8277E − 16
110	282	172	2.3167E − 16
110	283	173	6.5804E − 16
110	284	174	2.0160E − 16
110	285	175	7.7148E − 17
110	286	176	5.2263E − 16
110	287	177	7.3188E − 16
110	288	178	3.1740E − 16
110	289	179	5.8802E − 16
110	290	180	1.7518E − 16
110	291	181	4.1958E − 16
110	292	182	8.2522E − 18
110	293	183	3.2173E − 17
110	294	184	3.1662E − 19
110	295	185	2.2468E − 17
110	296	186	2.1134E − 18
110	297	187	1.8737E − 17
110	298	188	1.6171E − 18
110	299	189	1.7651E − 17
110	300	190	1.3270E − 18
110	301	191	1.5510E − 17
110	302	192	9.4871E − 19
110	303	193	1.2023E − 17
110	304	194	6.3305E − 19
110	305	195	8.6022E − 18
110	306	196	3.9304E − 19
110	307	197	5.6961E − 18
110	308	198	2.2053E − 19
110	309	199	3.5545E − 18
110	310	200	1.1019E − 19
110	311	201	2.0674E − 18
110	312	202	4.7327E − 20
110	313	203	5.4813E − 16
110	314	204	9.2947E − 20
110	315	205	6.4705E − 19
110	316	206	3.6753E − 20
110	317	207	2.6946E − 19
110	318	208	1.4966E − 20
110	319	209	1.1323E − 19
110	320	210	5.8445E − 21
110	321	211	4.8565E − 20
110	322	212	2.0476E − 21
110	323	213	2.0864E − 20
110	324	214	5.0057E − 22
110	325	215	8.4511E − 21
110	326	216	6.2166E − 23
110	327	217	3.5334E − 21
110	328	218	1.3947E − 24
110	329	219	1.2599E − 21
111	275	164	7.9550E − 16
111	276	165	8.9346E − 16
111	277	166	7.7497E − 16
111	278	167	9.0591E − 16
111	279	168	7.4925E − 16
111	280	169	9.2099E − 16
111	281	170	7.2028E − 16
111	282	171	9.4408E − 16
111	283	172	7.0028E − 16
111	284	173	6.0933E − 17
111	285	174	8.0374E − 16
111	286	175	8.0460E − 16
111	287	176	7.4037E − 16
111	288	177	7.6683E − 16
111	289	178	6.1901E − 16
111	290	179	7.1302E − 16
111	291	180	4.6063E − 16
111	292	181	6.3538E − 16
111	293	182	4.8877E − 17
111	294	183	1.5095E − 16
111	295	184	1.1096E − 18
111	296	185	1.2620E − 16
111	297	186	1.6080E − 17
111	298	187	1.0554E − 16
111	299	188	1.3240E − 17
111	300	189	1.0765E − 16
111	301	190	1.2151E − 17
111	302	191	1.0429E − 16
111	303	192	9.9834E − 18
111	304	193	8.9138E − 17
111	305	194	7.3431E − 18
111	306	195	7.0950E − 17
111	307	196	5.0385E − 18
111	308	197	5.2015E − 17
111	309	198	3.1739E − 18
111	310	199	3.4823E − 17
111	311	200	1.8650E − 18
111	312	201	2.1124E − 17
111	313	202	9.9181E − 19
111	314	203	1.1703E − 17
111	315	204	4.3198E − 19
111	316	205	5.4812E − 16
111	317	206	2.5607E − 19
111	318	207	1.8833E − 18
111	319	208	8.8136E − 20
111	320	209	7.8459E − 19
111	321	210	2.8781E − 20
111	322	211	3.3119E − 19
111	323	212	8.7679E − 21
111	324	213	1.3925E − 19
111	325	214	2.4759E − 21

Table A.1 (cont.)

Z	A	N	$\langle\sigma v\rangle$ (cm^3 s^{-1})	Z	A	N	$\langle\sigma v\rangle$ (cm^3 s^{-1})	Z	A	N	$\langle\sigma v\rangle$ (cm^3 s^{-1})
111	326	215	5.7442E − 20	112	323	211	2.3915E − 19	113	320	207	1.2128E − 17
111	327	216	4.9407E − 22	112	324	212	1.2999E − 20	113	321	208	3.7101E − 19
111	328	217	2.3529E − 20	112	325	213	1.0025E − 19	113	322	209	4.1948E − 18
111	329	218	5.5567E − 23	112	326	214	5.1232E − 21	113	323	210	5.6282E − 16
111	330	219	9.3238E − 21	112	327	215	4.3604E − 20	113	324	211	1.5921E − 18
111	331	220	1.8532E − 24	112	328	216	1.7406E − 21	113	325	212	7.8696E − 20
111	332	221	3.4786E − 21	112	329	217	1.8958E − 20	113	326	213	6.8030E − 19
				112	330	218	4.0435E − 22	113	327	214	2.5910E − 20
112	276	164	6.3304E − 16	112	331	219	7.7450E − 21	113	328	215	2.8631E − 19
112	277	165	9.1159E − 16	112	332	220	4.3479E − 23	113	329	216	7.7309E − 21
112	278	166	5.8063E − 16	112	333	221	3.2583E − 21	113	330	217	1.2169E − 19
112	279	167	9.1881E − 16	112	334	222	6.1122E − 25	113	331	218	2.1404E − 21
112	280	168	5.2953E − 16	112	335	223	1.1624E − 21	113	332	219	5.1048E − 20
112	281	169	9.3116E − 16					113	333	220	4.0729E − 22
112	282	170	4.8546E − 16	113	279	166	9.7444E − 16	113	334	221	2.1366E − 20
112	283	171	9.5922E − 16	113	280	167	1.0554E − 15	113	335	222	4.1879E − 23
112	284	172	9.2677E − 19	113	281	168	9.9462E − 16	113	336	223	8.6808E − 21
112	285	173	7.9524E − 16	113	282	169	1.1096E − 15	113	337	224	1.0853E − 24
112	286	174	7.2204E − 16	113	283	170	6.5710E − 19	113	338	225	3.3263E − 21
112	287	175	7.7614E − 16	113	284	171	5.2953E − 16				
112	288	176	5.9396E − 16	113	285	172	7.1411E − 16	114	280	166	8.8025E − 16
112	289	177	7.2289E − 16	113	286	173	7.7459E − 16	114	281	167	1.1356E − 15
112	290	178	4.0272E − 16	113	287	174	7.7218E − 16	114	282	168	8.8576E − 16
112	291	179	6.2596E − 16	113	288	175	7.7018E − 16	114	283	169	1.8488E − 18
112	292	180	2.5094E − 16	113	289	176	7.2922E − 16	114	284	170	2.4807E − 16
112	293	181	4.9483E − 16	113	290	177	7.4035E − 16	114	285	171	5.1639E − 16
112	294	182	1.7354E − 17	113	291	178	6.4476E − 16	114	286	172	6.8973E − 16
112	295	183	6.0170E − 17	113	292	179	7.0234E − 16	114	287	173	7.5832E − 16
112	296	184	6.8549E − 19	113	293	180	5.2543E − 16	114	288	174	7.2311E − 16
112	297	185	4.6895E − 17	113	294	181	6.4898E − 16	114	289	175	7.5176E − 16
112	298	186	5.1739E − 18	113	295	182	8.4796E − 17	114	290	176	6.2070E − 16
112	299	187	4.0772E − 17	113	296	183	2.1440E − 16	114	291	177	7.1185E − 16
112	300	188	4.1000E − 18	113	297	184	2.5819E − 18	114	292	178	4.6078E − 16
112	301	189	4.0494E − 17	113	298	185	1.9275E − 16	114	293	179	6.4053E − 16
112	302	190	3.5229E − 18	113	299	186	3.4490E − 17	114	294	180	3.1653E − 16
112	303	191	3.9669E − 17	113	300	187	1.7088E − 16	114	295	181	5.3976E − 16
112	304	192	2.8759E − 18	113	301	188	2.9597E − 17	114	296	182	3.1286E − 17
112	305	193	3.3937E − 17	113	302	189	1.7981E − 16	114	297	183	9.3694E − 17
112	306	194	2.0776E − 18	113	303	190	2.8515E − 17	114	298	184	1.3927E − 18
112	307	195	2.6881E − 17	113	304	191	1.7914E − 16	114	299	185	8.0019E − 17
112	308	196	1.4077E − 18	113	305	192	2.6678E − 17	114	300	186	1.1111E − 17
112	309	197	1.9927E − 17	113	306	193	1.7373E − 16	114	301	187	7.1512E − 17
112	310	198	8.9709E − 19	113	307	194	2.1855E − 17	114	302	188	9.0508E − 18
112	311	199	1.3789E − 17	113	308	195	1.5355E − 16	114	303	189	7.4781E − 17
112	312	200	5.3389E − 19	113	309	196	1.6593E − 17	114	304	190	8.2815E − 18
112	313	201	8.8099E − 18	113	310	197	1.2825E − 16	114	305	191	7.4928E − 17
112	314	202	2.9216E − 19	113	311	198	1.1680E − 17	114	306	192	7.3705E − 18
112	315	203	5.2920E − 18	113	312	199	1.0000E − 16	114	307	193	7.3164E − 17
112	316	204	1.4161E − 19	113	313	200	7.6794E − 18	114	308	194	5.9292E − 18
112	317	205	2.6731E − 18	113	314	201	7.1836E − 17	114	309	195	6.3622E − 17
112	318	206	3.3411E − 20	113	315	202	4.6474E − 18	114	310	196	4.3547E − 18
112	319	207	5.5337E − 16	113	316	203	4.6971E − 17	114	311	197	5.2236E − 17
112	320	208	7.8995E − 20	113	317	204	2.6346E − 18	114	312	198	3.0109E − 18
112	321	209	5.7223E − 19	113	318	205	2.7861E − 17	114	313	199	4.0199E − 17
112	322	210	3.1896E − 20	113	319	206	1.3633E − 18	114	314	200	1.9553E − 18

Table A.1 (cont.)

Z	A	N	$\langle\sigma v\rangle$ (cm^3 s^{-1})	Z	A	N	$\langle\sigma v\rangle$ (cm^3 s^{-1})	Z	A	N	$\langle\sigma v\rangle$ (cm^3 s^{-1})
114	315	201	2.8888E - 17	114	324	210	1.8571E - 20	114	333	219	4.4788E - 20
114	316	202	1.1978E - 18	114	325	211	4.3487E - 19	114	334	220	1.5511E - 21
114	317	203	1.9526E - 17	114	326	212	4.3007E - 21	114	335	221	1.8484E - 20
114	318	204	6.8685E - 19	114	327	213	9.8716E - 20	114	336	222	3.3597E - 22
114	319	205	1.2156E - 17	114	328	214	5.9437E - 22	114	337	223	7.9120E - 21
114	320	206	3.6539E - 19	114	329	215	5.8605E - 16	114	338	224	3.1300E - 23
114	321	207	7.0803E - 18	114	330	216	1.2087E - 20	114	339	225	3.3334E - 21
114	322	208	1.7312E - 19	114	331	217	1.0307E - 19	114	340	226	2.2421E - 25
114	323	209	1.6230E - 18	114	332	218	4.7522E - 21	114	341	227	1.1873E - 21

References

Allen, B.J., J.H. Gibbons and R.L. Macklin, 1971, Adv. Nucl. Phys. 4, 205.
Anders, E. and M. Ebihara, 1982, Geochim. Cosmochim. Acta 46, 2363.
Anders, E. and N. Grevesse, 1989, Geochim. Cosmochim. Acta 53, 197.
Applegate, J.H., 1988, Phys. Rep. 163, 141.
Applegate, J.H. and C.J. Hogan, 1985, Phys. Rev. D 31, 3037.
Applegate, J.H., C.J. Hogan, and R.J. Scherrer, 1987, Phys. Rev. D 35, 1151.
Applegate, J.H., C.J. Hogan and R.J. Scherrer, 1988, Astrophys. J. 329, 572.
Arnould, M., 1972, Astron. Astrophys. 19, 82.
Arnould, M. and K. Takahashi, 1990, in: Astrophysical Ages and Dating Methods, ed. J. Audouze (Editions Frontières, Gif sur Yvette) in press.
Arnould, M. and F. Tondeur, 1982, in: Proc. 4th Inter. Conf. Nuclei far from Stability, CERN-Report 81-09, p. 229.
Arnould, M., K. Takahashi and K. Yokoi, 1984, Astron. Astrophys. 137, 51.
Auerbach, N. and A. Yeverechyahu, 1975, Ann. Phys. 95, 35.
Baadwe, W., E.M. Burbidge, F. Hoyle, G.R. Burbidge, R.F. Christy and W.A. Fowler, 1956, Publ. Astron. Soc. Pac. 68, 296.
Back, B.B., O. Hansen, H.C. Britt and J.D. Garrett, 1974, Phys. Rev. C 9, 1924.
Bania, T.M., R.T. Rood and T.L. Wilson, 1987, Astrophys. J. 323, 30.
Bao, Z.Y. and F. Käppeler, 1987, At. Data Nucl. Data Tables 36, 411.
Baron, E. and J. Cooperstein, 1990, Astrophys. J. 353, 597.
Bartel, J., P. Quentin, M. Brack, C. Guet and H.-B. Hakansson, 1982, Nucl. Phys. A 386, 79.
Becchetti, F.D. and G.W. Greenlees, 1969, Phys. Rev. 182, 1190.
Beer, H., 1990, in: Astrophysical Ages and Dating Methods, ed. J. Audouze (Editions Frontières, Gif sur Yvette) in press.
Beer, H. and R.L. Macklin, 1985, Phys. Rev. C 32, 738.
Beer, H. and G. Walter, 1984, Astrophys. Space Sci. 100, 243.
Berman, B.L., 1975, At. Data Nucl. Data Tables 15, 319.
Berman, B.L. and S.C. Fultz, 1975, Rev. Mod. Phys. 47, 713.
Berman, B.L., D.D. Faul, R.A. Alvarez, P. Meyer and D.L. Olson, 1979, Phys. Rev. C 19, 1205.
Bethe, H.A., 1936, Phys. Rev. 50, 352.
Bethe, H.A. and R.F. Bacher, 1936, Rev. Mod. Phys. 9, 69.
Bjørnholm, S. and J.E. Lynn, 1980, Rev. Mod. Phys. 52, 725.
Blake, J.B. and D.N. Schramm, 1976, Astrophys. J. 209, 846.
Blake, J.B., S.E. Woosley, T.A. Weaver and D.N. Schramm, 1981, Astrophys. J. 248, 315.
Blatt, J.M. and V.F. Weisskopf, 1952, Theoretical Nuclear Physics (Wiley, New York).
Boesgaard, A. and G. Steigman, 1985, Annu. Rev. Astron. Astrophys. 23, 319.
Bohr, A. and B. Mottelson, 1975, Nuclear Structure I & II (Benjamin, New York).
Bonometto, S.A., P.A. Marchetti and S. Matarrese, 1985, Phys. Lett. B 157, 216.
Börner, G., 1988, The Early Universe (Springer, Berlin).
Bortignon, P.F. and R.A. Broglia, 1981, Nucl. Phys. A 376, 405.
Boyd, R.N. and T. Kajino, 1989, Astrophys. J. Lett. 336, L55.
Bruenn, S.W., 1989, Astrophys. J. 340, 955.
Burbidge, G.R., F. Hoyle, R.M. Burbidge, R.F. Christy and W.A. Fowler, 1956, Phys. Rev. 103, 1145.

Burbidge, E.M., G.R. Burbidge, W.A. Fowler and F. Hoyle, 1957, Rev. Mod. Phys. 29, 547.
Butcher, H.R., 1975, Astrophys. J. 199, 710.
Butcher, H.R., 1987, Nature 328, 127.
Butcher, H.R., 1988, ESO Messenger 51, 12.
Cameron, A.G.W., 1955, Astrophys. J. 121, 144.
Cameron, A.G.W., 1957, Chalk River Report CRL-41.
Cameron, A.G.W., 1973, Space Sci. Rev. 15, 121.
Cameron, A.G.W., 1982a, in: Essays in Nuclear Astrophysics, eds C.A. Barnes, D.D. Clayton and D.N. Schramm (Cambridge Univ. Press, Cambridge) p. 23.
Cameron, A.G.W., 1982b, Astrophys. Space Sci. 82, 123.
Cameron, A.G.W. and R.M. Elkin, 1965, Can. J. Phys. 43, 1288.
Cameron, A.G.W. and J.W. Truran, 1977, Icarus 30, 447.
Cameron, A.G.W., M.D. Delano and J.W. Truran, 1970, CERN 70-30 2, 735.
Cameron, A.G.W., J.J. Cowan and J.W. Truran, 1983a, Astrophys. Space Sci. 91, 235.
Cameron, A.G.W., J.J. Cowan, H.V. Klapdor, J. Metzinger, T. Oda and J.W. Truran, 1983b, Astrophys. Space Sci. 91, 221.
Cameron, A.G.W., J.J. Cowan and J.W. Truran, 1985, in: Nucleosynthesis: Challenges and New Developments, eds D. Arnett and J.W. Truran (Chicago Univ. Press, Chicago) p. 190.
Carlos, P., R. Bergere, H. Heil, A. Lepetre and A. Veyssiere, 1974, Nucl. Phys. A 219, 61.
Chaudhuri, A.K., D.N. Basu and B. Sinha, 1985, Nucl. Phys. A 439, 415.
Clark, J.P.A., E.P.J. van den Heuvel and W. Sutantyo, 1979, Astron. Astrophys. 73, 120.
Clayton, D.D., 1964, Astrophys. J. 139, 637.
Clayton, D.D., 1968, Principles of Stellar Evolution and Nucleosynthesis (McGraw-Hill, New York).
Clayton, D.D., 1969, Nature 224, 56.
Clayton, D.D., 1985a, in: Nucleosynthesis: Challenges and New Developments, eds D. Arnett and J.W. Truran (Chicago Univ. Press, Chicago) p. 65.
Clayton, D.D., 1985b, Astrophys. J. 288, 569.
Clayton, D.D., 1987, Nature 329, 637.
Clayton, D.D., 1988, Mon. Not. R. Astron. Soc. 234, 1.
Clayton, D.D., W.A. Fowler, T.E. Hull and B.A. Zimmerman, 1961, Ann. Phys. 12, 331.
Cosner, K.M. and J.W. Truran, 1981, Astrophys. Space Sci. 78, 85.
Cowan, J.J. and W.K. Rose, 1977, Astrophys. J. 212, 149.
Cowan, J.J., A.G.W. Cameron and J.W. Truran, 1980, Astrophys. J. 241, 1090.
Cowan, J.J., A.G.W. Cameron and J.W. Truran, 1982, Astrophys. J. 252, 348.
Cowan, J.J., A.G.W. Cameron and J.W. Truran, 1983, Astrophys. J. 265, 429.
Cowan, J.J., A.G.W. Cameron and J.W. Truran, 1984, in: Stellar Nucleosynthesis, eds C. Chiosi and A. Renzini (Reidel, Dordrecht) p. 151.
Cowan, J.J., A.G.W. Cameron and J.W. Truran, 1985, Astrophys. J. 294, 656.
Cowan, J.J., A.G.W. Cameron, J.W. Truran and C. Sneden, 1986a, in: Advances in Nuclear Astrophysics, eds E. Vangioni-Flam, J. Audouze, M. Cassé, J.-P. Chieze and J. Tran Thanh Van (Editions Frontières, Gif sur Yvette) p. 429.
Cowan, J.J., F.-K. Thielemann and J.W. Truran, 1986b, in: Advances in Nuclear Astrophysics, eds E. Vangioni-Flam, J. Audouze, M. Cassé, J.-P. Chieze and J. Tran Thanh Van (Editions Frontières, Gif sur Yvette) p. 477.
Cowan, J.J., F.-K. Thielemann and J.W. Truran, 1987, Astrophys. J. 323, 543.
Cowan, J.J., F.-K. Thielemann and J.W. Truran, 1991, Annu. Rev. Astron. Astrophys., in press.
Cowley, C.R. and P.L. Downs, 1980, Astrophys. J. 236, 648.
Da Silva, L., R. de la Reza and S.D. de Magalhaes, 1989, preprint.
Danos, M., 1958, Nucl. Phys. 5, 23.
Danziger, I.J., 1966, Astrophys. J. 143, 527.
Deupree, R.G. and P.W. Cole, 1983, Astrophys. J. 269, 676.
Dilg, W., S. Schantl, H. Vonach and M. Uhl, 1973, Nucl. Phys. A 217, 269.
Døssing, T. and A.S. Jensen, 1974, Nucl. Phys. A 222, 493.
Draper, J.E. et al., 1982, Phys. Rev. Lett. 49, 434.
Dutta, A.K., J.-P. Arcoragi, J.M. Pearson, R. Behrman and F. Tondeur, 1986, Nucl. Phys. A 458, 77.
Eccles, S.F., 1970, in: Engineering with Nuclear Explosives (American Nuclear Society) p. 1269.
Eichler, D., M. Livio, T. Piran and D.N. Schramm, 1989, Nature 340, 126.
Epstein, R.I., S.A. Colgate and W.C. Haxton, 1988, Phys. Rev. Lett. 61, 2038.
Eramzhyan, E.R., B.S. Ishkanov, I.M. Karpetonov and V.G. Nendatzhin, 1986, Phys. Rep. 136, 229.
Ericson, T., 1959, Nucl. Phys. 11, 481.
Fajardo, S. and J.M. Lattimer, 1990, Bul. Am. Astron. Soc. 22, 1292.
Fantoni, S., B.L. Friman and V.R. Pandharipande, 1981, Phys. Rev. Lett. 1048, 89.

Fowler, W.A., 1972, in: Cosmology, Fusion and Other Matters, ed. F. Reines (Colorado Associated Univ. Press, Boulder) p. 67.
Fowler, W.A., 1977, in: Proc. Welch Foundation Conferences on Chemical Research XXI, ed. W.D. Milligan (Robert A. Welch Foundation, Houston) p. 61.
Fowler, W.A., 1987a, Q.J.R. Astron. Soc. 28, 87.
Fowler, W.A., 1987b, Nature 330, 703.
Fowler, W.A. and F. Hoyle, 1960, Ann. Phys. 10, 280.
Fowler, W.A. and C.C. Meisl, 1986, in: Cosmogonical Processes, eds W.D. Arnett, C.J. Hansen, J.W. Truran and S. Tsuruta (VNU Press, Singapore) p. 83.
Fowler, W.A., G.E. Caughlan and B.A. Zimmerman, Annu. Rev. Astron. Astrophys. 5, 525.
French, J.B. and V.K.B. Kota, 1983, Phys. Rev. Lett. 51, 2183.
Fuller, G.M., G.J. Mathews and C.R. Alcock, 1988, Phys. Rev. D 37, 1380.
Funck, C. and K. Langanke, 1989, Astrophys. J. 344, 46.
Gallardo, M., M. Diebel, T. Døssing and R.A. Broglia, 1985, Nucl. Phys. A 443, 415.
Gallino, R., M. Busso, G. Picchio, C.M. Raiteri and A. Renzini, 1988, Astrophys. J. Lett. 334, L45.
Gardner, M.A. and D.G. Gardner, 1986, in: Nuclei off the Line of Stability, Am. Chem. Soc. Symp. Ser. 324, p. 100.
Gehren, T., 1988, Rev. Mod. Astron. 1, 52.
Gilbert, A. and A.G.W. Cameron, 1965, Can. J. Phys. 43, 1446.
Gill, R.L., R.F. Casten, D.D. Warner, A. Piotrowski, H. Mach, J.C. Hill, F.K. Wohn, J.A. Winger and R. Moreh, 1986, Phys. Rev. Lett. 56, 1874.
Gilroy, K.K., C. Sneden, C.A. Pilachowski and J.J. Cowan, 1988, Astrophys. J. 327, 298.
Goeke, K. and J. Speth, 1982, Annu. Rev. Nucl. Part. Sci. 32, 65.
Gratton, R.G., 1983, Astron. Astrophys. 123, 289.
Gratton, R.G. and C. Sneden, 1988, Astron. Astrophys. 204, 193.
Grimes, S.M. et al., 1974, Phys. Rev. C 10, 2373.
Gurevich, G.M. et al., 1981, Nucl. Phys. A 351, 257.
Hainebach, K.L. and D.N. Schramm, 1977, Astrophys. J. 212, 347.
Hallowell, D. and I. Iben, 1989, Astrophys. J. 340, 966.
Hansen, C.J., 1966, Ph.D. thesis, Yale University, unpublished.
Hardy, J.C., 1982, Phys. Lett. B 109, 242.
Hartmann, K. and T. Gehren, 1988, Astron. Astrophys. 199, 269.
Hasse, R.W. and P. Nerud, 1976, J. Phys. G 2, L101.
Haustein, P.E., 1988, At. Data Nucl. Data Tables 39, 185.
Haustein, P.E., D.S. Brenner and R.F. Casten, 1988, in: 5th Inter. Conf. Nuclei far from Stability, ed. I.S. Towner (AIP Conf. Proc. 164) p. 84.
Hilf, E.R., H. von Groote and K. Takahashi, 1976, in: Proc. 3rd Inter. Conf. on Nuclei far from Stability (Cargese), CERN 76-13, p. 142.
Hillebrandt, W., 1978, Space Sci. Rev. 21, 639.
Hillebrandt, W. and K. Takahashi, 1976, in: Proc. 3rd Inter. Conf. on Nuclei far from Stability (Cargese), CERN 76-13, p. 580.
Hillebrandt, W. and F.-K. Thielemann, 1977, Astron. Astrophys. 58, 357.
Hillebrandt, W., K. Takahashi and T. Kodama, 1976, Astron. Astrophys. 52, 63.
Hillebrandt, W., E. Müller and R. Mönchmeyer, 1990, in: The Nuclear Equation of State, eds W. Greiner and H. Stöcker (Plenum, New York) in press.
Hobbs, L.M. and D.K. Duncan, 1987, Astrophys. J. 317, 786.
Hobbs, L.M. and C. Pilachowski, 1988, Astrophys. J. Lett. 326, L23.
Hoff, R., 1986, in: Weak and Electromagnetic Interactions in Nuclei, ed. H.V. Klapdor (Springer, Heidelberg) p. 207.
Hoff, R., 1987, J. Phys. G 24, S343.
Hogan, C.J. and J.H. Applegate, 1987, Nature 320, 236.
Holmes, J.A., S.E. Woosley, W.A. Fowler and B.A. Zimmerman, 1976, At. Data Nucl. Data Tables 18, 306.
Howard, W.M., 1974, Phys. Scr. A 10, 138.
Howard, W.M. and P. Möller, 1980, At. Data Nucl. Data Tables 25, 219.
Howard, W.M., W.D. Arnett, D.D. Clayton and S.E. Woosley, 1972, Astrophys. J. 175, 201.
Howard, W.M., P. Möller, G.J. Mathews and B.S. Meyer, 1988, in: Origin and Distribution of the Elements, ed. G.J. Mathews (World Scientific, Singapore) p. 586.
Huizenga, J.R., A.N. Behkami, J.S. Sventek and R.W. Atcher, 1974a, Nucl. Phys. A 223, 577.
Huizenga, J.R., A.N. Behkami, R.W. Atcher, J.S. Sventek, H.C. Britt and H. Freiesleben, 1974b, Nucl. Phys. A 223, 589.
Ingley, J.S., 1969, Nucl. Phys. A 124, 130.
Jeukenne, J.P., A. Lejeune and C. Mahaux, 1977, Phys. Rev. C 16, 80.
Johnson, C.H., 1977, Phys. Rev. C 16, 2238.
Kajino, T. and R.N. Boyd, 1990, Astrophys. J., in press.

Kajino, T., G.J. Mathews and G.M. Fuller, 1989, in: Heavy Ion Physics and Nuclear Astrophysical Problems, eds S. Kubono, M. Ishihara and T. Nomura (World Scientific, Singapore) p. 51.
Käppeler, F., H. Beer, K. Wisshak, D.D. Clayton, R.L. Macklin and R.A. Ward, 1982, Astrophys. J. 257, 821.
Käppeler, F., H. Beer and K. Wisshak, 1989, Rep. Prog. Phys. 52, 945.
Käppeler, F., S. Jaag and Z.Y. Bao, 1990, preprint.
Kataria, S.K., V.S. Ramamurthy and S.S. Kapoor, 1978, Phys. Rev. C 18, 549.
Kawano, L., D.N. Schramm and G. Steigman, 1988, Astrophys. J. 327, 750.
Klapdor, H.V. and T. Oda, 1980, Astrophys. J. Lett. 242, L49.
Klapdor, H.V., T. Oda, J. Metzinger, W. Hillebrandt and F.-K. Thielemann, 1981, Z. Phys. A 299, 213.
Klapdor, H.V., J. Metzinger and T. Oda, 1984, At. Data Nucl. Data Tables 31, 81.
Kodama, T. and K. Takahashi, 1973, Phys. Lett. B 43, 167.
Kodama, T. and K. Takahashi, 1975, Nucl. Phys. A 239, 489.
Kolb, E.W. and M.S. Turner, 1990, The Early Universe (Addison-Wesley, Reading, MA).
Kopecky, J. and R.E. Chrien, 1987, Nucl. Phys. A 468, 285.
Kratz, K.-L., 1984, Nucl. Phys. A 417, 447.
Kratz, K.-L. et al., 1986, Z. Phys. A 325, 483.
Kratz, K.-L., F.-K. Thielemann, W. Hillebrandt, P. Möller, V. Harms, A. Wöhr and J.W. Truran, 1988, J. Phys. G 24, S331.
Kratz, K.-L., V. Harms, W. Hillebrandt, B. Pfeiffer, F.-K. Thielemann and A. Wöhr, 1990, Z. Phys. A 336, 357.
Krumlinde, J. and P. Möller, 1984, Nucl. Phys. A 417, 419.
Krumlinde, J., P. Möller, C.O. Wene and W.M. Howard, 1981, in: Proc. 4th Inter. Conf. on Nuclei far from Stability, CERN 81-09 p. 260.
Lamb, S.A., W.M. Howard, J.W. Truran and I. Iben, 1977, Astrophys. J. 217, 213.
Lattimer, J.M. and D.N. Schramm, 1974, Astrophys. J. Lett. 192, L145.
Lattimer, J.M. and D.N. Schramm, 1976, Astrophys. J. 210, 549.
Lattimer, J.M., F. Mackie, D.G. Ravenhall and D.N. Schramm, 1977, Astrophys. J. 213, 225.
Lauritzen, B., P. Arve and G.F. Bertsch, 1989, preprint, Michigan State University.
LeBlanc, J.M. and J.R. Wilson, 1970, Astrophys. J. 161, 541.
Lee, T., D.N. Schramm, J.P. Wefel and J.B. Blake, 1979, Astrophys. J. 232, 854.
Lepp, E.M. and G. Wallerstein, 1981, Mon. Not. R. Astron. Soc. 196, 543.
Le Tourneaux, J., 1956, Matt.-Fys. Medd. Dan. Vidensk. Selsk. 34, 11.
Lipparini, E. and S. Stringari, 1989, Phys. Rep. 175, 103.
Luck, R.E. and H.E. Bond, 1985, Astrophys. J. 292, 559.
Lund, E., K. Aleklett, B. Fogelberg and A. Sangariyavanish, 1986, Phys. Scr. 34, 614.
Lynden-Bell, D., 1975, Vistas Astron. 19, 299.
Lynn, J.E., 1968, The Theory of Neutron Resonance Reactions (Clarendon, Oxford).
Lynn, J.E., 1980, in: Nucl. Theory for Applications, ed. A. Salam, IAEA-SMR-43 (Inter. Atomic Energy Comm., Vienna) p. 353.
Lynn, J.E. and B.B. Back, 1974, J. Phys. A 7, 395.
Magain, P., 1989, Astron. Astrophys. 209, 211.
Mahaux, C., 1982, Phys. Rev. C 82, 1848.
Mahaux, C. and H.A. Weidenmüller, 1979, Annu. Rev. Part. Nucl. Sci. 29, 1.
Malaney, R.A., 1987, Astrophys. J. 321, 832.
Malaney, R.A. and W.A. Fowler, 1987, in: Origin and Distribution of the Elements, ed. G.J. Mathews (World Scientific, Singapore) p. 76.
Malaney, R.A. and W.A. Fowler, 1989a, Astrophys. J. Lett. 345, L5.
Malaney, R. and W.A. Fowler, 1989b, Mon. Not. R. Astron. Soc. 237, 67.
Malaney, R.A. and G.J. Mathews, 1991, Phys. Rep., to be published.
Malaney, R.A., G.J. Mathews and D.S.P. Dearborn, 1989, Astrophys. J. 345, 169.
Mampe, W. et al., 1989, Phys. Rev. Lett. 63, 593.
Mann, F.M., 1978, Hauser 5, a computer code to calculate nuclear cross sections, Hanford Engineering, HEDL-TME 78-83.
Mathews, G.J. and J.J. Cowan, 1990, Nature 345, 491.
Mathews, G.J. and D.N. Schramm, 1988, Astrophys. J. Lett. 324, L67.
Mathews, G.J. and R.A. Ward, 1985, Rep. Prog. Phys. 48, 1371.
Mathews, G.J., A. Mengoni, F.-K. Thielemann and W.A. Fowler, 1983, Astrophys. J. 276, 740.
Mathews, G.J., G.M. Fuller, C.R. Alcock and T. Kajino, 1988, in: Dark Matter, eds J. Audouze and Tran Thanh Van (Editions Frontières, France) p. 319.
Mathews, G.J., G. Bazan and J.J. Cowan, 1991, Astrophys. J., in press.
Mayle, R.W. and J.R. Wilson, 1991, in: Supernovae, ed. S.E. Woosley (Springer, New York) p. 333.
McCullagh, C.M., M.L. Stelts and R.E. Chrien, 1981, Phys. Rev. 23, 1394.
McFadden, L. and G.R. Satchler, 1966, Nucl. Phys. 84, 177.

Meier, D.L., R.I. Epstein, W.D. Arnett and D.N. Schramm, 1976, Astrophys. J. 204, 869.
Meyer, B.S., 1989, Astrophys. J. 343, 254.
Meyer, B.S. and D.N. Schramm, 1986, Astrophys. J. 311, 406.
Meyer, B.S., W.M. Howard, G.J. Mathews, P. Möller and K. Takahashi, 1985, in: Recent Advances in the Study of Nuclei off the Line of Stability, eds R. Meyer and D. Brenner (American Chemical Society, Washington, D.C.) p. 149.
Meyer, B.S., W.M. Howard, G.J. Mathews, K. Takahashi, P. Möller and G.A. Leander, 1989a, Phys. Rev. C 39, 1876.
Meyer, B.S., P. Möller, W.M. Howard and G.J. Mathews, 1989b, in: 50 Years with Nuclear Fission, ed. J. Behrens (American Nuclear Society) p. 587.
Michaud, G. and W.A. Fowler, 1970, Phys. Rev. C 2, 2041.
Miller, J.C. and O. Pantano, 1989, Phys. Rev. D 40, 1789.
Miller, G.E. and J.M. Scalo, 1979, Astrophys. J. Suppl. 41, 513.
Mitchell, L.W., M.R. Anderson, S.R. Kennett and D.G. Sargood, 1982, Nucl. Phys. A 380, 318.
Möller, P. and J.R. Nix, 1988, At. Data Nucl. Data Tables 39, 213.
Möller, P. and J. Randrup, 1990, Nucl. Phys. A 514, 1.
Möller, P., W.D. Myers, W.J. Swiatecki and J. Treiner, 1988, At. Data Nucl. Data Tables 39, 225.
Möller, P., J.R. Nix and W.J. Swiatecki, 1989, in: 50 Years with Nuclear Fission, ed. J. Behrens (American Nuclear Society) p. 153.
Mönchmeyer, R. and E. Müller, 1989, in: Timing Neutron Stars, eds H. Ögelman and E.P.J. van den Heuvel (Reidel, Dordrecht) p. 549.
Moretto, L.G., 1972, Nucl. Phys. A 185, 145.
Müller, E. and W. Hillebrandt, 1979, Astron. Astrophys. 88, 147.
Myers, W.D., 1976, At. Data Nucl. Data Tables 17, 411.
Myers, W.D., W.J. Swiatecki, T. Kodama, L.J. El-Jaick and E.R. Hilf, 1977, Phys. Rev. C 15, 2032.
Myers, W.D., W.J. Swiatecki, T. Kodama, L.J. EAl-Jaick and E.R. Hilf, 1977, Phys. Rev. C 15, 2032.
Myra, E.S. and S. Bludman, 1989, Astrophys. J. 340, 384.
Norman, E.B. and D.N. Schramm, 1979, Astrophys. J. 228, 881.
Olive, K., D.N. Schramm, G. Steigman and T. Walker, 1990, Phys. Lett. B 236, 454.
Pagel, B.E.J., 1965, Royal Observatory Bulletin No. 104.
Pagel, B.E.J., 1968, in: Origin and Distribution of the Elements, ed. L.H. Ahrens (Pergamon, Oxford) p. 195.
Pagel, B.E.J., 1987, in: A Unified View of the Macro- and Micro-Cosmos, eds A. De Rujula, D.V. Nanopoulos and P.A. Shaver (World Scientific, Singapore) p. 399.
Pagel, B.E.J., 1989, in: Evolutionary Phenomena in Galaxies, eds J.E. Beckman and B.E.J. Pagel (Cambridge Univ. Press, Cambridge) in press.
Pagel, B.E.J., 1990, in: Astrophysical Ages and Dating Methods, ed. J. Audouze (Editions Frontières, Gif sur Yvette) in press.
Pagel, B.E.J., 1991, Phys. Scripta, in press.
Pagel, B.E.J. and B.E. Patchett, 1975, Mon. Not. R. Astron. Soc. 172, 13.
Peters, J.G., 1968, Astrophys. J. 154, 225.
Peterson, R.C., 1976, Astrophys. J. 206, 800.
Peterson, R.C., R.L. Kurucz and B.W. Carney, 1990, Astrophys. J. 350, 173.
Prantzos, N., M. Hashimoto and K. Nomoto, 1990, Astron. Astrophys. 234, 211.
Prakash, M., J. Wambach and Z.Y. Ma, 1983, Phys. Lett. B 128, 141.
Press, W.H., 1986, in: The Use of Supercomputers in Stellar Dynamics, eds P. Hut and S. McMillan (Springer, Berlin) p. 184.
Raman, S., O. Shahal and G.G. Slaughter, 1981, Nature 331, 505.
Rebolo, R., P. Molaro and J.E. Beckman, 1988, Astron. Astrophys. 192, 192.
Reeves, H., 1979, Astrophys. J. 237, 229.
Rohr, G., 1982, private communication.
Rohr, G., 1984, Z. Phys. A 318, 299.
Sale, K.E. and G.J. Mathews, 1986, Astrophys. J. Lett. 309, L1.
Sargood, D.G., 1982, Phys. Rep. 93, 61.
Satchler, G.R. and W.G. Love, 1979, Phys. Rep. 55, 183.
Sato, K., 1974, Prog. Theor. Phys. 51, 726.
Schmidt, M., 1963, Astrophys. J. 137, 758.
Schramm, D.N., 1973, Astrophys. J. 185, 293.
Schramm, D.N., 1982, in: Essays in Nuclear Astrophysics, eds C.A. Barnes, D.D. Clayton and D.N. Schramm (Cambridge Univ. Press, Cambridge) p. 325.
Schramm, D.N. and Z. Barkat, 1972, Astrophys. J. 173, 195.
Schramm, D.N. and G.T. Wasserburg, 1970, Astrophys. J. 162, 57.
Seeger, P.A. and D.N. Schramm, 1970, Astrophys. J. Lett. 160, L157.
Seeger, P.A., W.A. Fowler and D.D. Clayton, 1965, Astrophys. J. Suppl. 11, 121.
Senbetu, L., 1973, Phys. Rev. C 7, 1254.

Sneden, C., 1990, in: Optical Spectroscopic Instrumentation and Techniques for the 1990's: Applications in Astronomy, Chemistry and Physics, SPIE Conf. 1318, eds B.J. McNamara and J.M. Lerner, in press.
Sneden, C. and M. Parthasarathy, 1983, Astrophys. J. 267, 757.
Sneden, C. and C.A. Pilachowski, 1985, Astrophys. J. Lett. 288, L55.
Snover, K.A., 1986, Annu. Rev. Nucl. Part. Sci. 36, 545.
Solomon, S.B. and D.G. Sargood, 1978, Nucl. Phys. A 312, 140.
Speth, J. and J. Wambach, 1980, Nucl. Phys. A 347, 389.
Spite, F. and M. Spite, 1986, Astron. Astrophys. 163, 340.
Spite, M. and F. Spite, 1978, Astron. Astrophys. 67, 23.
Spite, M. and F. Spite, 1985, Annu. Rev. Astron. Astrophys. 23, 225.
Staudt, A., E. Bender, K. Muto and H.V. Klapdor, 1989, Z. Phys. A 334, 47.
Staudt, A., E. Bender, K. Muto and H.V. Klapdor, 1990, At. Data Nucl. Data Tables 44, 79.
Steenbock, W., 1983, Astron. Astrophys. 126, 325.
Strutinsky, V.M., 1967, Nucl. Phys. A 95, 420.
Strutinsky, V.M., 1968, Nucl. Phys. A 122, 1.
Suraud, E. and P. Schuck, 1985, Phys. Lett. B 164, 212.
Symbalisty, E.M.D., 1984, Astrophys. J. 285, 729.
Symbalisty, E.M.D. and D.N. Schramm, 1981, Rep. Prog. Phys. 44, 293.
Symbalisty, E.M.D. and D.N. Schramm, 1982, Astrophys. Lett. 22, 143.
Symbalisty, E.M.D., D.N. Schramm and J.R. Wilson, 1985, Astrophys. J. Lett. 291, L59.
Tachibana, T., S. Ohsugi and M. Yamada, 1988, in: 5th Inter. Conf. Nuclei far from Stability, AIP Conf. Proc. 164, ed. I.S. Towner, p. 101.
Takahashi, K. and M. Yamada, 1969, Prog. Theor. Phys. 41, 1470.
Takahashi, K. and K. Yokoi, 1983, Nucl. Phys. A 404, 578.
Takahashi, K. and K. Yokoi, 1987, At. Data Nucl. Data Tables 36, 375.
Takahashi, K., M. Yamada and Z. Kondo, 1973, At. Data Nucl. Data Tables 12, 101.
Tepel, J.W., H.M. Hoffmann and H.A. Weidenmüller, 1974, Phys. Lett. B 49, 1.
Thielemann, F.-K. and M. Arnould, 1983, in: Proc. Inter. Conf. on Nuclear Data for Science and Technology, ed. K. Böckhoff (Reidel, Dordrecht) p. 762.
Thielemann, F.-K. and J.W. Truran, 1986, in: Nucleosynthesis and its Implications on Nuclear and Particle Physics, ed. J. Audouze (Reidel, Dordrecht) p. 373.
Thielemann, F.-K. and M. Wiescher, 1990, in: Primordial Nucleosynthesis, eds W. Thompson and B. Carney (World Scientific, Singapore) p. 92.
Thielemann, F.K., M. Arnould and W. Hillebrandt, 1979, Astron. Astrophys. 74, 175.
Thielemann, F.-K., J. Metzinger and H.V. Klapdor, 1983a, Z. Phys. A 309, 301.
Thielemann, F.-K., J. Metzinger and H.V. Klapdor, 1983b, Astron. Astrophys. 123, 162.
Thielemann, F.-K., M. Arnould and J.W. Truran, 1987, in: Advances in Nuclear Astrophysics, eds E. Vangioni-Flam et al. (Éditions Frontières, Gif sur Yvette) p. 525.
Thielemann, F.-K., M. Arnould and J.W. Truran, 1988, in: Capture Gamma-Ray Spectroscopy, eds K. Abrahams and P. van Assche (IOP, Bristol) p. 730.
Thielemann, F.-K., A.G.W. Cameron and J.J. Cowan, 1989, in: Fifty Years with Nuclear Fission, ed. J. Behrens (American Nuclear Society) p. 592.
Thielemann, F.-K., J. Applegate, J.J. Cowan and M. Wiescher, 1991, in: Nuclei in the Cosmos, eds H. Oberhummer and C. Rolfs (Springer, Berlin) in press.
Thomas, J., M.R. Zirnbauer and K. Langanke, 1986, Phys. Rev. C 33, 2197.
Tinsley, B.M., 1975, Astrophys. J. 198, 145.
Tinsley, B.M., 1977, Astrophys. J. 216, 548.
Tinsley, B.M., 1979, Astrophys. J. 229, 1046.
Tinsley, B.M., 1980, Fundam. Cosmic Phys. 5, 287.
Töke, J. and W.J. Swiatecki, 1981, Nucl. Phys. A 372, 141.
Tondeur, F., 1978, Nucl. Phys. A 303, 185.
Tondeur, F., 1983, Phys. Lett. B 123, 139.
Tondeur, F., 1985, Nucl. Phys. A 442, 460.
Tondeur, F. and D. Berdichevsky, 1985, in: Proc. 7th Inter. Conf. on Nuclear Masses AMCO-7, ed. O. Klepper (Technische Hochschule, Darmstadt) p. 472.
Tondeur, F., A.K. Dutta, J.M. Pearson and R. Behrman, 1987, Nucl. Phys. A 470, 93.
Tondeur, F., A.K. Dutta and J.M. Pearson, 1989, in: 50 Years with Nuclear Fission, ed. J. Behrens (American Nuclear Society) p. 627.
Trimble, V., 1975, Rev. Mod. Phys. 5, 877.
Truran, J.W., 1972, Astrophys. Space Sci. 18, 308.

Truran, J.W., 1973, in: Cosmochemistry, ed. A.G.W. Cameron (Reidel, Dordrecht).
Truran, J.W., 1980, Nukleonika 25, 1463.
Truran, J.W., 1981, Astron. Astrophys. 97, 391.
Truran, J.W., 1984, Annu. Rev. Nucl. Part. Sci. 34, 53.
Truran, J.W. and A.G.W. Cameron, 1966, Ark. Fys. 36, 509.
Truran, J.W. and A.G.W. Cameron, 1971, Astrophys. Space Sci. 14, 179.
Truran, J.W. and I. Iben, 1977, Astrophys. J. 216, 797.
Truran, J.W., A.G.W. Cameron and E. Hilf, 1970, CERN 70-30, p. 275.
Truran, J.W., C.J. Hansen, A.G.W. Cameron and A. Gilbert, 1966, Can. J. Phys. 44, 151.
Truran, J.W., J.J. Cowan and A.G.W. Cameron, 1978a, Astrophys. J. Lett. 222, L63.
Truran, J.W., J.J. Cowan and A.G.W. Cameron, 1978b, in: Proc. Inter. Symp. on Superheavy Elements, ed. M.A.K. Lodhi (Pergamon, New York) p. 515.
Twarog, B.A., 1980, Astrophys. J. 242, 242.
Ulrich, R.K., 1973, in: Explosive Nucleosynthesis, eds D.N. Schramm and W.D. Arnett (Univ. of Texas Press, Austin) p. 139.
Ulrich, R.K., 1982, in: Essays in Nuclear Astrophysics, eds C.A. Barnes, D.D. Clayton and D.N. Schramm (Cambridge Univ. Press, Cambridge) p. 301.
Von Egidy, T., A.N. Behkami and H.H. Schmidt, 1986, Nucl. Phys. A 454, 109.
Von Egidy, T., H.H. Schmidt and A.N. Behkami, 1988, Nucl. Phys. A 481, 189.
Von Groote, H., E.R. Hilf and K. Takahashi, 1976, At. Data Nucl. Data Tables 17, 418.
Von Weizsäker, C.F., 1935, Z. Phys. 96, 431.
Wallerstein, G., J.L. Greenstein, R. Parker, H.L. Helfer and L.H. Aller, 1963, Astrophys. J. 137, 280.
Wapstra, A.H., G. Audi and R. Hoekstra, 1988, At. Data Nucl. Data Tables 39, 281.
Wefel, J.P., D.N. Schramm, J.B. Blake and D. Pridmore-Brown, 1981, Astrophys. J. Suppl. 45, 565.
Weigmann, H. and G. Rohr, 1973, Reactor Centrum Nederland, Report 203, p. 194.
Wene, C.O. and S.A.E. Johansson, 1976, in: Proc. 3rd Inter. Conf. on Nuclei far from Stability CERN 76-13, p. 584.
Wheeler, J.C., C. Sneden and J.W. Truran, 1989, Annu. Rev. Astron. Astrophys. 27, 279.
Wiescher, M., R. Steininger and F. Käppeler, 1989, Astrophys. J. 344, 464.
Wiescher, M., J. Görres and F.-K. Thielemann, 1990, Astrophys. J. 363, 340.
Wilmore, D. and P.E. Hodgson, 1964, Nucl. Phys. 55, 673.
Woosley, S.E., 1986, in: Nucleosynthesis and Chemical Evolution, 16th Advanced Course of the Swiss Society of Astrophysics and Astronomy, eds B. Hauck, A. Maeder and G. Meynet (Geneva Observatory Press, Geneva) p. 1.
Woosley, S.E. and W.A. Fowler, 1979, Astrophys. J. 233, 411.
Woosley, S.E. and W.C. Haxton, 1988, Nature 334, 45.
Woosley, S.E. and T.A. Weaver, 1986, Annu. Rev. Astron. Astrophys. 24, 205.
Woosley, S.E., W.A. Fowler, J.A. Holmes and B.A. Zimmerman, 1978, At. Data Nucl. Data Tables 22, 371.
Woosley, S.E., D.H. Hartmann, R.D. Hoffman and W.C. Haxton, 1990, Astrophys. J. 356, 272.
Wu, C.-L., D.H. Feng, X.-G. Chen, J.-Q. Chen and M.W. Guidry, 1987a, Phys. Rev. C 36, 1157.
Wu, C.-L., X.-L. Han, Z.-P. Li and M.W. Guidry, 1987b, Phys. Lett. 194, 447.
Yang, J., M.S. Turner, G. Steigman, D.N. Schramm and K.O. Olive, 1984, Astrophys. J. 281, 493.
Yokoi, K., K. Takahashi and M. Arnould, 1983, Astron. Astrophys. 117, 65.
Zyskind, J.L. et al. 1980, Nucl. Phys. A 343, 295.